Non- Ferrous Metal Doped Magnetosomes: Growing Enhanced Magnetic Nanoparticles *in Vivo* for Biomedical Applications

By:

Zainab Abdulla M Alhursh

Supervisors:

Supervisor: Dr. S.S.Staniland

A thesis submitted in partial fulfilment of the requirements for the degree
of
Doctor of Philosophy

The University of Sheffield
Faculty of Science
Department of Chemistry

Abstract

Cancer is a major disease, affecting people globally. Breast cancer specifically, is one of the primary types of cancer affecting women between the ages of 50 and 70. Many treatments have been developed for this disease, but for certain types of tumour, current treatments are failing. Therefore, there is an urgent need for new treatments.

An example of a new type of treatment is the use of magnetic nanoparticles. These particles are nanoscale crystals of iron oxide such as magnetite. They can be magnetically driven to specific targets *in vivo* using a magnetic field external to the body. Drug molecules can be attached to them for magnetic drug delivery at lower doses. The particles can generate heat when an alternating magnetic field is present. This is known as magnetic hyperthermia, and it is capable of killing tumour cells. The particles can also be used in MRIs for cancer diagnosis.

For these applications, the particles must have a narrow size distribution, high purity, be biocompatible and stable, and have specific magnetic properties. Achieving all of these requirements is difficult using synthetic methods. However, magnetotactic bacteria use biomineralisation to produce precise size and shape particles of magnetite, which are known as magnetosomes.

This study aimed to test and enhance the leading magnetosomes for cancer treatment. Magnetosomes were synthesized with varying concentrations of Mn^{2+}, Co^{2+} and Cu^{2+} in order to optimise their magnetic properties for magnetic hyperthermia in cancer cell lines, where Co-doped magnetosomes displayed the highest coercivity (420 Oe) compared to native magnetosomes (125 Oe). This cobalt doping produced the highest apoptotic cell death *in vitro* (26.4%) and following the *in vivo,* testing confirmed that the presence of special magnetosomes with Co-doped magnetosomes within a tumour caused cell death around the sites of magnetosome localisation, compared to areas where there are no magnetosomes. In addition, for their MRI response, Mn doping enhances the T_2 relaxation with increasing concentration of manganese, whereas in native magnetosomes, the Mn doping showed the highest saturation magnetisation of Ms 112 emug^{-1} and the highest value of relaxivity 434 mM^{-1}S^{-1}, which indicates the high degree of sensitivity in MRI. Furthermore functionalising the magnetosome surface with streptavidin has confirmed cell uptake by fluorescence microscopy and flow cytometry for some future applications with bioactive substances. The

cell uptake was highest at 0.18 mg/ml concentration with low toxicity, as evidenced by the flow cytometry, MTT, and Endotoxin assays.

The outcome of this work is optimised concentrations of magnetosomes for cell uptake and cytotoxicity. The magnetic properties of magnetosomes have been enhanced through Co^{2+} and Mn^{2+} doping, and cell uptake has been investigated using TEM and fluorescence microscopy of functionalised magnetosomes. The more promising magnetosomes for magnetic hyperthermia have been tested in tumours in mice.

الي روح أبي الغالي

لا اجد الكلمات لكي اعبر عن شكري لوالدي، اللذي كان ليا عونا منذ طفولتي كنت اره خلفي يمسك يديا ليقود خطواتي وعندما كبرت فأنني اره بجانبي يساندني في كل نجاحاتي واليوم رغم انه تحت التراب ولكنه اراه امامي مبتسم لكل انجازاتي.

ويارب احفظ امي العزيزه وبارك لنا في عمرها.

وَاخْفِضْ لَهُمَا جَنَاحَ الذُّلِّ مِنَ الرَّحْمَةِ وَقُلْ رَبِّ ارْحَمْهُمَا كَمَا رَبَّيَانِي صَغِيرًا

آية 24 من سورة الإسراء

To my father spirit

I cannot find the words to express my thanks to my father, who has been my assistant since childhood. I saw him behind me holding hands to lead my footsteps. When I grew up, I saw him by my side supporting me in all my successes and today, even though he is in ground, I see him smiling in front of me for all my achievements. I wish he was here right now to give me a hug to complete my happiness

Acknowledgement

List of Content

List of Figures

List of Tables

Abbreviations

AMF	Alternating Magnetic Field
AMPs	Artificial Magnetic Particles
AMF	Alternative Magnetic Field
AC	Alternating Current
BirA	Enzymatic Biotinylation Of Proteins
BirA*	Mutant Enzymatic Biotinylation Of Proteins
BAP	Biotin Acceptor Peptide
BPL	Biotin Protein Ligase
B_o	Magnetic Field
CLIO	Crosslinked Iron Oxide
CM	Cytoplasmic Membrane
Cryo-ET	Cryo-Electron Tomography
CDF	Cation Diffusion Facilitator
CLIO	Crosslinked Iron Oxide
Cmag	Cell Rotation In A Magnetic Field
DM	Diamagnetic Maerial
dNTP	Deoxynucleotide Triphosphates
DpnI	Restriction Enzyme Which Digests Methylated DNA
DLS	Dynamic Light Scattering
DNA	Deoxyribonucleic Acid
EMF	External Magnetic Field
EU	Endotoxin
ER	Estrogen Hormone
EFTEM	Energy Filtering Transmission electron microscope
EDTA	Ethylene-Diamine-Tetraacetic Acid
EDXS	Energy Dispersive X-Ray Spectroscopy
EELS	Electron Energy Loss Spectroscopy
Fe_2O_3	Maghemite
Fe_2O_3	Hematite
Fe_3S_4	Greigite

Fe_3O_4	Magnetite
FCC	Face-Centered Cubic
FITC	Fluorescein Isothiocyante
FT-IR	Fourier-Transform Infrared Spectroscopy
FEG	Field Emission Gun
GFP	Green Fluorescent Protein
GDIO	Gadolinium Iron Oxide
GEIs	Genomic Island
Glc	Glycose
GDIO	Gadolinium Iron Oxide
Gal	Galactose
2G	Second Generation
1G	First Generation
H	Applied Magnetic Field
-H	Opposite Magnetic Field
H_c	Coercivity
HEPES buffer	(4-(2-Hydroxyethyl)-1-Piperazineethanesulfonic Acid)
H&E	Haematoxylin And Eosin Staining
Hep	Heptose
IPTG	Isopropyl β-D-1-thiogalactopyranoside).
IMAC	Immobilized Metal Affinity Chromatography
ICP-AES	Inductively Coupled Plasma-Atomic Emission Spectroscopy
IONPs	Iron Oxide Nanoparticles
Kv	Kilovolts
kDO	2-Keto-3-Deoxyoctonic Acid
K_d	Dissociation Constant
K	Anisotropy Constant
KA/m	Magnetic Field Strength Unit (Kilo Ampere Per Meter)
lacO	Lactose
LDV	Laser Doppler Velocimetry
Lys	Lysine

LB	Luria Bertani Medium
LAL	Limulus Amoebocyte Lysate
LPS	Lipopolysaccharides
mT	Millitesla
MNHT	Magnetic Hyperthermia Treatment
MTT	(3-(4,5-Dimethyl-2-Thiazolyl)-2,5-Diphenyl-2H-Tetrazolium Bromide)
MHT	Magnetic Hyperthermia Treatment
MFP	Mammary Fat Pad
MIC	Minimum Inhibitory Concentration
MTC-DOX	Magnetic Particles Doxorubicin
MNPs	Magnetic Nanoparticles
MRI	Magnetic Resonance Image
MTB	Magnetotactic Bacteria
MEIO	Magnetosomes Engineering Iron Oxide
M_r	Remanent Magnetisation
M_s	Saturation Magnetisation
MHP	Magnetic Nanoparticle Hyperthermia
Mms	Magnetosomes Membrane Specific
Mam	Magnetosome Membrane
MRI	Magnetic Resonance Image
M	Magnetisation
MD	Multi-Domain
MF	Magnetic Field
MM	Magnetosomes Membrane
MAI	Magnetosome Island
MSR-1	M. *Gryphiswaldense*
M	Magnetic Vector
MEIO	Magnetism-Engineered Iron Oxide
NHS- biotin	-Hydroxysulfosuccinimide Biotine
NHS	N-Hydroxysulfosuccinimide

NGc	N-Acetyl-Glucosamine
NPs	Nanoparticels
nm	Nanometer
Oh	Octahedral
Oe	Oersted
OM	Outer Membrane
ORFs	Open Reading Frames
OD	Optical Density
OA	Oleic Acid
SNPs	Synthetic Nanoparticles
OA-SNPs	Oleic Acid Coated Synthetic Nanoparticles
PR	Progesterone Hormones
PI	Propidium Iodide
PEG	Poly Ethyleneglycol
PVA	Poly (Vinyl Alcohol
PLA	Poly (Lactic Acid)
PNA	P-Nitroaniline
PBS	Phosphate-Buffered Saline
PAGE	Polyacrylamide Gel Electrophoresis
rcf	Relative Centrifugal Force
R_1	Longitudinal Relaxation Rate
RF/ B_1	Radiofrequency
RES	Reticuloendothelial System
SLP	Specific Lost Power
SAR	Specific Absorption Rate
SPION	Superparamagnetic Iron Oxide Nanoparticles
SPM	Superparamagnetic
SD	Single Domain
SAR	Specific Absorption Rate
SLP	Specific Loss Power
Sulfo-NHS- biotin	Sulfo-N-Hydroxysulfosuccinimide Biotine

SDS-PAGE	Sodium Dodecyl Sulfate– Polyacrylamide Gel Electrophoresis
SQUID	Super Quantum Interference Device
SPION	Superparamagnetic Iron Oxide Nanoparticles
T_1	Longitudinal Relaxation
T_2	Transverse Relaxation
Td	Tetrahedral
TBNC	Triple Negative Breast Cancer
TEM	Transtion Electron Microscopy
V	Magnetic Volume
VSM	Vibration Sample Magnetometer
U_e	Electrophoretic Mobility
ε	The Dielectric Constant
η	The Absolute Zero Shear Viscosity Of The Medium
ʃ(κa)	The Henry Function
χ	Magnetic Susceptibility

List of the conferences attended:

1	Doctoral Academy Conference - 21 June 2016.	Attendance
2	Symposium In Chemical Biology: New Horizons, Department Of Chemistry, The University Of Sheffield, (28/03/2018).	attendance
3	The Chemistry-Biology Interface (3-7-2017))The King's College London	Poster
4	Last Stage Functionalization For Synthesis And Medicines, (5/12/2016)Oxford University	Poster
5	Molecular Imaging Conference University Of Warwick And UHCW (15 Jul 2016)	attendance
6	The Science Around Us Symposium, 09/09/2016, The University Of Sheffield	Attendance
7	North West Advanced Drug Delivery Nowcadd 2016 Meeting, 23/09/2016, The University Of Manchester	attendance
8	International Conference On Materials Chemistry MC12 (22-23/7/2015) University Of York.	attendance

Chapter 1:

Introduction

1.1 Introduction

Since the 1970s micro and magnetic nanoparticles (MNPs) have been involved in many types of research. In the late 1970s, MNPs were shown to respond to an applied magnetic field within the concept for use in medicine. Some of these include; magnetic fluid hyperthermia, MRI, cell separation and targeting, enzyme immobilisation, bioseparation, gene transfection, sensing, targeted drug delivery and detection systems [1][2]. As a consequence, magnetic micro- and nanoparticles have received a lot of attention in the last four decades within the field of biomedicine. For their ability to detect the early stages of disease, and to deliver treatment dose to the right area [3]. Nanoparticles (NPs) are defined as particles that are 1-100 nm in size, which can be made of organic or inorganic material [4]. In 1854-1915 it was proposed by Paul Ehrlich that "if an agent could selectively target a disease-causing organism, then a toxin for that organism could be delivered along with the agent of selectivity" and he received the Nobel prize for medicine in 1908 for his work [2].

Nanotechnology research has progressed significantly, particularly in the field of nanomedicine. MNPs have a considerable impact on potential cancer diagnosis and treatments in medicine, especially as a contrast agent (MRI), for magnetic drug delivery and magnetic hyperthermia treatment. There are many types of MNPs that have different shapes, sizes and compositions [5]. MNPs have advantages when compared to non-magnetic nanoparticles, for example, they can be guided by external magnetic fields (EMF) to a target site and/or induce heating [4]. It is possible for therapeutic compounds to be bound to MNPs and guided to an area within the body using external magnetic fields, furthermore, inducing hyperthermia could be used to activate a drug. MNPs have also been used as enhance contrast agents in magnetic resonance image (MRI), by reducing the magnetic relaxation time of the local water protons [1][2]. Moreover, they have been used in hyperthermia treatment, especially for cancerous tumours, and for therapeutic genes as well as protein and biomolecules isolation from solution or biological matrix [2][1]. In summary MNPs have three advantages; they have the ability to be manipulated by EMF, they have a smaller size compared to the size of a cell (10-100 μm), virus (20-450 nm), protein (5-50 nm), or gene (10-100 nm long), and can produce heat when exposed to an alternative EMF [3]. This is promising for treating many diseases, potentially reducing the side effects of cytotoxic compounds by

being able to target specific areas and requiring lower drug doses. However, there are still challenges for choosing the materials and adjusting the chemical and physical characteristics [4]. Design and fabrication of functionalised particles at the nanoscale, within biocompatible requirements, is a major challenge [1].

1.2 Magnetism

In 1269 Peter Peregrinus was the first person to describe the properties of magnets, he described some particles application in large-scale sizes, such as the compass [6]. However, when the size of a magnetic material approaches the nanoscale, it will display new and different magnetic properties.

The response susceptibility of a magnetic material to an external magnetic field (EMF) can be recorded. Figure 1-1 shows a magnetisation curve of magnetisation (M) versus the strength of an applied magnetic field (H), this curve is generally sigmoidal as a result of increasing the magnetisation of the material with increasing H until it reaches magnetic saturation. This curve describes the magnetic behaviour of the material as a function of the strength of the external magnetic field, its coercivity (H_c), a remanent magnetisation (M_r) and saturation magnetisation (M_s) [7]. Applying increasing H to an unmagnetised material causes the unpaired electrons in an atom to align with the direction of the applied field until saturation (M_s). When H is the reversed back to zero, the magnetisation retreats back to a particular value, which is the remnant magnetisation (M_r) and not zero for materials which are not superparamagnetic (SPM). The magnetisation of the sample can be taken back to zero through the application of H in the opposite direction, the value of which is called coercivity (H_c). Coercivity is the resistance of a magnetic material to being demagnetised and is used to define a magnetic material as a soft magnetic material (easily demagnetised) or a hard magnetic material (retaining the magnetic memory) [7][8]. The material can then be magnetised to saturation in the reverse direction (-M_s) through the application of an opposite magnetic field (-H), shown in Figure 1-1. Once at complete saturation (M_s) in the reverse direction, the hysteresis loop can be completed when the particles are cycled between positive (+) and negative (-) fields.
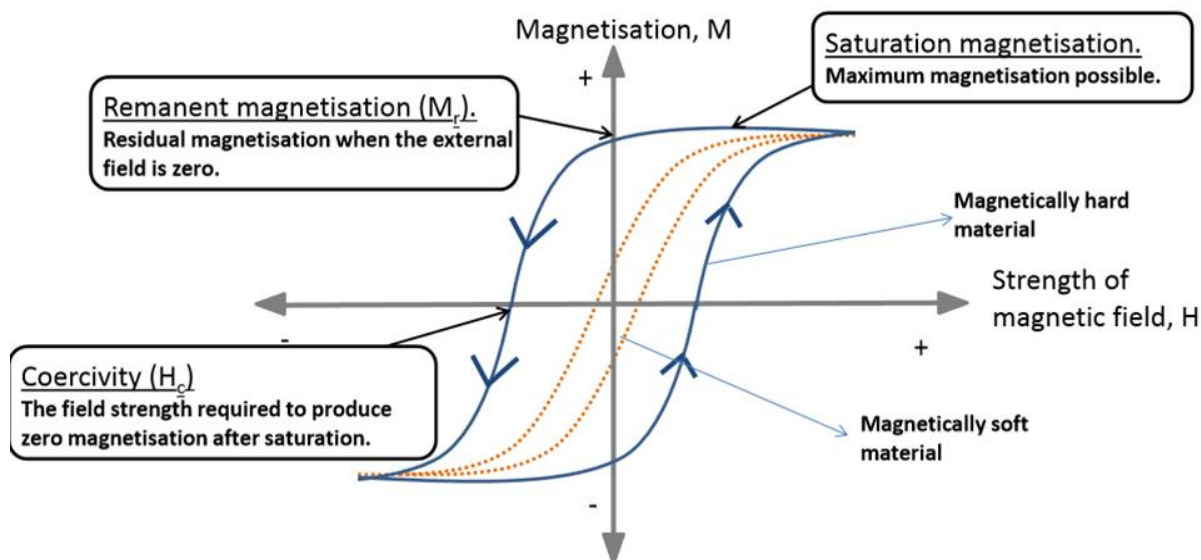
Figure 1-1: Schematic of the magnetic hysteresis loop (MH curve), it is used to measure the magnetization of material (M) as a function of the strength of EMF (H). The arrow indicates the direction of magnetization.

All materials have magnetic properties because they consist of atoms containing electrons that move. In these materials, at the atomic level, the magnetism still exists in the form of diamagnetism or paramagnetic. Diamagnetism is when all electrons are paired up in orbitals in a material (parallel and antiparallel to the external magnetic field) [9], [10]. This alignment means there is no net magnetic moment. In contrast, paramagnetic materials that have unpaired electrons in their atomic structure will align and attract to an applied magnetic field, but as they are only weakly coupled, they will be thermally reoriented when the field is removed. However, if the paramagnetic atoms are strongly coupled within a material after the external field is removed all of the magnetic moments remain aligned and the material is ferromagnetic. Ferromagnetic materials maintain their magnetic properties even after an EMF is removed Figure 1-2 [8]. If exactly half the dipoles remain aligned parallel to the field and half remain aligned antiparallel after the field is removed, then the material is antiferromagnetic (Figure 1-2) [11]. Finally, If the material has a net magnetisation with the majority of the dipoles aligned in one direction with a smaller amount aligned in the opposite direction, the material is known as ferrimagnetic (for example magnetite Fe_3O_4) (Figure 1-2) [12][13][14].

A magnetic materials properties can be classified according to its magnetic susceptibility (χ), defined as the ratio between induced magnetisation (M) and the applied magnetic field (H) equation 1.1 [8]:

$$\chi = \frac{M}{H} \tag{1.1}$$
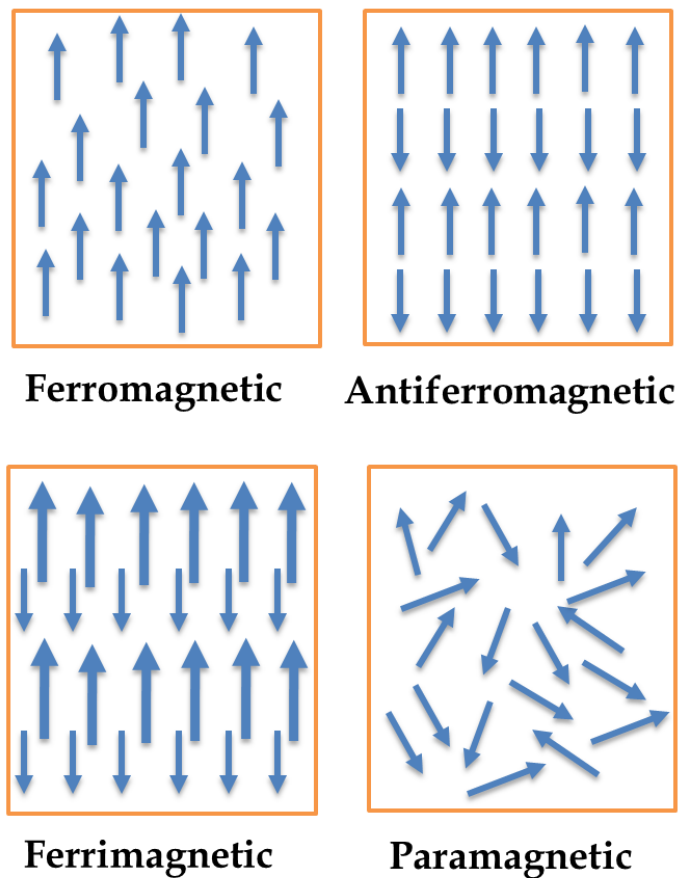
Figure 1-2: The magnetic properties of materials, where arrows represent the spin alignment of the magnetic moment. In case of ferromagnetic, Antiferromagnetic, ferrimagnetic and Paramagnetic.

Below a certain material specific size magnetic nanoparticles can become single domain, superparamagnetic and ferromagnetic (Figure 1-3 a), b) [7]. Bulk magnetic materials have a well-known multi-domain (MD) structure; it is with regions of uniform magnetisation separated by domain walls (Figure 1-3 c). A single domain (SD) magnetic nanoparticle has one magnetic domain uniformly magnetised with all spins aligned in the same direction [15]. The domains are a region within the magnetic material where range order of spins within the lattice. The number of domains in NPs increases as the particle size increases, the particles

coercivity is also affected by the number domains (Figure 1-3). The coercivity increases as particle size increases and the spins remain aligned in a single domain, as shown in Figure 1-3. To return the magnetisation back to zero, a high MF strength is required. As a result of the additive effect of all spins in a lattice, as the particle size increases particles become more multi-domain and then coercivity decreases. These multi domains with walls require lower MF strength to cause realignment due to inconsistent response in MF.
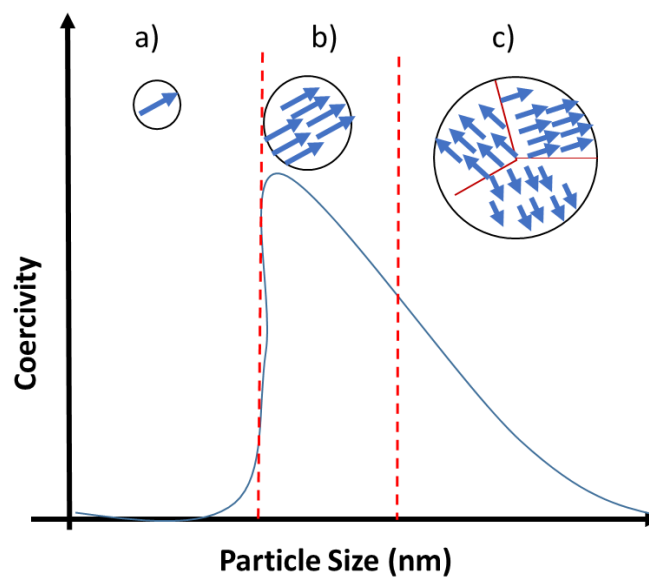
Figure 1-3: Schematic of magnetic nanoparticles shows domain formation and its effect on coercivity as magnetic particles size is increased arrange from: a) superparamagnetic NPs to b) single domain and finally c) multi-domain MNPs.

So, the large single domain magnets (all spins in alignment) are harder to flip than small particles. If the particle contains domain walls (larger particles than single domain with separate regions of aligned spin), the spin will flip at lower values of EMF.

1.3   Magnetite

Magnetite contains Fe^{2+} and Fe^{3+} in an inverse spinel structure with a 1:2 ratio of (Fe^{2+} $2Fe^{3+}O_4$) [16][17]. Table 1-1 shows the properties of magnetite. Magnetite has a ferrimagnetic structure that has the highest magnetic saturation of all iron oxides. In the crystal structure of magnetite (Figure 1-4), octahedral sites are occupied by Fe^{2+} and half of the Fe^{3+} ions. Tetrahedral sites are occupied by the remaining half of Fe^{3+} ions in a face-centered cubic (FCC)

lattice structure [18]. The ferric ions are paramagnetic (high spin configuration) with magnetic spin aligned in an MF [16]. The single domain structure of magnetite (20- 120 nm) shows an efficient and consistent response [9], [10]. The charges move between the mixed valences and this leads to rising magnetite ferromagnetic properties and a net magnetic moment in the lattice of the bulk crystal.

Table 1-1 : Physicochemical properties of magnetite [9], [10].

Property	Value
Formula	Fe_3O_4
Crystal lattice	Inverse spinel/ cubic octahedral
Magnetism	Ferrimagnetic
Solubility	35.7
Melting Temperature	1583 °C
Saturation magnetization	≈ 90 emug^{-1}
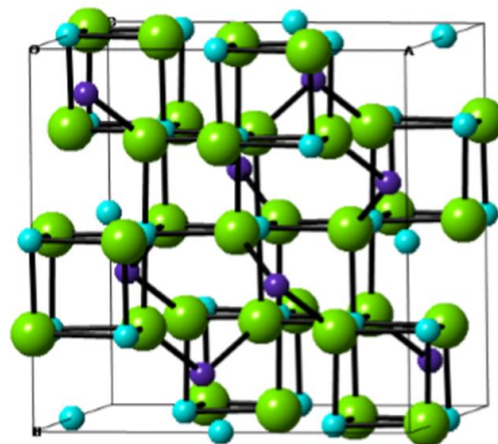
Figure 1-4: Magnetite crystal with inverse spinel unit cell, shows Fe^{3+} (pale blue) in a FCC lattice with oxygen (green) in both the octahedral and tetrahedral holes. Half of the octahedral holes are occupied with Fe^{2+} (purple).[19]

The particle size is an important factor for magnetite, MNPs which are less size than 35 nm show superparamagnetic properties [20]. Magnetite nanoparticles that are more than 120

nm become multi-domain, which are separated by domain walls [20], this reduces the particles magnetic response as an energy cost needs to be overcome [10][21][9]. So, to overcome energy in the domain walls and align the spins a higher magnetic field is required.

The metal oxides (for example Fe_3O_4, γ-Fe_2O_3) and transition metals (e.g. Co, Ni) can be utilised as a magnetic core in nanoparticles. Fe, Co and Ni as pure metals have the highest saturation magnetisations, but they are unstable when exposed to oxygen and water. The saturation magnetisation can be increased in the MNP when these pure metals are combined with other elements in the same particles [13]. For example, metal oxides such as $MnFe_2O_4$, $NiFe_2O_4$, $CoFe_2O_4$, and Fe_3O_4, that are less sensitive to oxidation give desirable stable magnetic responses [13]. Moreover, superparamagnetic particles can be synthesised by different routes, but some iron oxide particles can be prepared in the superparamagnetic diameter range of 20-50 nm [9].

Another natural preparation of iron oxide nanoparticles is those generated by magnetotactic bacteria, within lipid vesicles known as magnetosomes [9]. Most of the magnetosome particles (MPs) from the Magnetotactic bacteria lie in a range between 30-80 nm, are single domain, and composed of ferrimagnetic magnetite [22][20].

1.4 Formation of magnetic nanoparticles

MNPs can be prepared by many synthetic methods, and each one has advantages and disadvantages. For biomedical applications, MNPs should avoid agglomeration, and it is also necessary to ensure they are stable at physiological pH, pure [23], uniform in size and are biocompatible [24],[25].

For different applications the nanoparticles can vary in core size, surface functionality and shape all of which depends on the synthetic methods used to produce the nanoparticles. The formation of iron oxide (in the form Fe_xO_y) depends on the reaction pH, oxygen content and the ratio of iron oxide. When these conditions are correct magnetite is produced, otherwise, other iron minerals are produced [16]. Small disturbances in reaction conditions can result in changes to the iron oxide mineralisation.

1.4.1 **Chemical based synthesis**

1.4.1.1 Thermal decomposition

Thermal decomposition is one synthetic route to synthesise metal and metal oxide MNPs with a narrow size distribution and consistent shape [15],[26]. The size and shape are dependent on the reaction temperature and the ratio of reactants, as well as the time of the reaction and the time after synthesis [15]. This allows the shape, size and magnetic properties of MNP to be tuned by varying these conditions. However, thermal decomposition demands high temperatures ($\approx$250-300°C) as well as harsh chemical surfactants and solvents, for example, benzyl ether, toluene, hexane and chloroform [15],[26]. As a result, thermal decomposition is not environmentally friendly, and particles may remain non-biocompatible prohibiting their use in biomedical applications [27].

1.4.1.2 Co-precipitation

The co-precipitation method can be used for the synthesis of iron oxide NPs [28]. It is one of the simplest and fastest synthetic methods that produces a large amount of product. Magnetic iron oxides (e.g. maghemite and magnetite) can be produced from a mixture of aqueous solutions of ferric (Fe^{3+}) and ferrous (Fe^{2+}) ions under an inert atmosphere, by adding a base to raise the pH and using a mixed molar ratio of 2:1. The type of salts used and the molar ratio can affect the size, shape and composition of nanoparticles, (e.g., perchlorates, nitrates, sulphate, chlorides etc.) [29][15][30]. For more efficient magnetite synthesis the pH of the solution should be between 9-14 [30].The equation for the chemical reaction is as follows:

$$Fe^{2+} + 2Fe^{3+} + 8OH^- \longrightarrow Fe_3O_4 + 4H_2O \qquad (1.2)$$
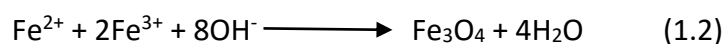
As the pH is raised the insoluble iron oxides precipitate out of solution, once base is added MNP formation occurs very quickly; this results in particles having a large size and shape distribution (14 ± 9.9) [31]. Owing to this rapid precipitation, there will be large local variations in pH and incomplete mixing of the reactant can occur [15]. In the presence of oxygen, magnetite (Fe_3O_4) tends to convert into maghemite (Fe_2O_3) and also $Fe(OH)_3$ via the following reaction: [29][30]

$$Fe_3O_4 + 0.25O_2 + 4.5\ H_2O \longrightarrow 3Fe(OH)_3 \quad (1.3)$$
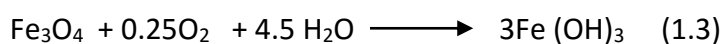
However, the co-preception method generates MNPs with a wide size distribution [30].

1.4.1.3 Partial oxidation of ferrous hydroxide

During the reaction, the ferrous hydroxide forms from a ferrous salt which is then partially oxidised at 80-90°C in the presence of nitrate. Heating and the use of a mild oxidant are required to form MNPs [31],[32]. Finally, the mixture of ferrous and ferric hydroxides are dehydrated to give magnetite.[33]

$$3Fe^{2+} + 6OH^- \longrightarrow 3Fe(OH)_2 \quad\quad\quad (1.4)$$

$$2Fe(OH)_2 + NO_3^- + H_2O \longrightarrow 2Fe(OH)_3 + NO_2^- \quad (1.5)$$

$$Fe(OH)_2 + 2Fe(OH)_3 \longrightarrow Fe_3O_4 + 4H_2O \quad (1.6)$$
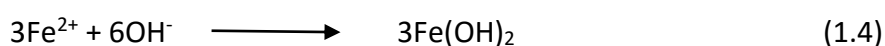
The size, shape and iron mineral produced through this reaction can be altered by varying the iron salts, the ratio of reactants, type of base and the temperature [34]. So, this method requires careful control of all these reaction conditions.

Another method to generate MNPs with tuneable size and distribution properties, is the thermodynamic stable isotropic dispersion of two immiscible liquids in presence of an appropriate surfactant. Microemulsions have large interfacial areas, ultralow interfacial tension and the capacity to solubilize in both oil-soluble and aqueous compounds [30].

Hydrothermal synthesis is another method used to produce MNPs with good shape control and narrow size distribution. This reaction requires high temperatures (130-250°C) and pressures (0.3-4 MPa) and is carried out in aqueous solution [30].

In summary, the simplest method is the co-precipitation method, because the reaction conditions are environmentally friendly, and scalable to industrial levels [5]. However, this method has a disadvantage. The MNPs generated are of uncontrolled sizes and shapes, the particles are inhomogeneous, and poorly crystalline. This inhomogeneity could impede using MNPs for precise purposes and require optimisation for the desired application. Another method is thermal decomposition whereby control of the temperature can result in tuned materials in terms of shape, size and composition. The advantage of this method is that it can

be used to generate a uniform crystalline product, which is critical to governing magnetic properties, because the thermal decomposition synthesised MNPs are prepared in an organic solvent. There is a disadvantage associated with this method, surface modifications are required for the nanoparticles surface to become hydrophilic [5]. Many attempts have been made recently to prepare MNPs for multi-use in both therapy and diagnosis, or "theranosis" [35], (theranosis has been used to describe these two process combined).[5] Table 1-2 compares some of the synthesis methods for iron oxide nanoparticles [30].

Table 1-2: Comparison of synthesis methods for iron oxide NPs.

Synthesis method	Operation all react	Temperature (°C)	Size distribution	Shape control	Duration
Co-precipitation	Simple and ambient	20-90	broad	poor	Minutes
Thermal decomposition	Complicate	100-320	Very narrow	Very good	Days
Microemulsion	Complicated and ambient	20-50	Relatively narrow	Good	Hours
Hydrothermal synthesis	High pressure temperature	≈220	Very narrow	Very good	Hours

1.5 Surface coating

The primary challenge for MNPs use in clinical applications is the tuning of surface coating materials. During the synthesis process, MNPs can be coated with various stabiliser materials such as polymer or surfactants. For example, oleic acid, dodecylamine, sodium oleate andsodium dodecylbenzene sulphonate have been used for coating [36]. The coating polymer materials can be either natural as dextran, chitosan and starch or synthetic polymer like poly(ethyleneglycol) (PEG), poly(vinyl alcohol) (PVA) and poly(lactic acid) (PLA) [30]. This coating can consist of long chains of organic/inorganic polymers or ligands. These polymers or ligands can be inserted during synthetic NP (in-situ) coating or the surface coating material is introduced to the SNPs core after its formation (post-synthetic coating). MNPs without coating have a hydrophilic surface that results in interactions between the particles that can cause particles to agglomerate and form a large cluster. For stability and dispersion, a coating is preferable. Coating also helps with solubility, it provides a suitable substrate for surface modification with bioactive substances such as an antibodies, proteins, and folic acid [36].

Furthermore, a coating prevents the MNPs from being attacked by the immune system and removed from the body, providing biocompatibility to prevent any toxicity from metal leakage from the magnetic mineral core into the surrounding environment [37]. Also, coating provides colloidal stability of organic solvent/water based suspensions [37], and good dispersion of MNPs in biological environment enhance compatibility in blood. Coatings also prevent oxidation of MNPs in air and loss of their magnetism and stability. Coating is a vital key to eliminate all of these [30].

Oleic acid that is used as a coating, is a monounsaturated fatty acid, which has (C18) oleic tail with a cis double bond in the middle [29] and an active group (carboxylic acid) that attaches to the surface of the magnetic core (Figure 1-5) [37].

Adding coating on MNPs can increase the mass of them, and as a result reduce the overall magnetization [37]. Magnetite and maghemite are widely used in biomedical applications such as in diagnostics (MRI) and for treatment by hyperthermia. However, it is essential to consider surface modification with functional molecules, such as antibodies, peptides, proteins and DNA. Surface modifications are based on outward-oriented amino acids of phospholipids that facilitate the immobilisation of functional molecules onto the magnetosomes surface through a cross-linking reaction [38].
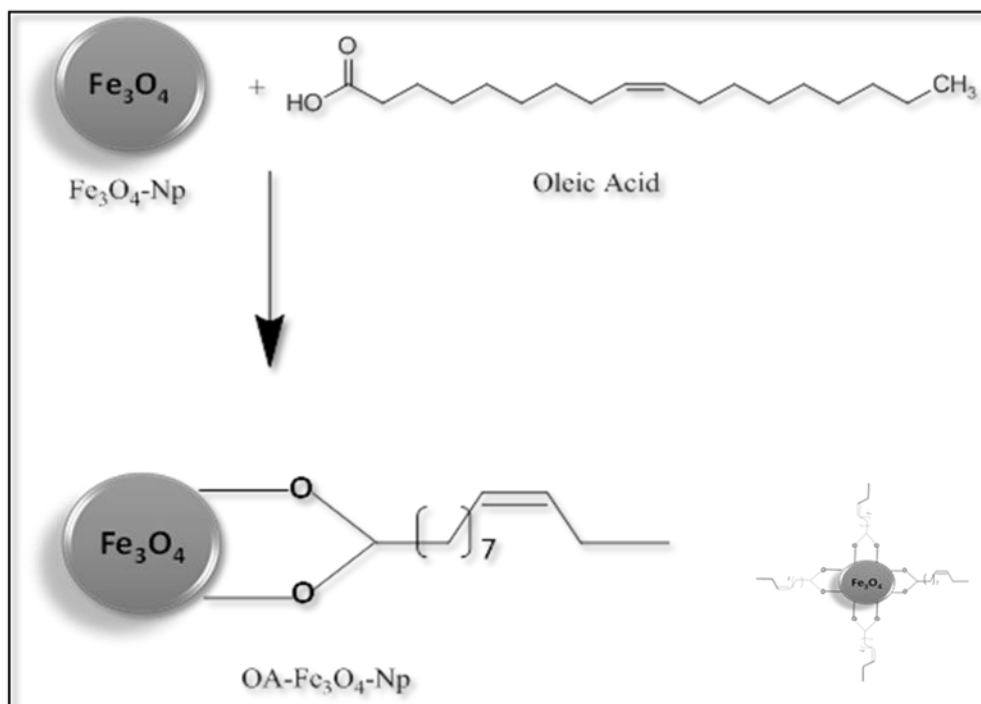
Figure 1-5:Coating scheme of bare SNPs using Oleic acid to produce OA-SNPs adopted from Liu *et al.* [39]

1.6 Introduction to Magnetotactic Bacteria MTB and synthesis of Magnetic Nanoparticles

1.6.1 Introduction to magnetotactic Bacteria (MTB)

Magnetotactic Bacteria (MTB) are part of the wide range of a group of phylogenetic bacteria, which includes δ-proteobacteria, α- proteobacteria, ɣ- proteobacteria and Nitrospira. These bacteria are found in a variety of marine, aquatic and freshwater environments [40]. MTB was first documented in 1963 by Savator Bellini [41]. He saw a certain group of bacteria under the microscope that swim to Earth's North Pole direction and gave them the name "magnetosensitive bacteria". Eleven years later Blackmore rediscovered them and developed the term magnetotaxis, for the cells as *Magnetospirillum magnetotacticum* (MS-1) [42]. Many other species of these bacteria have also been discovered.

They are able to thrive only in an microaerobic or anaerobic transition zone [43]. MTB are described as exhibiting magneto-aerotaxis because they passively align to a magnetic field and also use this to sense oxygen gradients to guide their swimming direction, away from advancing oxygen by using flagella [40][20]. The majority of these bacteria produce nano-

sized crystals (Figure 1-6) with specific morphologies; this could give MTB a massive impact in different disciplines [44][20].
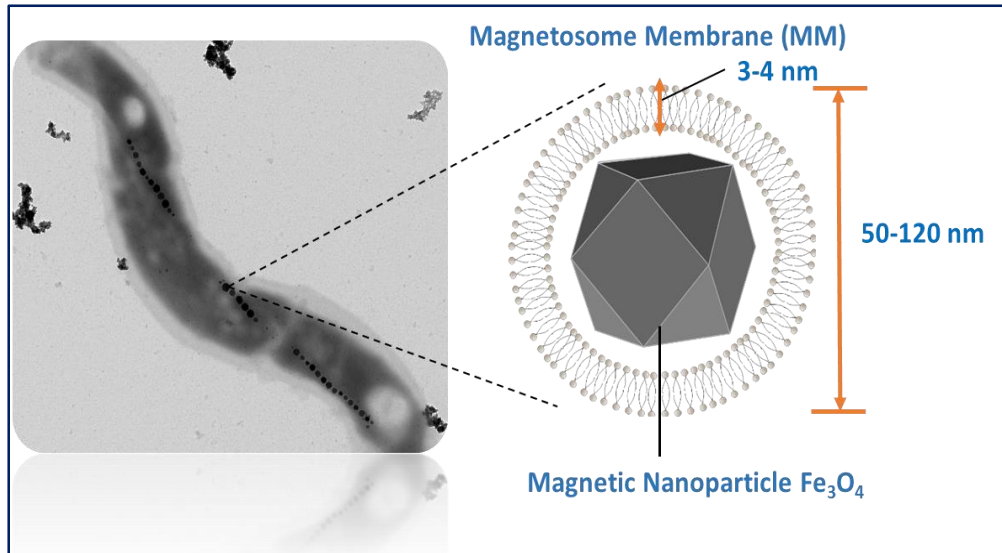
Figure 1-6: Transmission electron microscope (TEM) of Magnetospirillum magneticum AMB-1, which is a species of MTB with magnets inside their cell. Scale bar = 0.2µm.

All magnetotactic bacteria to date are Gram-negative; but have various morphology including spirilla, cocci, vibrio, ovoid, rod-shape and multicellular [40][45]. MTB are a group of heterogeneous bacteria that have the ability to orient themselves with a magnetic field, based on the presence of intracellular magnetosome arrangements [45],[20]. The magnetosome nanoparticles are a single magnetic domain (SD), having sizes ranging between 35-120 nm and permanent magnetic behaviours as a result from the magnetic crystal consisting of inorganic iron oxide covered with a lipid bilayer (Figure 1-6) [46]. Magnetosomes are organised in chains, which are perpendicular to the cell axis, this makes the cell able to migrate along the Earth's magnetic field lines and to maintain its location within the oxic-anoxic transition zone boundary [46]. Transmission electron microscopy shows that the thickness of the lipid bilayer membrane, encapsulating an individual magnetosomes is approximately 2-4 nm. The number of magnetosomes per cell varies between a few magnetosomes to many based on the strain [43][44]. AMB-1 magnetosomes have a size between 50-60 nm, have approximately 15-20 magnetosomes along a cell, and magnetosome particles that are produced by this bacteria are of high chemical purity and uniform size are made of magnetite (Figure 1-6) [47]. MTB were discovered several decades ago, despite that

the mechanism of the magnetosome formation and biomineralisation has not been fully elucidated yet [47]. The magnetosome membrane of AMB-1 consists of 58-65% phospholipids of the total lipids, fatty acid and proteins. Many proteins expressed are similar to those found in the cytoplasmic membrane. However, five concatenated magnetosome protein sequences have been shown to be unique to the magnetosome membrane. The lipid bilayer membranes offer simple dispersion of magnetosomes in an aqueous solution. They can be easily isolated from the heterogeneous solution using a magnetic field (MF).

1.6.2 Biosynthesis of Magnetic nanoparticles (Biomineralization and magnetosomes formation)

Biomineralisation is crucial for living organisms as it provides essential functions. For example, calcium carbonate ($CaCO_3$) is mineralised in molluscs to form shells for protection. In bones and teeth, hydroxyapatite ($Ca_{10}(pO_4)_6(OH)_2$), is used to give structural support and for mastication, as too are amorphous silica (SiO_2) in marine sponges and magnetite (Fe_3O_4) in chiton teeth. Such biominerals are generated under biological conditions, at ambient temperature and almost neutral pH and use environmentally abundant elements [47]. Some organisms such as bacteria and birds use magnetite nanocrystals as a biological sensor compass to find preferable habitats [47]. One of these organisms that can synthesise MNP crystals is MTB [43]. MTB are highly abundant in marine and freshwater habitats, but only a few strains have been cultivated in the lab [48]. Most MTB isolated are Alphaproteobacteria, which grow either in the microaerobic or anaerobic environment. Perhaps only a few strains have been isolated in pure culture because it is difficult to recreate the complex chemical gradients in the lab [49]. The magnetosomes are similar to eukaryotic organelles, where it consists of a lipid bilayer membrane that form into a vesicle, which is named the magnetosome membrane (MM) as well as an outer membrane (OM) and cytoplasmic membrane (CM) (figure 1-8 b) [50][51]. Understanding the fundamentals mechanisms of biomineralization in MTB may help understanding of biomineralisation in general. These magnetosomes contain single domain magnets with stable magnetic moment enhanced by being arranged in a chain to help the cells swim and to move along the magnetic field [48].

The genome of MTB has been sequenced and annotated. It was found to contain magnetosome forming proteins, which are found within the magnetosome membrane [40].

This means that the chemical, biochemical and genetic magnetosome formation is developing and allowed an understanding of the function of unique intracellular organelles.

The genome information from several magnetotactic α-proteobacteria has become available, during the last few years, when draft genome data identified for a complete genome sequence of M. magneticum strain AMB-1 [49], *M.magnetotacticum* strain MS-1 (http://www.jg.doe.gov), *M.gryphiswaldense* strain MSR-1 and the marine magnetic coccus strain MC-1 [50]. Because only a few species of MTB are available in pure culture, most current knowledge on magnetosome synthesis genes comes from analysis of *magnetospirillum* species, specifically those listed above [51].

Analysis of MTB genomes has identified some genes and proteins for specific function. Two facultative anaerobic *Magnetospirillum magneticum* AMB-1 and MGT-1, and *Desulfovibrio magneticum* RS-1 have been successfully isolated. These are all α-proteobacteria that are able to synthesise cuboctahedral shaped magnetosomes and are capable of growing in liquid and on solid media under both microaerobic and anaerobic conditions. This made them an ideal candidate for genetic manipulation and to provide more information for genes that are involved in magnetosome biomineralisation [38].

Magnetosome biogenesis has previously been described in three or four steps [38],[52]. The extra step can be considered as the assembly of magnetosomes into chains. Up to now, more than 40 different genes are identified related to producing magnetosomes [53]. Most magnetosome proteins in *M. gryphiswaldense* and other magnetospirilla are magnetosomes membrane specific (Mms) and magnetosome membrane (Mam) and so named. These tend to be clustered into operons within one specific region on the genome, described as the genomic Magnetosome Island (MAI), [54] or Genomic Island (GEIs) in other literature [55], which within 65 kb bases [51]. Mam and Mms proteins have many different roles during the magnetosome formation process. Beginning with membrane invagination, then protein sorting, biomineralisation controlling the shape and the size and finally magnetosomes assembly into a chain. They have been classified based on these stages [56]. The larger operon is mamAB, which has essential and sufficient roles to start primer biomineralisation, and the smaller operons are mamGFDC, mms6 and mamXY, which have accessory functions in regulating biomineralisation [52].

- mms6 operon is located 3.6 kb upstream of the mamGFDC operon and contains five genes (Figure 1-7) [51].

- mamGFDC operon is comprised four genes and located about 30 kb downstream of mamAB [51].

- mamAB covers 17 genes in a range of 16.4 kb of DNA [51].

- The mamXY operon encodes mamx and mamY within MAI located about 30 kb downstream of mamAB [51].
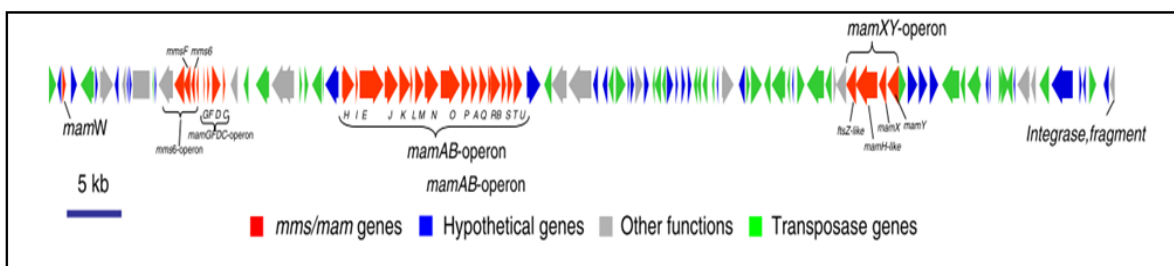
Figure 1-7: The genomic magnetosomes island from Magnetospirillum gryphiswaldens, including the genes encoding magnetosomes genes. The arrows in various colours, represent an open reading frame ORFs [51].

These gene clusters in Figure 1-7 are proposed to encode many genes required for magnetotaxis functionalisation and also several other genes, whose function either has not established is ambiguous, or not of a specific function in the cell. The genomic region in *M.magneticum* AMB-1 and other magnetospirilla that have a similar molecular structure, operon organisation and gene content were identified [55][51].

The first genome to be completely sequenced and annotated was described for *Magnetospirillum (species) sp*. Strain AMB-1 which has a 98 kb MAI abounds in genes related to the magnetosome synthesis. The genome sequence of MTB *Magnetospirillum sp*. Strain AMB-1, consists of a single circular chromosome of 4967148 bp and 4559 predicted open reading frames (ORFs) [55]. There are many homologous regions between the three MTB, (MS-1, MC-1 and MSR-1) in MAI [55]. Arakaki *et al* has identified that the 98 kb genomic region that shows the characteristics of MAI lacking this region was produced and is a non-magnetic mutant [38].

There is a comparative study that elucidated that approximately 891 genes are homologous to MS-1, AMB-1, MC-1 and MSR-1. This showed that an old MTB came into contact with another bacteria harbouring the magnetosome island [38]. In contrast, an exclusive set of 152 genus-specific genes was shared only among three *magnetospirillum* strains [51]. Another study has elucidated a set of genes in MTB that are most likely to be participatory in magnetosome biomineralisation [51],[57].

1.6.3 Magnetosomes formation

Since the complete genome sequence of *magnetospirillum magneticum* AMB-1 has been clarified, enormous improvement has been made to elucidate the chemical, biochemical, and molecular basis of magnetosome formation and to understand how these unique intracellular organelles function [58]. The genome information from the experimental data that was provided by the *magnetospirillum sp*. studies allowed the suggested the magnetosomes were synthesised through four major stages. These stages include: 1) membrane biogenesis magnetosome, 2) protein localisation, 3) biomineralisation under discrete genetic control and catalysed process and 4) assembling into a chain [56].
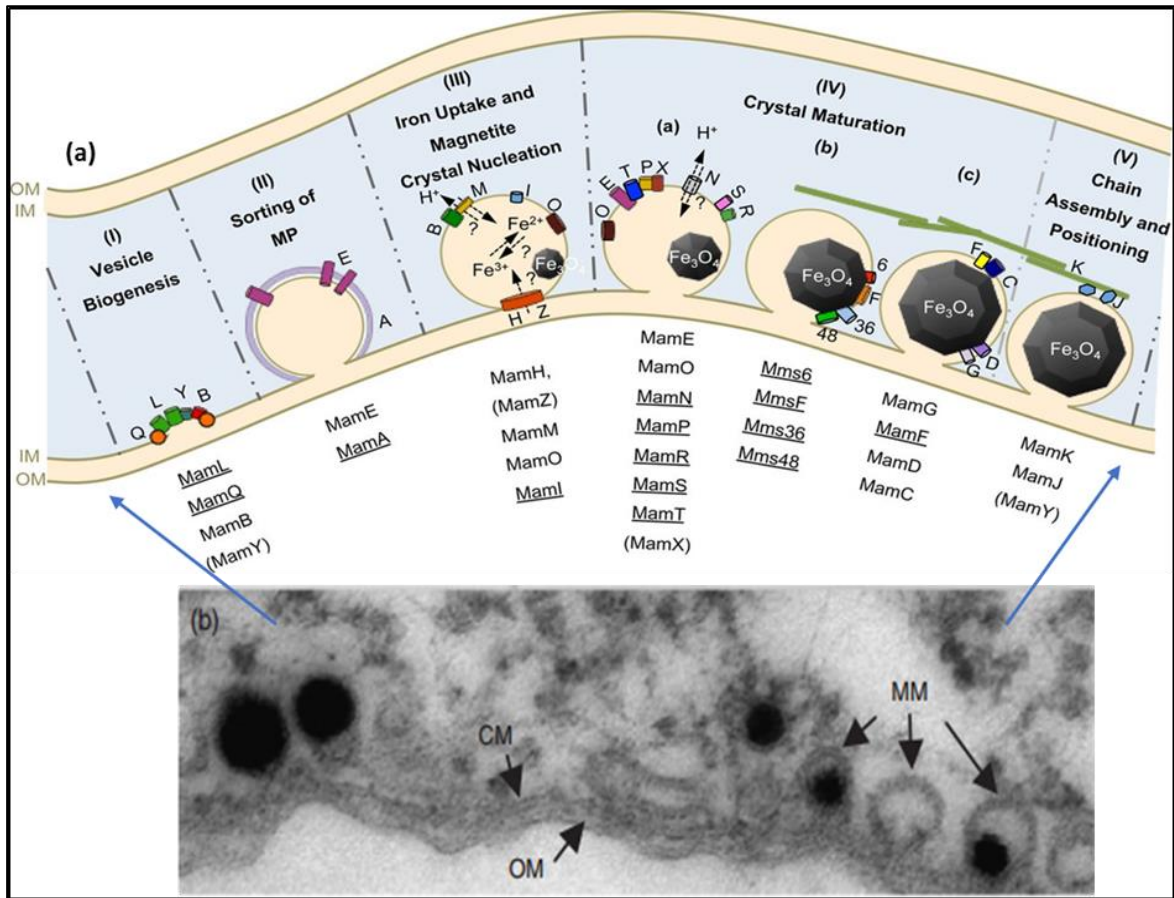
Figure 1-8: the magnetosomes for synthetic *M. gryphiswaldense* depends on many steps comprising various magnetosomes proteins. [59] (b): transmission electron microscopy of *M. gryphiswaldense* cell, showing empty, and partially filled magnetosome membrane vesicles [51].

Proteomic analysis has shown that roughly 20 proteins in the magnetosome membrane (MM) of *M. gryphiswaldense* are specific for magnetosomes formation. These are involved in vesicle formation, iron transportation and accumulation, control of crystal formation and aligning the magnetite particles in chains present in various amounts. Also, similar studies in *M.magnetotacticum* and *Magneticum* have proposed that most magnetite proteins are shared by different magnetospirilla [60]. Also, 28 conserved genes that are present in various MTBs were identified as magnetosomes phenotype, and most of them are located in MAI. [51]. Table 1-3 describes the suggested function of most (Mam) and (Mms) proteins [56][61].

Table 1-3: Key features of all Mms and Mam proteins

protein	Encoding operon	Suggested role	Relative abundance in %
MamA	mamAB	Protein sorting	10.5
MamB	mamaAB	Membrane invagination	8.4
MamC, MamD MamF, MamG	mamGFDC	Crystal size and shape control	MamC (16.3), MamD (3.1) MamF (11.8), MamG
MamH	mamAB	Iron transport	-
MamI, MamL, MamQ	mamAB	Membrane invagination	-
MamJ, mamK	mamAB	Magnetosomes alignment	-
MamM	mamAB	Iron transport	6.9
MamN	mamAB	pH control	-
MamO	mamAB	Crystal nucleation	-
MamP	mamAB	Redox control	-
MamR	mamAB	Crystal size and number control	-
MamS	mamAB	Crystal size and shape control	-
MamT	mamAB	Redox control	-
MamX	mamXY	Redox control	-
MamY	mamXY	Membrane invagination	-
MamZ	mamXY	Iron transport, redox control	-
Mams6, MamsF	mms6	Crystal size and number control	9.3

I- Invagination of magnetosomes membrane

The first stage of magnetosome formation involves the invagination of the inner cytoplasmic membrane (CM) to form a vesicle (Figure 1-8 b). However, the mechanism of vesicle formation of chambers remains unclear [56][58]. Deletion studies in AMB-1, resulting in a lack of magnetosome vesicles has indicated some potential vesicle formation genes. For instance, mamY from the MamXY operon is suggested to have a role in membrane invagination. It is thought that at least 5 proteins control this process [52][56].

II- Targeting protein to magnetosomes membrane.

In the second stage some proteins are tightly or loosely bound to the magnetosome membrane, some are for required to trigger magnetite crystal nucleation and some are for regulating morphology. Various proteins have been suggested to play functional roles in magnetite generation. Also, some induce accumulation of iron after supersaturation concentration is achieved. Another is for maintaining the reducing and oxidative conditions of iron needed to stimulate mineralisation helping with MamP, MamE and MamT during stage (II) (Figure 1-8 a) [38].

The magnetosome surface proteins are believed to have a crucial role in biosynthesis, [62], where numerous novel membrane proteins of AMB-1, MSR-1 and MS-1, in magnetosomes biomineralisation have been discovered [38].

MTB have three membrane layers, an outer membrane (OM), and a cytoplasmic membrane (CM) in addition to the lipid bilayer membrane, which represents the third one also known as the magnetosome membrane (MM). This is illustrated in Figure 1-8 b. The magnetosome membrane (MM) has been studied at a biochemical and structural level in *Magnetospirillum stains*, and this structure is suggested to be similar in other MTB. By using cryo-electron tomography (Cryo-ET) microscopy to image the MTB in starved iron or pre-magnetite cells, it is possible to see that the vesicular structure is either empty or partially filled by tiny immature crystallites Figure 1-8 b), [62],[53]. The studies in *M. magneticum* and *M.magnetotacticum* postulated that most of the magnetosome proteins are shared by other different MTB [60]. *Magnetospirillum gryphiswaldense* proteomic analysis shows that their MM is associated with a specific set of 20 proteins in various amounts. Some of these proteins were found still attached to isolated magnetosomes particles [38].

Some proteins are found loosely bound to magnetosomes crystals, in contrast, others seem to tightly attach or embedded within the membrane base on the deference resistance of magnetosomes protein against detergents and proteases. Approximately 78 proteins have been identified in the analysis of the magnetosome membrane protein from AMB-1,[38] a similar examination was attempted with MSR-1, where 30 proteins were identified from the surface of its magnetosomes,[61] a considerable number of these proteins were found to be assigned to gene clusters within the (MAI). Where a high degree of similarity was observed

between the profiles of cytoplasmic membranes and the magnetosomes of the AMB-1, some of these are dehydrogenases, ATPase subunit and cytochromes [38].

In functional analyses of some individual proteins from AMB-1 magnetosomes, five dominant proteins were identified, Mms12, Mms13, Mms24, Mms22, MamA, and some of these are observed in other MTB [63][38]. It has been suggested that the number of empty vesicles in MTB apparently exceeds the number of magnetosomes crystals. This may be activated by MamA protein in MM, which has been assumed to be required to activate the magnetosomes vesicles [53]. Defected MamA encoding genes in MSR-1,[64] have shown that fewer magnetosomes are synthesized in comparison with its wild-type counterpart. This confirmed that MamA might be required for the activation of magnetosomes compartment [53][65].

III- Biomineralization of magnetite crystals

The third stage is crystal nucleation carried out at optimal conditions for growth of magnetosomes [56]. This entails Fe^{2+} accumulation into vesicles by the transmembrane iron transporter proteins and siderophores. This internal iron is strictly controlled by an oxidation-reduction system [38].

1- Uptake and metabolism of iron

The process of biomineralisation occurs following the magnetosomes membrane invagination, a significant amount of iron needs to accumulate in the magnetosome vesicles where 4% of the dry weight of bacetria consists of iron, this represents more than 99.5% of intracellular iron in MSR-1 strain [52][51]. This iron can cause intracellular accumulation in both ferric and ferrous forms from micro concentrations [66][51] and this intracellular accumulation is under strict control and there are several proteins to control this. Both Fe^{2+} and Fe^{3+} can be taken up by MTB from micromolar extracellular concentration growth medium [57]. The iron uptake has been investigated under different iron concentrations, and it was revealed that three ferrous and two ferric iron uptake systems are encoded by specific genes. When under iron rich conditions, the ferrous iron transport genes were upregulated in magnetite crystal formation and in contrast, the ferric iron transport genes were downregulated, showing in rich iron conditions that ferrous uptake is dominant. In contrary, in poor medium, after most of the iron is taken up by magnetic cells, ferric or siderophore

transport genes were expressed [38]. This intracellular pathway for iron uptake is strictly controlled, based on the possibility of a harmful effect of free intracellular iron level [57].

2- Iron transport into magnetosomes:

The chemical and the mineral composition of the magnetosomes is strictly controlled by the bacteria. There are some reports, for cultured bacteria, that integrate trace amounts of other metals thatare not associated with magnetosomes. For example, copper, titanium, zinc, nickel, or manganese, were used [57]. The proteomic analysis of *M.gryphiswaldense* identified that MamB and MamM proteins, which are encoded within a mamAB operon, are members of cation diffusion facilitator (CDF) family of metal transporters and may be involved in putative iron transport [67]. CDF have another critical function as efflux pumps of toxic divalent cations, for example, Zn, Ca, Co and other heavy metal ions. However, iron has a highly specific pathway for magnetosome formation. Three possible pathways have been suggested for iron internalised into the magnetosome membrane. The first hypothesis, is by diffusion or direct transport from the periplasm,[68] where iron internalises in the vesicle membrane while the magnetosomes are still in contact with CM. The second hypothesis is by magnetosome-specific transporters,[69] where Fe^{3+} or Fe^{2+} are taken up into the cell and then cross the magnetosome membrane using cellular iron transport system. The third pathway is by ligating iron to unknown organic substrates, based on the Mossbauer spectroscopy data, where iron is directly transported from the CM to MM using this ligation and then released at the interface with MM [52].

There is evidence that a subfamily of CDF proteins mediates uptake of iron from the cytoplasm to accumulate it in MM vesicles. Also, MamH and MamZ may be involved in this step, which are members of major facilitator superfamily (MFS) [69]. Deletion of MamB and MamM in MSR-1 was found to prevent magnetite biomineralisation, similarly in MSR-1 deletion of MamH and MamZ resulted in a decrease in magnetite biomineralization [69]. The putative iron transport protein MagA, is another protein that encodes for H^+/Fe^{2+}, was suggested to play a role in magnetosomes biogenesis. It is located in both the CM and MM, and it plays a crucial role in iron efflux in the former and iron influx in the latter [38].

3- Nucleation and crystal growth of magnetite particles

Mms6 protein is a smaller protein that is expressed in the magnetosome membrane, holding Leu-Gly-rich motive that is a tightly bound constituent of the MM in *M. magneticum*. This proteinexhibited iron-binding activity and an in *vitro* study has shown a restricting effect on the morphology of magnetite crystals [70].

MamG, MamF, MamD and MamC are proteins that are encoded in the MamGFDC operon in *M. gryphiswaldense* and other magnetospirilla, these four proteins are shown to control the size of the magnetosomes [71]. Cells where mamGFDC has been the deleted, have formed vesicles with slightly reduced size compared with wild-type. MamGFDC proteins have a redundant function in the control and growth of magnetite crystals, but the mechanism is unknown [71]. There are small magnetosomes proteins (Mms5) suggested to template mineralisation by tight binding directly to the magnetite crystal. Also, they have been found to be able to control mineral shape *in vitro* via their highly acidic C-terminal sequence, these genes as shown previously, have an overlapping genetic function [72].

Moreover, four other novel proteins from the magnetosome membrane analysis were found to tightly bind to the magnetite crystal, which are Mms5, Mms6, Mms7 (identical to MamD) and Mms 13 (identical to MamC) [70]. Mms5, Mms6 and Mms7 have a common leucine and glycine repeating sequence in the N-terminal regions, located in AMB-1 genome. In Mms6, the C-terminal regions have carboxyl and hydroxyl groups, and it has been found to bind to iron sites [38]. *In vitro* experiments to synthesise nanoparticles have found that when Mms6 is present a cuboidal morphology is achieved, similar to that produced by the AMB-1 strain, with 20 - 30 nm size. These results proposed that Mms6 binds to iron ions to initiate magnetosome formation and regulates the morphology [38].

IV- Redox control magnetite biomineralization

The crystallisation of nanoparticles has shown the involvement of genes from mamCD, mam6, mamXY and mamAB stage (IV) (Figure 1-8 a) [58].

Magnetite is produced by biomineralisation of mixed soluble valent iron ($2Fe^{3+}$ and $1Fe^{2+}$) via membrane vesicles [72]. So, the magnetite nanocrystals in magnetosomes require oxidation of Fe^{2+} to Fe^{3+}. Iron oxidation-reduction proteins were suggested to play a role in the control

balance of Fe^{2+} and Fe^{3+} in the biocrystallisation process [56]. The presence of a specific domain is associated with redox function and is thought to be involved in regulation the redox conditions. Each MamE, MamP, MamT and MamX have two or three conserved CXXCH C-type cytochrome haem-binding motifs [52].

In literature, it was proposed that three genes (MamE, MamP and MamT) in the MAI putatively have been involved in electron-transfer reactions. Owing to electron transfer between different parts, this domain MamPET, is strictly conserved in all known MTB and cannot be found in any other species to date, and it is denoted the magnetochrome domain [58]. *In vitro* iron mineralization experiments revealed recombination of MamP from AMB at various pH produce mixed valent iron oxide from a soluble Fe^{2+} species [72]. Few hypotheses have been made about their function, the magnetochrome can give electrons to Fe^{3+} or can extract electrons from Fe^{2+} in order to be involved in crystallisation [58]. While, MamE plays a key role in biomineralisation, and was identified as cytochrome c-like domain, recent studies of deletion of mamE produce empty magnetosomes vesicles, suggesting the MamE acts as a molecular switch to initiate the crystal biomineralization [56]. Moreover, MamE is crucial for further crystal growth, where it has a function to maturate smaller crystals. Furthermore, MamO and other proteins can mediate this biomineralisation process [56].

V- Assembly of magnetosome chain

Finally, these individual vesicles targeted with protein and magnetite crystal are assembled with cytoskeleton into a linear chain,[58] this chain generates a permanent magnetic dipole moment. It has been shown that formation of magnetosomes with differing chain lengths is a highly controlled [73]. The genes that have the responsibility of this are located in (MAI), and are MamK andMamJ (Stage (V) in Figure 1-8 a) [56],[58].

The magnetic dipole moment of a single magnetite crystal is not enough to align a bacterial cell in the geomagnetic field, so the cell maximises its magnetic dipole by arranging the magnetosome into chains, resulting in a single magnetic dipole, which is a sum of the permanent magnetic dipole moment [51].

Assembling magnetite crystal chains and forming of the magnetosome filament (MF) seems to be the responsibility of two proteins, MamJ and MamK that are encoded by single operon

mamAB in all MTB. Evidence for this is that cells of gene *M. magneticum* that lack mamK results in loss of their filament-like magnetosome structure [51]. Where MamK is revealed to created filaments to establish the chain-like structure and its homologs of the bacterial actin-like protein [38],[74]. While MamJ directs the assembly of the magnetosomes chain and is an acidic protein associated with the filamentous structure that suggested that MamJ has a crucial role in chain assembly and maintenance [38].

1.7 Application of Magnetic Nanoparticles

MNPs have advantages to be used in some biomedical applications such as hyperthermia, MRI, targeted drug delivery, magnetic separation, immunoassay, biosensor, tissue repair and cellular labelling [13] [10]. Where the core and coating of MNPs made the most crucial challenges for these applications [13].

1.7.1 Magnetic Nanoparticles as MRI Contrast Agents

In the last few decades, physicists, chemists, engineers and medical researchers have tried to enhance the sensitivity and resolution of biomedical imaging techniques, to detect diseases with high accuracy in either clinical settings or preclinical research. These techniques include MRI, single-photon emission computed tomography (SPECT), magnetic particle imaging (MPI), positron emission tomography (PET), optical fluorescence imaging, ultrasound (US) imaging and photoacoustic (PA) imaging (Table 1-4) [75]. The images are of complex environments, and therefore many strategies are used to enhance the imaging techniques. One of them is using MNPs as contrast agents, owing to their tuneable properties, for instance, the magnetisation size and composition [75].

Table 1-4: Comparison of the representative imaging modalities [75]:

Imaging technique	Signal measured	sensitivity	Spatial resolution	Penetration depth	Preclinical use	Clinical use
MRI	Radio frequency waves	+	+++	+++	yes	yes
PET	γ-rays	+++	+	+++	yes	yes
SPECT	γ-rays	++	+	+++	yes	yes
MPI	Radio frequency waves	++	+	+++	yes	yes
US imaging	High frequency waves	+	++	+	yes	yes
PA imaging	High frequency waves	++	++	+	yes	No
+: poor, ++: good, +++: excellent which represent the strength and weakness of imaging techniques						

Magnetic resonance imaging (MRI) is one of the most essential diagnostic procedures for anatomical and physiological analysis in the medical field [3]. It can allow the discrimination between healthy and disease affected cells. This non-invasive technique can give precise localisation of disease, with no harmful radiation risk, and are widely available in hospitals [76].

MRI uses a magnetic field B_o and radiofrequency (RF) B_1. The strength of an MRI instrument is measured in Tesla (T), and the majority of MRI systems in the clinical setting are 1.5-3T, which produces an extremely strong magnetic field [77][78]. MRI relies on the cumulative magnetic properties of a proton (H^+) atoms of water Figure 1-9 A. The human body is composed of more than 70% H_2O. In MRI the contrast arises from the physiochemical environment of water protons in different tissues [3]. In addition, it is sensitive to the concentration of other macromolecules and iron ions within the tissues [79]. Under an external magnetic field B_o, proton are aligned parallel or antiparallel to a magnetic field, which is known as longitudinal magnetisation, on the long axis of the magnetic field [77]. The majority of alignment is parallel (low energy) more than antiparallel (high energy), that gives a net magnetic vector (M) in the director of the magnetic field. When radiofrequency B_1 pulses are applied with the same precession frequency Figure 1-9 B, some low energy parallel protons flip to a high energy state, and aligned anti-parallel with B_o, thus decreasing

longitudinal magnetisation [80][77]. As a consequence, the net magnetisation vector turns towards the transverse plane, which is the same angle to B_1 and is known as transverse magnetisation [75]. There are two different relaxation types: longitudinal relaxation T_1, that is parallel to B_o (Z axis), and results in recovery of longitudinal magnetisation (T_1- recovery); and transverse relaxation T_2, when perpendicular to B_o (X-Y axis), and involves the decay of transverse magnetisation (T_2- decay) [77]. This is shown in Figure 1-9 [81].

When the B_1 pulse is removed, the excited protons relax to a ground state (aligned parallel with B_o) via emission of energy that is gained from a radiofrequency pulse and gives up the energy to the surrounding lattice [77]. This change to longitudinal relaxation is known as T_1 or (spin-lattice relaxation) [3]. In contrast, if the radiofrequency pulse protons, they become dephased and local MF induces the energy exchange between spins themselves, called spin-spin or transverse relaxation, and causes faster and slower precession in xy-plane [82], that causes transverse relaxation known as T_2 or spin-spin relaxation [79]. These relaxations can be monitored to generate an MR image [83]. The MRI technique represents them as grey scale images when the picture is collected [84].
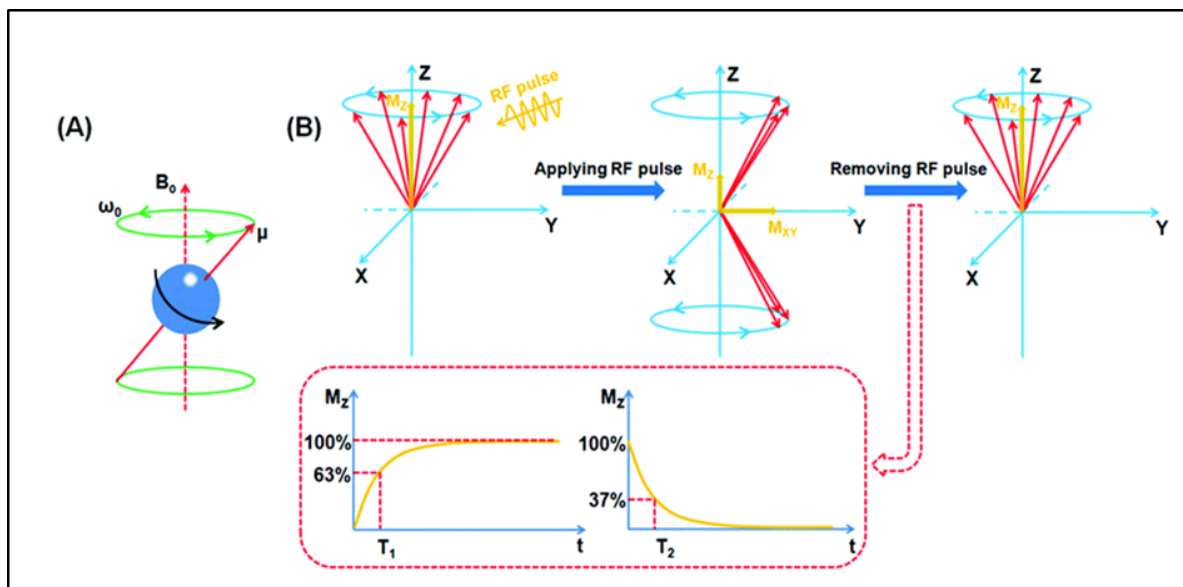
Figure 1-9: The origin of T_1 and T_2 relaxation in MRI. A) The effect of external magnetic field B_o on the proton of water. B) Following application of a radiofrequency (RF) B_1 pulse, the proton of water are excited, with relaxation occurring after removal of RF pulse. The graphs represent Longitudinal magnetisation T_1 (Z axis) and transverse magnetisation T_2 (X- Y axis). The image is taken from [81].

However, it can be challenging to locate the target region of interest, when the differentiation between the contrast in pathological tissue and the contrast in the healthy tissue is small. To resolve this limitation and to give an image with high sensitivity researchers have tried combining MRI with another agent to create an image with high sensitivity. The region can be accelerated using an MRI contrast agent to enhance the T_1 or T_2 relaxation rate. This can improve the image quality, by changing the magnetic resonance relaxation times of H in the tissues and thus the contrast. MNPs have extensive applications as MRI contrast agents. Their surface coating, composition, size, and degree of aggregation and tuneable magnetic properties can have a significant effect on their MRI properties. Controlling all of these parameters can help to develop and engineer MNPs with good contrast for MRI. [85]. Those tissues which contain T_1 agent will appear as a bright region in the image, and those which contain T_2 agents will appear as dark regions in the image [79] as shown in Figure 1-10. In most MRI applications when the EMF is applied, MNPs are distributed and created a large microscopic field gradient that causes dephase and shortening of longitudinal relaxation time (T_1), transverse relaxation time (T_2), of nearby protons of water [85]. The ability to accelerate the relaxation of water protons in various tissues has promising advantages for MNPs for nanomedical applications [82].
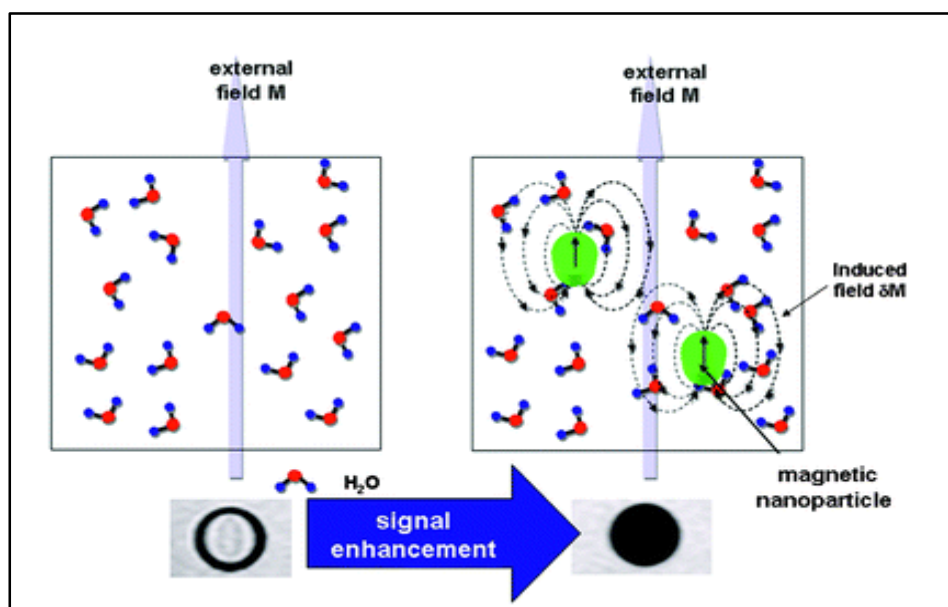
 Figure 1-10: schematic illustration, the effect of MNPs in water, by perturbs the magnetic relaxation of water proton that induced by a magnetic field, causing shortening T_2 of the proton with dark MRI contrast [80].

Magnetosomes have been used as contrast agent in some studies. Benoit *et al.* have developed AMB-1 (whole bacteria) as MRI reagents to target tumors in mice, when they are injected intravenously [86]. The small magnetosomes (~25 nm diameter) generated T_1-weighted positive contrast in MRI, providing a potential too for improved tumour visualization in preclinical studies to track cancer [86]. Optimum contrast agents typically have very high relaxivities.

The magnetic nanoparticles rely on the chemical nature that has been used in MRI application, can be divided into three groups: (i) Magnetic oxide nanoparticles. (ii) Rare earth nanoparticles. (iii) Metal alloy nanoparticles.

Magnetic oxide nanoparticles, for example, nanoparticles of magnetite (Fe_3O_4) and maghemite (γ-Fe_2O_3) are superparamagnetic if these particles are tiny in size (10nm), which increases the colloidal stability. This superparamagnetic iron oxide nanoparticles (SPION) one of the preferred candidates for MRI application. Some of this SPION at physiological temperature serve as T_2-relaxing contrast agent and there negative enhance of image produce dark spot anywhere they are delivered. Many attempts have been made recently to enhance T_2 MRI contrast agents by using other magnetic nanoparticles of metal oxides. For example, MnO nanoparticles have been reported as useful material for T_2-weighted of liver, brain, spinal cord and kidney. In animal models, MnO nanoparticles have shown the tremendous anatomic structure. Also, MnO nanoparticles can be utilised for specific tumour imaging because they can be conjugated easily with the antibody. Furthermore, the composition of the MNPs can affect proton relaxivity, such as doping another transition metals into magnetic nanoparticles. This can be one of the crucial parameters to enhance MRI contrast effect. As shown by Lee *et al.* at Yonsei University in Seol who studied the effects of nanoparticles on MRI by developing innovation approach to enhance MNPs engineering iron oxide (MEIO), through replacing Fe^{2+} in octahedral place with some other transition metal dopants which is MFe_2O_4 (M= Co^{2+}, Ni^{2+}, Fe^{2+}, Mn^{2+}) and this shows saturation magnetisation (M_s) which improve of magnetic properties. Interestingly, $MnFe_2O_4$ nanoparticles elucidated robust MRI detection of cancer *in vivo* in a small area, and strong magnetic properties compared to other metals, as shown in Figure 1-11. Where the relaxivity value decreased respectively for the sample of $FeFe_2O_4$, $CoFe_2O_4$, $NiFe_2O_4$ and crosslinked iron oxide CLIO [78].

The oxide nanoparticles of gadolinium (Gd) and dysprosium (Dy), which are rare earth metals, have shown significant promise for MRI as a contrast agent. Because they have many unpaired electrons per unit of contrast agent. However, they are very reactive, so they must be coated with a biocompatible shell that suitable for physiological media [12]. Another strategy has been used to enhance T_1 which use contrast effect of rare earth metals Gadolinium embedded, into iron oxide NPs [75]. This Gadolinium iron oxide (GDIO) showed a higher T_1 contrast effect than iron oxide nanoparticles of the same size, that enhancement of the T_1 signal in a cardiovascular system when it is injected into a mouse.

Transition metal nanoparticles, for example, pure iron (Fe) and cobalt (Co) or their metallic alloys FeCo, have been shown promising as T_1 and T_2 contrast agent, with the metallic nanoparticles, appear to have a more significant magnetic moment compared to iron oxide [12].

The MRI contrast can be affected by the size of NPs. For example, a study by Kim examined that T_1 contrast effect can be enhanced by reducing the size of NPs, where they used different size of extremely small iron oxide NPs at 2.2, 3, and 12 nm diameter [75], 3 nm enhances the T_2 signal visualization MCF-7 cancer cell *in vitro*. In addition, it provides sufficient susceptibility for small diameter (0.2mm) blood vessel in MR image [75]. However, more recent by Shin *et al*. has reported that 5.5 nm iron oxide NPs has strong T_2 contrast effects [75].
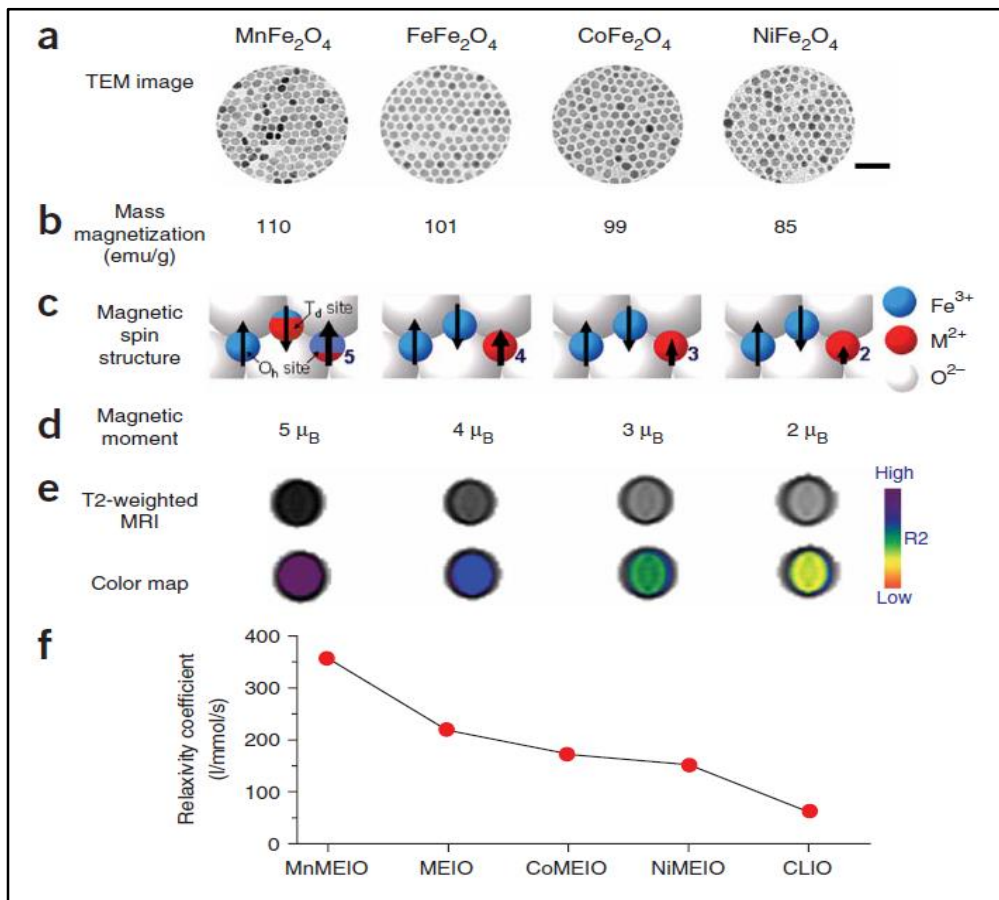
Figure 1-11: The effect magnetic engineered iron oxide nanoparticles and magnetic on MRI. a) TEM image of MFe_2O_4. b) Mass magnetisation amount of MFe_2O_4. c,d) Schematic of magnetic ions spin alignments in spinel structure under EMF. e) T_2 weighted spin for MR image and their colour maps and relaxivity R_2 of MFe_2O_4 at 1.5 T [78].

The majority of previous work proved the effect of magnetic nanoparticles, in suspension as a biocompatible ferrofluid, is absorbed by some specific tissue, which is apparently visible by MRI. One of these studies has improved the use of MNP as MRI contrast to detect solid tumours in a small interesting area 2-3 mm diameter in liver tumours [83]. In addition, MNPs with a diameter of 5-10 nm have been shown to efficiently identify the lymph node metastases under MRI. Another study shows the application of MNPs in brain tumours to improve the delineation and quantify tumour values [83].

The different amounts of magnetic nanoparticles have been absorbed in different ways by different kinds of tissues, which give a variety values of T_2 and it can distinguish images between tumours and healthy cell because infected cells do not have the sufficient macrophage system of healthy cells [3]. For this reason, the contrast agent does not affect their relaxation time; this makes them more significant from other surrounding healthy cells

[3]. However, synthetic MNPs are in great demand for using a contrast agent which satisfies theses following characteristic: intracellular uptake, accumulation, easy surface modification, actively labelling, easy delivery; and safe clearance with insignificant side effects from patients [3]. However, many concerns have been reported about the biocompatibility of the metallic components as MRI contrast agent, and their chemical instability [75][83]. Although the iron oxide nanoparticles are known to be biocompatible, other doping metals have shown safety issues. For example, Gd that cause toxic side effects when liberation from NP at organ uptake [75]. Despite the many successes of using MNPs as MRI contrast agents, there are some challenges can be realised. First, they are complicated preparation and functionalization which included many synthesis steps and multistep purification stages. Second, they are able to aggregate in solution [12].

1.7.2 Magnetic Nanoparticles in Hyperthermia

The application of sufficient heat to kill cells in the treatment of cancer is referred to as hyperthermia this idea is not new [36]. Hyperthermia treatment is a thermal cancer therapy which uses hot water, capacitive heating and induction heating to particular tumour sites. Those sites have fewer blood vessels and are less oxygenated than normal cells [36]. As a result of this, they are more sensitive to the temperature above 42°C, and quickly died at this local temperature [36] Normal tissues, which are able to resist temperatures of 42-45°C, compared to cancer cells which suffer apoptosis at this temperature [11].

There are two ways of using hyperthermia to treat cancer:

- Using very high temperatures (at least 50°C) to destroy a small area of tumour cells with exposure for at least a few minutes, which is known thermoablation [9]. It is not preferable because it can be harmful or even deadly.

- Raising the temperature a few degrees higher than normal (42-45°C) for up to a few hours, in the part of the body, or even the whole body, can help (especially incorporation with other cancer treatment such as immunotherapy, radiation or chemotherapy to work better) by increasing the oxygenation [76][2]. This often called regional hyperthermia. Although such combinations have shown efficacy in clinical trials [87] [88].

33

However, this temperature needs to be controlled prevent it raising too high and causing the death of healthy cells. It can be used to treat all kinds of cancer cells. There is another way to induce heating into the desired site, this is magnetic hyperthermia. MNP can be guided by a magnetic field gradient to the tumour site, and then an external applied an oscillating alternating magnetic field (AMF)to induce the hyperthermia [36].

The concept of inducing intracellular hyperthermia was first shown in 1979 by Gordon *et al.* where local induce magnetically heat energy has been used to treat cancer by MNP colloidal suspension which was injected intravenously and then alternating magnetic field (AMF) applied. This lead to the destruction of cancer cells with only a small effect on healthy cells [89]. After this seminal paper, much research on this area has been published. The significant limitations of hyperthermia are the selectivity of the interesting area, delivery of homogenous heating within a tumour which still preserving the healthy cells and tissues without injuring or killing patient [90]. For example, metal nanoparticles have nonselective heating, which causes damage to healthy tissues that are surrounding cancer cell [76]. Therefore, a significant challenge is to enhance and increase the selectivity of hyperthermia to prevent necrosis in the normal cell [76]. Many studies discussed later are currently focused on using MNPs for generating heat that is successful in targeting a tumour through blood circulation and magnetic field presenting an opportunity of localized heating [91]. Magnetic hyperthermia is a method treating cancer, where MNP delivered receives an AMF, causing them to heat and release energy so a local tumour would be destroyed, the primary key for a hyperthermia agent is to convert the absorbed magnetically induce the energy to cytotoxic heat [30] [37].

SPM in size below 30 nm, do not have magnetic remanence, this leads the thermal energy continuously changes their direction of magnetization (unstable magnetic moment), while SD range size (30- 120 nm) has a stable and large magnetic moment [92]. In MNPs can force the magnetic moment to overcome the energy barrier and rotate (equation 1.7).

$$E = KV \qquad\qquad (1.7)$$

Where magnetic volume is V, external magnetic field (E) and, where K is anisotropy constant. When the MNP relaxes to their normal orientation, then this energy is converted to heat, is emitted from the MNPs [8].

The heating is proportional to the magnetisation value, size and the magnetic anisotropy, also their concentration in tissues finally the intensity and frequency of AMF [5]. However, some limitations can prohibit therapy application, that is a high concentration of MNP and low treatment, so that why we need to induce the magnetic nanoparticles properties where the magnetisation value, coercivity and anisotropy are represented this magnetic property of nanoparticles.

Iron oxide MNPs can be utilised for magnetic nanoparticles hyperthermia treatment (MNHT), [90]. This heating is related to process losses during the magnetisation reversal, which depends on different parameters; applied a magnetic field, the frequency of alternative coercivity of MNPs, magnetic particle properties like particle shape and size [9]. Furthermore, to concentrate the MNPs heating can be localised to an area of interesting by using an external magnetic field [90].

Magnetic hyperthermia has been tested on a variety of cancers in animal models such as prostate, mammary, melanoma, glioma, breast, head and neck cancer in various stages of research right up to a clinical trial [93]. MHT has advantages compared to traditional treatments firstly if MNPs is injected it is less invasive, they also can be injected and localised anywhere in the body, that helps to treat different kinds of tumours with minimal side effects [11].

The heating efficiency of MNPs in an AMF is characterised by specific loss power (SLP), which is also termed specific absorption rate (SAR). This related to the area of the hysteresis loop defines the thermal energy that can be released to the environment [9] [94]. When the target concentration is very low then the SLP must be high enough. According to data reported by Hergt *et al*. on specific loss power the magnitude of 10-100 Wg^{-1} and the frequency of about 400Hz, for a field amplitude of 10 KAm^{-1} was recommended to be useful for breast cancer thermoablation [9].

Huang and Hainfeld [95] have reported that magnetic nanoparticles of iron have achieved a suitable concentration that is needed for effective hyperthermia by intravenous (IV) delivery. This was with 38 KAm^{-1} applied field at 980 KHz. Tumours could be heated in 2 minutes to reach 60°C. That destroy them with millimetre precision, without any harm to the surrounding tissues, (Figure 1-12 A and B) [95].
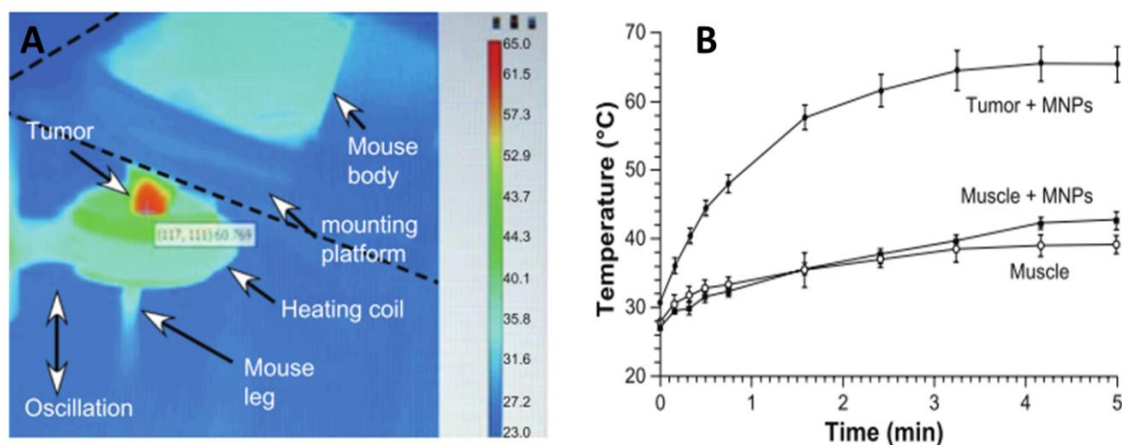
Figure 1-12: The thermal image of a tumour in the legs of mice (red region) implanted with subcutaneous squamous cell carcinoma was heated by an alternative magnetic field, B) Heating of tissues in mice after 24 hours of taking an IV injection of MNPs using magnetic field [95].

More recently Wilhelm *et al*. showed that maghemite anionic coated nanoparticles were capture and concentrate within intracellular vesical of the human prostatic tumour [36]. Some of the researchers have proposed the modification of the superparamagnetic particle surface. Where Zăvišová *et al*., coated magnetite nanoparticle with poly (ethylene glycol) and sodium oleate, they found that these particles partially inhibited the growth of cancerous B16 cell at a highest tested dose (2.1 mg/ml of Fe_3O_4)[96]. Zăvišová *et al*., used Fe_3O_4 core/shell nanoparticles coated with dopamine-oligo-ethylene glycol ligands (range size d <15 nm). These were intravenously administrated, then for three days was followed by applied AMF, the results show a decrease in tumour size of murine B16-F10 melanoma in first 24 hours after injection then exposure to 30 min of AMF (360 KHz). At the end of this treatment showed reduced in tumour size without the effecting associated surrounding a normal cell [97]. Another study in 2006 by Kim and his group have used uncoated (9.9 nm), chitosan- coated and starch-coated MNP (10.7 nm) as hyperthermia agent. L929 normal cells and KB carcinoma cells were used to test the cytotoxicity; the result showed the rate of capturing of MNP was 96% and the temperature rise of 23°C under AMF (150 KHz). Also, the study showed that Chitosan-coated NPs have a higher affinity of KB carcinoma cell than the normal cell of L929 [98]. The first study for MNP (55.6 nm) loading with anti-HER2 immunoliposomes, which act as tumour targeting vehicle, a combination of antibody therapy with hyperthermia on SKBr3 breast cancer, have been tested by Ito *et al*., where the results show, 60% of MNP were

36

incorporated into these cells and following the cell have been heated at 42.5°C under AMF (360 KHz), strong cytotoxic effect observed [99]. In another study on different tumour models, BT474 and SKOV3 cell in nude mice using HET2-tagged immunoliposomes (HML) loaded on Fe_3O_4 nanoparticles size 10 nm, where HMLs were injected into these cancer modules [100]. The result showed after exposure to 30 min of AMF (118 KHz) twice at 2 hrs intervals that accumulation of HML was significantly higher in BT474 (HER2-expression) a tumour than SKOV3 (Low HER2-expression). After this hyperthermia treatment, the temperature in a tumour was increased to 45°C, while the body temperature stayed around 38°C and 10 weeks after the hyperthermia treatment the tumour was the regression [100]. Although in all these studies above the time of the exposure to AMF is almost the same, with variance in the strength of magnetic field, the size of MNPs and types of cancer cells, but overall studies show the efficiency of MNPs for cancer treatment.

Many materials have been prepared to investigate their ability for use in magnetic hyperthermia, for instance, Fe, Co and Ni metallic NPs. These pure metals show the highest saturation magnetisation, but on the other hand, they have limited utility in biomedical applications because of their chemical stability and inherent toxicity. However, metal ferrite shows excellent chemical stability, magnetic properties and SAR values, which makes them a suitable candidate for magnetic hyperthermia. Also, metal ferrite NPs can be doped with other metals such as Co and Zn which enhances their SAR [11]. To date, most NPs tested clinically, or pre-clinically were lab synthesised, and most of them SPION [101]. Later the iron oxide nanoparticles (IONPs) doped with yttrium were used by Gozde *et; al* for hyperthermia treatment combined with MRI for liver cancer [30]. The drug release also combined hyperthermia, where Hayashi *et al*., have used the IONPs functionalized with folic acid and beta-cyclodextrin, where the hydrophobic interaction through beta-cyclodextrin was used to incorporate into the interest area. So when the high-frequency magnetic field was applied the IONP was heated up to 42-45°C and there the hydrophobic interaction between beta-cyclodextrin and the drug was depressed, causing releasing drug [102]. The most limitations of application the magnetic hyperthermia in human are that how to deliver the MNPs to tumours, the cell uptake with low toxicity, the size of the tumour, and finally how to generate stable heating.

In the comparison experiment (Figure 1-13) between the magnetosomes and SNPs (synthetic magnetic iron oxide particles produced by two different rokus as well as ground magnetite crystals), where SNPs at low MF (10 KA/m) has shown low energy losses per cycle in range (0.01-0.05 J/Kg), while magnetosomes at the same MF, has shown higher energy losses per cycles (0.5 J/Kg), which could deliver a greater specific heating power to be released at low MF compared to other SNPs. This may be because the magnetosome surface is well defined with a lipid bilayer compared to coated and uncoated SNPs [9]. This is useful as you would need to subject the patient to a much higher MF to achieve the same heating and high fields may be unsafe (Figure 1-13).
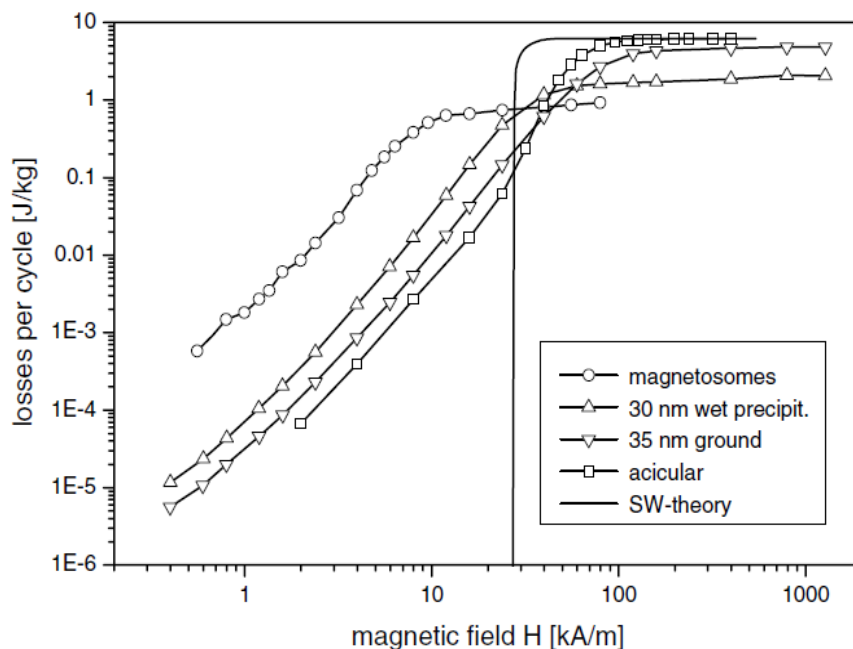
Figure 1-13: Comparison Stoner-Wohlfarth theory with experimental data of some iron oxide NPs prepared in a different way, a dependence of losses per cycle [9].

This also confirms by *in vivo* study for the treatment of xenografted breast tumours four different types of suspensions were tested, which were SPION, whole MTB, magnetosomes organised in chains and individual magnetosomes. 10 mg/ml of iron oxide suspension was administered by injection into the centre of the xenografted breast tumour. Then the mice were exposed to the AMF strength of 40 mT and frequency of 198 KHz thrice for 20 min. As shown in Figure 1-14 [101].

The treatments which used chains of magnetosome suspensions were efficient in several mice, where the tumour disappeared. In contrast, the heat treatment with full MTB and individual magnetosomes and SPION suspension were unable to stop tumour growth. The efficiency of magnetosomes bacteria in these results cannot be only due to their large size, but also due to their arrangement in chains that made them less prone to aggregation. Rats survived an administered amount of magnetosomes of low dose up to (480 mg/Kg), their acute toxicity was low [101].
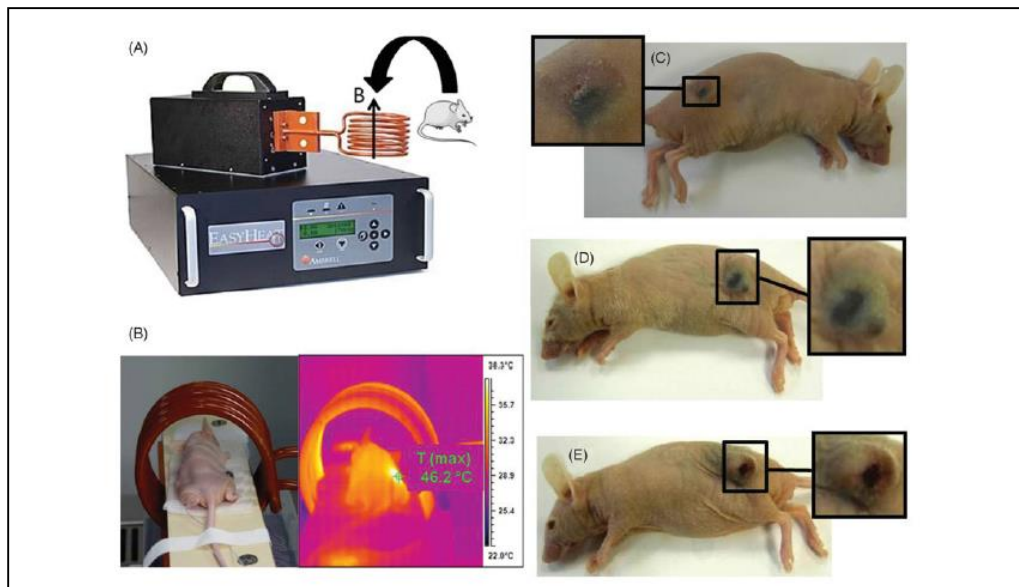
Figure 1-14: Induction system was used to general AMF for treatment. B) The temperature measurement throughout the treatment. C) Treatment mice image with a suspension containing chains of magnetosomes. D) Individual magnetosomes. E)) SPION [101].

Staniland *et al*. have reported that cobalt doped magnetosomes *in vivo* in three cultured strains of magnetotactic bacteria can increase coercivity by 36-45% [24]. This doping method can be expanded into other metal ions, such as copper, nickel, and titanium. Another study by Alphandery and his group shows that the cobalt doping of magnetosomes has high hysteresis losses that may be promising for magnetic hyperthermia treatment [103]. Furthermore, the magnetic properties, hysteresis losses and heating efficiency were enhanced after the magnetosomes doping with cobalt.

1.7.3 Drug delivery with Magnetic nanoparticles

Nanoparticles have unique features for drug delivery both in *vivo* and *vitro* especially in targeting tumours. Significant advantages of using NPs for drug delivery are: (i) Targeting interesting locations in the body (ii) Reduction of doses needed (iii) Minimization of side effects, which it may be generated due to the high concentrating the drug at the nonspecific site [1], [2], [104].

The development of drug delivery in nanotechnology started 60 years ago. During the first period of research first generation (1G) the focus was on the drug release mechanisms. Drugs released in the oral administration typically took up to 12 hours and in the transdermal administration took one week. Since then, the market has become saturated with many oral delivery clinical products [99]. Between 1980 and 2010, the second generation of drug delivery was started (2G). However, it did not achieve the goal to innovate a useful system in the clinical product. Turning to the 21st century the field has now looked to nanotechnology for the next generation of products. The properties of nano-sized materials are potentially advantageous when compared to equivalent microsized or larger materials [104].

Active targeting is a nano based technique where a drug is directly targeting a specific cell, organism or tissues system [4]. It is dependent on the receptor or expression of different epitopes in the tumour cell. Alternatively, it may rely on overexpressed species, for example; proteins (antibodies, folic acid, sugars) polysaccharides (hyaluronic acid), peptides, polyunsaturated fatty acid, DNA [2]. Drug target delivery can be active, passive or physical. The active targeting technique is feasible in addressing short circulation times and low NPs concentration that occur with current cancer therapeutics. They do this by helping to have the drug concentration at feasible or below therapeutic levels [2]. In contrast, within physical targeting the carriers have been developed to be sensitive to physical stimuli through external influences, e.g., pH, temperature, sound, light, electric charge, and magnetism, to conjugate to drugs [104], [105].

Polymeric NPs, micelles, liposomes as organic materials, have all been used as nanovectors in drug delivery through active and passive targeting with molecules such as antibodies or by using a physical stimulus (e.g. magnetism in magnetoliposomes) in active targeting. However, these organic materials suffer from an uncontrolled drug release rate, limited chemical

stability, high costs and susceptibility to attack by microbiological cells. Developing an effective drug delivery mechanism is a major hurdle researchers face.

Researchers have looked to iron oxide magnetic nanoparticles as a potential mechanism. This is because they can be visualised in MRI, have the ability to drive to specific locations using EMF, but more specifically when heated in a magnetic field can cause drug release, generate hyperthermia and ablation to tissue [2]. The coating around the NP and the surface chemistry are essential in increasing the half-life circulation from minutes to hours, an event to days and to avoid the reticuloendothelial system (RES) in the immune system [2]. MNPs can be used for cancer treatment and also for disorders associated with the musculoskeletal system, anaemia chronic and kidney disease [2].

In drug delivery, MNPs are used as a drug carriers. They have the ability to carry cytotoxic drugs to a target site. This occurs through injecting this drug carrier into a subject via interatrial or intravenous injection. An external magnetic field can then be used to guide nanoparticles-drug composites to tumour or other target sites *in vivo* resulting in high concentrations of therapeutics. Next, the therapeutic agent is released from the MNPs carriers, either via activating enzymes or physiological conditions changing such as osmolality, pH or temperature. This should lead to increased cell tumour uptake of the drug at these specific sites and reduce the distribution of cytotoxic drugs, to the next of the body so large doses are not needed [2]. The magnetic targeting drug was first used in clinical trial by Labbe *et al*. in 1996, where phase I clinical trial was tested on rats with cancer using ferrofluids bound to epirubicin. This was demonstrated to 14 patients studied and was targeted successfully to tumour location in 6 patients [106]. In another study shows magnetic particles doxorubicin (MTC-DOX) was loaded with 22 patients with hepatocellular carcinoma and was successful in directing to the tumour location in 20 of them [36].

Many factors must be considered when designing these MNPs as target systems. Magnetic properties, size, binding capacity and field strength are the key characteristics[107]. However, it is also important to consider the surface engineering for chemical and biological functionalization to ensure both the biocompatibility and bioselectivity. Finally, the core of MNPs properties for magnetic emission [3].

Compared to traditional techniques MNPs have numerous advantages. They can be localised anywhere when injected into the body. This reduces the invasiveness of the procedure and enables the treatment of different kinds of tumours with fewer side effects. Moreover, MNPs can be directed by the magnetic field towards targeted regions of interest. They can also be coupled with an active substance, for example, antibody proteins to increase the ability to select the malignant cells, then increase the internalisation in cancer cells [11]. By improving MNPs design for therapeutic functions such as hyperthermia, MRI and drug delivery their capacity to be used as. Cancer therapeutics improves. This will potentially result in the next generation of cancer therapeutics, with low doses for treatment and minimal side effects [11].

1.8   Endotoxin

Shear and Turner were the first researchers to use term Lipopolysaccharide (LPS) to name the endotoxin extract in 1943 [108]. LPS also known as endotoxins, are the major component of the outer cell membrane of gram-negative bacteria and can be liberated into the environment [109], during their growth and division, but mainly during cell death. They do not react directly against the cell but it is activation by the immune system. Endotoxin can act indirectly against cells or organisms by activation of the monocytes and macrophages of their system. The cells liberated mediator have a strong biological activity that causes the side effects of endotoxin [108]. Where the endotoxin effects change metabolic function, increase the body temperature and activation of coagulation cascade [108]. Endotoxin is possible to present in pharmaceutical production processes or in the final product [108].

Escherichia coli is a gram-negative bacteria that is widely used to generate recombinant DNA products; and as such these product are contaminated with endotoxin [110]. However, any biological synthesis protein must be as free as possible of endotoxin, to reduce the side effects during administration to humans and animals. On the other hand, gram-positive bacteria can generate LPS, but at a low level, and is easy to denaturalise by heat compared to gram-negative bacteria that are more resistant to heat. LPS in gram-negative bacteria finds in the outer part layer of the bacterial cell wall [108].

In the pharmaceutical industry and biological reagent, keeping endotoxin at threshold level or lower is a challenge. EU is used as a term to describe the biological activity of endotoxin,

and the 0.5 EU/ml defines as the threshold concentration between pyrogenic and non-pyrogenic samples [108].

The chemical structure of LPS consists of hydrophilic polysaccharide moiety and hydrophobic lipid moiety (Lipid A) that are covalently linked to each other Figure 1-15, and LPS consist of three distinct region lipid A, core oligosaccharide and O-antigen [109] [108].

Region I: lipid A: have the most responsibility for biological activities of endotoxin, and it is the most conserved part contains the hydrophobic membrane anchoring region of LPS.

Region II: core oligosaccharide is usually containing heptose (Hep) and 2-keto-3-deoxyoctonic acid (KDO). This KDO in LPS has been used as an indicator to measure endotoxin in an assay for LPS, due to their unique and invariable in LPS [108].

The inner core of oligosaccharide and the lipid A, region are partially phosphorylated, and as a result, the endotoxin molecules display a net negative charge. Core oligosaccharide is attached to the position 6 of one N-acetylglucosamine (NGa) or (NAa) and consist of a short chain of sugars (KDO-Hep-Glc-Gal-Glc-NGa) [108].

Region III: O-antigen is attached to the outer core of oligosaccharide, and it consists of three to eight monosaccharides, and the primary antigenic determinant of gram-negative bacteria resides in the O-antigen region [108].
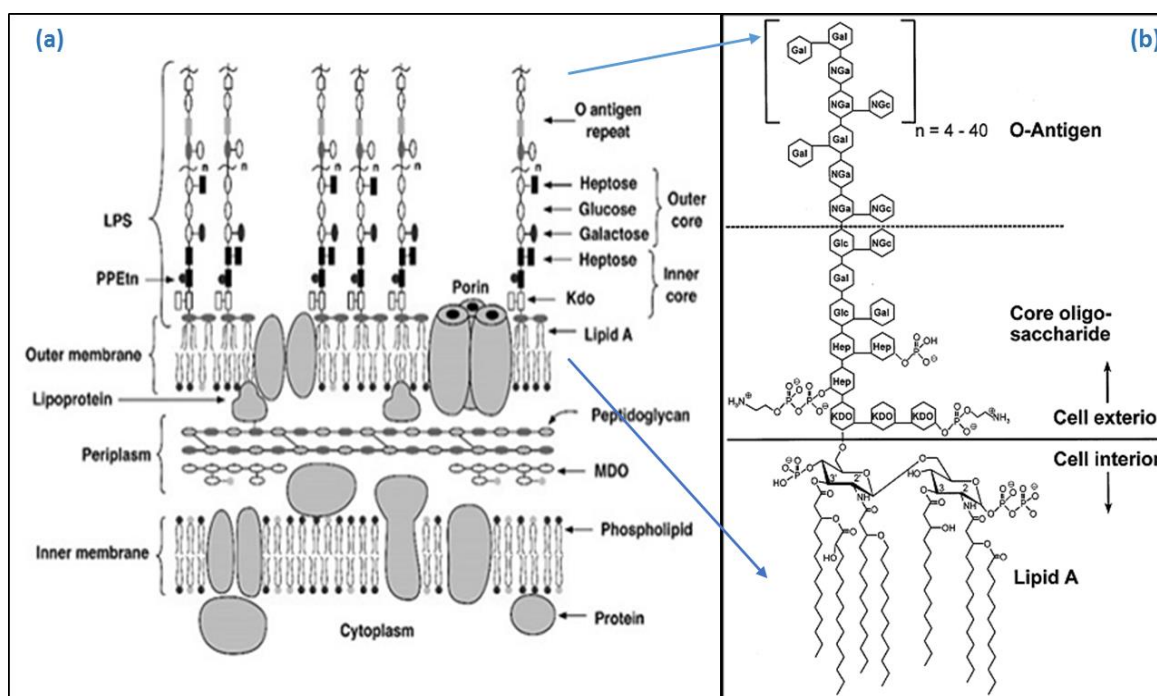
Figure 1-15: (a): the structure of cell envelop of inner and outer membranes of gram-negative bacteria (*E.Coli* K12), where rectangles and ovals represent sugar residues, while circles represent polar head groups of different types of lipids.(b): the chemical structure of Endotoxin (*E.Coli* O111: B4). The abbreviation: PPEtn (ethanolamine pyrophosphate; LPS (lipopolysaccharide); kDO (2-keto-3-deoxyoctonic acid); Hep (L-glycerol-D-manno-heptose); Gal (galactose); Glc (glycose); NGc (N-acetyl-galactosamine) [109] [108].

1.9   Magnetosome biotinylation

Biotin (vitamin H) is an essential coenzyme that is present in all forms of life which is used as a cofactor for carboxylase enzyme. It is synthesized by some fungi but most bacteria and plants [111] and occurs primarily in a protein-bound state within the cell. Biotin is small in size (244 g/mol), so it can be conjugated to various proteins without altering their biological activities, it has high affinity binds to avidin and streptavidin proteins [112][113]. The biotin is bound to the specific protein via amide linkage between the biotin carboxyl group and a unique lysine amino group via a reaction catalysed by biotin ligase known as biotinylation [114]. Biotinylation is the ability to covalent bind biotin to the specific amino acid on a protein, nucleic acid or other macromolecules either chemically or through an enzymatic reaction. This attachment facilitates easy detection, immunodetection, immobilisation and purification of the bound protein material [115][116][112],[117]. There are a variety of biotinylation reagent that able to targeting specific functional group or residues including carboxyls,

carbohydrate, primary amines and sulfhydryl [116]. This is extremely useful to reaseachers when choosing target macromolecule without interacting with undesirable functional groups. These advantages make the biotinylation rapid, specific also and is unlikely to perturb the function of the molecules, due to the small size of the biotin [116] [118].

The biotin interaction with avidin or streptavidin is useful for immobilisation of drugs, targeting and labelling [118]. There is an extremely high affinity between biotin and streptavidin, once its formed it is resistance to extremes in pH, heat, organic solvents, and other denaturation agents. These interactions are exploited in many areas of biotechnology [115]. Streptavidin is homotetramer (~56KDa) protein complex produced by the bacterium *Streptomyces avidinii*, fungus, chicken, and frogs [119],[120]. It has four binding sites for biotin molecules (as does avidin) with a dissociation constant $K_d \sim 10^{-14}$ M, which is known as one of strongest protein- ligands interaction [111] [120]. Furthermore, the protein has high thermostability for biotin (T_m 112° C) and is resistant to very harsh conditions such as, extreme pH, denaturing agents and enzymatic degradation. These characteristics make the interaction between biotin and streptavidin ideal for the use within a wide range of experimental conditions and numerous chemical/biological applications [120]. It is widely used in post biotinylation and molecular science research and many of streptavidin applications demand the biotinylation of target molecules. Moreover, it has been exploited by researchers by attached biotin tags to protein for labelling, detection, purification and immobilization. Biotin labelling has also been applied to drug targeting [111].

In chemical biotinylation, there is a variety of biotinylation reagents with different chemical functionalities which are able to target specific functional groups or residues, including carboxyl, carbohydrates, sulfhydryl and primary amines [121]. This functional flexibility allows for the design of biotinylation reagents. Such as; the introduction of improved solubility either inside or outside cells, cleavability and reversible biotinylation reagent from biotin-binding proteins by using specific elution.

An alternative approach to the chemical method is Enzymatic biotinylation, which was first demonstrated by Cronan 1990 [114]. The enzymatic technique is mild and highly specific [122] and can be used for *in vivo* and *in vitro* [122]. Enzymatic biotinylation can also be performed both *in vitro* and *in vivo*. However, the results of these methods are randomly and suffering

from non-specificity, which may cause negative impact on catalytic activity due to changing of the enzyme structure, alter of immobilized enzyme, or steric hindrance at active site [122][111] It does however provide more uniform biotinylation than chemical [118].

1.9.1 Chemical biotinylation Sulfo-N-hydroxysulfosuccinimide (Sulfo-NHS- biotin)

The most popular type of biotinylation reagent is the NHS esters of biotin, the stable amide bonds performed in buffers between pH 7-9 when NHS-activated biotins react with primary amino groups ($-NH_2$). Proteins, including polypeptide chain, membrane and antibodies, mostly have several primary amino groups in the side chain of lysine K (Lys) residues. In this study sulfo-N-hydroxysulfosuccinimide biotin (sulfo-NHS-Biotin) which are more soluble in water have been used.

 Sulfo-NHS-biotin is water soluble because of the charged sulfonate group ($-SO_3^-$), located on the NHS ring. This charge group does not affect the chemical functional group that facilitates the reaction but allows it to be performed in water instead of organic solvents, such as dimethyl sulfoxide or dimethylformamide. Sulfo-NHS-biotin is a cell surface labelling biotinylation reagent as it does not penetrate the cell membrane. Thus the cell remains intact. It does this by spontaneously reacting with primary amines exposed on the cell surface, forming a biotinylated amide bond (Figure 1-16) [123]. The magnetosomes lipid bilayer provides an ideal platform for a stable conjugate to form between a primary amine on the magnetosomes protein, and carboxylic group on Sulfo-NHS-biotin. The biotinylated magnetosome can couple with streptavidin immobilisation, which well known as biotin-streptavidin interaction. This allows conjugation with different types of antibodies and antigens.
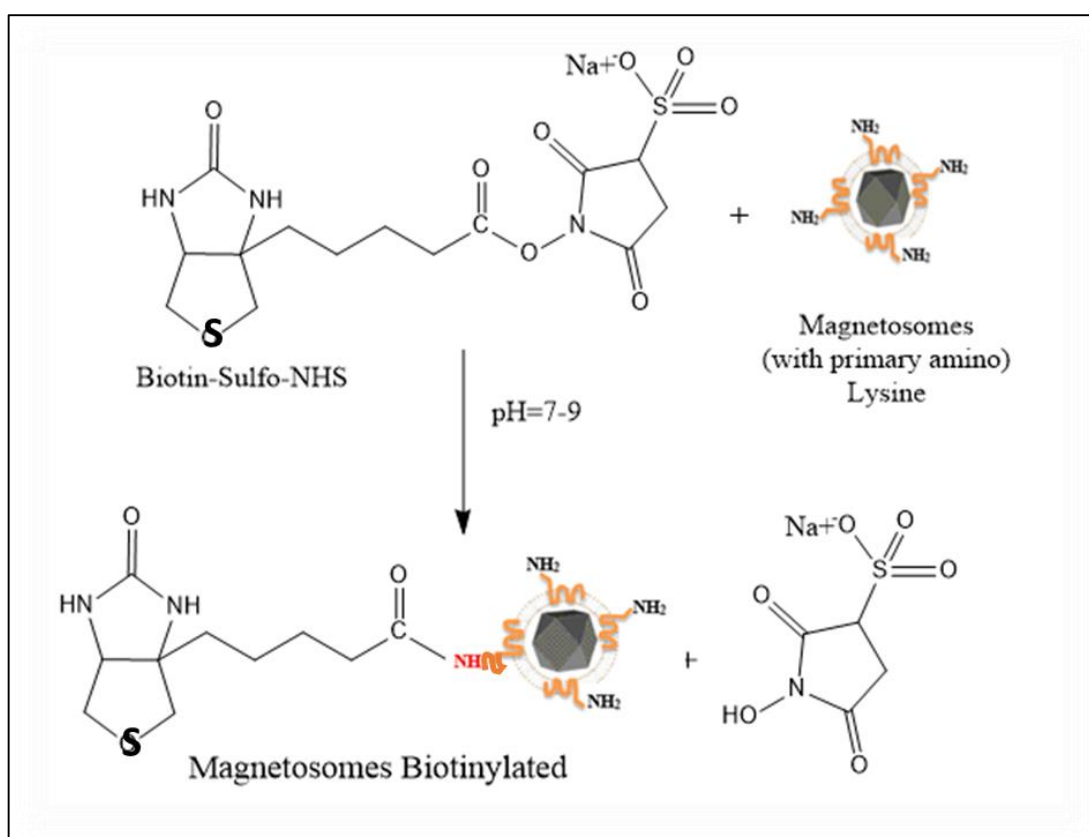
Figure 1-16: Scheme, represent the strategy used for conjugation of biotin to magnetosomes particles

Another attribute of the Streptavidin-biotin interaction include the stability of the protein and its ability to utilize various enzymatic and chemical biotinylation methods that are available within a range of different experimental designs. Streptavidin-biotin can be used as pre-targeted drug delivery for cancer and gene therapy.[120]. The streptavidin-biotin interaction carrying the targeting agent (e.g. antibody) and a drug that can be a separated targeting agent from the actual drug to enhance the therapeutic index of treatment [120]. For example; one of the methods to develop the cancer therapy was streptavidin using base on pre-targeting by biotinylation. The antibodies against a known cancer biomarker can be used with streptavidin as recruit radiolabeled Streptavidin [120]. But first, the patient must clear from unbound antibodies before addition of streptavidin.

1.9.2 Specific Enzymatic biotinylation of proteins using BirA*

One of the most widely used for enzymatic biotinylation site is BirA [112] also it is known as Biotin Acceptor peptide (BAP) [122] and Biotin protein Ligases (BPLs) [117] are enzyme that [122] are the *Escherichia coli* biotin ligase, that show extraordinary specificity to sites of

biotinylated [112] lysine side chain with 15 amino acid acceptor peptide (also known as Avi-tag) [112] Figure 1-17 [119], where (N`- GLNDIFEAQKIEWHE) contain single lysine residue (K) that biotin can be covalent attach by BirA biotin ligase [122]. Biotin protein ligase (BPL) which also known as holocarboxylase synthetase is one of few metabolic enzymes in living cells, which play enzymatic roles in several reactions, for example in metabolic carboxylation and decarboxylation, could make naturally biotinylated through post-translation modification[111], [114].
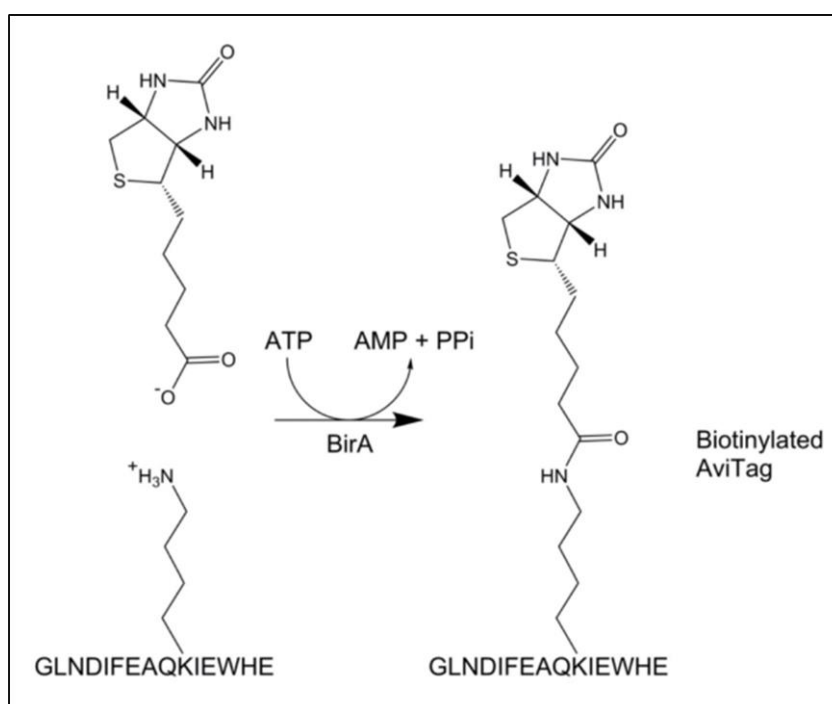
Figure 1-17: Biotin ligase (BirA) reaction uses for covalent link free biotin to the lysine of AviTag [119].

However., there are limits for using BirA enzymes for biotinylation, one of them is the target protein must be fused with a peptide tag [119] [117] for site-specific biotinylation. Study by Eunjoo and his co-worker report, that mutant BirA (BirA*) can attach biotin to a large number of cellular proteins *in vivo* and to an immunoglobulin, bovine serum albumin, light chain and RNase *in vitro*. It is also a self-biotinylated *in vivo* and *in vitro* [117] compare to wild-type BirA protein which is less active in these reactions. The interaction between biotin ligases and their protein substrates are shown a very high degree of conservation [111]. The solubility of biotinylation reagent can allow access to target proteins in the hydrophilic or hydrophobic environment [121].

In a study by Maeda *et al.* biotinylated magnetosomes were synthesized by AMB-1 *in vivo*. In this example BAP was fused to these magnetosomes via the protein Mms13. Biotinylation was confirmed using an alkaline phosphatase, conjugated antibiotin antibody [123]. In the work present in this thesis we aim to simplify this process by using a mutated BirA enzyme which can biotinylate magnetosomes without needing the BAP fusion.

1.10 MDA-MB-231 breast cancer cell

The MDA-MB-231 breast cancer (BC) cell line has been taken from patient in 1973 at M.D Anderson cancer centre. The cells that are established from the pleural effusion of a 51-year-old woman metastatic a breast cancer have epithelial-like morphology, with spindle-shaped cell. In addition it is a triple negative breast cancer (TNBC) cell line, which resistant to the most hormonal and chemotherapy therapies, so the patients have partial treatment options[124]. Triple negative BC (MDA-MB-231) represent ~20 % of all BC cases that grow without the support of both hormones progesterone (PR) and estrogen (ER), also without express HER-2. Thus they cannot be treated with Herceptin or hormone therapy [125]. Where about two out of three women contain receptors for progesterone (PR) and estrogen (ER), also about 20-30 % of breast cancer have excess amounts of HER2 receptors [126]. So the hormone therapies can be used as a treatment for ER and PR positive. Furthermore, anti-HER2 medications can be used for breast cancer with many HER2 receptors, however, the triple-negative breast cancer that lack of any receptors for PR, ER or HER2 cannot be treated with drugs or hormone therapies [126]. The MDA-MB-231cell line was used as one of the most common breast cancer cell lines Figure 1-18. It is a highly aggressive, invasive, limited treatment ability. MDA-MB-231 is triple a negative breast cancer that which means lack oestrogen receptor (ER), human epidermal growth factor receptor 2 (HER2) and progesterone receptor (PR) [127].
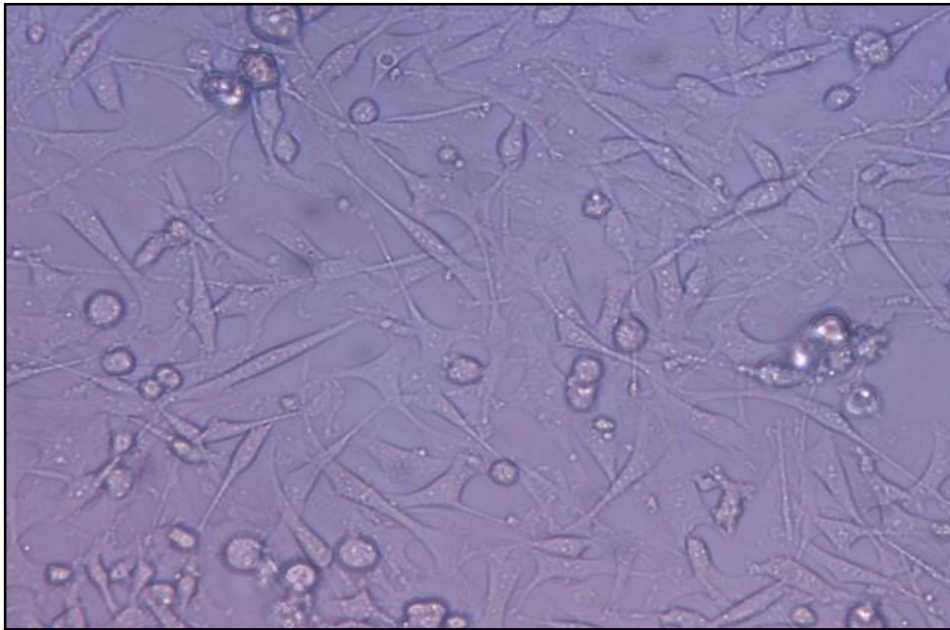
Figure 1-18: MDA-MB-231 cell line was growing in RPMI media

The breast cancer is a malignant tumour, which the most common among women between 50 and 70 years old [128]. There are many methods to decrease the mortality rate of breast cancer by first, improving BC diagnosis, secondly improving BC treatment diagnosis of breast cancer and finally by improving breast cancer treatment methodologies. Some of the novel methods for the diagnosis and treatment of triple-negative breast cancer are based on magnetic nanoparticles (MNPS). MNPs have the potential to be used as a magnetic guide delivery mechanism for therapeutic. This field has gained increasing attention over the past two decades. Research examples include their use in targeting therapy, magnetic hyperthermia and as MRI contrast agents. This allows the disease to be detected in early stages and to deliver a treatment dose at the desired area.

1.11 Aim of the study

The overall aim of this project was to optimise the magnetisation and surface functionalization of magnetosomes for MRI and magnetic hyperthermia applications as shown in

Figure 1-19.

1.11.1 The specific aims of this PhD study

Aim 1: To enhance and optimise the magnetic properties of magnetosomes by doping magnetosomes with non-ferrous metals by growing magnetotactic bacteria in different concentrations of Co^{2+}, Cu^{2+}, and Mn^{2+}.

Aim 2: Functionalize the surface of magnetosomes, via biotinylation to demonstrate the possibility of functionalisation and examine the effect on cell uptake and toxicity. To then investigate conjugation of molecules to their surface as a proof of concept study, and see whether uptake is affected.

Aim 3: Test the doped magnetosomes for their potential in biomedical applications. 1) -MRI to find which has the best signal for diagnostics *in vitro*, 2)- in hyperthermia to examine which produces improved heating properties, 3) cancer cell uptake *in vitro* and cancer cell hyperthermia *in vitro* and *in vivo.*

Chapters	State of art	In this thesis
Chapter 3: Doping the magnetosomes with Mn^{2+} Co^{2+} and Cu^{2+}	Research has formed ferrite SNP with MFe_2O_4 synthetically, M=Fe, Mn, Co and Cu. Mn^{2+} Co^{2+} and Cu^{2+} have been used to dope magnetosomes at low levels, but this is yet to be optimised.	Consolidates, optimized the single doping and tested double and triple doping.
Chapter 4: Functionalizing the surface of the magnetosomes via biotinylation	There is study for biotinylated magnetosomes by fusing a BAP to the Mms13 protein. Although this is a specific labelling method it is time consuming and complex. Group of researchers have labelled proteins using BirA, then used these as probes for protein interaction in a variety of cells. Chemical biotinylation is well developed.	In the work present in this thesis we aim to simplify this process by using a mutated BirA enzyme which can biotinylate magnetosomes without needing the BAP fusion. provides a simple, low-cost method for producing biotin- or streptavidin-label magnetosomes. Attempted enzymatic (mutation pBirATrx) biotinylation. Investigated the cell uptake of biotinylated magnetosomes.
Chapter 5: Measuring cell uptake and toxicity	Some studies evaluated the cytotoxicity of MTB in vitro. Also investigated cell uptake of MTB with a variety of cancer cells	Studied the internalization of magnetosomes within specific cancer cells. The presence and absence of magnetic delivery and the presence and absence of magnetosome membranes was tested in this strain. Cell toxicity was measured by different methods including MTT and flow cytometry as well as endotoxin contamination.
Chapter 6: Using the magnetosomes for *in vitro* magnetic hyperthermia treatment and MRI	The most recent data published on the use of native magnetosomes for MHT of tumours, also studied the effect of changing the composition of MNPs on MRI. Mn^{2+}, Cu^{2+}, Gd^{3+} used as contrast agents for MRI to enhance T_1, T_2 sensitivity of signal.	In this thesis doped magnetosomes with Mn^{2+} Co^{2+} and Cu^{2+} used to investigate MHT in vitro for MDA-MB-231 cells as well as MRI.
Chapter 7: Using the magnetosomes for *in vivo* magnetic hyperthermia treatment	Some studies investigate MHT of native magnetosomes in vivo in mouse models. They use high field strengths.	In this study, native and Co^{2+} doped magnetosomes were used in vivo for MHT on MDA-MB-231 for MHT in mild condition of field strength and frequency

Figure 1-19: Comparsion of the work investigated in this thesis with current state of the art in literature

Chapter 2:

MATERIALS AND METHODS

2 Preparing culture medium of *magnetosoprillium* AMB-1

2.1.1 Bacteria culture and growing condition

The bacteria used in this project are MTB, specifically, *Magnetospirillum magneticum* AMB-1. This strain was obtained from the Matsunaga group, Tokyo Institute of Agriculture and Technology. This is as α-proteobacteria capable of synthesising internal magnetite particles with cuboctahedral shape and in the size range 50-100 nm [129] in both anaerobic and microaerobic conditions and on solid or in liquid medium [38]. The bacteria is typically grown in a liquid medium within microaerobic conditions (1% oxygen and 99% nitrogen) at 30°C. Water used for preparing media was ultrapure MilliQ (18.2 MΩ cm) deoxygenated and with N_2 sparging before use. Most of the chemicals were purchased from Sigma, Sigma Aldrich and Fisher BioReagents chemical company.

2.1.2 Preparing culture media

The culture media preparation partially following the media methodology of DSMZ 380 Table 2-1 [130].

Table 2-1: Magnetospirillum growth medium.

Medium Component	Amount required
Ultrapure MilliQ	2000 ml
KH_2PO_4	1.36g
$NaNO_3$	0.24g
L(+)-Tartaric acid	0.74g
Succinic acid	0.74g
Na-acetate	0.10g
Resazurin	1mg

All the components were dissolved by stirring in the order given in Table 2-1. The medium was adjusted with 1 M NaOH solution to reach a pH 6.75. Then, the AMB-1 culture medium was split between 5 sterilised 500 ml bottles, each filled with 400 ml. These bottles were then autoclaved using a standard cycle (121 °C for 15 mins at 15 P). After autoclaving, and slight

cooling, the media bottles are placed in a microaerobic cabinet (Whitley VA 500 workstation cabinet) at 30 °C and 99% nitrogen gas with lids lose. After equilibrating in the cabinet for one day, Na-thioglycolate (sterilized via cellulose nitrate membrane filter pore size 0.22 µm) was added. Two days after these vitamins, minerals and 40 µM ferric quinate solutions were added to the medium as shown in Table 2-2, but it was added in consecutive days rather than the same day. The medium was a blue colour before the autoclave (due to adding the resazurin and adjusting pH), but after the full preparation, the colour changed to purple (due to the addition of Na-thioglycolate and ferric quinate, and absence of oxygen). The ferric quinate was added to feed the cells to get them to a provide growth and moderate magnetism, and also to produce magnetite.

Table 2-2: Preparation of 400 ml of magnetotactic bacterial growth medium.

Medium Component	Amount required
Na-thioglycolate (1 % w/v)	2 ml
Ferric quinate (0.01M) solution **Table 2-3**	160 µl
Welfer´s mineral **Table 2-4**	1 ml
Welfer´s vitamins **Table 2-5**	4 ml

The following (Table 2-4 and Table 2-5) detail the preparation of Ferric quinate, mineral, and vitamin solutions in separate bottles as a stock solution to add them later as needed to the culture media. All of these solutions were sterilized with a 0.22 µm filter under aseptic conditions. For the mineral solution, the nitrilotriacetic was dissolved first then the pH was adjusted to 6.5 with NaOH. Following that the remaining minerals were added. Final pH was adjusted to 7.0.

Table 2-3: 0.01M Ferric quinate

Medium Component	Amount required
Ultrapure water	20 ml
FeCl$_3$.6H$_2$O	0.45 g
Quanic acid	0.19 g

Table 2-4: Welfer´s vitamins solution.

Medium Component	Amount required
Ultrapure water	1000.00ml
Biotin	2.00 mg
Folic acid	2.00 mg
Pyridoxine-HCl	10.00 mg
Thiamine-HCl	5.00 mg
Riboflavin	5.00 mg
Nicotinic acid	5.00 mg
D-Ca-pantothenate	5.00 mg
Vitamin B12	0.10 mg
P-Aminobenzoic acid	5.00 mg
Lipoic acid	5.00 mg

Table 2-5: Welfer´s mineral solution:

Medium Component	Amount required
Ultrapure water	250.00 ml
Nitrilotriacetic acid	1.50 g
MgSO$_4$.7H$_2$O	3.00 g
MnSO$_4$.7H$_2$O	0.50 g
NaCl	1.00 g

FeSO$_4$. 7H$_2$O	0.10 g
CoSO$_4$. 7 H$_2$O	0.18 g
CaCl$_2$. 2H$_2$O	0.10 g
ZnSO$_4$. 7H$_2$O	0.18g
CuSO$_4$. 5H$_2$O	0.01g
KAl(SO$_4$)$_2$.12H$_2$O	0.02g
H$_3$BO$_3$	0.01g
Na$_2$MoO$_4$.2H$_2$O	0.01g
NiCl$_2$.6H$_2$O	0.03g
Na$_2$SeO$_3$	0.30mg

*The minerals solution was kept in the dark.

2.2 Inoculation of AMB-1 bacteria to medium

1 ml of frozen (-80°C) stock of *Magnetospirillum magneticum*, strain AMB-1, was inoculated into small bottles of medium (75 ml) and left between 4 days or one week to reach maximum density (this is dependent on the concentration and type of metals added). This culture was used to inoculate 400ml of the medium and left for 3-4 weeks with the optical density measured at points over this period to check on growth. The culture was placed on a magnetic stirrer plate to check the cells were magnetic by observing a flickering effect.

2.3 Checking magnetotactic bacteria growth rates

In general, to check the bacterial growth and formation of magnetosomes, the magnetic stirrer was used to look for a flickering effect when the magnetic field is on. However, more quantitative methods were also used.

2.3.1 Optical density and C$_{mag}$

Light scattering was used to measure the optical density of the culture to monitor cell growth, and C$_{mag}$ was used to check the cell response in a magnetic field.

1 ml volume of culture was placed in a cuvette and placed in a single beam scanning UV/Visible spectrophotometer (UV-Visible spectrophotometer CARY 50 probe). Light of 600

nm wavelength passes through the solution inside the cuvette and an amount of light is scattered by the cells in the solution. The wavelength of measurement of OD depends on growth of culture, to still stay in linear part of relation between cell number and OD measurement. Because we measured OD during 24 hours, and we expect low cell number then we need to be more sensitive in OD measurement and do it at 600 nm. A spectrophotometer can display this measurement as either transmittance or absorbance. In biological applications, it is usual to report the absorbance of a given sample. There may be other compounds in the solution which absorb at this wavelength, Therefore, the absorbance of the cell-free medium was also compared as a reference blank, and that contains everything found in the sample except the cells that are being in measured.

For C_{mag} the experiment was the same except a large bar magnet was used. The bar magnet (15 kg pull strength neodymium magnet) was placed parallel and perpendicular to the cuvette for less than minute, and the maximum and the minimum absorbance readings at 600 nm wavelength were recorded. The ratio of the maximum to a minimum was designated as C_{mag}. If the cells are magnetic they will align with the external magnet and the scattering will change.

$$Cmag = \text{ maximum Abs./minimum Abs} \qquad (2.1)$$

2.3.2 Hemocytometry

Hemocytometry was used to count the number of cells using a hemocytometer. 1 ml of AMB-1 culture was harvested by centrifugation in TX-750 at 2000 rpm for 10 min. Then the pellet of concentrated bacteria was re-suspended in 1 ml fresh magnetotactic bacterial growth medium. Approximately 100 μl of this suspension was pipetted onto a hemocytometry slide, then a coverslip was placed on the top, and a microscope at 40X magnification was used for counting cells.
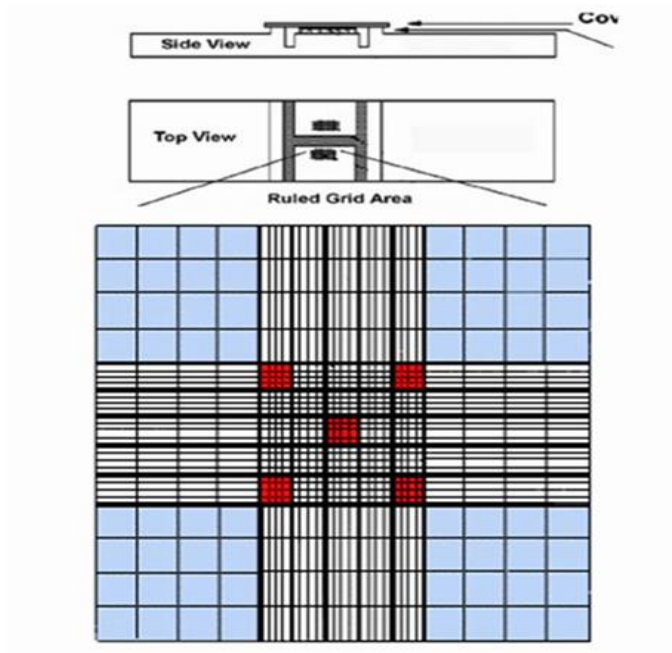
Figure 2-1: hemocytometry and load a chamber.

The hemocytometer is a square chamber, consisting of a large square with other smaller squares inside, all carved into a piece of thick glass which has a specific depth as in Figure 2-1.

The large square consists of nine squares of equal surface area. Inside the four corner squares are sixteen smaller squares that are used to count cells. The average number of cells in four of the smaller graded squares was considered to be representative of the cell density of the whole culture.

To calculate the number of MTBs cells/mL:

1. Take the average cell count from each of the sets of 16 corner squares.

2. Multiply by 10,000 (10^4).

2.4 Doping AMB-1 with various concentrations of Mn^{2+}, Co^{2+} and Cu^{2+}.

AMB-1 bacteria were doped with varying concentrations of Mn^{2+}, Co^{2+}, and Cu^{2+}, in a growth medium to produce magnetosomes with modified chemical composition. For the metal doping experiments, instead of adding ferric quinate, the various concentrations of metals (as shown in following Table 2-6) were added instead. However, the iron present in the minerals solution is adequate for the growth of the bacteria.

Table 2-6: The various concentration of metal quinate tested

Con. Metals	10 µM	20 µM	30 µM	40 µM	50 µM	60 µM	70 µM	1 mM
Mn^{2+}								
Co^{2+}								
Cu^{2+}								

2.5 Harvesting and lysing the cells

The cultures were concentrated by divide and centrifugation in 50 ml centrifuge tubes, in TX-750 at 4700 rpm for 45 minutes at 4°C in a centrifuge (Heraeus megafuge 40 R centrifuge, Thermo scientific). Then the supernatant was removed and the pellet of cells transferred to a 1.5 ml microcentrifuge tube. The magnetic cells were isolated from the suspension by positioning them for 1 day against a strong neodymium magnetic rack (0.1-0.6 mT). The magnetic pellet was re-suspended in 10 mM Tris-HCl buffer (pH 7.4) and sonicated for 1 hour (10 min pulse every 25 min, 50% amplified) using a microprobe tip sonicator (Sonics Vibra cell, USA). The magnetosomes were separated from sonicated cell debris suspension by magnetic separation, by positioning the mixture next to a neodymium magnet again. The magnetosomes were washed 4 to 6 times in 10 mM Tris-HCl buffer (pH 7.4) then re-suspended in PBS (pH) at 4°C.

2.6 Chemical synthesis and coating of MNPs

2.6.1 Room temperature co-precipitation of magnetite nanoparticles

The magnetite nanoparticles were synthesized using a co-precipitation of ferrous and ferric iron at room temperature in the presence of sodium hydroxide (NaOH), as an alkali to raise the pH under an inert atmosphere. Nitrogen was used to deoxygenate the solution to prevent uncontrolled oxidation of Fe^{2+} into Fe^{3+}. Fe^{3+} and Fe^{2+} ions generally precipitate in basic solution and form magnetite when the iron salts are present in a 1:2 molar ratio [131]

$$Fe^{2+} + 2Fe^{3+} + 8OH^- \longrightarrow Fe_3O_4 + 4H_2O \qquad (2.2)$$
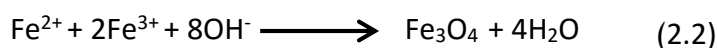
The chemicals used were, $Fe_2(SO_4)_3$, $FeSO_4$, and NaOH (from Sigma Aldrich). First, iron salts were dissolved in 10 ml of deoxygenated ultrapure water to give 50 mM total iron concentration. This was transferred into a 250 ml three-neck flask. Second, at room temperature, a syringe pump driver at a slow flow rate of 20 µl/minute pumped NaOH into the flask (500 mM deoxygenated solution). The reaction solution was stirred at 300 rpm while nitrogen gas flowed into the flask, and the reaction was carried out for 200 minutes. After that, the solution was decanted, and the particles were washed with deoxygenated deionised water 3 times. Finally, the particles were suspended in deionized water [131].

2.6.2   Surface modification of Fe_3O_4 nanoparticles with Oleic acid (OA- Fe_3O_4 NPs)

In order to make Fe_3O_4 particles suitable for biomedical applications, they have been coated with Oleic Acid (OA), which is the most common small molecules that can complex with magnetite. They have a head of polar carboxylic acid groups and a tail of non-polar hydrocarbon. Oleic acid (OA) is widely used for coating iron oxide SNP because it can form a thick protective monolayer, which produces monodispersed and highly uniform particles and a strong bond to the surface of the NPs.

The surface of magnetite coordinates with a carboxylate anion as it is presumed through coordination of iron atoms with both of the carboxylate oxygens. The polar head group is anchored on the magnetite surface, while the nonpolar tail extends into the solution. As a result, this makes the NPs of magnetite hydrophobic and disperse in organic solvents [132].

Magnetite nanoparticles, synthesized as previously described, were ultrasonicated in 200 ml of methanol to make sure they are well dispersed. Then 50 ml of oleic acid was added, with constant stirring at 80°C. Finally, after OA- Fe_3O_4 nanoparticles formed, they were filtered through a no.1 filter paper, and after that, they were separated by using acetone. Then the particles were dried at room temperature to evaporate all the acetone [132].

2.7   Characterisation of magnetosome particles, SNPs and OA-SNPs

Many methods are used to characterize and image AMB-1 cells and their magnetosomes. Transmission Electron Microscopy (TEM) was used to image magnetosomes. Elemental

mapping, Energy Dispersive X-Ray Spectroscopy EDXS, and Inductively Coupled Plasma-atomic emission spectroscopy (ICP-AES) for elemental analysis. For the magnetic properties, Superconductive Quantum Interference Device (SQUID) was used for appropriate samples.

2.7.1 Transmission electron microscopy

TEM is a technique that was used to observe the intact magnetotactic bacterial cells, individual magnetosomes, SNPs, and OA-SNPs. The TEM used in this work was an FEI Tecnai Biotwin operated at 120 kV with an Orius 1000 camera and image capture by Gatan Digital Micrograph. TEM allows higher resolution imaging by using an electron beam in comparison with light in conventional microscopy (Figure 2-2). A different TEM (JEOL 2010F FEG-TEM with the scanning unit and bright field and annular dark field electron detectors) was used for determination of the elemental mapping, and elemental analysis through Energy Dispersive X-Ray Spectroscopy EDXS and Electron Energy Loss Spectroscopy EELS. EDXS has been used for microscopic analysis to provide elemental identification of material at the nanoscale, EELS also was a compliment to EDXS, which is more sensitive to detect the metals in magnetosome samples. The TEM was used to image magnetosomes at high resolution to determine the particle size. ImageJ was used to measure the length of the longest axis of particles.

To prepare the samples for TEM, a droplet of 10 µl of cell suspension was mounted onto carbon-coated copper grids. After 1 minute, the filter paper was used to remove the excess fluid and vacuum pump also used to dry the grid. Additionally, uranyl formate stain was applied to grids of the magnetosomes particles and cells to increase the contrast of the soft matter (i.e. magnetosome membrane).

TEM uses a monochromatic beam of electrons that is produced through a potential of 40 to 100 Kilovolts (Kv) with a Schottky style field emission gun (FEG) [133]. This electron beam is passed through a strong magnetic field, which acts as a lens, and it kept under vacuum and focussed onto the sample with a series of magnetic lenses [133] in Figure 2-2. The resolution of TEM is about 0.2 nm. The image is formed by projecting the transmitted beam onto a phosphorescent screen. The thicker region of the sample or higher atomic number regions will appear dark, whilst other regions will appear bright [133].
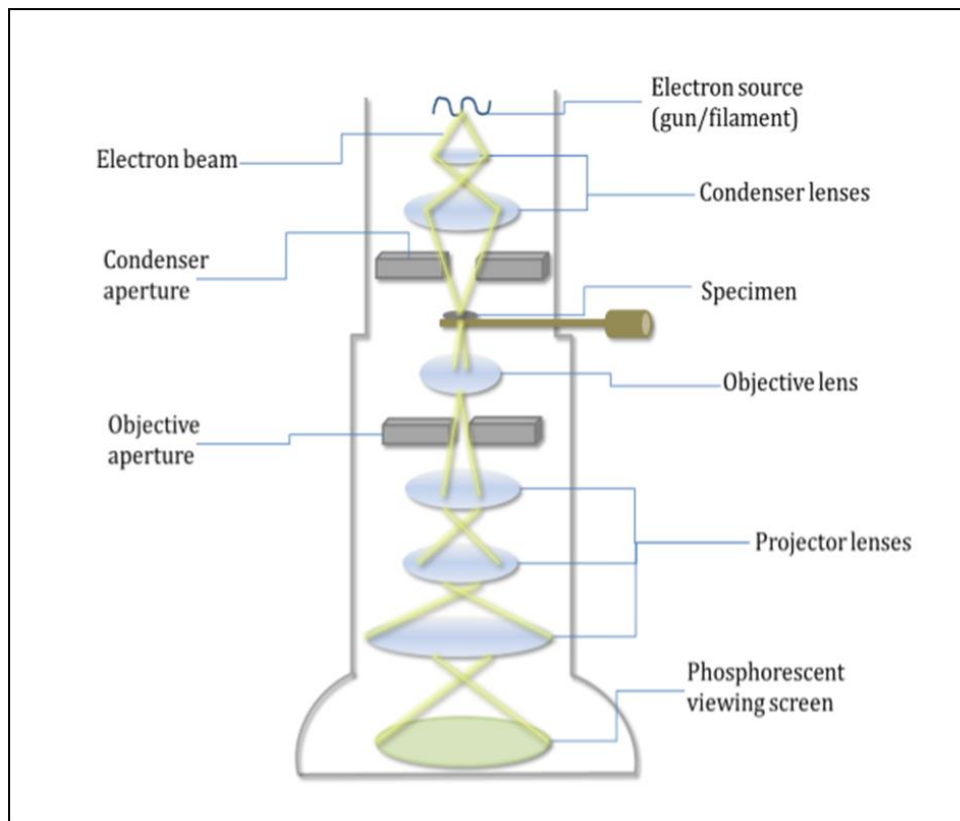
Figure 2-2: Schematic of transmission electron microscopy, reproduced from [19].

2.7.2 EDAXS

When an electron beam hits a core electron in a sample, then an electron in the ground state can become excited, which creates an electron hole. An electron from an outer, higher shell will fill this vacancy. The difference between the higher energy state and lower energy state results in x-ray emission [134]. An element present can be detected by identifying specific peaks in the EDX energy spectrum, by using the energy dispersive X-ray detector in the chamber. Samples are prepared identically to those described in 2.7.1. However, for Co-doped magnetosomes sample, gold TEM grids are used rather than copper, to prevent a background copper reading.

2.7.3 EELS

Electron energy loss spectroscopy is based on the energy loss of electrons that are absorbed by a specific element. When the incident electron beam with known energy is scattered on the sample, these electrons cause ejection of an electron from the atoms of the samples. The energies of the scattered electrons can be measured, and energy loss can be calculated, to

identify which elements are present in a sample. Samples were prepared as described in section 2.7.1, gold TEM grids were used for Co-doped magnetosomes sample.

2.7.4 Zeta potential for MNPs stabilization

Zeta potential is a physical property which is exhibited by any particle in suspension, and it is used to assess the stability of colloidal systems, by measuring the magnitude of charge or the electrostatic attraction/ repulsion between particles.

The particles that have a high repulsion, will resist flocculation, and the colloidal system will be stable. If there is no repulsive mechanism then coagulation will eventually take place. So, colloids with high zeta potential (+, −) are electrically stabilized, whereas, colloids with low zeta potential tend to coagulate [135]. The particles in the solution have a net charge that affects the distribution of ions surrounding it. This increases the concentration of counter ions [136], surrounding these particles, and this electrical double layer exists as two separate regions, Figure 2-3 [136]. An inner region knows as the Stern layer, where the ions are strongly bound and of opposite charge to the particles. An outer region called the diffuse layer, where the ions are less associated.

When the particles move through solution due to an applied voltage or gravity, these ions move with it. The ions existing within the boundary do not move with particles. This is called the slipping plane, or the surface of hydrodynamic shear, and exists with the diffuse layer. The potential at this slipping plane is the zeta potential,

Figure 2-3 [136]. The magnitude of the zeta potential determines the stability of the colloidal system. In cases where all the particles in suspension have a high negative or positive zeta potential, so the suspension will be stable because the particles will tend to repel each other and have a low tendency for coagulation. On the other hand, particles in suspension with a low zeta potential will be unstable, and there will be no force to prevent the particles from coming together and coagulating. The particles with zeta potentials more negative than -30mV or more positive than +30mV are normally considered stable [137].

Laser Doppler Velocimetry (LDV) was used in zeta potential measurement when an electrical field was applied to the sample, causing the movement of the nanoparticles. This movement was measured by (LDV) [135] to calculate the zeta potential (z); the Henry equation (2.3) was used.

$$Ue = \frac{2\varepsilon z\, \int(\kappa a)}{3\eta} \qquad\qquad (2.3)$$

Where U_e is the electrophoretic mobility, ε is the dielectric constant, η is the absolute zero shear viscosity of the medium, $\int(\kappa a)$ is the Henry function, and κa is a measure of the rate of the particle radius to Debye length.
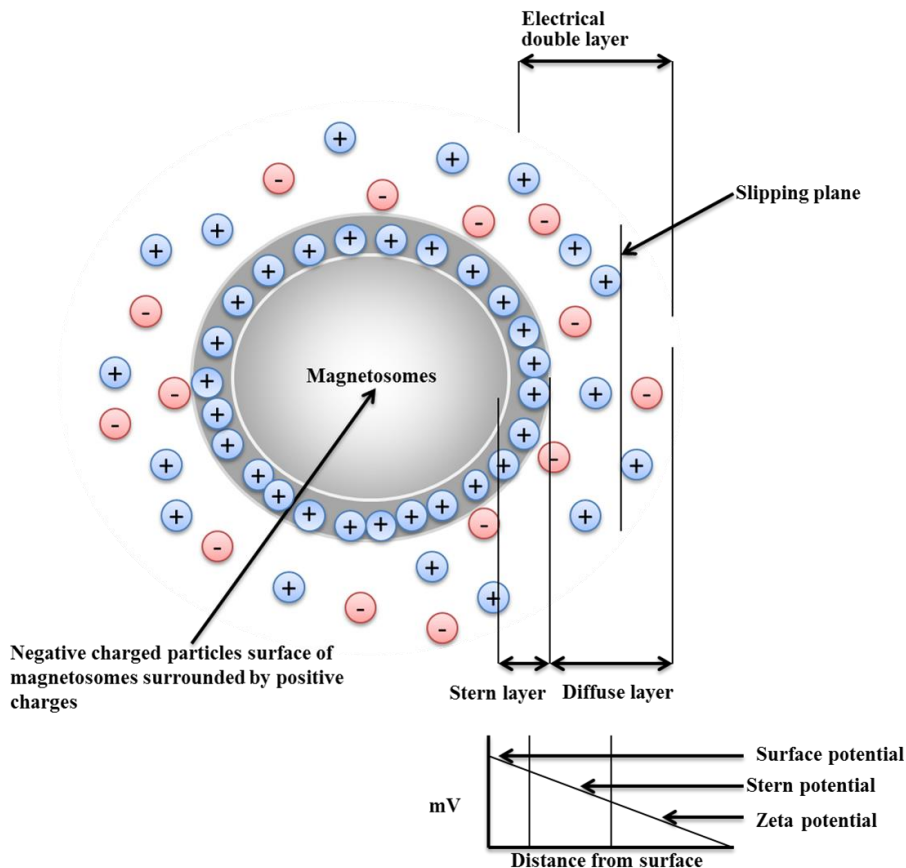
Figure 2-3: Schematic representing of Zeta potential, modified from reference [135]. Electric double layer exists around particles, that contain two regions, an inner region where the ions are strongly bound, and an outer region where they are less bound.

The Brookhaven Instruments Corporation Zeta Plus was used to measure the zeta potential of nanoparticles (Magnetosomes, SNPs, OA-SNP) with zeta potential range -150 to +150 mV and with 35 mW solid-state red laser (660 nm wavelength), at room temperature (20 °C), 8.35 V/cm Electric Field, 4.00 V and pH=7.00.

The sample of 0.50 mg/ml magnetosomes was re-suspended in 1 ml water. 200 µl of this sample was transferred to a zeta cell cuvette and 500 µl of 1 M KCl was added (note, this

medium was filtered prior to sample preparation using a 0.1 μm size membrane). Finally, the electrodes were inserted fully into the sample cell in the sample cell holder. The instrument was adjusted to measure three runs each comprising of ten cycles.

2.7.5 Dynamic Light Scattering

Dynamic light scattering (DLS) was utilised to explore the size distribution stability and aggregation of nanoparticles, by measuring the random change of fluctuation observed in light scattered from nanoparticle samples. These fluctuations are related to diffusion within the sample, due to Brownian motion, and can be used to calculate particle size. The intensity of light scattered is measured with respect to time [1]. Large particle cause more scattering than smaller particles, and is related to the diffusion coefficient (D) shown in (equation 2.4).

$$D = \frac{KT}{3\eta\pi D^H} \qquad (2.4)$$

Where η is solution viscosity, KT is the Boltzmann's constant at absolute temperature, D^H is the hydrodynamic radius of particles [1].

For the all magnetic nanoparticles, 0.5 mg was suspended in 1 ml of PBS, then sonicated in a water bath for 15 minutes. Then 20 μl of particle suspension was diluted in 1 ml of 2.5 mM KNO_3 in disposable DLS cuvette with a scattering angle of 173°, these samples were scanned three times, and each scan has 10 runs. The data was analysed using Malvern Zeta sizer Software.

2.7.6 Powder X-ray Diffraction

X-ray diffraction (XRD) can be used to identify materials based on their crystal structure. When a solid crystalline sample is hit with X-rays, they will diffract, producing a distinct scattering pattern. X-ray diffraction consists of X-ray sources that interfere with the crystalline lattice of the sample. The scattering angle (θ) is the angle between beam axis and the sample surface, and it relates to crystal lattice spacing (d), can be described by the Bragg Equation [138]:

$$n\lambda = 2d\sin\theta \qquad (2.5)$$

Where n is an integer and λ is the wavelength of the x-ray. The characteristic peaks in the XRD spectrum are produced by the crystallographic planes in the crystalline sample at a precise angle, using a Brucker-AXS D80 series 2 diffractometers, set to Bragg Brentano Parafocussing geometry.

Each crystalline iron oxide will produce a different pattern that is similar to a fingerprint technique, to identify crystal planes. The dried powder sample was spread onto a silica flat-plate and rotated in the X-ray beam. The X-ray spectrum was collected between 2θ=5° and 80° on a Braun position sensitive detector. MNPs were analysed using x-rays generated from a Cu Kα_1 source (λ= 1.54056 A°), operating at 40 kV at room temperature.

2.7.7 IR spectroscopy

About ~30 mg of purified magnetosomes were dried in an oven at 37°C and 13 mg of Fe_3O_4 synthetic nanoparticles were suspended in water, and 20mg of OA-SNP were suspended in acetone. The samples were directly scanned via FT-IR (a Perkin-Elmer Paragon 100 FTIR spectrometer.) using transmission mode under ambient conditions (over the wavenumber range 500-4000 cm^{-1}).

2.7.8 Inductively coupled plasma Atomic Emission Spectrometer (ICP-AES)

ICP is an analytical technique used for elemental analysis. It is used to produce excited atoms and ions which emit electromagnetic radiation at specific wavelengths that are characteristic of a particular element. The intensity of this emission can be related to the concentration of a particular element within a sample. The quantity of Mn, Fe, Co, and Cu were measured as a ratio of metal ion using a Spectro-Ciros-Vision Inductively Coupled Plasma Atomic Emission Spectrometer ICP-AES. Approximately 0.05 mg of magnetosomes were dissolved in 1 ml aqua regia (molar ratio of 1:3 nitric acid to hydrochloric acid) and diluted to reach 10 ml with added water. The sample was then bath sonicated for 4 hours. For the elemental content, this sample was run through the ICP-AES instrument.

2.7.9 Super Quantum Interference Device (SQUID)

Superconducting quantum interference device (SQUID) was used to measure the magnetic properties of selected samples. A SQUID-VSM (vibration sample magnetometer) model MPMS3 from Quantum Design, were used. A known mass of dry magnetosomes, SNPs and

OA-SNPs. sample and magnetosomes samples were packed into small gelatine capsules (size 3). The capsule sample is then mounted on the end of a carbon fibre rod and then inserted into the instrument to sit between a pair of pick up coils at 55 Hz vibration inside the VSM. The magnetization generated by the vibrating sample creates a magnetic flux that induces an AC voltage in the pick-up coils. The magnetic moment of the sample is measured by passing it through the superconducting pick-up coil while supplying a magnetic field up to ~ 1 T (Tesla). To describe the response of these MNPs to different MF, the magnetization (M) can be plotted against the applied magnetic field (H), this is known as the magnetization curve (M-H). The resulting hysteresis is dependent on the type of material that is analyzed and can reveal several important parameters [137][139]. The area enclosed by the hysteresis loop is proportional to the amount of energy that is released to the environment from the nanoparticles in an oscillating magnetic field and depends upon the magnetic saturation (M_s), coercivity (H_c) and remnant magnetization (M_r). The magnetization measurement of magnetosome samples was carried out at 300 K (room temperature).

2.8 Chemical biotinylation

Sulfo-N-hydroxysuccinimide biotin (Sulfo-NHS) (EZ-Link ^{TM} sulfo-NHS-Biotin 21326, Thermo Scientific) was used for simple and efficient biotin labelling of primary amine groups (-NH_2). The groups are found on the side chains of lysine (K) residues on the magnetosome surface exposed proteins in the magnetosome membrane. Biotin is a vitamin that binds to the streptavidin protein with high affinity, and it can be conjugated to many proteins, often without changing their biological activities.

Sulfo-NHS ester biotinylation reagent is water soluble as a result of the charge carried on sodium sulfoxide group in the succinimidyl ring, which enables reactions to occur in the absence of organic solvents such as DMSO or DMF. Furthermore, it cannot permeate intact cell membranes, meaning biotinylation will be performed only on primarily amines on the membrane surface.

Also, HEPES buffer (4-(2-Hydroxyethyl) piperazine-1-ethanesulfonic acid, N-(2-Hydroxyethyl) piperazine-N`-(2-ethanesulfonic acid) sigma H4034-100G) was used in this experiment.

3 mg of magnetosomes were washed three times with 100 μl (ice cold) HEPES buffer (20 mM pH 7.4), to remove amine groups contained in the medium. Note; every time the magnetosomes were collected with a magnet before removing the HEPES solution. Then 3 μl of 2 mM sulfo-NHS-Biotin was added to the suspended magnetosomes and the reaction mixture was incubated for 1 hour on ice in the dark, and vortexed every 15 min. The magnetosomes were next washed 3 times with 100 μl of cold HEPES buffer to remove the sulfo-NHS-Biotin solution. The magnetosomes were then resuspended in 100 μl of cold (4°C) 20 mM HEPES buffer (pH 7.4) and 1 μl of streptavidin conjugated with Alexa Fluor 488 was added. Streptavidin, Alexa fluor® 488 conjugate (Thermofisher S32354) is streptavidin covalently attached to a fluorescent label (Alexa Fluor®dye) for specific detection of a variety of biotinylated nucleic acid, proteins and other molecules. The reaction was incubated for 1 hour on ice in darkness with agitation every 15 min. Finally, the magnetosomes were washed 3 times with 100 μl of 20 mM cold HEPES buffer to remove non-bound streptavidin. A fluorescence microscope (Zi Zeiss inverted microscopy 20X, 40X, and 100X lens) was used to image magnetosomes biotinylated and bound to the fluorescent streptavidin (using green signal).

2.9   Enzymatic Biotinylation

2.9.1   Transformation of competent *E. coli* cells

The vector PET-32a containing the *birA* gene was provided by the Department of Biochemistry at the University of Texas Health science centre at San Antonio [112]. The vector was introduced into *E. coli* strain XL10 Gold using a heat shock protocol, which is heating at 42° C for 30 seconds in a heat-shock step, and returned to ice for a further 5 minutes. Cells are allowed to recover in 400 μl of LB (Luria Bertani) at 37 o C for 1 hour. .Where an aliquot (100 μl) of competent cells was taken out of -80°C and thawed on ice (approximately 20-30 minutes). 2 μl of the final product from the DpnI reaction or purified plasmid was added with gentle swirling, then incubated in ice for 5 min. After that, the tube was quickly transferred to a heating block at 42 °C for 30 seconds, before putting this transformation mixture back on the ice for 5 minutes. 400 μl of LB (Luria Bertani) Table 2-10, without antibiotic was added to allow the cells to recover, and placed in an incubator with shaking for one hour at 37 °C. 100 μl of the transformation mixture was plated out onto LB-Agar, (recipe in Table 2-10)

containing 40 μg/μl (50 mg/ml) of carbenicillin and incubated at 37 °C overnight. Finally, only cells that contain the plasmid will be able to grow and form colonies as described in section 2.9.7.

2.9.2 Site-Directed Mutagenesis

DNA sequences can be specifically altered at a certain site using a process called Site-Directed Mutagenesis, which is also called oligonucleotide-directed mutagenesis. This is a powerful technique to selective mutate a specific DNA sequence. This technique uses primers which are complementary to the desired plasmid except for a specific base mismatch encoding the desired mutation. Besides the mutation of a single base change, there is the possibility of introducing larger insertions or deletions.

2.9.3 Oligonucleotide Mutagenic Primers

A key step in the mutagenesis procedure is to create two short DNA primers that are complementary to the region of the plasmid to be altered, except for a mismatch of bases at the mutation site. Primers used in this study were designed using software called PrimerX, and the sequences are shown below (The red colours letter represent the mismatch of arginine to glycine codons).

BirAR118G-F   5' GGCTGGCCGTGGT**GGT**CGGGGTCGGAAATG 3'

BirAR118G-R   5' CATTTCCGACCCCG**ACC**ACCACGGCCAGCC 3'

2.9.4 The mutagenesis reaction

Synthesis of copies of the plasmid of interest from the mutagenic primers was performed using an *in vitro* enzymatic reaction PCR. The reaction requires several necessary components, first is plasmid DNA template. Secondly, a primer pair carrying the desired mutation (2.9.3), deoxynucleotide triphosphates (dNTP), a high fidelity DNA polymerase, polymerase buffer, and finally, magnesium sulphate and water (Table 2-7) [140].

There are three thermal steps in the reaction: denaturation (or melting), annealing, and elongation (or extending). They are typically completed in 16-35 cycles. The cycle begins with denaturation of double-strand template DNA, which occurs at 95 °C for 20 to 30 seconds. This temperature is above the melting temperature of DNA, to ensure that all hydrogen bonds between complementary base pairs are broken, to yield only single-stranded DNAs. The next

step is called annealing where the single-stranded template is cooled, and the primers bind with the complementary template strands. The annealing temperature is 3 to 5 °C below the lower melting temperature of the two primers. Annealing occurs for 20 to 40 seconds. The third step is elongation where the temperature is raised to 72 °C, which is optimal for polymerase activity, and dNTPs are used to extend the primers in the 5′to 3′ direction complementary to the template strand to make double-stranded DNA (Figure 2-4). The number of bases that need to be added and the efficiency of the enzyme determines the extensions time. The next cycle begins once the elongation completes Table 2-8.

Table 2-7 : Mutagenesis reaction components

The reaction mixture for a 50 µl volume:		
Component	**Concentration**	**Volume required (µl)**
dNTP	2 mM	5 µl
KOD polymerase buffer	10X	5 µl
Magnesium sulfate	25 mM	3 µl
DNA template	> 50 ng/ µl	1 µl
Bir-A 118G-F forwards primer	100 pmol/µl	1 µl
Bir-A 118G-R Reverse primer	100 pmol/µl	1 µl
KOD DNA polymerase	> 1 unit/ µl	1 µl
H_2O	nuclease free	33 µl

Table 2-8 : Thermocycling parameter for site direct mutagenesis reaction:

Steps	Temperature	Duration/ second	Number cycles
Initial Denature	95	30	1
Denature	95	30	18
Anneal	55	60	
Extend	72	420	
Hold	10	∞	1

2.9.5 Digestion Reaction (DpnI treatment)

Following the mutagenesis reaction, the product was digested, by adding 1 µl of endonuclease DpnI, and incubating for 1 hour at 37 °C. DpnI only cleaves at methylated sites, breaking down the template plasmid. (Black circle) and leaving the synthesized mutant product (green circle) intact Figure 2-4.

Table 2-9 : Reaction components DpnI digestion:

Reaction component	Volume required (µl)
Mutagenesis reaction product	21.5
Cut Smart buffer	2.5
DnpI	1
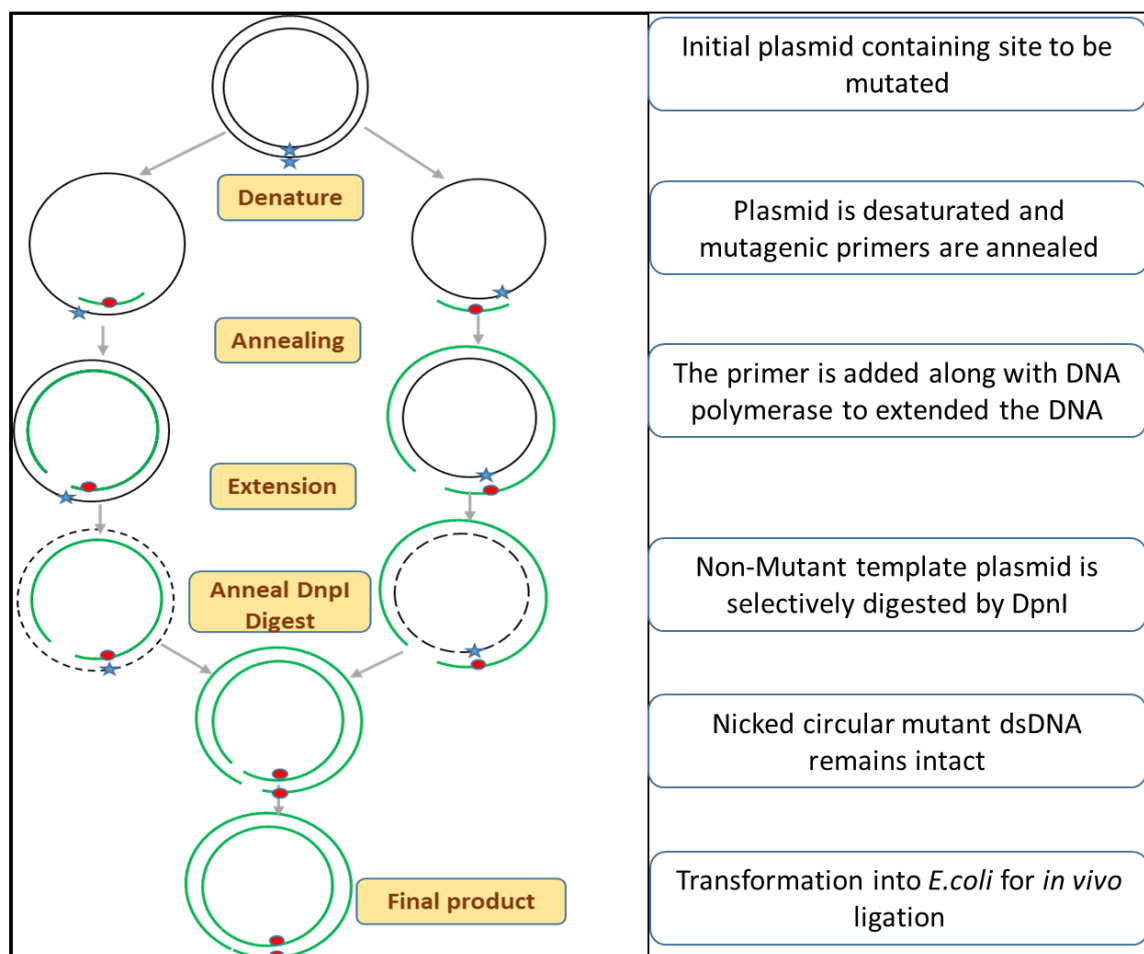
Figure 2-4: Site directed mutagenesis. The template plasmid is shown by black circles, the blue star represents the gene of interest and the red dots represent the mutation target site, the green line represent the primer, and synthesized mutant DNA is present as a green circle.

2.9.6 **Agarose Gel Electrophoresis**

Agarose gel electrophoresis is a technique used for assaying the form, purity and size of DNA that is present in solution sample. An electric field is applied to a gel containing a low percentage of agarose so that the charged DNA will migrate through the gel matrix. The phosphate backbone of the DNA molecule is negatively charged at neutral pH, causing the negative charge of DNA to migrate towards the positively charged cathode. Agarose gel electrophoresis is also used to distinguish between linear DNA and plasmid DNA (relaxed circular and supercoiled). Relaxed circular DNA is more retarded in the gel than the tight supercoiled conformation.

The DNA ladder consists of DNA fragments of a known size that are used to estimate the size of unknown samples based on their migration distance in the gel. To visualize the resolved bands of DNA that are present in a gel the Sybr Safe DNA gel stain was used. Sybr safe binds between individual DNA bases and fluoresces in the visible spectrum when subjected to UV light sources.

To make 1% agarose gel, 0.5 g of agarose was added to 50 ml Tris-Acetate-EDTA (TAE) (40 mM Tris-acetate pH 7.5, 1mM EDTA) and heated until fully dissolved. An appropriate amount of Sybr safe DNA gel stain (3 µl), was added. The melting agarose was poured into the casting tray a comb inserted to form wells. The casting tray containing set gel was placed into the gel tank and submerged in TAE buffer to cover the gel 3-6 mm. Approximate 5 µl DNA samples are supplemented with 1 µl of 6X concentration loading dye (6xMassRuler DNA loading dye),. The 1Kb DNA ladder was also pipetted into the gel. 120 V potential was applied to the gel for 45 min. To visualize the DNA fragment, the gel was exposed to UV light using a ChemiDoc (BioRad) camera system.

2.9.7 **Transformation of competent *E. coli* cells**

Transformation is the process where foreign DNA is up-taken into a cell. The bacterial cells that can accept plasmid or extra-chromosomal DNA from the environment are known as competent cells. Most plasmids carry both antibiotic resistance genes and origin of replication. The antibiotic resistance gene can be used as a selectable marker in bacteria. There are two methods to generate competent cells: natural competence, and artificial competence [141]. The natural one occurs naturally, where the bacterium has a genetic ability

to receive environmental DNA, while the artificial one occurs under chemical treatment and heat shock to make DNA pass through the cell membrane. The chemical transformation has been used in this procedure [141] for the transformation of XL10 Gold and BL21(DE3) *E. coli* cells.

An aliquot (100 µl) of chemical competent cells was taken out of -80°C and thawed on ice (approximately 20-30 minutes) these cells were prepared and provided by Dr. A. Rawlings using a standard protocol of calcium chloride and rubidium chloride treatment [142]. 2µl of the final product from the DpnI reaction or purified plasmid was added with gentle swirling, then incubated in ice for 5 min. After that, the tube was quickly transferred to a heating block at 42 °C for 30 seconds, before putting this transformation mixture back on the ice for 5 minutes. 400 µl of LB (Luria Bertani) Table 2-10 without antibiotic was added to allow the cells to recover, and placed in an incubator with shaking for one hour at 37 °C. 100 µl of the transformation mixture was plated out onto LB-Agar, containing 40 µg/µl (50 mg/ml) of carbenicillin and incubated at 37°C overnight. Finally, only cells that contain the plasmid will be able to grow and form colonies as described in

Figure 2-5

Table 2-10: Preparation of Luria Bertani (LB) medium:

	Component	Amount	Conditions
500 ml LB	Tryptone	5 g	Adjust pH to 7.2 with 1M NaOH. Autoclave solution
	Yeast extract	2.5 g	
	NaCl	5 g	
	Water	500 ml	
500 ml LB Agar	Tryptone	5 g	Adjust pH to 7.2 with 1M NaOH. Autoclave solution
	Yeast extract	2.5 g	
	NaCl	5 g	
	Water	500 ml	
	Agar	7.5 g	
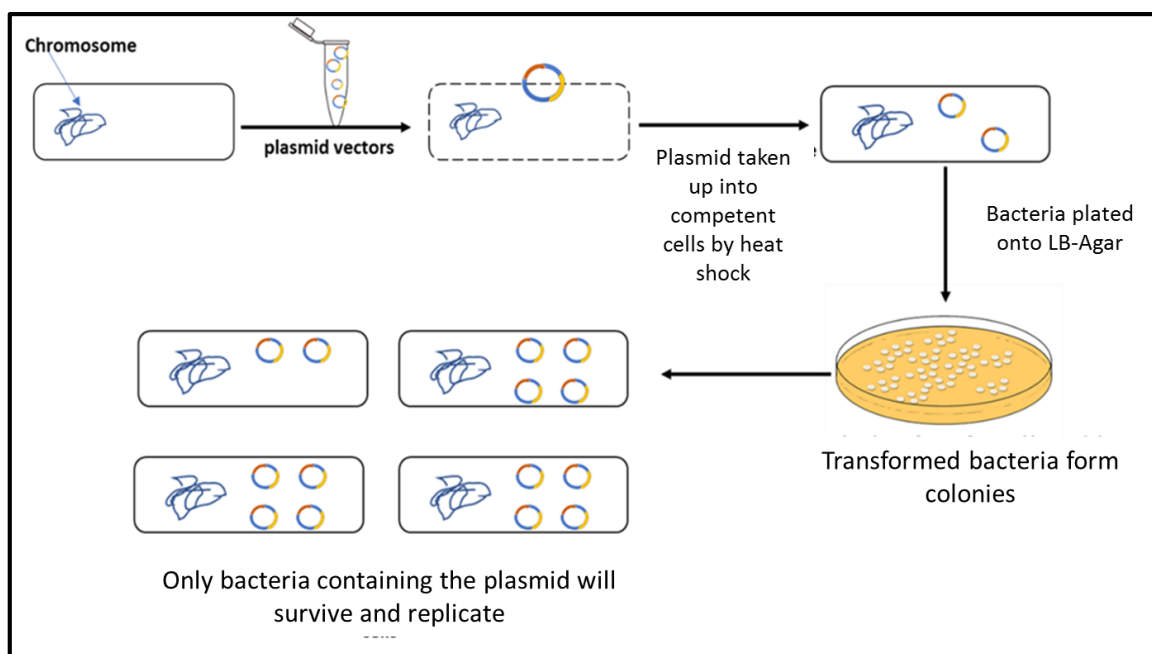
Figure 2-5: Transformation of recombinant DNA into competent cells.

2.9.8 Extraction of plasmid

To identify colonies that contain the recombinant DNA or required mutation small colonies are selected and cultured, and the plasmid extracted and DNA sequenced.

A single colony from an LB-Agar plate was picked using a sterile pipette tip, and grown in a 50 ml falcon tube that contained 5 ml LB and 10 µl of carbenicillin antibiotic (50 mg/ml), then incubated in a shaker for one day at 37°C with 175 rpm shaking. After 24 hours cells were harvested by centrifugation for 10 min using Fiberlite F15-6X100y at 3500 rpm. The supernatant was removed and the plasmid purified using a GeneJet MiniPrep Kit. Pure DNA plasmid was stored at -20 °C after checking with agarose gel electrophoresis (section 2.9.6), and quantified using a Nano drop. 15 µl samples at 100 ng/ were prepared for DNA sequencing at Genewiz.

2.9.9 The UV-VIS spectrophotometer

The Nanodrop spectrophotometer from ThermoScientific was used for measure the nucleic acid and protein concentrations in a sample volume of 2 µl, and it is able to scan the sample through the 220-750 nm range. Nucleic acids absorb UV light at 260 nm due to the aromatic

base moieties in their structure (purines and pyrimidines), while proteins strongly absorb at 280 nm based on aromatic amino acid side chains (tryptophan and tyrosine).

The Beer-lambert law equation (2.6) [143], which links absorbance and concentration, can be used to determine DNA and protein concentration by measuring the UV absorption of the solution.

$$A = \log \frac{I_0}{I} \ = \ A = \varepsilon cb \qquad (2.6)$$

Where A= absorbance, ε= the molar absorption coefficient for the samples, C= concentration, b=path length.

2 μl of a sample was loaded onto the sensor, and the absorbance at the required wavelength was recorded. A baseline zero reading prior to measurement of samples was carried out first.

2.10 Protein production

One microliter of plasmid (pBirATrx) was taken and added to 100 μl of BL21 (DE3) *E. coli* cells and introduced into the cells following the protocol described in section (2.9.1). A colony from the plate was used to inoculate 5 ml LB medium, including 10 μl of carbenicillin (50 mg/ml), and to generate a dense culture it was incubated overnight at 37 °C with shaking at 175 rpm. This 5 ml culture was added to 500 ml of LB in a 2 l fluted conical flask with 1 ml carbenicillin, with further shaking at 175 rpm and 37 °C for 4 hours, before adding 500 μl of (1mM) IPTG (Isopropyl β-D-1-thiogalactopyranoside). The plasmid was introduced into a strain of *E. coli* that containing a source of T7 RNA polymerase. The *birA* gene is under the control of the lactose inducible promoter and has a T7 RNA polymerase binding site. Adding IPTG (a synthetic analogue of lactose) allows the T7 RNA polymerase to bind at the promoter site on the plasmid and starts the transcription of the *birA* gene. IPTG binds to the Lac repressor protein and releases it from the lacO site, Figure 2-6. So this induces a large yield of the target protein to be produced. The culture is incubated with the IPTG for 4 hours at 18 °C with shaking at 175 rpm.
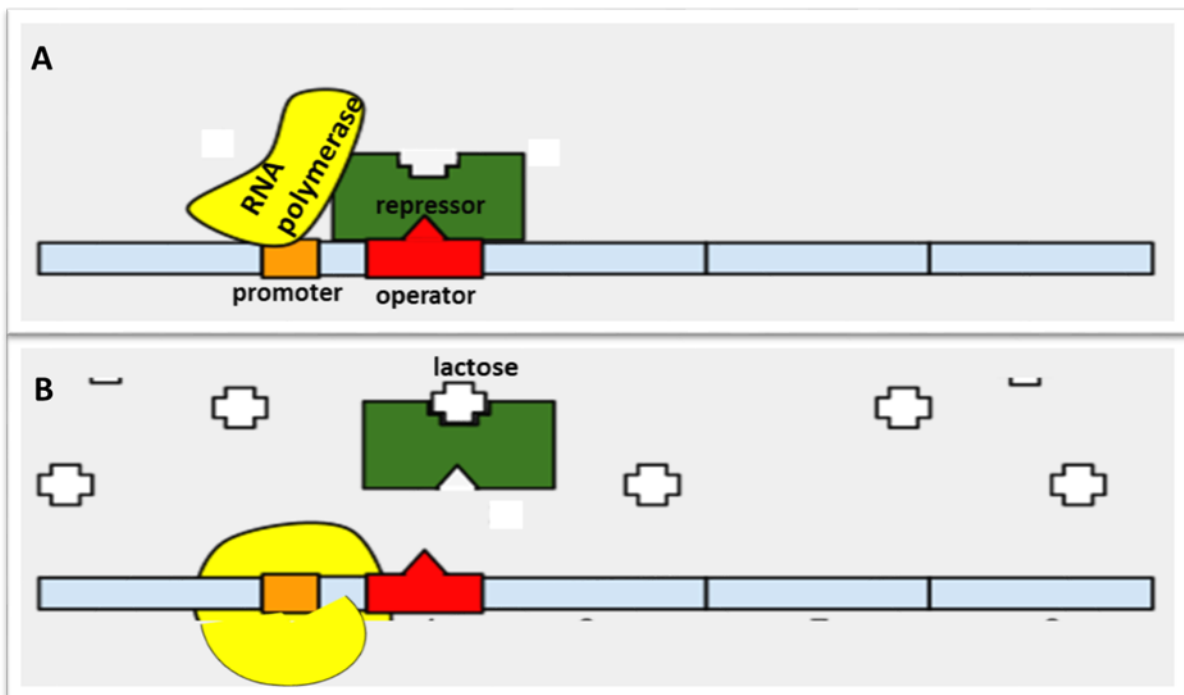
Figure 2-6: Induction of the target gene with lactose or IPTG; A- repressor binds to the lacO site and prevents transcriptionn. While in B- Lactose inhibits the repressor protein and allows RNA polymerase to bind with the promoter and express the gene. This figure modified from reference [144].

2.10.1 Harvesting and lysing cells

After 4 hours at 18 °C the cells were harvested by centrifugation in Fiberlite F15-6X100y at 5000 rpm, for 20 minutes, then the pellet was re-suspended in 20 ml of lysis buffer (buffer A) (Table 2-11), with shaking and vortexing. The cells were then sonicated, using a large sonicator probe (8mm) for 3 minutes at 40% power with breaks for collins on ice. It was then transferred to a centrifuge tube, for further centrifugation using Fiberlite F15-6X100y at 12,000 rpm for 45 minutes at 4 °C, to clarify the cell lysate so that insoluble proteins and material is removed (section 2.11.1.) Finally, 10 µl of the supernatant was taken to analyse by SDS-PAGE (section 2.12.1).

Table 2-11 : The component and recipe of protein purification:

	Component concentration
Buffer A	25mM Tris pH 7.4 100mM NaCl
Wash A	25mM Tris pH 7.4 100mM NaCl 30mM Imidazole pH 7.5
Elution buffer	25mM Tris pH 7.4 100mM NaCl 300mM Imidazole pH 7.5

2.11 Protein purification

It is necessary to remove other cellular proteins from *E. coli* that are present with the target protein. Various protein purification protocols are available depending on the protein being purified such as proteins charge state, hydrophobicity, size or by using engineered protein tags. For the protein used in this research, BirA, Immobilized metal affinity chromatography was used.

2.11.1 Immobilised Metal-ion affinity chromatography

Immobilized metal affinity chromatography (IMAC) is commonly used for recombinant protein purification, where a small peptide tag of poly-histidine is present at one of the protein's termini. In this study, the six histidine residues known as 6xHis tag was used. This tag has an affinity for many transition metal ions, e.g. nickel [145], and can interact usingh the side chain of histidine to form coordination bonds via electron donor groups to the metal [145]. IMAC uses a solid phase matrix decorated with Ni^{2+} ions to trap 6xHis tagged proteins from a protein mixture.

HiTrap global column (GE Healthcare) one milliliter was used for protein purification. It is prepacked with an agarose-based matrix with chelating groups that allows the column to be

charged with a variety of different divalent cations. For BirA purification, 5 ml of 100 mM nickel sulphate was used to charge the column and it was then equilibrated with the lysis buffer. The supernatant produced in section (section 2.10.1), was loaded onto the column using an Akta Pure purification system. The liquid that passes straight through the HiTrap column was collected and referred to as the flow-through. Buffer A was used to wash the column (Table 2-10) until the UV baseline returned to zero, showing that all the unbound protein had been removed. Following that, the column was washed again with elution buffer, to elute the bound protein. The 300 mM imidazole acts as a competitive chelator of the Ni^{2+} ions. The peaks fraction were collected, and stored at 4°C and then analyzed by SDS-PAGE as described in section (2.12.1).

2.12 Protein Analyses

2.12.1 Polyacrylamide Gel Electrophoresis (SDS-PAGE)

Electrophoresis refers to the mobility of charged molecules responding to an electric field, causing their separation [146]. Proteins, coated in the negatively charged detergent sodium dodecyl sulphate (SDS), move towards the positive electrode. This movement is based on the size of the protein. Electrophoresis can be used for many of applications. The key applications are assessing protein purity and estimating their size (molecular weight). When electrophoresis is performed in polyacrylamide gels, the gel serves as a size-selective sieve during separation, and adjusting the concentration of acrylamide in the gel makes it more or less dense with smaller or larger pore sizes which affect the resolution. The smaller the protein, the more rapidly it will travel in the gel.

In most PAGE applications, the gel is mounted between two buffer chambers with a vertical orientation (Figure 2-7 A). The gels were prepared according to the recipes in Table 2-12, the gel was prepared in two sections, with different buffers and acrylamide percentages, with the large-pore stacking gel on top of a small pore resolving gel (Figure 2-7 B).
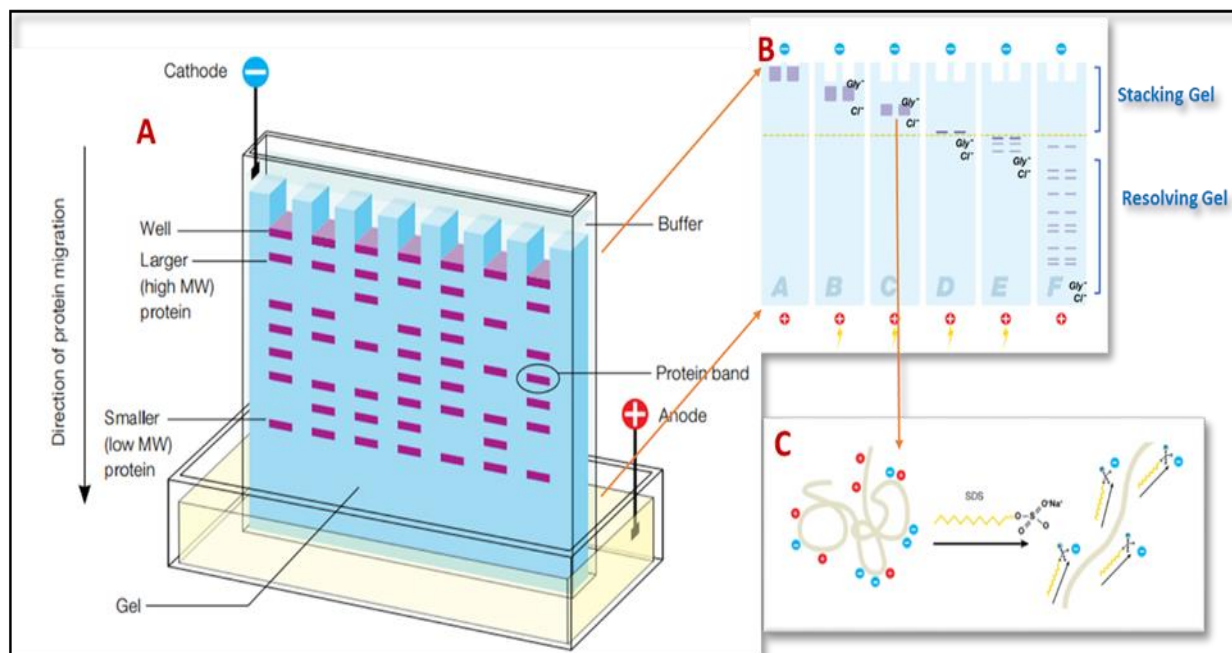
Figure 2-7: A-schematic of electrophoretic protein separation in a polyacrylamide gel. B- Migration of individual proteins according to molecular weight in denaturing discontinuous PAGE buffer. C-SDS binds to proteins to denature protein, making them negatively charged [146].

In this gel system [147] the resolving gel (pH 8.8) with a high percentage of acrylamide (≈ 12-15 %) was poured into the cavity first. Once set, the stacking gel (pH 6.8) with a low percentage of acrylamide (4%) is poured on the top, and the comb placed to make wells for sample loading. The gel is then placed in a tank and covered with running buffer. The samples should contain approximately 1-10 µg of protein for good resolution and clear visualization on the gel with Coomassie staining. Sodium dodecyl sulfate (SDS) is used with the discontinuous denaturing buffer system, to overcome the limitation of using native PAGE system and give an accurate measurement of the protein molecular weight. [147] SDS is a 12 carbon hydrophobic chain with a negatively charged sulphate head group that wraps around the peptide backbone noncovalently to denature the proteins, Figure 2-7 C. The protein samples were mixed with blue loading dye (Thermo scientific) in a ratio of 25 µl of sample and 5 µl of loading dye, and then denatured for 5 minutes at 95°C. The loading dye contains SDS, β-mercaptoethanol to reduce disulfide bonds, glycerol to increase the density of sample, and a blue dye to make it easy to visualize. The SDS coating makes the proteins negatively charged, masking the normal charge of the protein since the SDS binds at a consistent ratio of 1.4 g of SDS per 1 g protein (stoichiometry of about 1 SDS molecule: 2 amino acid),[146] making a

similar charge to mass ratio for all proteins. As a result, the measurement of migration in the gel between different rod-shaped protein SDS complexes depends on its size, allowing molecular weight estimation. 20 µl of samples were loaded to the wells of the gel and a 200 V electric field was applied to separate proteins for 55 minutes 5 µl of molecular weight ladder (PagRuler, Life Technologies) between 10 to 180 KDa was also added, so unknown protein molecular weight can be compared to the ladder proteins to provide a reliable estimate of molecular weight. The proteins in the stacking gel migrate quickly through the large pores, and then slow as they enter the small pore resolving gel. Figure 2-7 B. After the separation is finished, InstantBlue (Expedeon), a colloidal Coomassie blue stain, was used as a stain to bind to proteins for 20-60 minutes but not bind to the gel. In the final step, the gel was washed with water to remove excess stain and produce a transparent colorless gel to show only the blue protein bands. The gel was imaged using a ChemiDoc (Bio-rad) camera system.

Table 2-12: The component of the SDS-PAGE experiment:

Gel solution	Component	Concentration/ amount
SDS-PAGE Resolving Gel (for 2 gels)	30 % Acrylamide	4 ml
	10 % APS	60 µl
	TEMED	13 µl
	Milli-Q water	3.43 ml
	Resolving buffer	2.5 ml
4X Resolving Buffer made up to 1 litre with milliQ	Tris-HCl pH 8.8	1.5 M
	SDS	0.4 %
SDS-PAGE Stacking Gel (for 2 gels)	30 % Acrylamide	700 µl
	10 % APS	60 µl
	TEMED	20 µl
	Milli-Q water	3 ml
	Stacking buffer	1.25 ml
4X Stacking Buffer made up to 1 litre with milliQ water	Tris-HCl pH 8.8	0.5 M
	SDS	0.4 %

Running Buffer	Tris-HCl pH 8.8	25 mM
	Glycine	200 mM
	SDS	0.1 %

2.12.2 Western blot technique

Western blotting is a very useful technique to analyse proteins after SDS-PAGE [147]. Involving sample preparation, gel casting, and protein electrophoresis, this technique electrophoretically transfers the protein to a nitrocellulose membrane from the SDS-PAGE gel, blocking the membrane with non-specific proteins, binding an antibody to the protein of interest, and detecting the antibody and collecting an image.

 The gel, nitrocellulose membrane and the filter papers were soaked in transfer buffer for 15 minutes (Table 2-13), and then assembled into a stack in a semidry transfer unit (Transblot Turbo, Bio-Rad), and the electric field applied for 30 minutes to transfer the protein bands from the gel to the nitrocellulose membrane. Then to block the membrane surface, the membrane was incubated with 25 ml of blocking buffer for one hour with gentle shaking. 4 µl of the primary antibody (anti 5xHis HRP conjugate antibody, Qiagen) was added to the blocking buffer which binds specifically to the target protein (the antibody recognises the 6xHis affinity tag) for one hour. Following that, the membrane was triple washed for ten minutes with PBST. Finally, BioRad Clarity chemiluminescence solution was added to the membrane. This contains hydrogen peroxide and luminol. The antibody HRP is a peroxidase enzyme that breaks down hydrogen peroxide to peroxide radicals which interact with the luminol. The luminol emits light at 425 nm in the excited state, so the Chemo-luminescence is limited to areas that contain only the protein of interest. This emission is visualized using a Bio-Rad ChemDoc MP imaging system. All component recipes are shown inTable 2-13.

Table 2-13: The recipe buffer for western blot

	component	amount
Towbin transfer buffer	Tris	1.5 g
	Glycine	7.2 g
	Methanol	100 ml
	MilliQ water	500 ml
Blocking buffer	BSA (Bovine Serum Albumin)	0.75 g
	PBS	25 ml
Washing buffer (PBST)	tween	250 µl
	PBS	500 ml

2.13 Cell culture

MDA-MB-231 was obtained from Dr Munitta Muthana, Oncology Department, the University of Sheffield Medical School. Cells were grown in Roswell Park Memorial Institute media (RPMI). This type of triple negative cancer cell line was used during this study and supplemented with, 1% L-glutamine (20mm in 0.85% NaCl solution), 10% Foetal Bovine Serum (FBS), 1% penicillin (5000 U/ml) and streptomycin (5000 µl/ml) (all from Lonza®). The MDA-MB-231 cells were cultured in T75 flasks. The medium was changed every 3-4 days and passaged when the cells reach 70-80%. Confluence can be used for sub-culturing. Incubation conditions were 37°C with 5% CO_2. Furthermore, the cells were regularly Mycoplasma tested and all Lab work took place within a Biological Safety Cabinet under sterile condition.

2.14 Cell harvesting and seeding densities

All cells were harvested once 70-80% confluence, using 3 ml of trypsin EDTA (Lonza® 200 mg/l versene and 170,000 U Trypsin/l), then neutralized with 7 ml RPMI medium. Then they are centrifuged for 5minutes at 21°C, 1000rcf (sanyo® Harrier 18/80). Then cells were re-suspended in 10ml of RPMI medium and in order to determine cell viability when cell counting 10 µl of this sample was taken and mixed with 10 µl trypan blue. Next, 10 µl was placed onto

a cell counting slide and analysed using a TC 20 automated cell counter. The Trypan blue negative was used for counting live cells.

Cells were prepared as follows: in 6 well plates a seeding density of 300,000 cells/well was used in a final volume of 2 ml of RPMI medium for preparing LSRII analysis; in 24 well plates with 13mm cover slips (BDH cover glass), using a seeding density of 50,000 cells/well in 1 ml of RPMI medium for Prussian blue staining; in 96 well plates using a seeding density of 1000 cells/well in 200 μl of RPMI medium for the MTT assay.

2.15 Incubation of magnetic nanoparticles (MNPs) with cell lines

MNPs used throughout this study, were the natural MNPs extracted from magnetotactic bacteria AMB-1 that were doped with various concentrations of Co^{2+}, Cu^{2+}, Mn^{2+}. Synthetic magnetite nanoparticle SNPs and coated Oleic Acid synthetic Nanoparticles OA-Fe_3O_4 (OA-SNPs) were used as well. All MNPs and magnetosomes used in this study were prepared at the following concentrations; 0.022 mg/ml, 0.043 mg/ml, 0.087 mg/ml, 0.18 mg/ml, 0.35 mg/ml, 0.5 mg/ml, 1 mg/ml, and 1.5 mg/ml.) 24 after hours after plating the cells, the culture medium was removed, the cells were then washed with PBS, and dispersions of nanoparticles added.

The nanoparticle dispersions were prepared and re-suspended into different volumes according to the size of wells that have been used as follows : 1 ml were added to each 6 well plate, 500 μl to the 24 well plates, and 100 μl to the 96 well plates. For the control samples the same amount of culture medium was added. Following this adding of nanoparticles, all plates were transferred to a shaking platform and positioned in an incubator at 37°C for one hour. Immediately after this, another 1 ml of medium was added to the 6 well plates, 500 μl to the 24 well plates and 100 μl to the 96 well plat and then incubated at 37°C for 24 hours depending on the experimental protocol.

2.15.1 Sonication of magnetosomes MNPs

The aggregation of the magnetosomes and MNPs was reduced by using sonication (Bioruptor® Sonication System, Diagenode). The magnetosomes and MNPs were re-suspended in RPMI culture medium, then sonicated for 10 minutes at 4°C on the highest setting.

2.16 Flow cytometry (LSRII) to assess cellular death and MNPs and magnetosomes cell uptake

The cellular uptake of magnetosomes and MNPs was measured by flow cytometry (BD LSRII flow cytometer, BD Bioscience) to quantify the uptake of iron. To determine the effect of magnetosome/MNP incubation on cell death after 24 hours, MDA-MB-231 cell was incubated with various concentrations of MNPs and magnetosomes (0.022 mg/ml, 0.043 mg/ml, 0.087 mg/ml, 0.18 mg/ml, 0.35 mg/ml, 0.5 mg/ml, 1 mg/ml, and 1.5 mg/ml). After 24 hours the cells were trypsinised by adding 1 ml of trypsin to each well, leaving for 3 minutes in an incubator, and then adding 2 ml of culture medium. Next, the cells in suspension were transferred to 15 ml falcon tubes and subjected to centrifugation for 5 minutes at 1000 rcf. Following that the supernatant was discarded, and the pellet re-suspended in 5 ml of PBS, and returned to the centrifuge for 5 minutes at 1000 rcf again. The supernatant was removed again, and the pellet re-suspend in 1 ml of PBS for LSRII analysis. Propidium iodide stain (PI) 2 µl was added to all samples immediately prior to flow cytometric measurement. This dye binds to DNA of the cells that have their membrane damaged. In contrast, it is not permeable to live cells that have intact membranes. The flow cytometric analysis used a fluorescence (FL3-H) laser at wavelength 575 nm to detect the PI and distinguish between the populations of dead and live cells. The results were analysed using FlowJo® software.

2.17 MTT test to assess cell viability

MTT, is a colorimetric assay was used test the in vitro cytotoxicity of MNPs and magnetosomes after 72 hours. Unlike the flow cytometry, the MTT can provide information for longer term effect of these MNPs on cells. MTT (3-(4,5-dimethyl-2- thiazolyl)-2,5-diphenyl-2H-tetrazolium bromide) can be reduced by mitochondrial succinate dehydrogenase. This reduction of MTT can only occur in metabolically active cells, and the level of activity can provide a measure of cell viability. 96 well assay plates that contained cells in the culture medium at a desired density (1000 cells per well in 200 µl of complete medium) 72 hours after adding MNPs to the cells. 100 µl of MTT (0.0160 mg/in 5 ml PBS) was added to all wells without removing the media and then incubated for 3 hours at 37°C. Then the culture medium and yellow MTT were removed and 200 µl Dimethyl Sulfoxide (DMSO) was added to each

well. After that formazan crystal formed can then be dissolved in DMSO. To detect the differences in dissolved purple formazan that is produced by the viable cells, a plate reader measuring absorbance at 570 nm was used. Microsoft Excel was used to analyse the results, in which the fold change over the control (cell cultures medium without MNPs suspension) was calculated. Cell viability (%) was calculated using equation 2.8:

$$CV\,\%\ =\ (OD\ sample/\ control)\ X\ 100 \qquad (2.8)$$

2.18 Prussian blue staining assay of MNP uptake in cancer cells

Following overnight incubation, as described previously in section 2.14, the medium were removed from each well, then cells were washed twice with 500 µl of PBS. 200 µl of acetone was added quickly to all wells and incubated for 10 minutes at 4°C, followed by extraction of the acetone and washing twice with 500 µl PBS. Carefully 200 µl 1:1 dilution of 1 M hydrochloric acid and 2 % potassium ferrocyanide was added to each well and the plate was incubated at 37°C for an hour. A further two washes with 500 µl PBS was given to the cells. Before the cover slips were removed from the wells, cells were counter stained with 200 µl of 1% eosin (sigma- Aldrich) and then mounted onto slides using immune-mount (sigma-Aldrich). To visualize MNP uptake, the light microscope (Leica DM 1000) was used to view slides at 40X magnification and a microscope camera and Mitotic Images plus 2.0 software were used to take images.

2.19 Incubation SNPs and the magnetosomes using magnetic sheet

Comparing the cell uptake and the toxicity of magnetosomes, SNPs and OA-SNPs with and without magnetic forces. 0.2 mg of magnetosomes, 0.5 mg OA-SNPs and 1.5 mg SNPs were prepared and incubated with MDA-MB-231 cells in 6 well plates as described in section 2.14, in the presence of a magnetic sheet (5 kg pull strength magnetic sheet of neodymium magnets positioned under the culture plate) and the cells were incubated for 24 hours with this sheet before flow cytometry measurement Figure 2-8.
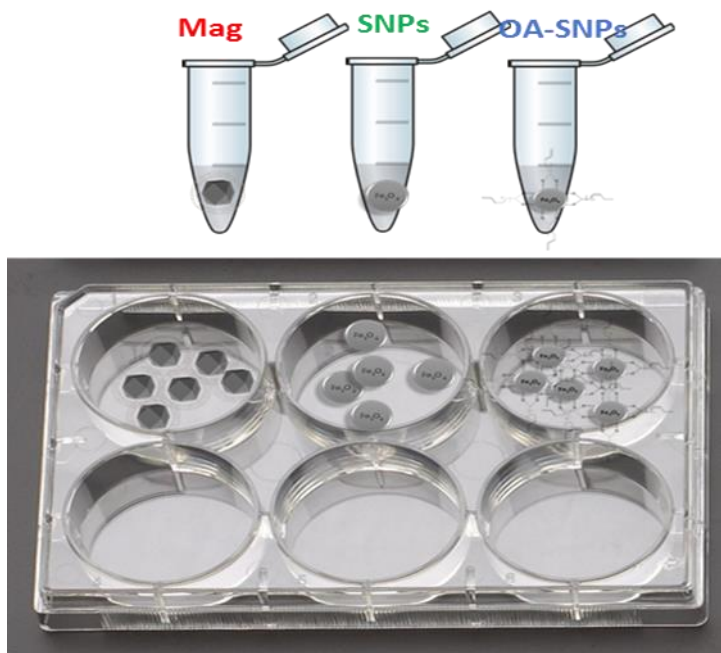
Figure 2-8: The magnetosomes, SNPs, and OA-SNPs in 6 well plate, with magnetic sheet placed underneath (grey rectangle)

2.20 Endotoxin Detection

The testing for endotoxin contamination is mandatory in pharmaceutical production and is often required in life science and medical research. A Limulus Amoebocyte Lysate (LAL) assay, is the most commonly used endotoxin detection system. It is based on LAL, which is extracted from horseshoe crab blood. The turbidity of the solution increases as a result of protein coagulation due to the presence of endotoxin in a sample.

A standard curve of absorbance was measured as a dilution series from samples that contained a known amount of endotoxin so that the absorbance of the various test samples can be compared to this standard curve and correlated to endotoxin concentration. 0.5 EU/ml is defined as the threshold concentration between pyrogenic and non-pyrogenic samples [108].

Endotoxin is associated with gram-negative bacteria such as *E. coli* and can trigger a severe physiological reaction. Bacteriophages (commonly referred to as phages), are viruses that infect bacteria and first bind highly specifically to proteins displaying lipopolysaccharides on the cell surface. It is the lipopolysaccharides that act as the endotoxin. LAL chromogenic endotoxin quantitation was used for detection of gram-negative bacterial endotoxin. This kit

contains: *Escherichia coli* Endotoxin standard (26EU/ml of lyophilised endotoxin); Limulus Amebocyte Lysate LAL; which was prepared from the circulating Amoebocyte of horseshoe crab Limulus Polyphemus); Chromogenic substrate and Endotoxin- free water. The endotoxin standard was dissolved in endotoxin-free water with vortexing for 10 minutes to make a 26 EU/ml solution of endotoxin.

The standard dilution was from endotoxin standard stock for series comprising 1.0 EU/ml, 0.5 EU/ml, 0.25 EU/ml and 0.1 EU/ml. was prepared as described in Table 2-14. Important note for accurate measurement, all materials in this experiment (e.g., pipette tips, glass tubes, 96 well microplates) were endotoxin free.

Table 2-14 : The standard dilution consists of 1.0 EU/ml 0.5 EU/ml, 0.25 EU/ml and 0.1 EU/ml.

Stock solution series dilution	Endotoxin stander solution	Endotoxin-free water	Endotoxin stock solution
1 EU/ml	50µl	1250 µl	-
0.5 EU/ml	-	250 µl	250 µl
0.25 EU/ml	-	750 µl	250 µl
0.1 EU/ml	-	900 µl	100 µl

All the reagents were equilibrated at room temperature before use, including the microplate. After that, add 50 µl of LAL was added to each well to allow activation of the proenzyme by bacterial endotoxin in the modified LAL. The plate was covered and shaken for 10 seconds and then incubated for 10 minutes at 37 °C. 50 µl of the test sample or dilution series was added to wells, and the plate covered again and incubated37°C for 5 minutes. The P-Nitroaniline (PNA) is catalysed to beak down from the transparent substrate by activation of the proenzyme. This activation rate is proportional to the sample endotoxin concentration. Afterwards, 100 µl of chromogenic substrate solution was added to each well, the plate covered and gently shaken for 10 seconds, before incubating for 6 minutes at 37 °C. Finally, 50 µl of stop reagent (25% acetic acid) was added with gentle mixing. At this step the released PNA is photometrically measured at 405-410 nm using a plate reader (BMG FLUOstar OPTIMA Microplate Reader). The average measurements of the blank are subtracted from all

individual standards and samples, and the standard curve was prepared by plotting the correlation between absorbance for each standard concentration versus the endotoxin concentration, which gives a linear relationship for concentrations in the range 0.1-1.0 Eu/ml. The amount of Endotoxin present in each sample isproportional to the intensity of the colour, and can be calculated using this standard curve.

2.21 Magnetosomes application *in vitro*

2.21.1 *In vitro* MRI measurements

An Eppendorf containing 1 ml of magnetic particles (Co^{2+}, Cu^{2+}, and Mn^{2+} doped magnetosomes) suspended in PBS were placed inside a 50 ml tube of saline (for homogenous shimming purposes) and this was placed at the iso-centre of a 7 Tesla magnet (Bruker BioSpec Avance III, 310 mm bore, MRI system B/C 70/30). The system used a 660 mT/m imaging gradient set with integrated shimming coils (BGA-12S Bruker, Germany). A proton quadrature resonator (300 MHz, 1 kW max, outer diameter 114 mm/inner diameter 86 mm) was used for both transmission and reception of RF. Transverse relaxation rates, R_2 & R_2*, were measured using a Multi-Spin-Echo and Multi-Gradient-Echo sequence, and Longitudinal relaxation rates, R1, were measured using a RAREvtr sequence respectively. Image matrix size was 256*256, FOV = 40 mm, slice thickness = 1 mm between 8-9 slices were taken through the images covering the full depth of the Eppendorf. For R_2 estimation TR = 3.5 s, minimum TE = 10.5 ms increasing in steps of 10.5 ms for 16 echoes. For R_2* estimation TR = 2.5 s, minimum TE = 2.8 ms increasing in steps of 2.5 ms for 12 echoes (excitation flip angle = 60 degrees). For longitudinal relaxation rate (R1) estimation multiple TRs=0.3s, 0.5s, 0.6s, 0.8s, 1.2s, 1.6s, 3.0s, TE= 8.3 ms were used. Images were analysed independently in Bruker Image Analysis toolbox (ISA), ImageJ. Two single ROIs were drawn within the third (centre) slice of the Eppendorf and the corresponding saline (control) and the signal as a function of echo time was fitted using non-linear-least squares to a simple mono-exponential decay function to estimate the R2 and R2* relaxation rates and longitudinal (R1) rates were estimated by fitting a T1 saturation recovery function Y = A+C*(1-exp (-t/T1)). Relaxivity was estimated by dividing R1 and R2 with the accurately calculated magnetic particle concentrations as described before.

2.21.2 Cancer magnetic hyperthermia treatment (MHT)

Apoptosis is a genetically programmed process that occurs normally during embryonic development under pathological conditions [148] [149]. The process is characterised by many steps including cell shrinkage, loss of asymmetry of the plasma membrane, budding of the plasma membrane, cytoplasm and nucleus condensation, and internucleosomal cleavage of DNA [150]. Apoptosis can be induced to different degrees in cells within hyperthermia treatment in the temperature range 41-45°C. Early apoptosis can be characterized by loss of the plasma membrane asymmetry, where phospholipid phosphatidylserine (PS) on the membrane is translocated from the inner to the outer leaflet of the plasma membrane, so it becomes exposed to the external cellular environment. Annexin V has a high binding affinity for PS, which is a 35-36 kDa Ca^{2+}- dependent phospholipid- binding protein. Annexin V will therefore conjugate to PS on the apoptotic cell surface [150] [151] [152]. Therefore the cells undergoing apoptosis can be detected by fluorescently labelled (FITC) Annexin V that serves as a sensitive probe for flow cytometric analysis. Since the first markers are PS translocation, it also accompanies the later stages of cell death that result from either apoptotic or necrotic process. Therefore another method is necessary to identify early and late apoptosis, such as Propidium iodide (PI) dye. Necrosis is the accidental cell death. This process is summarised in Figure 2-9.
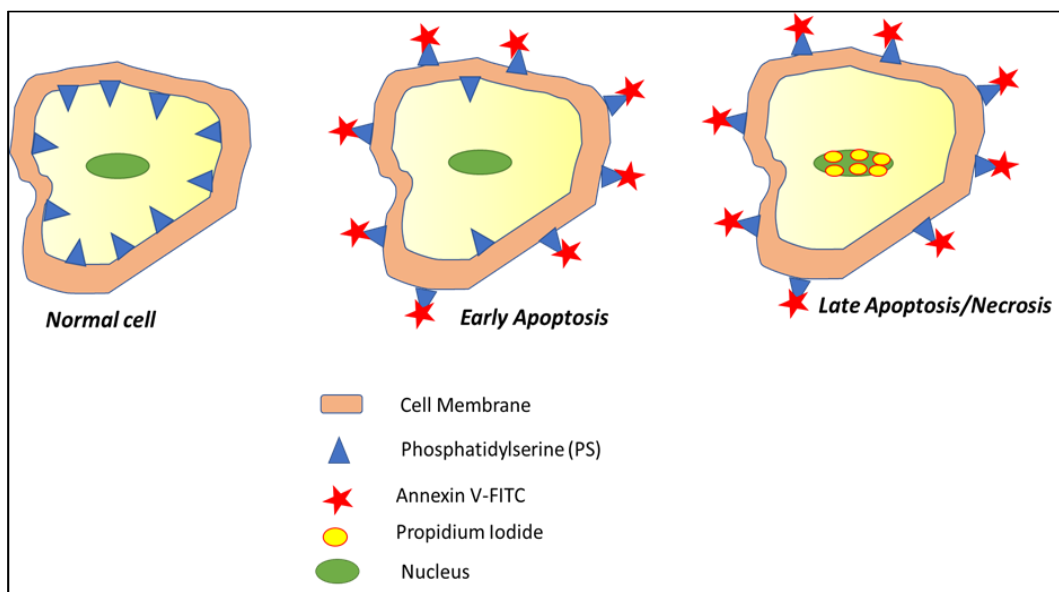
Figure 2-9: Detecting Apoptosis and Necrosis with Annexin V-FITC and PI.

The viable cells with intact membranes are impermeable to PI, while the dead and damaged cells with damage membranes are permeable to PI. So the cells showing both Annexin V and PI negative are considered as viable cells, while the cells showing Annexin V and PI positive are considered to be in late apoptosis, and the cells which are Annexin V positive and PI negative are considered to be in early apoptosis. This is described in the apoptosis necrosis assay with plots and gates for untreated and treated samples, Figure 2-10
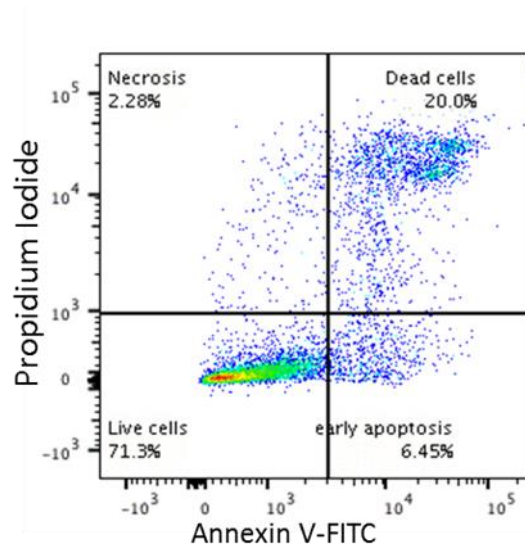
Figure 2-10: Apoptosis and necrosis assay, for untreated MDA-231 cell line, with quadrant gate set up by using untreated cells single stainedwith FITC Annexin V, untreated cells single stained with PI, and untreated cells double stained with FITC Annexin V and PI.

2.21.3 Apoptosis and necrosis assay

To determine the hyperthermia effects of doped magnetosomes (Co^{2+}, Cu^{2+}, and Mn^{2+}) on breast cancer cells *in vitro*, $2x10^5$ cells/ml of MDA-MB 231 cells were seeded in 35 mm culture petri dishes in 2 ml medium, for 24 hours. After this, magnetosome samples were added to the cancer cells in the petri dish. Then after 24 hours, they were subjected to magnetic hyperthermia treatment (MHT), using a magnetic hyperthermia machine (nanoTherics)., The petri dish was localised inside the coil,

Figure 2-11, (at a magnetic field frequency of 174 KHz and magnetic field amplitude of 9.7 mT for 20 minutes), and the applied magnetic field was adjusted to 9 mT. Four different conditions were tested to explore hyperthermia effects of doped magnetosomes on the MDA-MB-231 cell: 1- untreated cells without both magnetosomes and MHT (control sample 1), 2- cell treated without magnetosomes but with MHT (control sample 2), 3- cells treated with magnetosomes and MHT, 4- cells treated with magnetosomes and without MHT. The

concentration of magnetosomes was 0.2 mg/ml in each case. 24 hours after MHT, the amount of apoptosis and necrosis was analysed.
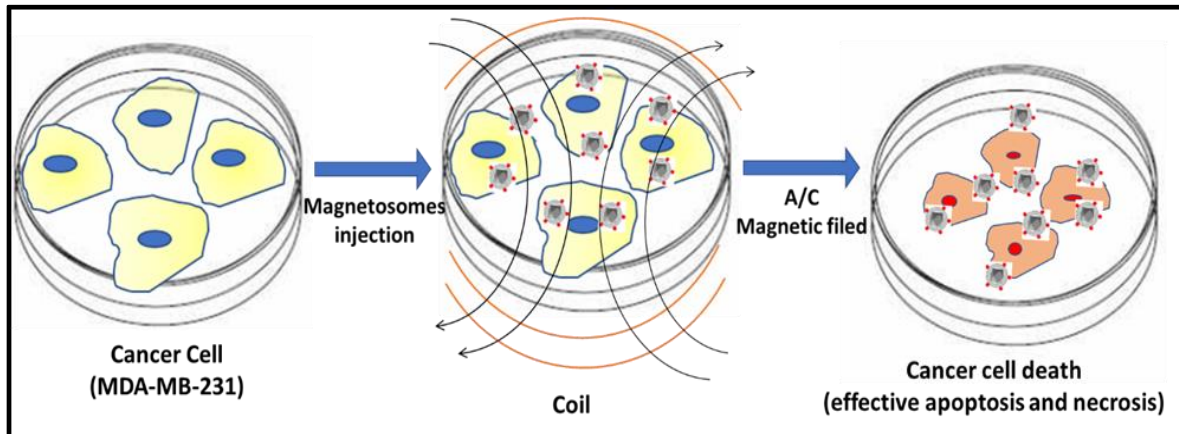
Figure 2-11: schematic showing the localization of magnetic hyperthermia treatment on cancer cells.

Firstly, the adherent cells were washed directly twice with cold PBS then 0.5 ml of non-enzymatic dissociation buffer (TrypIE Express (1X)) was added to detach the cells gently for 2-4 minutes at 37°C. Directly after that 1.5 ml of fresh medium was added, then transferred into a 15 ml falcon tube to centrifuge at 2000-2500 rpm at room temperature for 5 min. Then the supernatant was discarded and the cells washed twice with 1 ml cold cell staining buffer, then centrifuged again for 5 minutes. This step was repeated twice, then the cells were resuspended in 100 μl of Annexin V binding buffer, and transferred to a 5 ml polypropylene round tube. The cell suspension was incubated with 5 μl of FITC Annexin V and 10 μl of PI at room temperature, gently vortexed and kept in the dark. Finally, 400 μl of Annexin V binding buffer was added to each tube and the cells kept on ice. In this experiment, three staining samples were prepared (untreated cells single staining with FITC Annexin V, untreated cells single staining with PI, and untreated cells double staining with FITC Annexin V and PI). The fluorescence of the cells was estimated by flow cytometry. The maximum absorption for FITC Annexin V is 495 nm, and its fluorescence emission maximum is 530 nm (blue FITC). Propidium iodide, when bound to DNA, has fluorescent emission at 575 nm, and 610 nm (orange, PI), and Annexin V-FITC, and PI can be detected with a blue channel with bandpass filter 530-30 and 610-20 respectively. The flow cytometry analysis was performed using an LSRII (BD

Biosciences). Annexin V-FITC apoptosis detection kit with PI (Biolegend cat No. 640941) was used to determine the proportion of apoptosis and necrosis within a cell population.

2.22 Magnetosomes application *in vivo*

2.22.1 Murine Model of breast cancer

6-7 week old female BALB/c mice were purchased from Charles River and housed in a temperature controlled room (17°C), at an ambient humidity of 45%, light/dark cycles of 12 hours and allowed free access to standard rodent chow and water throughout the study. All procedures were carried out under licence (70/8670) according to regulations laid down by Her Majesty's Government, United Kingdom (Animals Scientific Procedures Act, 1986).

2.22.2 An orthotopic model of breast cancer

Following acclimatisation period of one week, mice underwent mammary fat pad (MFP) implantation of luciferase expressing brain- seeking 4T1-BR cell line (1X 10^5 cell/ml) via intra-nipple injection (20 µl per MFP). Mice were anaesthetised using isoflurane (IsoFlo) and the hair around nipples 5 and 6 was removed using hair removal cream. Following disinfection with Hibiscrub, 1X 10^5 mLUC-4T1-BR cells in 20 µl PBS were injected into the MFP using an insulin syringe. The mice were monitored for daily health assessments including body weight and tumour size measured using callipers every three days. The estimates of the volume (V) of the tumour were calculate using the following equation.

$$V=AxB^2/2 \qquad\qquad (2.9)$$

Where A is longer, and B is the shorter lateral diameter of a tumour [153].

Tumour growth was also monitored by bioluminescence using a non- invasive *in vivo* system (IVIS, Perkin Elmer). Mice were injected with 100 µl of d-luciferin (150mg/ml) intraperitoneally with images acquired after 10 minutes, under isoflurane anaesthesia received via a nose cone.

Once a tumour reached 550 mm^3 mice were anaesthetised with isofluorane and received 0.1ml intratumoral injections of either PBS, native magnetosomes (10mg/ml) or co-doped magnetosomes (10mg/ml), n=2-3 per group and were immediately placed on a polystyrene

bed (Figure 2-12). The experimental set up applied to treat the mic, it contains Magnetherm, NanoTherics (a commercial AC field product, Magnetherm, NanoTherics Ltd, Newcastle, United Kingdom) with a coil of 6.7 cm in diameter. The figure shows the position of the mouse inside the coil for the treatment under anaesthesia. Hyperthermia was performed at a magnetic field frequency of 174 KHz and magnetic field amplitude of 9.7 mT for 20 minutes after which the mice were euthanised and tumours excised for subsequent analysis.
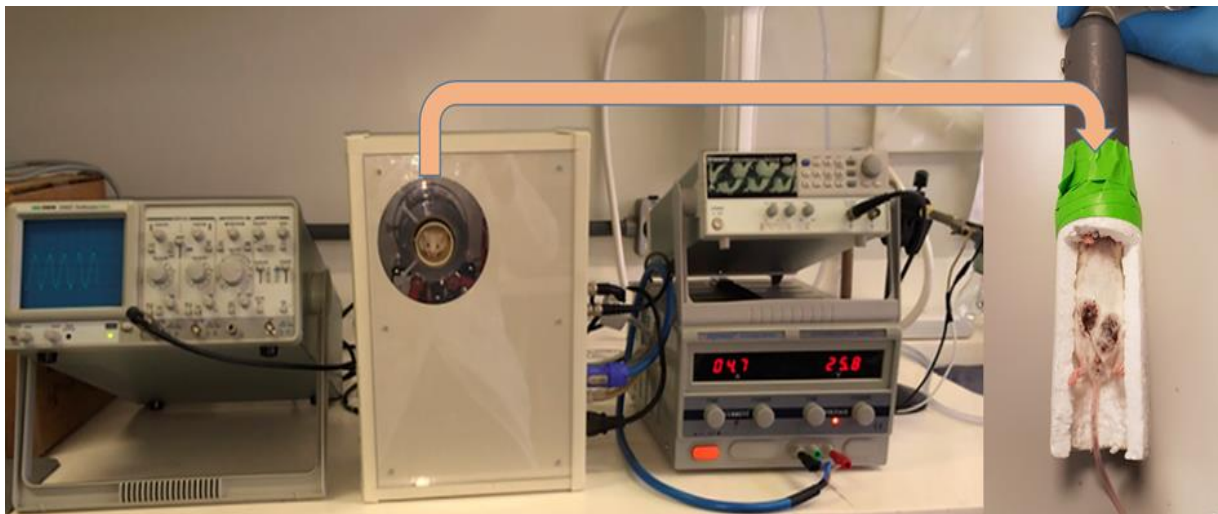
Figure 2-12: A commercial AC field product (Magnetherm, NanoTherics). Where mice were anaesthetised and subjected to 20 minutes magnetic hyperthermia following intratumoral injection of magnetic therapy.

2.22.3 Tissue preparation of samples for post-mortem analysis

Excised tumours were divided in two with one half fixed in 10% formalin solution for 24 hours prior to paraffin wax embedding and sectioning. The other half was minced and snap frozen in 90% FBS/10% DMSO, for slices of thickness 4 µm. the section was stained with H&E and Prussian blue to detect the presence of the magnetosomes.

2.22.3.1 Haematoxylin and Eosin staining (H&E)

The cells tissue are colourless and transparent, so staining the histological section is important to visualise the cells. A dye that stains some of the components a certain bright colour, can be used with another counterstain that stains the rest of the cell with a different colour. Inhere, Haematoxylin and Eosin staining was used. Hematoxylin basic dye stains the nucleus with purple, while the eosin is an acidic dye that stains the cytoplasm pink.

Tissue sections were rehydrated through a series of graded ethanol baths and washed twice with PBS. The slides were placed in Gill's haematoxylin solution for 1 minute then washed with tap water for 5 minutes, until the water became clear. Slides were placed in 70% ethanol for 3 minutes followed by 2 minutes in 90% ethanol. After that slides were placed in eosin for 1 minute and rinsed in 100% ethanol for 5 minutes before mounting with DPX. Images were acquired Hamamatsu Nanozoomer XR with 40X objective lens.

2.22.3.2 Prussian Blue Staining for iron

A small amount of Fe^{3+} is present normally in bone marrow and spleen. While in hemochromatosis and hemosiderosis there are excessive amounts of ferric iron. The Prussian blue reaction involves the treatment of slides with ferrocyanide (acid solution), so any Fe^{3+} present in the tissue will combine with ferrocyanide and produce a bright blue pigment, (called Prussian blue or ferric ferrocyanide). The nuclei stain red while cytoplasm is pink. Tissue sections were deparaffinized and hydrated with distilled water. Where mix equal parts 1:1 dilution of 20% hydrochloric acid and 10% potassium ferrocyanide were mixed and the slides immersed in this solution for 20 minutes, then washed in distilled water (3 changes, 5 seconds, 2X2 minutes), nuclei were counterstained with 200 µl of 1% eosin with nuclear fast red for 5 minutes, then rinsed twice with distilled water. Dehydration of the slides was via by washing through 95% alcohol and 2 change of 100% alcohol. Finally, slides were immersed in xylene 2 times for 3 minutes each. Then for visualization by light microscopy, the slides were covered with resinous mounting medium. Under the microscope, the iron will be stained with bright blue, and nuclear with red, while the cytoplasm will be pink.

Chapter 3:

Characterization of Magnetosome, doped Magnetosomes and control synthetic MNPs

3.1 Introduction

This chapter investigates the effects of altering the magnetism of magnetosomes from the bacterium *Magnetospirillum magneticum strain* AMB-1 by doping with nonferrous metals Mn^{2+}, Co^{2+}, and Cu^{2+} to enhance the inherent magnetic properties. The ability to tailor the magnetic properties of these magnetosomes could make them suitable for potential cancer treatments such as magnetic hyperthermia or for more sensitive diagnosis of cancers, such as a contrast agent for diagnostic MRIs for breast cancer. In this chapter, I will provide full characterisation of AMB-1 using a range of techniques: size by TEM and X-ray; assess the surfaces using IR and zeta potential; the doping composition by ICP and magnetization by SQUID. Furthermore, I perform the first double and triple doping of magnetosomes with cobalt, copper manganese and fully characterise these also.

It is important to deliver particles with consistent magnetic properties under variable conditions and doping with these metals could tune the magnetisation appropriately to those required for specific applications. Tailoring these novel properties could thus have a huge impact on developing new nanomaterials for medical application, such as diagnosis, detection, and even therapeutic use where drugs can be delivered with these particles [154]. Doping magnetosomes has been investigated previously by the Staniland group, originally in the form of cobalt doping [24]. Co^{2+} was doped into the magnetosomes of three strains of Magnetospirillum bacteria (magnetotactic strains *M. magnetotacticum* MS-1, M. *magneticum* AMB-1, and M. *gryphiswaldense* MSR-1), and the maximum level of cobalt content was found to be between 0.2 and 1.4% for 20 µM of cobalt ions added to the media (depending on the strain). However, this research study only focussed on 20 µM cobalt content of the medium without looking to further *in vivo* or *in vitro* applications [24]. Following that, the effects of higher levels of cobalt, as well as copper and manganese were investigated [155]. In this later study Co^{2+}, Cu^{2+} and Mn^{2+} were doped into magnetosomes of the AMB-1 strain grown in higher concentrations of the metal ions leading to a higher percentage of doping: Co^{2+} (3.0%, in 40 µM), Mn^{2+} (2.7% in 1 mM) and Cu^{2+} (15.6% in 20 µM). Recently, Mn doping of magnetosomes of *Magnetospirillum gryphiswaldense (M.gryphiswaldense) MSR-1*, have been studied at low doping levels [156]. Another study which used $MnCl_2$ to dope the MSR-1 strain at 50 µM concertation

in the medium, and end up with 1.04% - 1.14% of Mn content in the magnetosome crystals. However, these studies give no more detail about the effect of doping on size, there is no clear data about coercivity and saturation magnetization, and the previous studies do not offer biological applications [156]. Also doping with Cu has been reported in varying quantities [157] based on the environmental nature of the sample. This study does not represent controlled doping under laboratory conditions, and thus detailed analysis of the range in which this can be achieved and its suitability for applications is unavailable. There is still no complete characterisation data for magnetosomes compiling data such as size, IR, either *in vivo*, *in vitro* or an assessment for biomedical cancer treatment applications [155]. In this chapter I complete this analysis for the Co^{2+}, Mn^{2+} & Cu^{2+} singularly, double and triple doped magnetosomes.

Various concentrations of non-ferrous metal ions were added to the culture medium prior to inoculation, in the ranges 20 µM to 60 µM for cobalt, 10 µM to 40 µM for copper, and 10 µM to 1 mM for manganese. The concentrations, as shown in Table 3-1, were selected to each be equal to or below the literature [155] value of the minimum inhibitory concentration (MIC) of Co, Cu and Mn for AMB-1 [155]. Copper inhibits growth at 40 µM, with the comparable concentrations being 60 µM for cobalt and 1 mM for manganese.

Table 3-1 : Concentrations **of non-ferrous metal doping investigated**.

Metal doping concentration	10 µM	20 µM	30 µM	40 µM	50 µM	60 µM	70 µM	1 mM
Manganese	▮	▮	▮	▮	▮	▮	▮	▮
Cobalt		▮	▮	▮	▮	▮		
Copper	▮	▮	▮	▮				

3.2 Synthesis of MNPs

3.2.1 Synthesis SNP and OA-SNP

The Synthetic Magnetic Nanoparticles (SNPs) were prepared in this research (as a control for the magnetosomes) using room temperature co-precipitation of mixed valence iron salts with the addition of hydroxide ions, which is one of the most common and simplest chemical methods for preparing SNPs in an aqueous medium at ambient temperature [158] [159]. This method has advantages of producing large quantities of SNPs (about 55 g/l) and using just iron salts and NaOH precursors as described chapter 2; section 2.6.1. SNPs produced by this method have unavoidable problems associated with their uncontrolled size and shape and the effects of oxidation and corrosion. The major disadvantage of the co-precipitation methods is the impurity of the products, with multiple different iron oxide forms as well as the main product of magnetite, reducing the magnetic properties of the bulk product [160]. However, this method is used as it is accessible, rapid, inexpensive, and simple, and it requires no complex or expensive chemical equipment. In general for SNPs many conditions need to be controlled to control particle formation, such as pH, the concentration/ratio of chemical reagents, and temperature, with issues arising with tailoring their properties (such as their magnetism) if the particle population has uncontrolled shape and a broad size distribution [131], [161]. Biocompatibility is the key biomedical requirements for MNPs, which can be addressed by encapsulating them with an appropriate coating. Coating magnetite nanoparticles also protects them from oxidation. Further requirement for the coating materials are: have high affinity to iron oxide core, and have some sites that can be functionalised later [162]. In this study, the particles were coated with oleic acid (OA-SNP), chosen as a simple and small monounsaturated fatty acid; the magnetosomes were then compared to SNPs and OA-SNPs. In this case coating with oleic acid is a multi-step process which ended up with reduces the yields of OA-SNP compared to SNPs after filtration, heating and washing (32 g/l verses 55 g/l).

3.2.2 Growth the MTB and scale up the experiment

The growth media for MTB requires adding of many chemical reagents such as vitamins and minerals, as described in section 2.1 compared to few chemical reagents in SNPs, but all these chemicals are environmentally friendly. The magnetosomes crystals are single-domain

magnets with pure chemical stoichiometry, and uniform size and precise shape because there is biological strict control governed by different genes. Magnetosomes also already has a biocompatible coating, a lipid bilayer membrane that provides a nice platform to immobilize biomolecules.

In order to investigate whether it is possible to scale up the production of magnetosomes, cultures of different volumes were prepared. The results of this experiment showed that cells grew in 75 ml, 400 ml, 800 ml, and 4-litre batches, as seen in Figure 3-1 a.

The AMB-1 cell growth inside the cabinet under the addition of various metals displayed different growth rates: incubating 75 ml of media to 400 ml of standard iron media showed bacterial growth in three to five days, while cobalt doping media showed growth in ten days, no growth was observed in the presence of the manganese and copper metals until two weeks after inoculation.
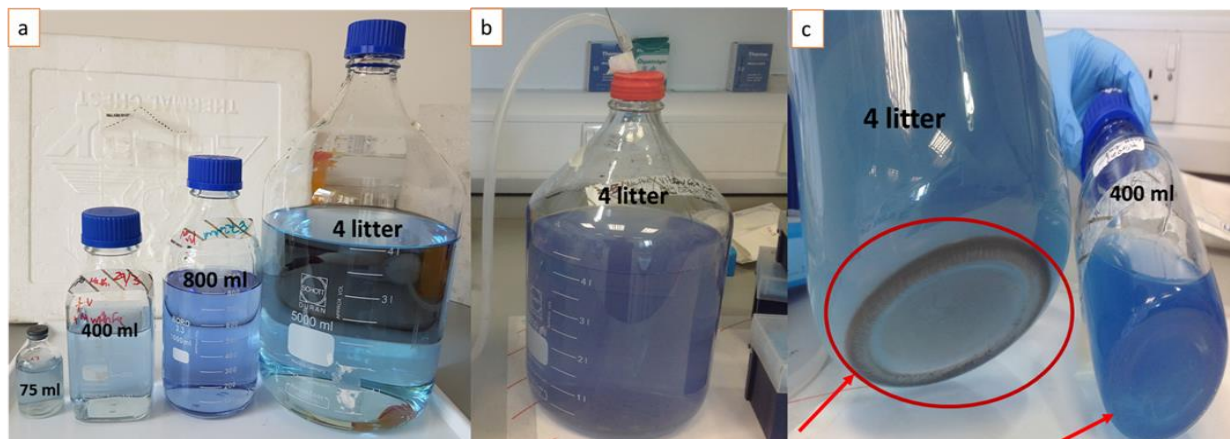
Figure 3-1: Scaling up the experiment a) different volumes of bottles, ranging from 75 ml to 4 litres, were prepared for inoculation in order to increase the amount of MTB; b) 4-litre bottle with fermentation outside the cabinet with N_2 pumped into the system using a nitrogen supplier with sterilising filter to enhance cell growth; c) a comparison of the results of incubation.

The magnetotactic strains *M. magnetotacticum* MS-1, M. *magneticum* AMB-1, and M. *gryphiswaldense* MSR-1 produce magnetite only under microaerobic conditions. Higher oxygen concentrations repress growth and inhibit magnetite formation [163]. The nanoparticle size of pure biomagnetite depends mainly on bacterial species [164], [165]. At the beginning of the growth experiments, cells were thus cultivated in flasks under a microaerobic gas mixture containing 1% oxygen in 99% nitrogen in the cabinet. In the scaled-

up experiments, microaerobicity was achieved by bubbling nitrogen gas (through a sterilising filter) into the media, supplier with a sterilising filter. Over a 4-week period, the 4-litre set-up gave a large amount of bacteria growth compared to the other culture volume, despite being outside the microaerobic cabinet, Figure 3-1 b. The quantity of bacteria in 4 litres was ≈ 4 mg/l, compared to ≈ 2.36 mg/l collected from the 400 ml culture seen in Figure 3-1 c. Four weeks after inoculation, the cells were collected by centrifugation and magnetosomes extracted by sonication, as described in chapter 2 (section 2.5). The main purpose of this experiment was to assess the capacity to scale up MTB production successfully to provide larger yields using inexpensive facilities. It is, however, noteworthy that the yield for doped and multi- doping was lower than native magnetosomes. For example, ≈ 1.5 mg/l of MTB for the triple-doped cells compared to 2.34 mg/l of a standard cell in the 400 ml growth medium.

Table 3.2: Summary of weight, C_{mag} and optical density for different volume growing medium

The volume of the media growing the bacteria	mg/l (weight of AMB-1 bacteria)	C_{mag}	OD
400 ml	2.36 mg/l	1.183 ± 0.16	0.093
4 litres	4 mg/ l	1.73 ± 0.24	0.189
400 ml double and triple doping	1.5 mg/l	1.03 ± 0.09	0.035

Table 3.2 shows the cell rotation in a magnetic field (C_{mag} magnetization) of the 400 ml and 4-litre cultures. C_{mag} is the ratio of absorbance at 600 nm of cells aligned using an external magnetic field parallel and perpendicular to the spectrometer beam. Growing the bacteria at a larger scale produced a high C_{mag} of 1.73 ± 0.24 compared to 1.19 ± 0.16for the 400 ml sample and 1.03 ± 0.09 for double and triple doping. The optical density (OD) was also measured, showing higher optical density for the 4-litre sample, which indicates that the population of growing bacteria in this sample is large. The 400 ml medium yielded 2.36 mg/l of magnetosomes, at a low price and with without cabinate. The 4-litre sample bacteria

displayed increased responses to EMF, which may be the result of producing a larger of a number of magnetosomes using this method.

In a comparative study, the productivity of 5.3 mg/litre was found for *Magnetospirillum sp*. for AMB-1 magnetosomes in a 4-litre medium, compared to 2.36 mg/litre from cultivation in a 400 mL flask within the cabinet [163]. Substitutions with Mn, Co, Cu, or even with other metals such as Zn (as shown in the literature [164], [165]) demonstrates using microbial processes to produce of large quantities of MNPs by increasing the volume of media, thus overcoming the limitations of commercial nanoparticles which currently cost $500/kg for sizes between 25 to 50 nm for pure or substituted magnetite [164]. In this experiment, larger cultivation costs were around £140/kg (calculated only for the cost of just chemicals), and no microaerobic cabinet was required. This approach also utilises ambient room temperature and ambient pressure, which makes it easier than traditional inorganic methods [166], [164]Large volumes can indeed be obtained by using a growth method that yields a high level of magnetosomes via the cultivation of AMB-1 or other MTB in large volumes [101].
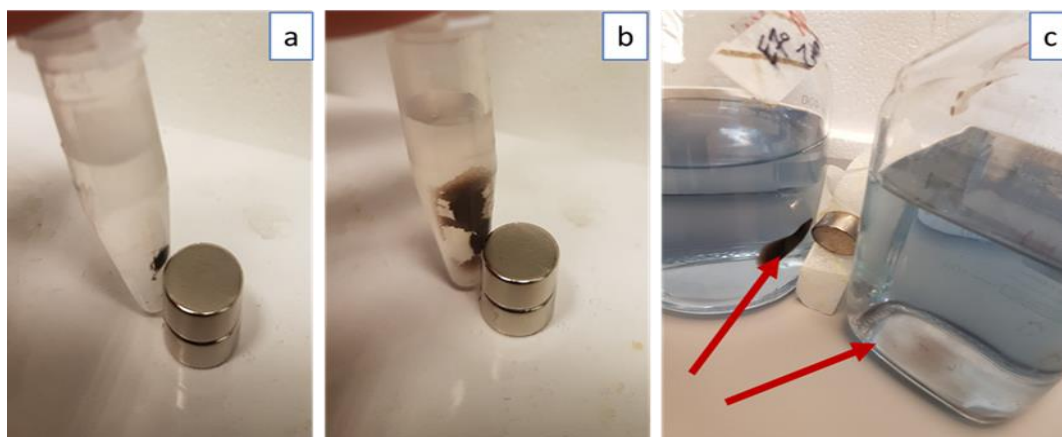
Figure 3-2: Magnetic collection of magnetotactic bacteria. a) the magnetosomes after extraction from the bacteria collected by a permanent magnet; b) the magnetotactic bacteria AMB-1 before extraction of the magnetosomes, collected with a permanent magnet; c) MAB-1 sedimenting to the bottom of the bottle without a magnet, compared to the magnetically collected AMB-1 in the presence of a permanent magnet.

Figure 3-2 a shows that the extracted magnetosomes are attracted to the permanent bar magnet on the exterior of the Eppendorf tube; it also shows the same for magnetotactic bacteria as seen in Figure 3-2 b. The magnetosome response to the permanent bar magnet confirms that the magnetosomes retain their magnetic properties after extraction from the

magnetotactic bacteria AMB-1. Figure 3-2 c shows MTB sinking to the bottom of the bottle when there is no magnet next to them compare to next bottle that shows the MTB stick to the magnet when it is a presence.

3.3 Characterisation of magnetosomes and MNPs

Many techniques can be used to characterise the MTB, the control MNPs the magnetosomes and the doped magnetosomes. TEM is used to image bacterial cells so that the size of the magnetosomes and the number of magnetosomes per cell can be measured. TEM is used to assess the effectiveness of separation and clean-up of magnetosomes extracted from the bacteria, and to confirm if the membrane around the magnetosome crystals is present. It is also be used to measure the size of the magnetosomes, SNPs and OA-SNPs. Elemental analysis using EDXS and EELS as well as ICP-AES was used to determine the presence and quantity of various metals in the doped magnetosomes. Furthermore, to aid characterisation, the functional groups of the SNPs, OA-SNPs, and magnetosomes were analysed using FI-IR, X-ray diffraction reveals the crystalline structure of the magnetite (or other iron-oxide crystalline material) and zeta potential and can thus be used to characterisation the particle surface in terms of stability and aggregation. Finally, a SQUID magnetometer was used to measure the magnetisation of the magnetosomes SNP and OA-SNP crystals at room temperature.

3.3.1 Sizes and structures: (TEM, X-ray)

In this study, TEM analysis of the magnetosomes found the size to be 51.7 ± 12 nm (Figure 3-3 a), which was in agreement with previous results [94] that showed similar size ranges of AMB-1. SNPs (52.29 ± 15.11 nm), and OA-SNPs (58.10 ± 16.32 nm) Figure 3-3 c and d show a very similar size and range which make them ideal control particles. It should be noted that the magnetosomes crystal size distribution is asymmetric with a narrower size distribution (Figure 3-3 b). This provides supporting evidence for the bio-limited size of magnetosomes to specific sizes and morphologies, and it could help provide stronger markers to distinguish between chemical SNPs and biosynthesised nanoparticles [161], even where they share similar particle sizes. SNPs and OA-SNPs show broader size distributions (Figure 3-3 E, F), this will be due to the particles being produced using co-precipitation, which is a less controlled process [161], even where these share similar particle sizes. SNPs and OA-SNPs show broader size distributions (Figure 3-3 E, F), this could be due to procedure particles using co-

precipitation may have one or more crystals that nucleate for the same particle [160]. The reasons for the differences in particle size could also include aggregation of small particles to produce large particles and the broader size distribution attributed to a decaying rate of nucleation accompanied by surface-controlled growth [167].
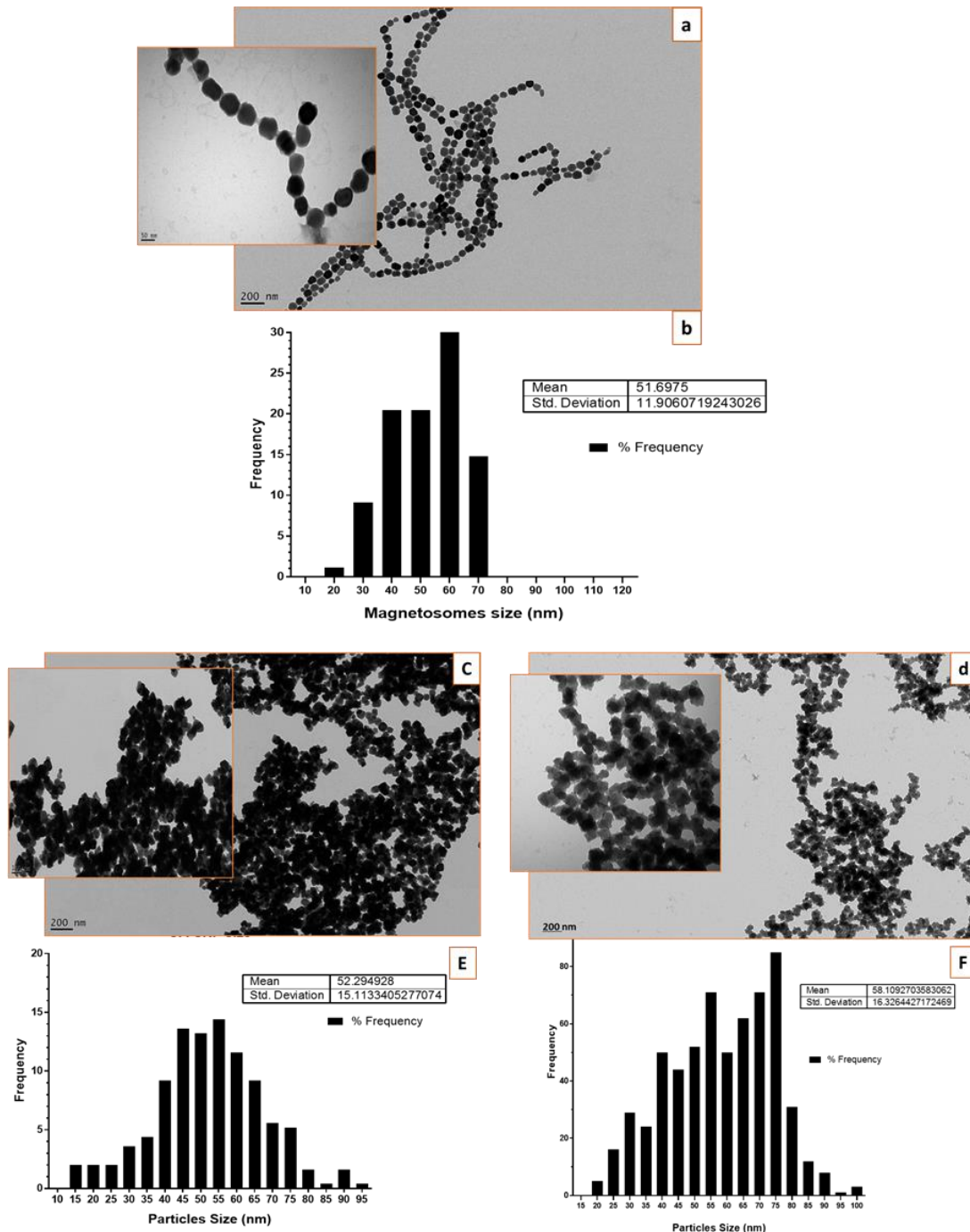
Figure 3-3: A) TEM image of the chain of magnetosome particles extracted from AMB-1, b) Histogram of the magnetosomes, c) TEM image of SNPs d) TEM image of oleic acid coated nanoparticles ,E) histogram of the SNPs, and F) histogram of the OA-SNPs.
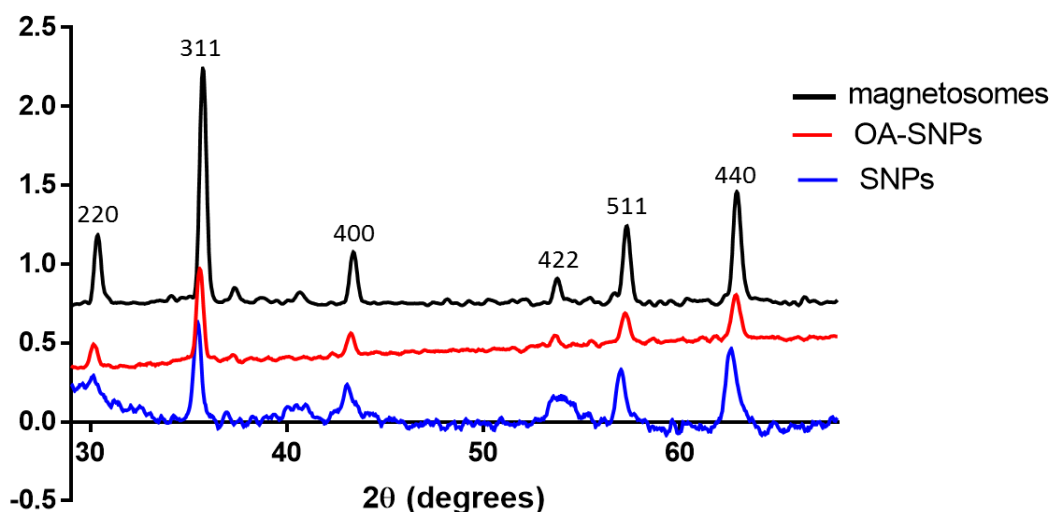
Figure 3-4: Powder XRD crystallinity data for magnetosomes (black), OA-SNPs (red), and bare SNPs (blue); peak positions labelled in black.

The crystalline structures of magnetosomes, SNPs and OA-SNPs is characterised by XRD, as shown in Figure 3-4. The relative diffraction peaks of 220, 311, 400, 422, 511, and 440 reflect a magnetite crystalline cubic spinel structure [160],[168]. This magnetite crystal can oxidize in the air easily to produce the maghemite γ-Fe_2O_3, and can be transformed into hematite (α-Fe_2O_3) [160], [169]. The XRD signal for SNPs are noticeably poorer than OA-SNPs, with more noise and shoulder peaks with weak intensities, indicating some poor impurities and poor differentiation of crystallite size in SNPs [170] compared with those in OA-SNP, which display clear intense and narrow peaks which indicates that the coating may prevent the particles degrading or oxidising. However, the magnetosomes show more intense and clearer narrow peaks which reflect the precise composition and uniform size and shape of the magnetosomes.

The crystallite sizes calculated from taken from XRD for the magnetosomes, bare SNPs, and OA-SNPs are 52 nm, 37 nm, and 40 nm respectively, as shown in Table 3-3. Magnetite particles arising from room temperature preparations are typically 20 nm in size [158]; however, as mentioned in the literature, slower addition of a basic solution to the reaction results in the production of magnetite nanoparticles of larger sizes (range between 12.6-63 nm) [171], and it is also dependant on the intermediates form, type of base solution, and pH values [171]. A

105

slow addition of base increases the time available for the continuous growth of the nuclei [171], for example, so many conditions can cause a change in the size of SNPs. The particle size in this instance, as obtained from the TEM images, is slightly larger than the XRD crystallite size. The XRD yields the crystallite size, which corresponds to the size of a single crystal, while TEM measures the diameter of what appears to be a particle as a whole. This suggests that the particles may contain more than one crystallite each, causing the TEM measurement to be greater.

Table 3-3: Characterisation of nanoparticle sizes and structures obtained by TEM, Zeta potential, and X-ray

MNP samples	Mean of particle size on TEM d(nm)	Zeta potential	Mean of particle size on XRD d(nm)
Magnetosomes	51.7±12.0	-43.79±1.52 mV	52
SNPs	58.1±16.3	-49±0.87 mV	37
OA-SNPs	52.3±15.1	-50±1.33 mV	40

3.3.2 Surface and coating analysis of SNPs, OA-SNPs and purified magnetosomes

The FT-IR measurement was taken across a wave number range of 4000-500 cm^{-1} for the magnetosomes, bare SNPs, and OA-SNPs. For SNPs (Figure 3-5 a) the peak at 580 cm^{-1} corresponds to Fe-O vibration bands, and the peaks at 3303 and 1642 can be attributed to the stretching vibration of hydroxyl groups on the surface of the SNPs [160], [172], [173]. The spectum of coated OA-SNPs (Figure 3-5 b) shows five new bands appearing at 1467, 1410, 1709, 2860, and 2927 cm^{-1} which correspond to the asymmetric and symmetric stretching vibrations of a carboxyl group (COO-), (1467 and 1414 cm^{-1} respectively [160]. The absorption band at 1709 cm^{-1} shows the stretching vibration of the C=O of a carboxyl group, which indicates the presence of oleic acid on the nanoparticle surface. The Fe-O (magnetite) stretching signal appears at 580 cm^{-1} as before [173]–[176] [172]. The polar carboxylic acid head groups of the oleic acid are coordinated with the surface of magnetite by both carboxylate and oxygen ion via the iron ions [132]. The nonpolar tails, therefore, extend into the solution to produce a hydrophobic nanoparticle coating [132]. The last two bands, at 2927

and 2860 cm^{-1}, corresponding to the symmetric and asymmetric CH$_2$ stretching of the oleic acid that covers the surface of SNPs [160].
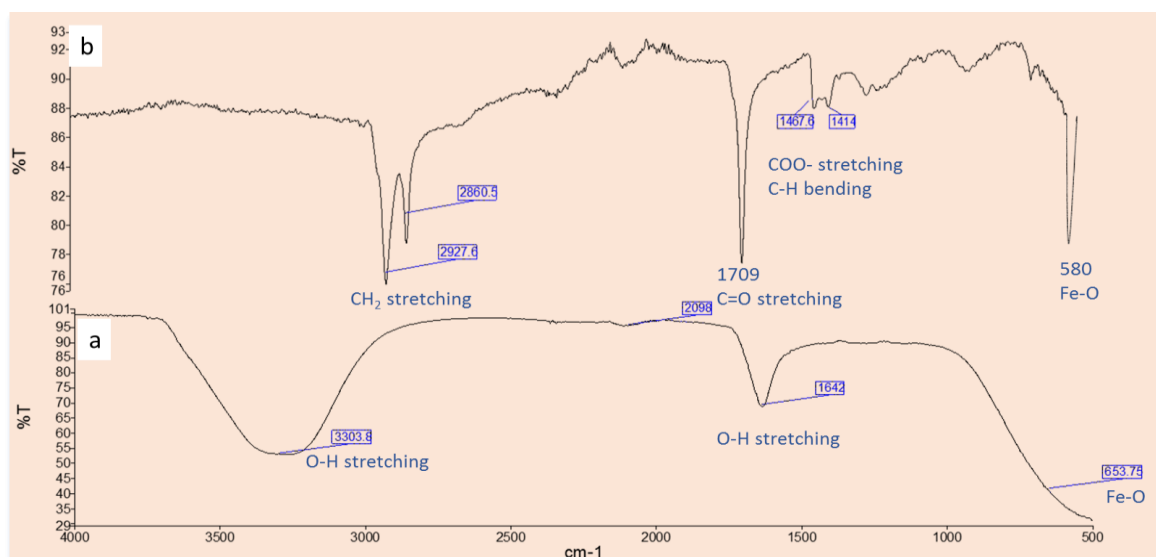
Figure 3-5: Fourier transforms of infrared spectroscopy (FT-IR) of magnetic nanoparticles (a) characteristic peaks of bare Fe$_3$O$_4$ and (b) FT-IR the oleic acid-coated iron oxide nanoparticles

Fourier-Transform infrared spectroscopy (FT-IR) was also used to examine of the purified magnetosomes (Figure 3-6 a), showing the peaks of carboxylic acid, amine, amide, and phosphate functional groups by characteristic vibrations at 3343, 1580, 1634, and 1054 cm^{-1}. From the spectrum, it can be seen that the bending vibrations of the primary amino group occur at 3343, and 1580 cm^{-1} (red circle) [177], [178],[179]; a peak at 3343 cm^{-1} (red circle) is indicative of the existence of an OH/NH group on the magnetosomes. A peak also appears at 1634 cm^{-1} (mainly due to C-O stretching), which suggests the existence of amide I and amide II bands in the protein-peptide band due to absorption of the protein [179] and a P-O peak at 1054 cm^{-1} [176].

107
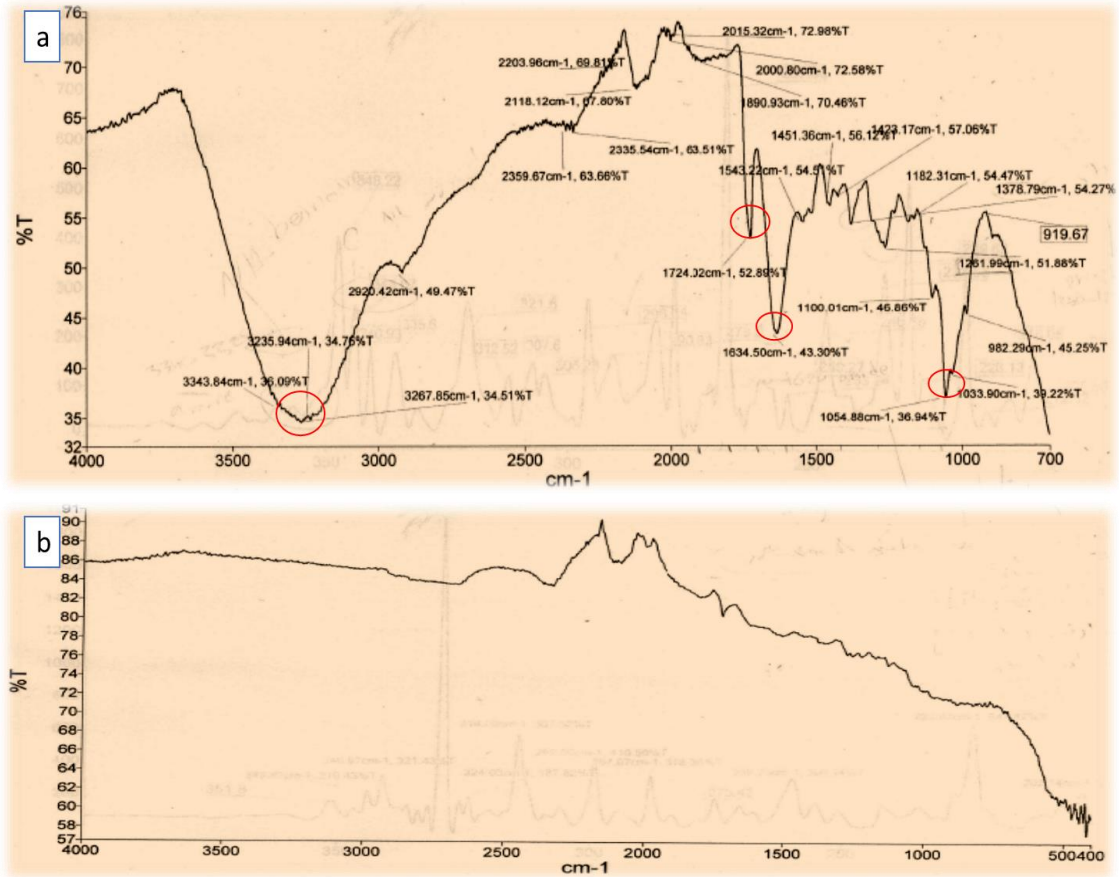
Figure 3-6: FT-IR spectra of purified magnetosomes using transmission mode. (a) The transmission peaks of purified magnetosomes (from left to right) are at 3235, 2920, 1724, and 1634 cm^{-1}. (b) and after sonication for one hour in lysis buffer.

These peaks on FT-IR spectrum after extraction of the magnetosomes suggest that a lipid bilayer surrounding each magnetosome particles remains; which may consist of magnetosome-associated proteins keep [179], a proposal supported by the TEM image of a chain of magnetosomes that did not aggregate seen in Figure 3-7 c. This is in contrast to those magnetosomes that have been treated with lysis buffer, as seen in Figure 3-6 b, where the spectrum shows that most of the strong organic peaks for the organ content (lipid bilayer) of the magnetosomes are absent (Figure 3-6 b), suggesting that sonication of the magnetosomes with a lysis buffer for 1 hour effectively removes the bilayers membrane surrounding each magnetosome [179], and as a consequence, allows individual magnetosomes to aggregate with each other as confirm by REM Figure 3-7 d.

The magnetosome particles extracted from these bacteria show crystals with an iron oxide core (Fe$_3$O$_4$ magnetite) individually dispersal in single chains based on the TEM images (Figure 3-7 a, c); these are surrounded by a membrane, which is clearly visible, as compared to the same magnetosomes in Figure 3-7 d, which shows aggregation caused by magnetosomes losing their membranes after sonication in lysis buffer. The magnetosomes extracted with 10 mM Tris-HCl are effectively a suspension of the bent chain [180], and the presence of a lipid membrane covering the magnetosomes helps to prevent them aggregation, better disperse compared to SNPs [180]. This makes it clear that, during the process of extraction of magnetosomes, it is important to preserve the integrity of their membranes, as the lipid membrane prevents aggregation and oxidation of the iron oxide core and is required for later functionalisation of the surface with other small biomolecules for surface conjunction [168] and further provides biocompatibility.
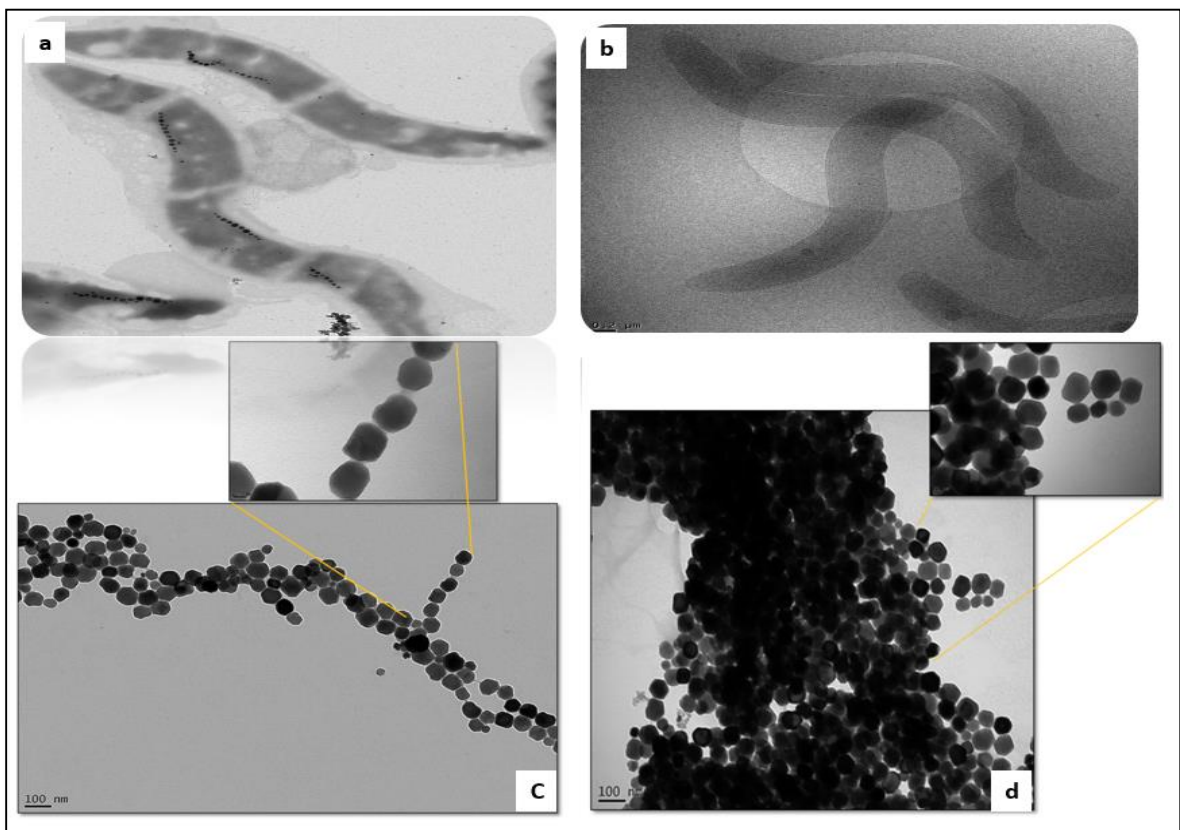
 Figure 3-7: a) TEM images of AMB-1 bacteria and magnetosomes. b) Cryo-TEM of wild type AMB-1 in an iron free medium showing the complete absence of magnetosomes; c) A panel of TEM images showing AMB-1 derived magnetosomes in a chain; c) The chains of magnetosomes after one hour of sonication with 10 mMTris-HCl buffers (pH 7.4); d) TEM image of magnetosomes heating for 5 hours with 1% SDS.

The colloidal dispersion of magnetosomes and SNPs nanoparticles are crucial for biomedical applications as they need to be stable against aggregation in both magnetic fields and biological media [181]. The key indicator of the stability of a colloidal dispersion is the zeta potential [182], which gives the difference in potential of the surrounding liquid medium and the area immediately surrounding the particles of interest [182]. The zeta potentials at pH 7 for isolated magnetosomes, SNPs, and hydrophobic nanoparticles (OA-SNPs) were all negative, showing the surfaces to be negatively charged; these were -43.79±1.52 mV, which agreed with the literature [183], [172]; -49±0.87 mV; and -50±1.33 mV, respectively, as seen in Table 3-3. These results show that magnetosomes, SNPs, and OA-SNPs have sufficient colloidal stability. The primary amino groups present in the proteins embedded in the phospholipid from the magnetosome membrane are the source of the negative surface charge on the magnetosomes [184] [185] [168]. It has been reported that magnetite nanoparticles produced by co-precipitation have only hydroxyl groups on the surface [39]. The current results of zeta potential confirm that MNPs have sufficient colloidal stability for biological applications [174] and that magnetosomes offer less aggregation due to the lipid bilayer than other nanoparticles [186].

3.4 Single M^{2+} ion doped magnetosomes

3.4.1 TEM Microscopy analysis of single doped magnetosomes (addition of 20 μM M^{2+} ion) (EDXS, EELS, EFTEM)
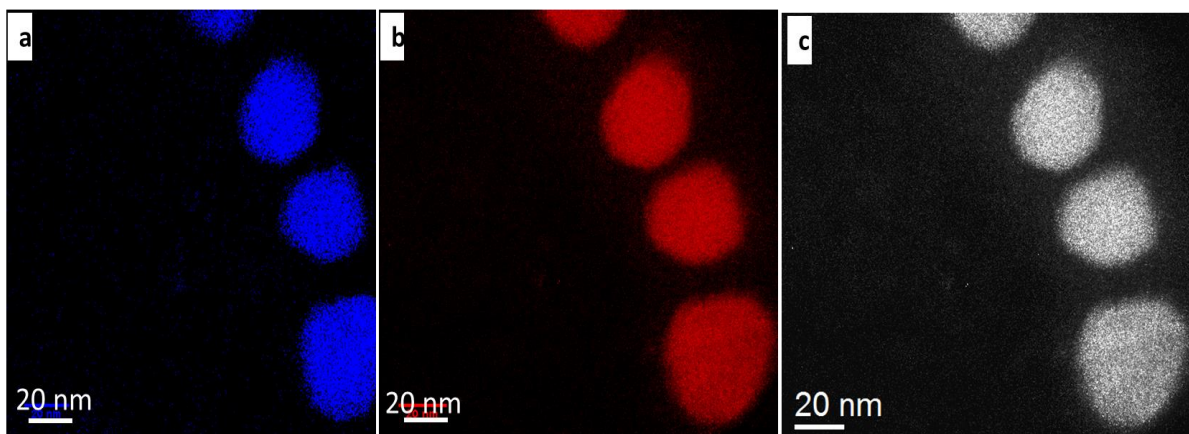
Figure 3-8: EFTEM Elemental mapping of magnetosome samples showing the distribution of a) oxygen and b) iron compared with c), the original chain of magnetosomes

Energy filtering Transmission electron microscope (EFTEM) was used to provide elemental mapping of native magnetosomes, as seen in Figure 3-9 which show oxygen and iron as the main elements in the magnetosomes consistent with magnetite and the literature [187].
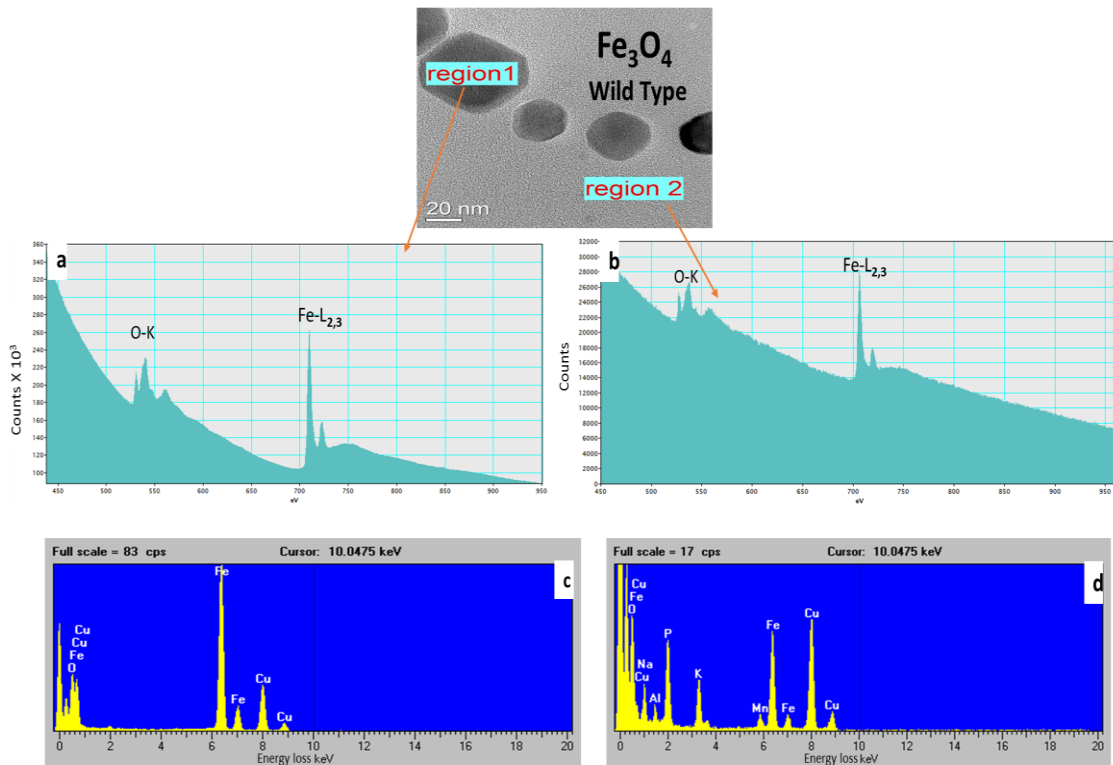
Figure 3-9: Electron energy loss spectroscopy (EELS) spectra of wild-types cells of AMB-1 from a) region 1 (magnetosome) and b) region 2 (cytoplasm) showing an Fe-L2,3 peak at the edge threshold in both spectrum regions; in both cases, the O-K peaks are clearly observable. Images c) and d) show energy-dispersive X-ray spectroscopy (EDXS) spectra from region 1 and region 2, respectively, showing Fe and O as the main elements in the magnetosome. The Cu original test is shown in the grid bar.

The electron energy loss spectra were taken for the doped magnetosomes, and energy dispersive X-ray analysis was also performed to determine the chemical and the elemental composition of the doped samples. These confirmed the absence of any other metal except iron in wild-type magnetosomes (Figure 3-9 a and b), both the magnetosomes particle region 1 and the cytoplasm area around region 2 of a wild-type cell sample show the expected peak characteristics of oxygen and iron when analysed by EELS, with both spectra containing and two sharp peaks $L_{2,3}$ (O-K, Fe-$L_{2, 3}$), for iron at the edge threshold around 709 eV. Lower intensity iron peaks are also present in region 2, which could represent soluble iron ion taken

up by MTB from the medium prior to magnetosomes synthesis. Al, K, and Mn are also apparent, which are normally to be found in the cytoplasm as a part of the metabolic process.
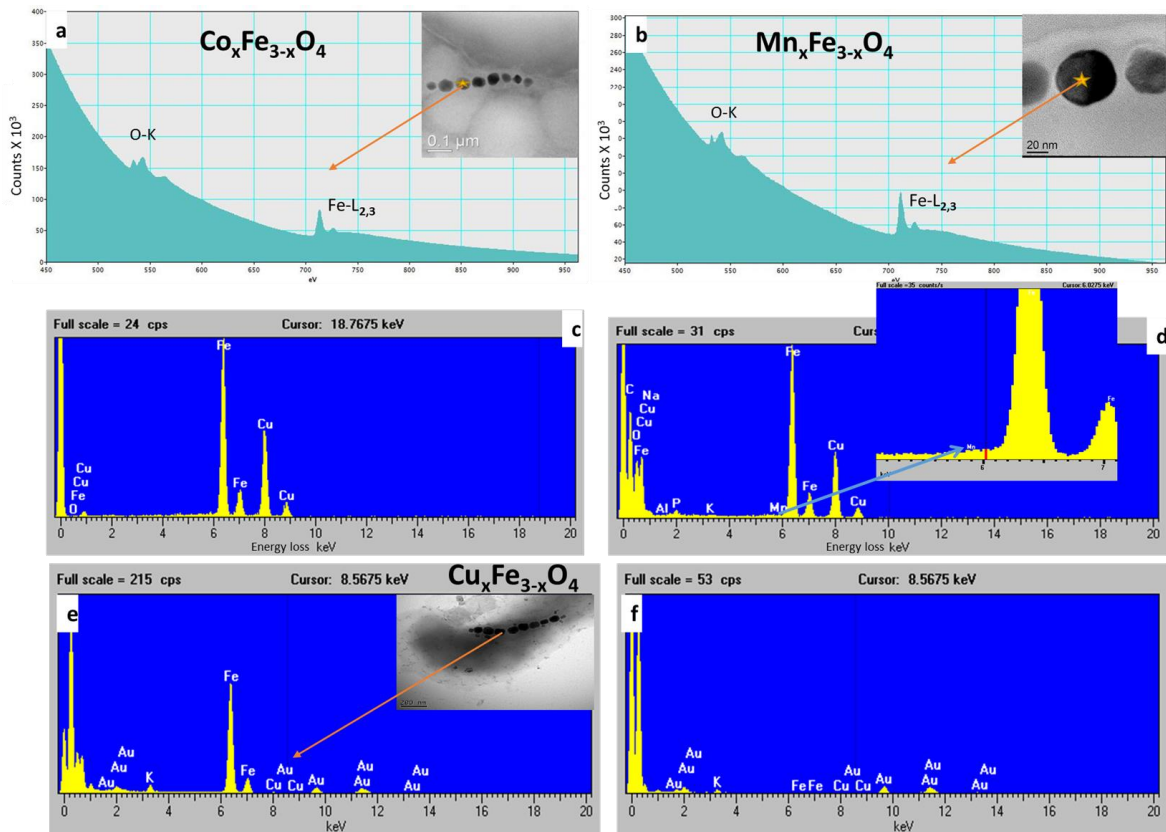
Figure 3-10. a) and b): Electron energy loss spectroscopy (EELS) spectra from Co-doped magnetosome and Mn-doped magnetosome showing Fe-$L_{2,3}$ peak at edge thresholds in both spectra, as well as O-K peaks; c) and d): Energy-dispersive X-ray spectroscopy (EDXS) spectra from Co-doped and Mn-doped magnetosomes respectively; e) and f): Energy-dispersive X-ray spectroscopy (EDXS) spectra from Cu doped magnetosomes on gold grid.

In the Co-doped sample grown in 20 µM cobalt (Figure 3-10 a), the Co peaks are more difficult to observe, as the larger of the two peaks is masked by the larger Fe edge and the smaller peak at 807 eV is masked by noise. ICP-AES analysis was thus used to identify the quantity of cobalt in the sample, which indicated the presence of 0.004 mg/ml Co, representing 1.80% of the total metal in the magnetosomes, as shown in Figure 3-12.

The Mn-doped sample of magnetosomes from MTB grown in 20 µM of manganese (Figure 3-10 b) produced a barely observable peak in EEL; ICP-AES measurements were thus

required again and showed Mn concentration of 0.007 mg/ml in the dissolved magnetosomes solution. This is a doping percentage of 1.63% of the total metal in the magnetosomes. As with cobalt, the absence of a clear peak in the EELS spectrum could be attributed to the low quantity of Mn in the sample compared to iron and is too small to be seen over the noise (expected at 650 ev). Alongside the ICP analysis, examination of the EDAX spectrum revealed a small peak alongside the iron peak that was attributable to Mn (Figure 3-10 d) [188] [155]. The Copper-doped magnetosome sample grown with 20 μM copper shows a small peak of Cu, as seen in Figure 3-10 e, indicating successful incorporation of this element. In the copper doping case, gold TEM grids were used (Figure 3-10 e) as the regular copper grids would have masked the presence of copper doping. ICP-AES confirmed the doping percentage at 6.32% of the total metal in the magnetite of the magnetosomes.

3.4.2 Effect of various levels of doping: TEM and ICP Elemental analysis

The biomineralisation of the magnetosomes is strictly controlled by MTB, although the interplay between the chemical and biological mechanism of mineral deposition in magnetosomes is not clear at present. The magnetosome stops growing once it reaches a certain size based on the bacterial strain under investigation. In this section we explore, the effect of various amounts of non-ferrous metals in the growth medium affects the magnetosome size, cell phenotype, and level of doping into the magnetosomes. We know from the previous section that the MTB has the ability to incorporate Mn^{2+}, Co^{2+}, and Cu^{2+} ion during biomineralisation; as confirmed by elemental analysis. TEM microscopy shows that there is also no significant effect of the dopants observed on cell shape.
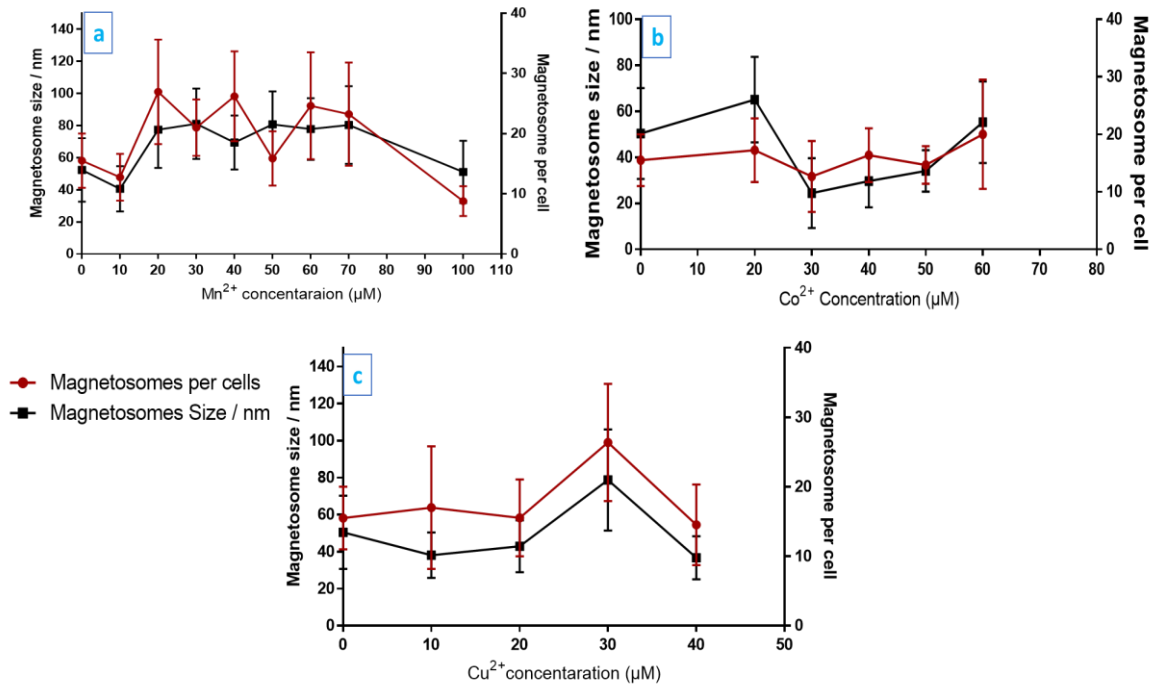
Figure 3-11: Magnetosomes number per cell and sizes at different concentrations of metal ion addition to the media: a) $Mn_xFe_{3-x}O_4$; b) $Co_xFe_{3-x}O_4$; and c) $Cu_xFe_{3-x}O_4$

Figure 3-11 a, b, c reveals that the availability of different micromolar amounts of non-ferrous metal causes no obvious differences in crystal morphology and has no significant obvious effect on the mean size of the magnetosomes except in the case of manganese, where there is an increase in the size of magnetosomes to an average of 71 - 80 nm compared to 51 nm for native magnetosomes. An increase is seen in that the number of magnetosomes per cell with Mn doped sample, increasing to an average of 24 to 27 compared to 14 magnetosomes per cell as seen in the literature [189], [190]. In addition, the cobalt doped into magnetosomes display an increased size of 65 nm at 20 μM Co^{2+} addition, while copper ion addition at 30 μM give magnetosomes with an increased size of 70 nm. The remainder of copper and cobalt doped samples show a reduced size and number of magnetosomes, especially at high concentrations, which is in agreement with the literature [155], [166].
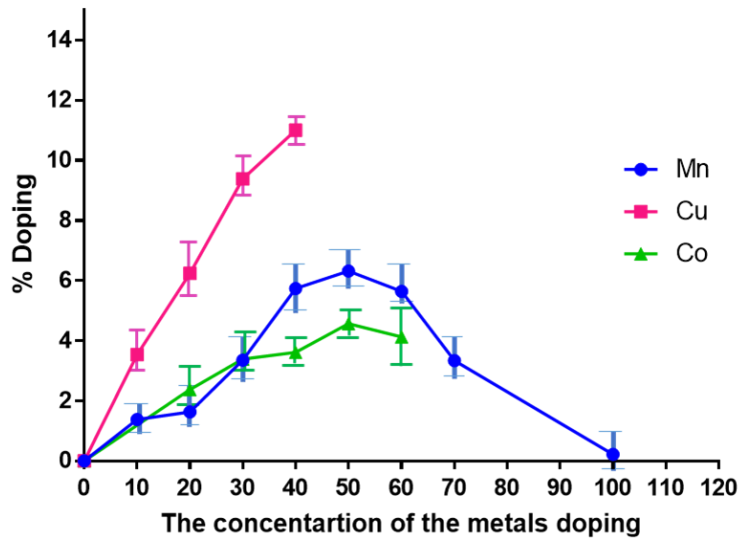
Figure 3-12: The percentage of M^{2+} doping in t magnetosome particles $M_xFe_{3-x}O$

The magnetosomes from the bacterial cells from the full range of doped media were extracted from the cell, membranes stripped, magnetically purified and dissolved in aqua regia for ICP elemental analysis. The results for the percentage of doping in the magnetosomes of AMB-1 grown bacteria in the presence of transition metals ions Mn^{2+}, Co^{2+}, and Cu^{2+} at various concentrations can be seen in Figure 3-12.
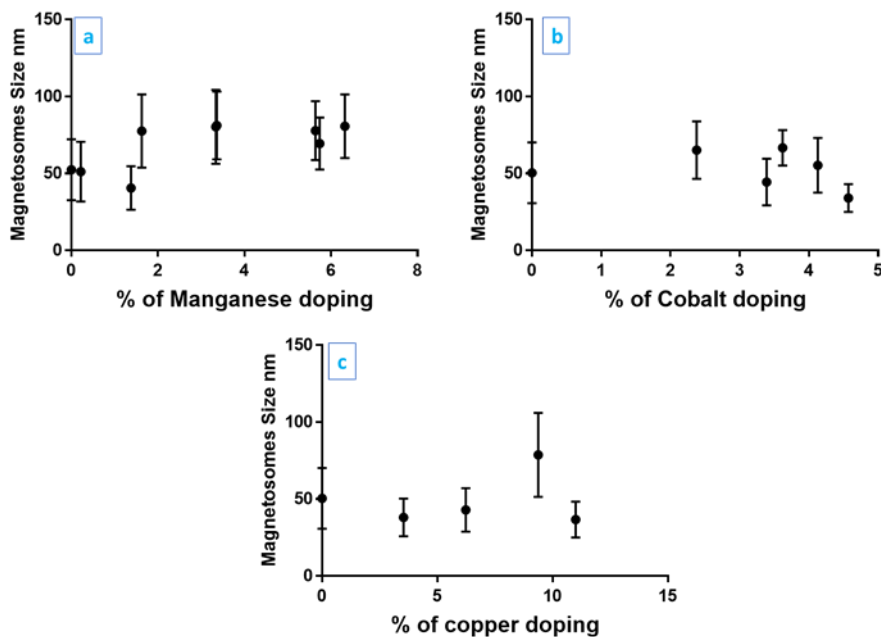
Figure 3-13:The magnetosomes sizes relative to the percent of metal doping: a) $Mn_xFe_{3-x}O_4$; b) $Co_xFe_{3-x}O_4$; and c) $Cu_xFe_{3-x}O_4$

Using this information and the values obtained from Figure 3-13, we can relate the sizes to the % doping quantity (Figure 3-13 a), and shows that when percent of Mn^{2+} doping increase between range 1.83%-6.23% there is also a subsequent increase in size of the magnetosomes, correlating to the level of doping rather than concentration of Mn ions added to the media. The percent of cobalt doping Figure 3-13 b, shows the size of magnetosomes is higher at 2.36 % doping then start to decline when the percent of doping increase to reach a size 34.11 nm of 4.57%. While the percent of copper doping in Figure 3-13 c, shows small size variation from the control (within error) across all doping concentrations From this results of doping, we could conclude that the Mn doping affects the size most consistently showing larger particle size with higher levels of doping. In contrast, the copper doping shows the smallest particle size (38.1 nm, 42.90 nm and 36.70 nm) compare to other metals doping (Co and Mn). This result shows that dopants could be used to tune magnetosomes specific size when the AMB-1 is grown in the presence of different metal ions.

$Mn_xFe_{3-x}O_4$ showed a high percentage of Mn^{2+} accumulation in the magnetosomes on average (1.38 to 6.32% Mn), and a size increase was associated with increasing Mn concentration, as observed in Figure 3-13 a, until >50 µM, when the amount of doping reduced again. These results agree with the size and number of magnetosomes results: where Mn > 50 µM a decreased in both the size and number of magnetosomes (down to 41 nm, 9 magnetosomes per cell for 70 µM) was seen, with negligible (0.22%) doping at 1 mM of Mn) indicating less manganese incorporation into magnetosomes at very higher concentrations of Mn^{2+} ion in the media, suggesting increased resistance to manganese at high concentrations. In the literature, manganese has been shown to be incorporated into magnetosome crystals when bacteria are exposed to manganese where the amount of this metal was up to 2.8% of the total metal content (Fe+Mn), based on uncultured magnetotactic bacteria from a coastal lagoon in Rio de Janeiro [188]. In the current research, the magnetite crystal formation was inhibited at 1 mM of manganese in the growth medium, which can be compared with the literature on manganese doping with magnetosomes in M. gryphiswaldense MSR-1 and with AMB-1 [155], where the manganese percentage was 2.7% within magnetotactic coccus, with a final concentration of 25.6 mM [188]. The current study thus shows the highest level of doping (6.32%) at 50 µM, compared to the literature with much lower % of doping of Mn^{2+}(2.7%) at 40 µM. A probable reason for the percentage of doping being highest at 50 µM of

doping with Mn compared to the 2.7% seen at 1 mM [155] is that there is a toxicity effect which inhibits cellular functions, suggesting that the percentage of doping up to this concentration had an opposing effect on cells.

Bazylinski *et al* [157] found that copper accumulates in iron sulphide magnetosomes of magnetotactic prokaryote (MMP), providing the first evidence that another transition metal ion could be incorporated in mineral phase of magnetosomes of MTB [166]. Overall, $Cu_xFe_{3-x}O_4$ shows the highest percentage of doping within magnetosomes compared to the other metals investigated. Copper doping at 40 µM with 11% of doping yields lower numbers and sizes of magnetosomes, which could be caused by the negative effect of metal at high concentrations of doping, which seems to be due to toxic concentrations for bacterial cell growth. This agrees with previous studies, which have shown low levels of growth of the bacteria at these concentrations supporting by the MIC of AMB-1 in copper [155]. Several different mechanisms could be responsible for high levels of Cu uptake, some of which may involve homologues of the copper dependent iron transporter protein in AMB-1 such as amb094, amb939, and amb0939, which are present in the magnetosomes island [155], so the bacteria has a propensity to take up copper in toxic quantities if in high concentration in the media.

In the current research, the small amount of cobalt doping of 1.80% can be seen to produce slightly higher numbers of magnetosomes compared to a larger concentration, which shows a slight decrease in the number and size of the magnetosomes in agreement with previous observations [166], [155]. The roles of genes in the transport and incorporation of cobalt into magnetosomes are worth further study. It has been suggested that Co^{2+} maybe largely taken up by MTB only when the Fe^{2+} is present in the medium has already been consumed in large amounts to build magnetosomes [166]. The maximum amount of cobalt doped into extracellular magnetite in this study was 4.57%, which is higher than the to 1 to 3% achieved in some studies [24], [155], yet lower compared to the 4 to 6% achieved in another [166].

Another study on doping Mn (50 µM) in MSR-1 reported that Mn content was 1.04 to 1.14% of the total amount of metal in the magnetosomes [156] which is low compared to the current results. This could be due to the high resistance of the cation efflux systems at high concentrations [155]. There are several possible explanations for these results, however, one of which is that Co^{2+}, Cu^{2+}, and possibly Mn^{2+} somehow passively infiltrate during formation

process when there is no iron in the medium [155]. This has proposed for both Mn and Co, while Cu relies simply on passive doping, where a small amount of excess foreign metals is inadvertently incorporated during magnetosomes crystals synthesis, causing high levels of doping.

The literature shows that cobalt ions can be co-precipitated within ferrihydrite, which could be a precursor for magnetosome magnetite formation [166],[191], which could explain cobalt is incorporated [166]. The excess of cobalt would be transported actively or passively to the cell for co-precipitation as a cobalt doped magnetosomes when magnetosomes are grown in a high concentration of Co medium [166]. Cobalt is a bio-essential metal for life either as vitamin B12 (the central formation of the Corrin complex of cobalamin) or in binding directly to an enzyme such as carbonic anhydrase and nitrile hydratase.

Another study showed that the AMB-1 is not a metallophile, which would have high resistance to the metal ion, compared with E.coli; AMB-1 shows less than 10% of the resistance to metals shown by *E.coli*, suggesting that MTB has little to no efflux systems, with low resistance to most transition metals [155]. This was apparent in all three cases of doping in this study. When the medium contains a high concentration of transition metals, the AMB-1, possibly to takes up these metals, but cannot efflux them. In another study, the researchers assumed that MTB has an efflux system with a high tolerance to Mn with low resistance. This is reasonable because it is generally considered to be nontoxic [155] Conversely, AMB-1 has shown high resistance to doping of most transition metals such as Ni^{2+} and Zn^{2+}[155]. Examining AMB-1 bacteria in the presence of transition metals ions Mn^{2+}, Co^{2+}, and Cu^{2+} at various concentrations shows the percentage of doping increasing for all three with increases in the concentration of ions.

3.4.3 The magnetisation of magnetosomes, SNPs, OA-SNPs and doped Magnetosomes

The magnetic properties of doped magnetosomes of the form $M_{x-n}Fe_{3-x}O_4$, (where M = Mn^{+2}, Co^{+2}, and Cu^{+2}) SNPs and OA-SNPs (shown in Figure3-16) were measured using a SQUID magnetometer. The M-H curves of magnetisation versus a field at 300K were measured for doped magnetite magnetosomes.

The incorporation of M^{2+} can change the magnetic properties of magnetosomes compare to pure magnetosomes; so we have doped the magnetosomes with Mn, Co and Cu, this dopant

M^{2+} incorporated into the magnetosomes crystal structure, substituting Fe^{2+} ions to change the magnetisation either by changing the saturation magnetisation or the coercivity.

The cubic magnetosomes spinal structure of the unit cell consists of tetrahedral sites and octahedral, referred to structure formula $(Fe^{3+})_{Td}[Fe^{2+}Fe^{3+}]_{Oh}O_4$, resulting in distribution 1:1:1 of Fe^{2+}_{Oh}: Fe^{3+}_{Td}: Fe^{3+}_{Oh}, where Fe^{2+} and half of Fe^{3+} occupy octahedral site, while tetrahedral site occupy with half remain of Fe^{3+} cation in cubic lattice structure [18], [160] (Figure 3-14).

The distribution of cations in the crystal structure within the octahedral (Oh) and tetrahedral (Td) sites is another crucial parameter which affects magnetic moment [18], [37]. When a magnetic field is applied, the magnetic moments of cations in Oh sites align parallel to the magnetic field, while in tetrahedral sites they align antiparallel, cancelling out some of the parallel magnetic moment [160]. The distribution of Fe^{3+} within the spinal lattice in both lattice sites (Td, Oh) thus effectively cancelled out, resulting in net magnetisation being based on Fe^{2+}. Dopants Co^{2+}, Cu^{2+}, and Mn^{2+} will substitute into the Fe^{2+} (Oh) cations sites in the magnetosomes, and thus serves as a method of changing the magnetic moment and coercivity of biosynthesised magnetite [183].
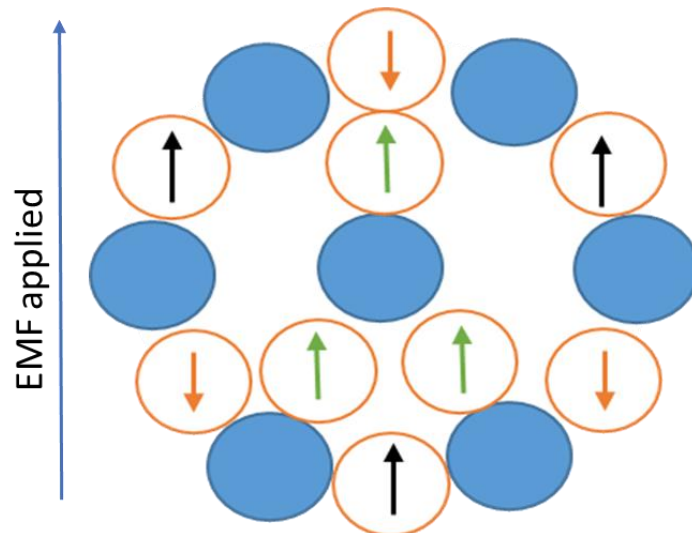
Figure 3-14: As EMF is applied, half of the (Fe^{3+}) Td black arrows have a spin moment in the same direction as the EMF, and the other half (Fe^{3+}) Oh orange arrows take the opposite direction, decreasing the overall magnetic moment to that contributed by (Fe^{2+}) Oh ions, shown by the green arrows.

So we expect when the Fe^{2+} is replaced by M^{2+} = Mn, there will be a higher magnetic saturation without an increase in coercivity, because of Mn^{2+} is isotropic. So then, there are more magnetic electrons aligned parallel to field in Mn^{2+} doped magnetosomes, which result in the high magnetic moment and high saturation magnetisation.

When the Fe^{2+} is replace by M^{2+}= Co and Cu there will be extra electron that pairs up to reduce the moment as shown in table 3-4, which causes reduction in the number of unpaired electrons, so this lowers the saturation magnetisation of cobalt and copper. However, the cobalt and copper have anisotropy properties that increase the coercivity of the magnetosomes.

Table 3-4 : E**lectron configuration and magnetic moment of Mn^{2+}, Co^{2+} and Cu^{2+}**

Metals	Electron configuration		Magnetic moment
$Mn^{2+}\,d^5$	↑ ↑ ↑	↑ ↑	5µB
$Fe^{2+}\,d^6$	↑↓ ↑ ↑	↑ ↑	4µB
$Co^{2+}\,d^7$	↑↓ ↑↓ ↑	↑ ↑	3µB
$Cu^{2+}\,d^9$	↑↓ ↑↓ ↑↓	↑↓ ↑	1µB

Anisotropy energy is a propensity to for particles to align in certain crystallographic directions of magnetic moment. Cobalt has a higher anisotropy than other metals, due to preference for a hard crystallographic {100} direction over the easy one {111}. This is due to the asymmetry of electron spin configuration of cobalt in d orbital special in t_2g as is described in Figure 3-15 that require high energy to resort to the easy axis and this energy convert to coercivity. This shows a dependence on the materials' magnetic properties and the direction of the applied field with respect to the crystal lattice [192]. Anisotropy is an important physical property, and it depends on the chemical composition or crystallographic orientation, size, and shape of crystals [193]. Crystalline anisotropy and shape anisotropy are thus common forms of anisotropy in magnetic materials [193].
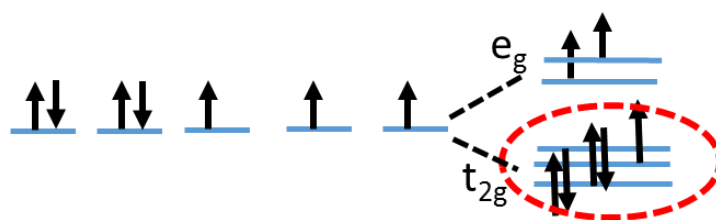
Figure 3-15: The energy level splitting of 3d^7 into t$_2$g and e$_g$ level for the **Co^{2+}.**

The hysteresis loop gives the saturation magnetisation (M$_s$), and coercivity (H$_c$) after application of a variable field. The curve for magnetosomes from AMB-1, the magnetosomes have the highest magnetisation saturation at 92.99 emu/g, which matches the value for pure magnetite [42, 6, 43], with a coercivity of 125 Oe exhibiting clear ferrimagnetic behaviours [168]. Mn^{2+}, Co^{2+}, Cu^{2+} at 20 μM doping media yielded magnetosomes with 1.63%, 2.38% and 6.24% levels of doping respectively, which had magnetic saturations of 53.4, 62.50, and 40.15 emu^{-1}g, respectively (Figure3-16), the saturation magnetisation of Mn-doped magnetosomes was lower than expected. This is maybe because the magnetosome size at this concentration was smaller (40.1 nm) compared to the native magnetosomes (52 nm). For both SNPs and OA-SNPs, the magnetisation at room temperature is less than that of bulk magnetite (92 emug^{-1}) [194] [158] [195]. SNPs had Ms 73 emu g^{-1} in agreement with previous results [171], and the 67 emug^{-1} for OA-SNPs agreeing with another study [132]. This reduction is expected due to the OA-SNPs sample containing non-magnetic coating adding slightly to the mass [196], [29]; if the saturation of the magnetisation of SNPs of 1 mg is just pure magnetite, 1 mg of OA-SNPs would be 90% magnetite and 10% non-magnetic oleic acid. Thus, saturation magnetisation decreases as a result of reducing the proportion of the magnetic core compared to the whole mass [197]. The Ms of SNPs was higher than most reported in the literature (33 emu g^{-1} [198], 72 emug^{-1} [180] [8], and 50.3 emug^{-1} [192]) although lower than one other (81.9 emug^{-1} [18]) and in agreement with some previous results [171]. These variations are due to differentiation in size and the condition of reactions such as chemical solutions, pH of the reaction also synthesised method can effect on the magnetisations [171]. However, it is clear that the SNP have reduced magnetic saturation than magnetite, showing the room temperature synthesis does not yield pure magnetite. The synthetic MNP also showed negligible hysteresis in their magnetisation curves of 10 and 33 Oe for SNPs and OA-SNPs, respectively. The native magnetosomes showed a coercivity of 125.1 Oe compared to

magnetosomes doped with Mn^{2+}, Co^{2+}, and Cu^{2+}, which were at 209, 292, and 250 Oe respectively. This result indicates strongly that biosynthesized magnetite has enhanced magnetic properties, with respect to magnetic saturation and coercivity due to the purity of the magnetite when compared with SNP, and in the native magnetosomes have the highest magnetic saturation but coercivity increasing dramatically when doped, compare to native magnetosomes, SNPs and OA-SNPs.
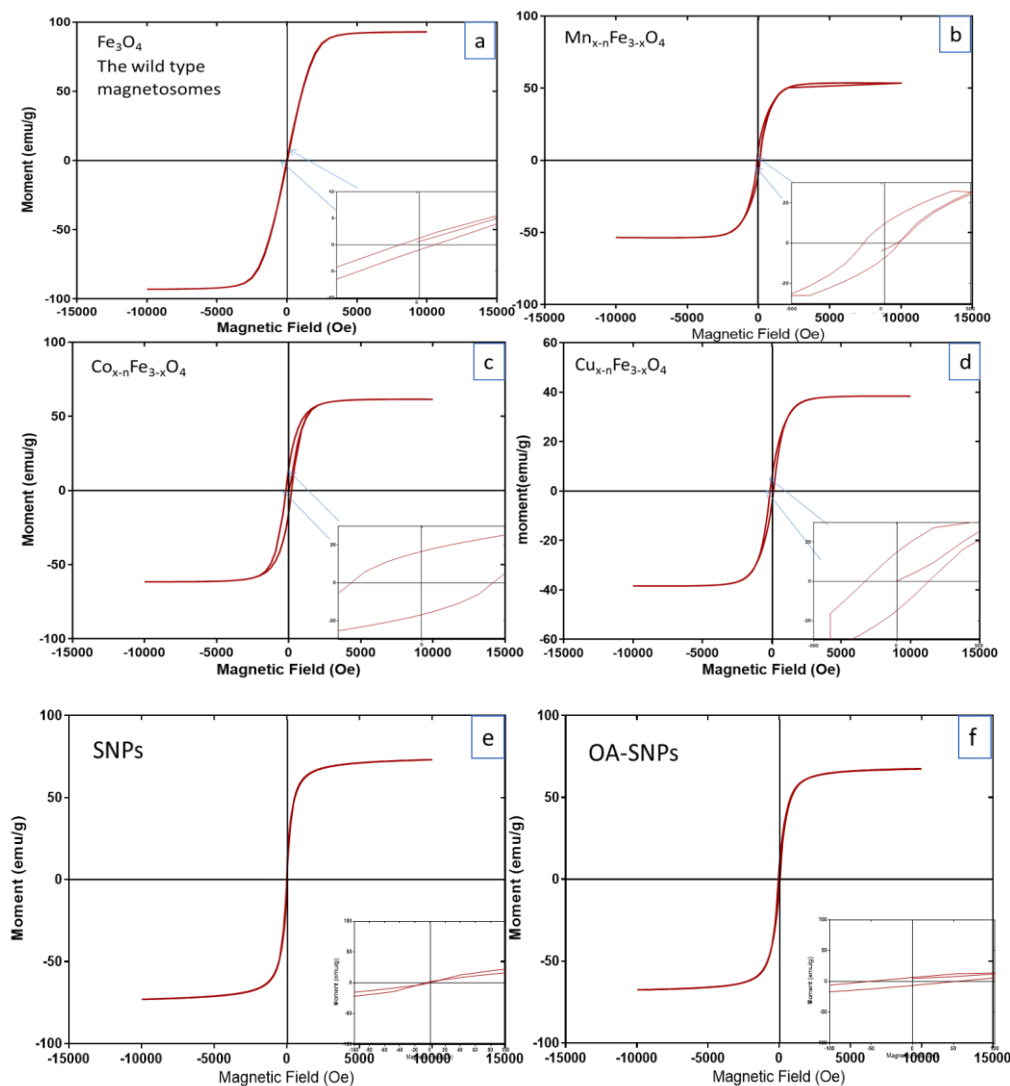
Figure3-16: Superconducting Quantum Interference Device (SQUID) analysis of magnetosomes. Hysteresis loops recorded at T=300 K. a) Fe_3O_4 wild-type magnetosomes, b) $Mn_xFe_{2-x}O_4$ doped, c) $Co_xFe_{2-x}O_4$ doped, and d) $Cu_xFe_{2-x}O_4$ doped, all at 20 μM; e) bare SNPs; f) coating magnetic nanoparticles

Table 3-5: Summary of the size and the magnetic properties of doped and non-doped magnetosomes.

Magnetization for the just 20 μM con.	Mean of particles size on TEM d(nm)	Saturation magnetisation M_s (emug^{-1})	Coercivity H_c (Oe)	% doping
Fe_3O_4	51.70±11.95	92.99	125.1	-
$Mn_xFe_{2-x}O_4$	67.51±23.97	53.41	209	1.63
$Co_xFe_{2-x}O_4$	65.16±16	61.50	292	1.08
$Cu_xFe_{2-x}O_4$	78.33±27.30	40.15	250	6.32
Bare-SNPs	52.29±15.11	73	10	-
OA-SNPs	58.10±16.34	67	33	-

As expected, cobalt doped magnetosomes increases coercivity by twofold due to the anisotropic nature of the cobalt, which has low magnetic saturation and high coercivity compared to magnetite. This result was confirmed by Galloway *et al*. with cobalt-doped magnetite nanoparticles [170] and it is also in agreement with previous studies with magnetosomes [24] [192] [183]. Another study of AMB-1 doping with cobalt [24] showed an increase in coercivity as high as 340 Oe, which is higher than the current result (292 Oe) which may be due to a greater percentage of cobalt doping (1.2 ± 0.3) compared to that used in this study (1.00± 0.1). This suggests that increasing the concentration cobalt ions increases coercivity by increasing the cobalt concentration in magnetosomes, which in turn increase the magnetosomes crystalline anisotropy increasing magnetic hysteresis [166] [195].

Coercivity and magnetization saturation are magnetic properties dependent on the grain size and strength of crystal anisotropy, [199], [200]. Magnetic anisotropy depends on the magnetic properties and the direction of the applied field with respect to the crystal lattice,

requiring a lower or high magnetic field to reach saturation magnetisation. The crystalline anisotropy of $CoFe_2O_4$ is higher (0.22 Jcm^{-3}) than Fe_3O_4 (0.078 Jcm^{-3}) magnetic nanoparticles [192].

Magnetite is an isotropic crystal that is therefore magnetically soft, with no preferred axis of magnetization. When Co^{2+} is substituted for Fe^{2+} in the magnetite octahedral sites, it gives rise to an anisotropic structure with a preferred magnetic orientation [195]; thus, cobalt doping increases coercivity [170]. Where Co creates a hard axis inside the crystal, this requires the use of a large applied magnetic field to reach the Ms [194]. Magnetocrystalline anisotropy thus refers to the applied energy required to deflect a crystal from an easy to a hard position [194]. Another study [201], where Co^{2+} was exchanged for Fe^{2+} in Fe_3O_4, showed that the coercivity increased significantly; it was suggested that the reason for this was anisotropy caused by the higher spin-orbital coupling at Co^{2+} sites [18],[166]; doping cobalt into magnetosomes thus allows the coercivity to increase and Ms to decrease even at low levels of doping [170], 33]. Another study by Sytnyk *et al*. [201] examined the cationic exchange of Fe^{2+} for Co^{2+} in post-synthesis of Fe_3O_4, showing as Fe_3O_4 converts to $CoFe_2O_4$ coercivity to increase significantly [166]. The magnetic properties of magnetite crystals can, therefore, be determined based on the location of M^{2+} within the structural crystal [192] (Figure 3-14).

This has been confirmed by a study using SNP that compared $MnFe_2O_4$, $CoFe_2O_4$, $NiFe_2O_4$, and $FeFe_2O_4$ at a size of 12 nm. Another study by Deng *et al*. on $FeFe_2O_4$, $MnFe_2O_4$, $CoFe_2O_4$, and $ZnFe_2O_4$ at size 200 nm [187] shows that regardless of the size, the composition of MNPs affect their magnetisation and allow tailoring of their properties. The key results are shown in Table 3-6 and this finding is also demonstrated by other researchers [201], [78] [187]. The key influence on coercivity is size-dependence [200], as nanoparticle size is increased, coercivity increases to a maximum before decreasing [200] due to the formation of multiple magnetic domains [170]. This has been confirmed by most previous studies. The results in this work agree with this trend in terms of Mn, Co, and Cu doping; all of these have large nanoparticle sizes compared to native magnetosomes.

Table 3-6: Summary of the magnetic properties of two types of MNPs.

Reference	Magnetic nanoparticles	Size (nm)	M_s (emu/g)
Lee *et al*. [78]	$FeFe_2O_4$	12	101
	$MnFe_2O_4$	12	110
	$CoFe_2O_4$	12	99
	$NiFe_2O_4$	12	85
Deng *et al.* [187]	$FeFe_2O_4$	200	81.9
	$MnFe_2O_4$	200	53.2
	$CoFe_2O_4$	200	61.6
	$ZnFe_2O_4$	200	60.0

3.5 Multiple M^{2+} ion doped magnetosomes

3.5.1 TEM Microscopy size analysis of double and triple doped magnetosomes

This is the first study to dope two or three non-ferrous metals into the same magnetosomes. Double doped and triple doped magnetosomes were produced by using different concentrations of metal ions (50 µM Mn^{2+}, 30 µM Cu^{2+}, and 50 µM Co^{2+}). The concentrations chosen were of the highest percentage of doping success achieved in the single doped samples. However, the yield of cells for multi- doping was low at ≈ 1.5 mg/l of Magnetotactic Bacteria (MTB) compared to 2.34 mg/ l in the normal growth medium. The size of TEM measured multi-doped magnetosomes (Figure 3-17) show double and triple doping magnetosome sizes between 40 and 48 nm size range, which are smaller than native magnetosomes, meaning multiple doping results could reduce magnetosomes size.
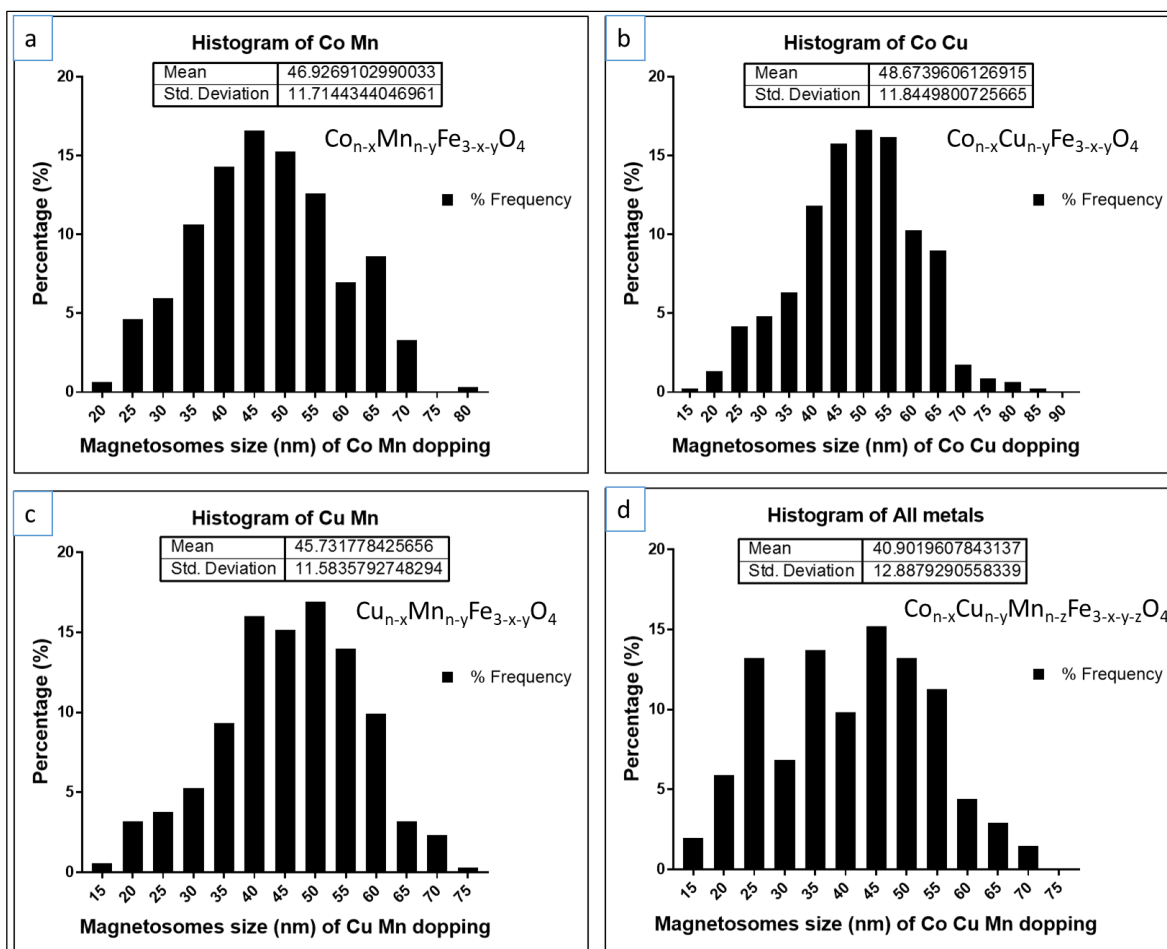
Figure 3-17: Histogram of the magnetosomes particles extracted from AMB-1. a) cobalt and manganese double, b) cobalt and copper double doping, c) copper and manganese double doping, d) all metal doping

3.5.2 Quantity of doping: ICP Elemental analysis

The concentrations chosen for multi-doping were the concentrations which generated the highest percentage of doping success in the single doped samples. These different concentrations of metal ions were 50 µM Mn^{2+} = 6.32%, 30 µM Cu^{2+} = 9.38%, and 50 µM Co^{2+} = 4.57%. The one except was the Cu-doped magnetosomes where 40 µM has shown the highest doping but also the most toxic effect, so 30 µM concentrations were chosen instead). These concentrations were used for both double and multi-metal doping.

Table 3.7: Double and triple doping of magnetosomes.

	Mean of particles size on TEM d(nm)	M_s (emug^{-1})	H_c (Oe)	Number of magnetosomes per cells	% of doping of MTB
$Fe_{3-yx}O_4$	51.70±11.95	92.99	125.1	20.69 ± 3.98	
$Co_{n-x}Mn_{n-y}Fe_{3-x-y}O_4$	46.92±11.7	30.49	399	18.79 ± 5.45	Co=2.37%
					Mn=2.92%
$Co_{n-x}Cu_{n-y}Fe_{3-x-y}O_4$	48.67±11.84	32.28	399	16.38 ±5.39	Co=2.33%
					Cu=13.95%
$Cu_{n-x}Mn_{n-y}Fe_{3-x-y}O_4$	45.73±11.58	40.07	73.13	15.43 ± 6.70	Mn=3.06%
					Cu=10.20%
$Co_{n-x}Cu_{n-y}Mn_{n-z}Fe_{3-x-y-z}O_4$	40.90±12.87	13	399	15.37 ± 5.60	Co=3.73%
					Mn=3.06%
					Cu=12.42%

Multi-metals doping results in, especially with copper, the highest doping more than 10% compared to other double and triple with cobalt and manganese doping Unsurprisingly, the highest percentage of doping occurred for copper (12.42%, 10.20%, 13.95%) in all samples the copper was present (double and triple doping), despite the presence of Mn^{2+} and/or Co^{2+}, as seen in Table 3.7

 The total percent of metal doping for double doped magnetosomes was: For Co, Mn 5.3%, Co, Cu 16.3% and Cu, Mn was 13.3%, with a total percent for triple doping of 19.2% which is highest compared to double doping. These results show the maximum percent or the maximum capacity for AMB-1 to take up to 19.2% of non-ferrous dopants into the magnetosomes, which demonstrates the maximum % of doping for the magnetosomes and still enable the formation of magnetite. It can be assumed that when MTB biomineralize magnetite, the bacteria could have a low resistance to Cu resulting in high-level of Cu doping and toxicity, causing a reduction in magnetosomes size, while it could has high resistance to Co and Mn that results in lower incorporation. This suggests that a different mechanism is responsible for high copper doping and this could involve homologues of copper dependent

iron transporter amb4411, amb0939 and amb0940 that present in magnetosomes island [155].

It is interesting to compare the levels of doping between the single doped samples, and the double and triple doped samples. Comparing the doping levels at the same concentrations in each case (50 µM Mn^{2+}, 30 µM Cu^{2+}, and 50 µM Co^{2+}) shows that Co and Mn produce higher levels of doping when they are incorporated in single doping experiments (4.57% and 6.32% respectively) compared to experiments when they are incorporated with other metals. It could be that combinations of different metal ions in the growth media reduce the uptake of cobalt and manganese. The opposite case is true for Cu, which shows a higher percentage (approximately 13%) when present in the double and triple doped experiments. A decrease is seen in the number of magnetosomes per cell in the presence of copper ions, as shown in Table 3.7, with Co & Cu, and Mn & Cu, doped magnetosomes 16.38 ±5.39 and 15.43 ± 6.7 respectively. Also this is observed in multi-metal doping results (15.37 ± 5.60), compared with native magnetosomes (20.69 ± 3.98). While the number of magnetosomes in Co and Mn doped cells (18.79 ± 5.45), where no copper is present, shows only a slight decrease in the number of magnetosomes. This shows that copper is having an inhibiting effect on magnetosome number.

3.5.3 Magnetism of multiple M^{2+} doped magnetosomes
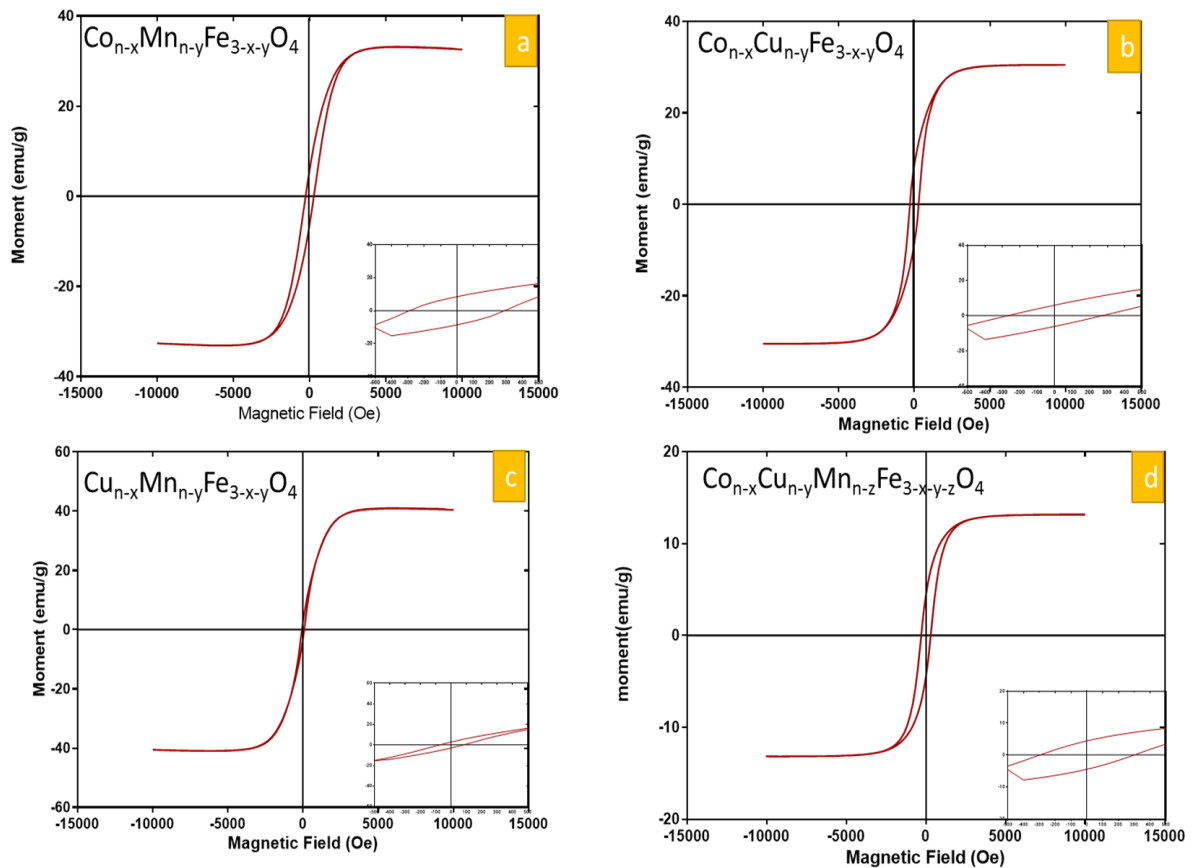
Figure 3-18: Superconducting Quantum Interference Device (SQUID) analysis of magnetosomes. Hysteresis loops recorded at T=300 K. a) cobalt and manganese doped sample, b) cobalt and copper double doped sample, c) copper and manganese doped sample, d) cobalt, copper and manganese metal doped sample.

Figure 3-18 shows the magnetic hysteresis curves of double doped and triple doped magnetosomes. All the samples containing cobalt have the same and highest coercivity of 399 Oe compared to single doping, with lower magnetic saturation levels compared to undoped magnetosomes. The $Cu_{n-x}Mn_{n-y}Fe_{3-x-y}O_4$ showed lower coercivity at 73.13 Oe with a higher magnetic saturation (40.07 emug^{-1}) compared to other samples. It is interesting that the triple doping results showed the same coercivity as double doping even with lower Ms compared to all double doping samples Table 3.7. The observed increase in coercivity (399 emug^{-1}) in double and triple doping is thus attributable to the Co doping based on an increase in coercivity correlated to the presence of cobalt content in the magnetosomes increasing, and in particular, compared to the absence of cobalt doping seen in $Cu_{n-x}Mn_{n-x}Fe_{1-2x}O_4$ doping (73.13 emug^{-1}).

Multi-metals doping, especially with cobalt, shows the highest levels of coercivity compared to single Co doping; a possible explanation for this may be that doping with more than one metal increases coercivity because of the increase of overall Co^{2+}, Cu^{2+}, and Mn^{2+} content in magnetosomes. Comparisons to non-doped magnetosomes indicate that increasing the concentration of metals dose increase coercivity. Where more metals are used in doping, coercivity increases, even in double and triple doping, the size of the magnetosomes is small compared to native magnetosomes.

Doping the magnetosomes with different micromolar amounts of Mn, Co and Cu have no clear effect on crystal morphology and size compared to native magnetosomes. However, it does cause an increase in the percentage of doping for all three metals. Doping magnetosomes could be used to tune the magnetosomes magnetic properties for specific applications. Interestingly the double-doped samples have higher coercivity compared to single doped samples. This could open the door for more research on multi-doping to know why it increases and how we could increase it even more for some applications.

The magnetic cores of the magnetosomes consist of magnetite, in this research, the results confirm that doped magnetosomes show the variations in magnetic saturation and coercivity after doping with nonferrous metals, due to the introduction of alternative metal ions in the Fe_3O_4 magnetite crystal of the magnetosomes, even at low concentrations, revealing that doping can influence the ferrimagnetism of biogenic magnetite crystals. This offers promise for developing metal doped magnetite crystals with appropriate magnetic properties for biomedical and biotechnological applications, which will be explored further in later chapters.

Chapter 4:

Functionalization of the

magnetosomes surface

4.1 Introduction of Functionalization of the magnetosomes surface

Malignant tumours are more prone to internalisation of MNPs than healthy cells [182], as they have a higher endocytic potential than healthy cells as a consequence of their large demand for nutrients [182], high metabolic activity and high proliferation rate. [182][202][203]. These features mean MNPs are suitable for delivery of drug therapy to tumour cells however most of them are still in the development phase [91]. MNPs can be functionalized with specific drugs or biomolecules for treatment of diseases, or for performance as a nanoprobe for disease diagnosis.

Many cancer therapeutics are relatively non-specific for tumours and often require a large dose to achieve a high local concentration, which can result in biodistribution of the drug throughout the body [204]. If treatment is localised to a tumour site it can reduce the side effects on the rest of the patient. Many researchers have tried to attach drugs to MNPs to minimise drug doses and side effects as well as the cost of the drug treatment [36] [94]. The properties of magnetosomes make them suitable as such a nano-carrier providing they can be suitably functionalised. The characterisation and doping of magnetosomes were described in the previous chapter. In this chapter their functionalisation is investigated. Specifically, this chapter concerns the streptavidin-biotin interaction as a mean of attachment and functionalization by using either an enzymatic or chemical system of biotinylation [122]. This is a process whereby biotin molecules are covalently attached to amine groups [114], [123]. The magnetosomes feature amine groups on the membrane and the surface exposed proteins. It has been found that 90% of total primary amino groups are distributed in an external lipid membrane [168]. After immobilisation of biotin on the magnetosomes via conjugation to the amino group, streptavidin can interact with the biotin for later binding with bioactive substances.

4.2 Enzymatic biotinylation

Chemical or enzymatic methods can be used for protein biotinylation. The chemical biotinylation of protein is by modification of available amine groups with biotin Sulfo-N-hydroxysuccinimide, (NHS activated biotins react efficiently with primary amino groups)

[205]. The chemical biotinylation of any available amines groups produces nonspecific biotinylation. On the other hand, an enzymatic (

Figure 4-1 a and b) approach is mild and highly specific to a biotinylation site on the protein [122] which is known as the biotin accept peptide (BAP) or Avi-Tag. BAP consists of a specific 15 residue sequence (GLNDIFEAQKIEWHE)[112]. This sequence contains a single lysine residue on which a biotin molecule can be specifically covalently coupled using BirA, the biotin ligase, from *Escherichia coli* [116][206] Figure 4-1 a However, there is no BAP naturally occurring on the magnetosome membrane. An alternative is to perform enzymatic biotinylation using a mutant form of BirA, which is referred to as BirA* Figure 4-1 b. This variant can biotinylate proteins on any accessible lysine, not just those with the BAP sequence.

Biotinylation route if BAP is available on magnetosomes.

Biotinylation route using mutant BirA to modify any available lysine residues.
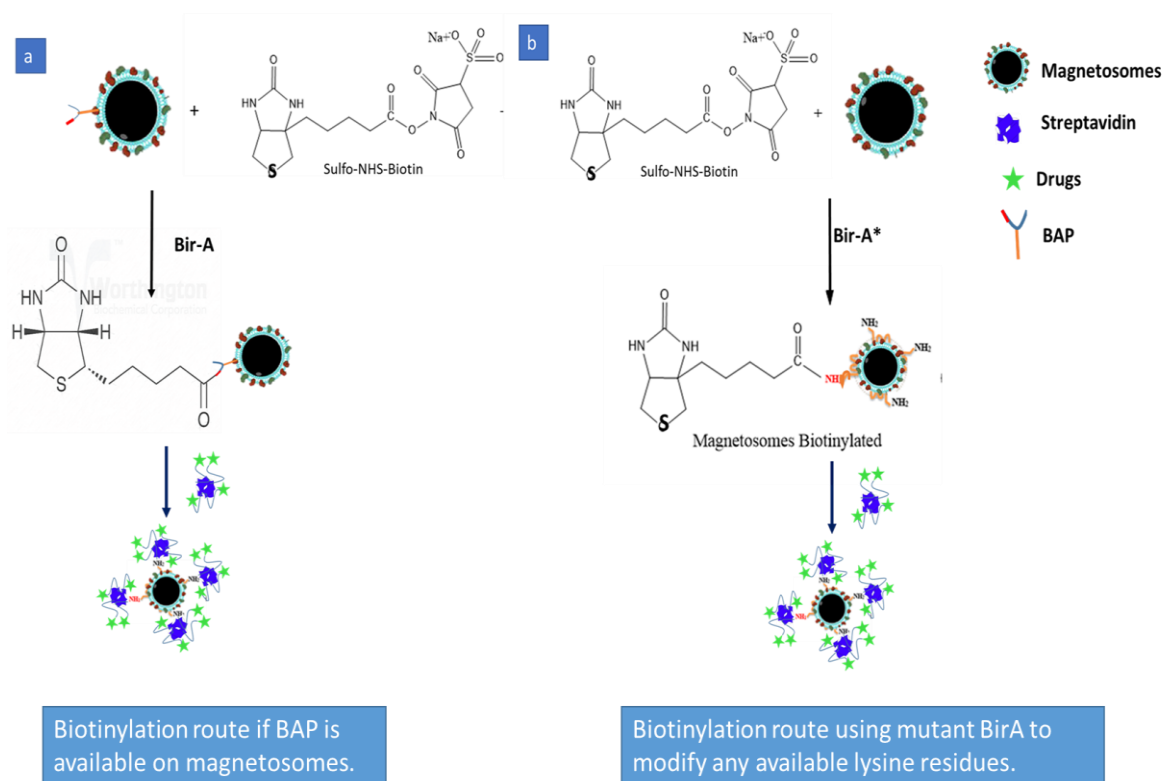
Figure 4-1: The Biotin is conjugated to primary amino groups on the magnetosome membrane in enzymatic biotinylation with BirA to form an amide bond. The schematic represents the enzymatic biotinylation using two methods of reaction. a) The magnetosome membrane has a BAP specific biotin site (red rectangle), for biotinylation with BirA. b) The Biotinylation of available amine groups on the magnetosome surface without BAP but by using BirA*. Biotinylated magnetosomes are then bound to streptavidin.

Once the magnetosomes are biotinylated they can be conjugated to streptavidin, which has four identical biotin binding sites, that can serve as bridge molecules to allow the introduction of another bioactive biotinylated substances [207]. Streptavidin can bind biotin with high affinity (K_d of 10^{-14} mol/l) which is one of the strongest known protein-ligand interactions. The biotin-streptavidin system has been used in many different biotechnological applications [120][208]. In the future, the MTB could be engineered to produce BirA* which would biotinylate the magnetosomes *in vivo*.

A plasmid encoding BirA was kindly donated by Sousa [112]. The plasmid, designated pBirATrx, was amplified in *E. coli* cells and purified using a miniprep kit (section 2. 10 and 2.11). The product was analysed by agarose gel to confirm it was supercoiled and the correct size, and subjected to DNA sequencing to confirm the *birA* gene was present and free from unwanted mutations. The plasmid was amplified by polymerase reaction using overlapping primers (Table 4-1) which encoded a single amino acid substitution at position 118 to change an arginine to glycine (R ⟶ G)

Table 4-1: Mutagenic primers for BirA (R118G):

Primer name	sequence	Primer length	Melting temperature °C
BirAR118G-F	5' GGCTGGCCGTGGTGGTCGGGGTCGGAAATG 3'	30 bp	77.7 °C
BirAR118G-R	5' CATTTCCGACCCCGACCACCACGGCCAGCC 3'		

The red colours letter represents the mismatch.

The *birA* gene was modified with the site-directed mutagenesis process (see chapter 2 section 2.9.2) to produce the BirA*mutant. It was transformed into XL 10-Gold *E. coli* strain, to produce BirA* plasmid and to confirm the mutation by DNA sequencing. DNA sequencing from the T7 terminator indicated a positive mutation was present (Figure 4-2).

Figure 4-2: Sequence alignment of native BirA (subject) and mutant BirA* (query), the arrow indicates the residue substitution.

It is necessary to overexpress native BirA and BirA* biotin ligase to generate enough material for later experiments. BirA and BirA* were produced in BL21 (DE3) *E. coli* strain. BL21 derivatives are designed to enhance the expression of proteins. BirA and BirA* in this work was expressed as a thioredoxin fusion because BirA overexpressed in *E. coli* was found to be mainly insoluble [112]. This fusion increases the protein solubility [112]. Also, it provides affinity handles for protein purification (6XHis tag) [112].
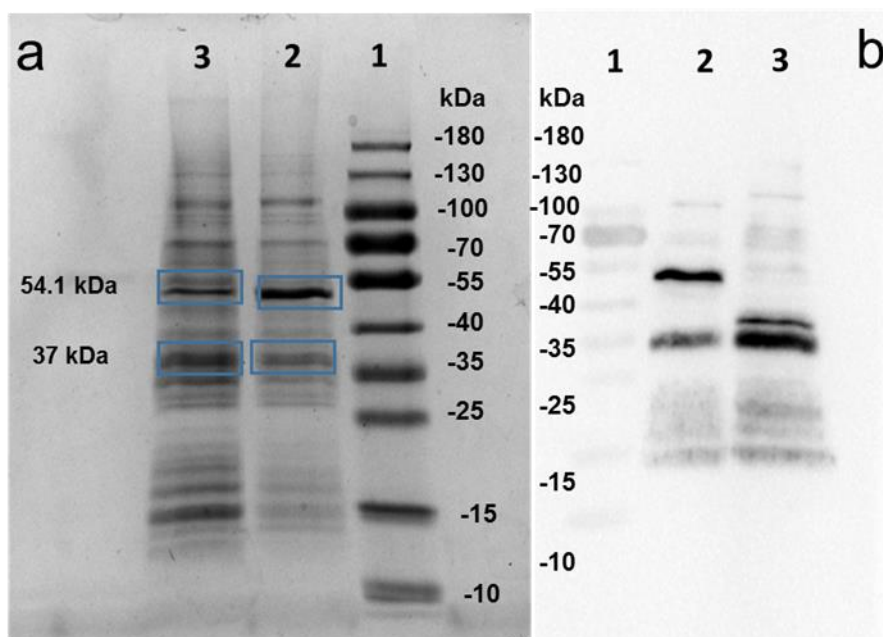
Figure 4-3: Expression and purification of the BirA wild-type lane 2 and BirA*mutant fusion as followed by SDS-PAGE (12%). The target protein was expressed as thioredoxin fusion in a) lane 2,3 in 12% SDS page , b) lane 2 in western blot.

Expression of BirA, and BirA* was performed by induction with IPTG. Figure 4-3, shows an SDS-PAGE of induced cells. Two intense protein bands appear in lanes 2 and 3 with estimated molecular weights 37 and 54.1 kDa. The larger molecular weight band (54.1 kDa) is consistent with the estimated molecular weight of the thioredoxin-BirA fusion protein (54.1 kDa) [112] [117]. The bands were probed with an anti-His6 antibody using a western blot protocol (section 2.12.2). This confirmed the 54.1 kDa band in lane 2 was the fusion protein. However, this band was absent in lane 3, showing that the BirA*-thioredoxin protein was not present. In both lanes 2 and 3, the 37 kDa band gave a positive signal with the antibody. The identity of this protein is not known. The His6tag is between the thioredoxin and BirA. If the Thioredoxin was missing the molecular weight would be 41.7 kDa, and if the BirA was missing the molecular weight would be 18.3 kDa. The actual band is at 37 kDa, which could be due to partial loss of the BirA protein from the fusion tag.
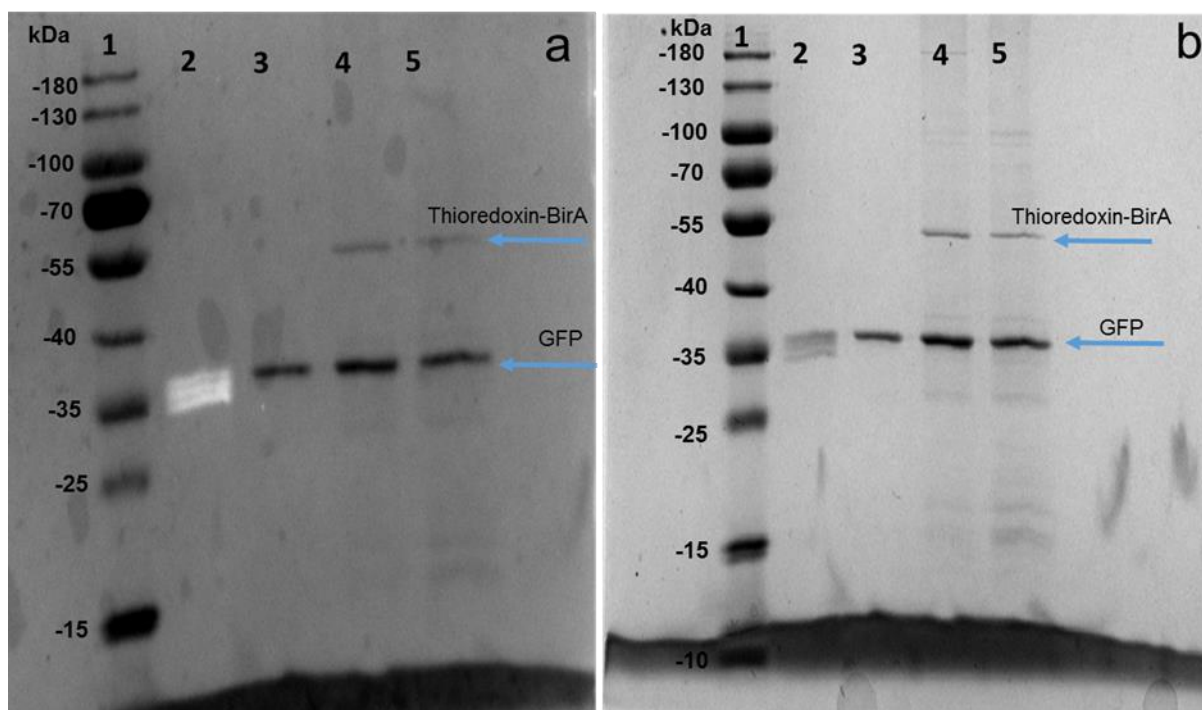
Figure 4-4: SDS-PAGE for in vitro biotinylation with bright light and without b, comparing enzymatic biotinylation using wild-type BirA or BirA* to chemical biotinylation lane 2 chemical biotinylation (GFP+biotin-NHS). Where lane 3 is the control (GFP + biotin + ATP only), the enzymatic biotinylation lane 4 (GFP + biotin + ATP + BirA) and 5 (GFP + biotin+ ATP + BirA*).

The efficiency of biotinylation using the expressed BirA and BirA* was also studied by incubating biotin and ATP with GFP as a test substrate. This was compared to GFP which was biotinylated synthetically. The samples were analysed by SDS-PAGE together with untreated GFP as a reference (lane 3, GFP + biotin + ATP only). The gel was stained by Instant Blue protein stain and also probed with fluorescently labelled streptavidin. The GFP band in the chemical biotinylation appears diffuse and gives a positive (bright) signal with the streptavidin. The enzymatic biotinylation appears to be unsuccessful, with no diffuse GFP and no signal from streptavidin on lane 4 and 5 (Figure 4-4). Although BirA and BirA* were produced it was unable to function in this experiment. This may be due to misfolding of the BirA, or incorrect experimental conditions. Furthermore, BirA was mostly insoluble even when the conditions for protein expression were changed by reducing the temperature to 18°C after the addition of IPTG. The result for the wild-type BirA protein was expected because the GFP does not contain a biotin acceptor protein (BAP). However, BirA* did not successfully biotinylate the GFP, perhaps due to non-solubility of biotin or ATP, or it might be blocking access to the active site.

4.3 Chemical biotinylation

The most common type of biotinylation is chemical biotinylation performed using Sulfo N-hydroxysulfosuccinimide biotin (Sulfo-NHS-Biotin). Where NHS-activated biotins react with primary amino groups (-NH$_2$) to form stable amide bonds. In this study water soluble Sulfo-NHS-Biotin was used which enables efficient labelling of proteins, antibodies and any other primary amine-containing molecules. In this regard, a carrier system has been developed by using the combination of interactions of streptavidin-biotin molecules with can be attached directly to the magnetosome surface as described in Figure 4-5.
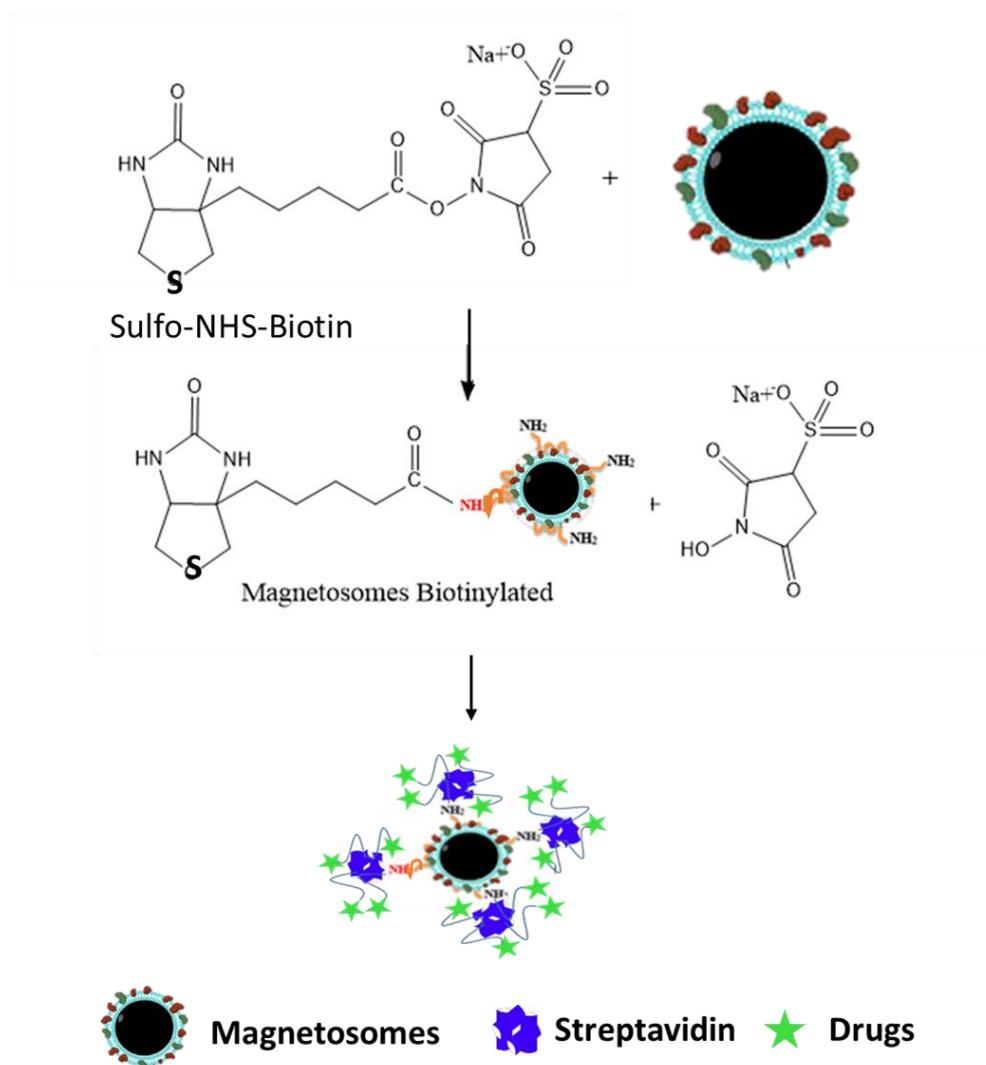
Figure 4-5: Scheme represents the strategy used for conjugation of biotin on magnetosomes surface then coupled with streptavidin to use as a platform to carry bioactive substance.

The successful biotinylation of GFP, showed that the chemical biotinylation kit was active and could be used for magnetosome samples. The magnetosome surface was conjugated to NHS-Biotin via primary amino groups. Streptavidin Alexa Fluor 488 (streptavidin covalently attached to the fluorescent label (Alexa Fluor®dye) for specific detection of a variety of nucleic acid, protein and other molecules was mixed with the biotinylated magnetosomes. Labelling and imaging were performed 4 hours after biotinylation. To determine if the florescent streptavidin was bound to the magnetosomes it was possible to use a magnetic field to move and align the magnetosomes and observe movement of the florescent probe. This can be seen in

Figure 4-6 with fluorescent magnetosomes chains all aligned towards the magnetic field. The successful conjugation of biotin to magnetosomes was confirmed by confocal microscopy. The images of extracted magnetosomes, shows they are well dispersed in small chains. The reason for the good dispersion and functionalisation is that the existing stable lipid membrane is intact and surrounds the magnetite core. This is likely to prevent the magnetosomes from completely sticking together and aggregating by magnetic and electrostatic attraction [168].
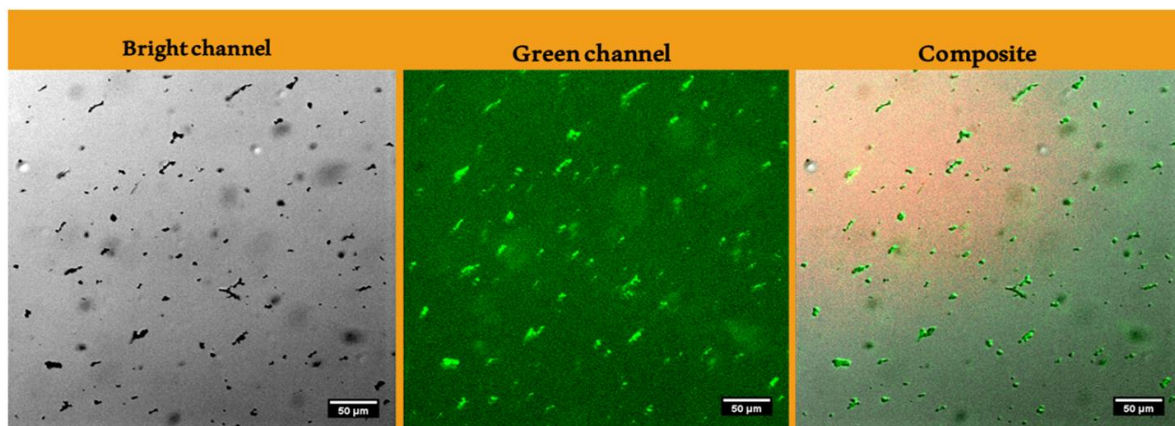
Figure 4-6: Biotinylation magnetosomes conjugated to a fluorescent probe. 100 µl of magnetosomes conjugated to 24 µl of NHS biotin and 2 µl of streptavidin which was attached with Alexa Fluor 488 dye (green) with scale bar = 50 µm.

To confirm the uptake and stability of biotinylated magnetosomes inside the cells fluorescence microscopy of magnetosome dosed cells was performed. The magnetosomes were modified with biotin and streptavidin Alexa flour 488. 0.05 mg/ml of labelled magnetosomes were dosed into cells cultured in 6 well plates with 2 ml of culture medium.

The biotinylated magnetosomes were followed by fluorescence imaging after 24 hour incubation (

Figure 4-7).The transport and internalisation of these biotinylated magnetosomes was observed inside the cells. The biotinylated magnetosomes were distributed as green spots in the cytoplasm in the live cells in the green fluorescent channel, and as dark spots in the bright channel images. The magnetosomes appear outside of the nucleus, and some appear closely associated with the nuclear membrane. This imaging result shows that the biotinylated magnetosomes are able to be uptake and that the presence of the biotin and fluorescent streptavidin does not seem to block cell uptake.
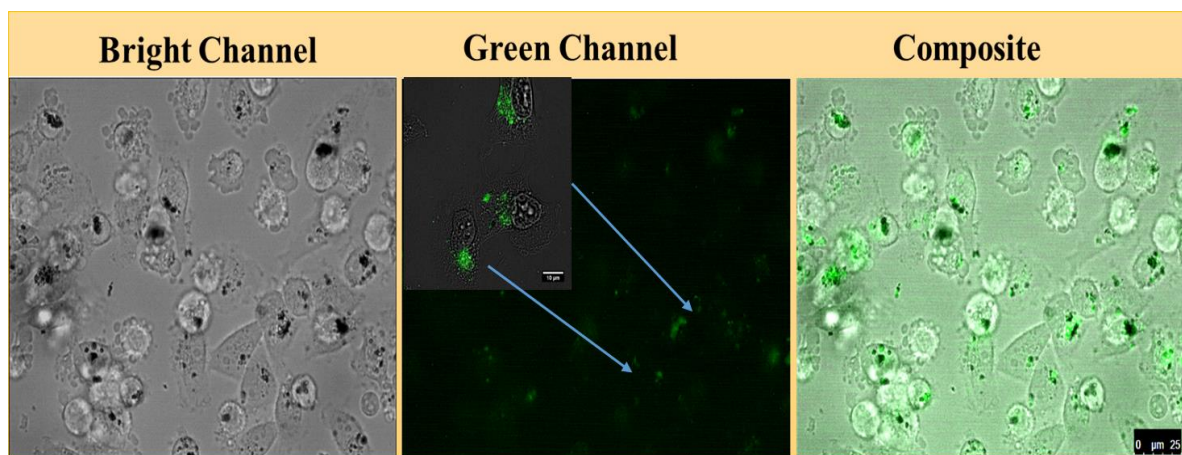
Figure 4-7: the fluorescence images of the intracellular distribution of magnetosomes in the MDA-MB-231 cell were incubated for 24 hours with biotinylation magnetosomes conjugate with Alexa Flouro®488 (green fluorescence).(Leica AF600LX inverted microscope).

To date, there is a lack of functionalisation of magnetosomes for drug delivery to cancer cells in the published literature. Biotinylation of magnetosomes appears to be one way of easily functionalising the magnetosomes, allowing conjugation to any biotinylated molecule via a streptavidin link. The biotinylation does not appear to prevent uptake of the magnetosomes into the cell. By using the biotinylated magnetosomes I succeeded in preparing in this chapter using chemical biotinylation, they could be attached via the biotin-streptavidin system to drugs or bioactive substance for more applications in the future.

Chapter 5:

Cell uptake and cytotoxicity

5.1 Introduction for cell uptake and cytotoxicity

Cancer is a significant cause of death in developed countries [107] [210]. The most common type of cancer in women is breast cancer, where about one million new cases of breast cancer are diagnosed worldwide each year among women aged between 50 and 70 [126]. Of these cases two out of three women contain progesterone (PR) and estrogen (ER) receptors, also about 20-30% of breast cancer have excessive amounts of HER2 receptors [127]. Hormone therapy can be used as a treatment for ER and PR positive cases of breast cancer. Furthermore, anti-HER2 medications can be used for breast cancer with many HER2 receptors. However, triple-negative breast cancer that lack any receptors for PR, ER or HER2 cannot be treated with drugs or hormone therapies [127] [128]. The MDA-MB-231 cell line is an example of a triple negative breast cancer cell line. It is a highly aggressive, invasive cell line with limited treatment availability. Fortunately, there are novel methods for the diagnosis and treatment of triple-negative breast cancers. An example of this is the use of magnetic nanoparticles, which have gained attention over the past two decades. Novel therapies such as the targeted therapy, magnetic hyperthermia and MNPs contrast agent. Thus allowing the disease to be detected in the early stages and to deliver a treatment dose at the desired area.

The results of doped biosynthetic magnetic nanoparticles with Mn^{2+}, Co^{2+}, Cu^{2+} showed enhance of magnetic properties of cobalt, copper and manganese compare to magnetite alone this could make them more suitable for biomedical applications such as drug delivery, MRI and hyperthermia. In the previous chapter it was shown that it was possible to functionalise the surface of doped magnetosomes. This was successfully achieved through the use of biotinylation making these magnetosomes suitable for biomedical application. Biotinylation may help to bind or attach a variety of bioactive substance such as an antibodies, antigen and drugs driven by an external magnet as shown in Figure 5-1. Helping to concentrate the desired therapy at the preferred sites. In this chapter the native and doped magnetosomes with Mn^{2+}, Co^{2+}, Cu^{2+}, SNPs and OA-SNPs, (SNPs and OA-SNPs as controls) were prepared in a range of concentration between (0.022 mg/ml, 0.043 mg/ml, 0.087 mg/ml, 0.18 mg/ml, 0.35 mg/ml, 0.5 mg/ml, 1 mg/ml, and 1.5 mg/ml). This will assess the different levels of toxicity and uptake in MDA-MB-231 cancer cells and establish which particles showed the greatest uptake with the lowest cell toxicity. Many techniques, such as

TEM, Prussian blue staining and flow cytometry have been used to investigate MDA-MB-231 cell uptake. To evaluate potential therapeutic use of these MNPs. This requires assessment of their toxicity, which consisted of (I) - MTT assay, which was used to assess the cells metabolic activity, (II) - propidium iodide (PI), this stained the for cells for death, and (III)- Limulus Amebocyte Lysate (LAL) assay monitored the presence of Lipopolysaccharide (LPS), also known as endotoxin, it is essential to measure for the safety in MNPs therapy.
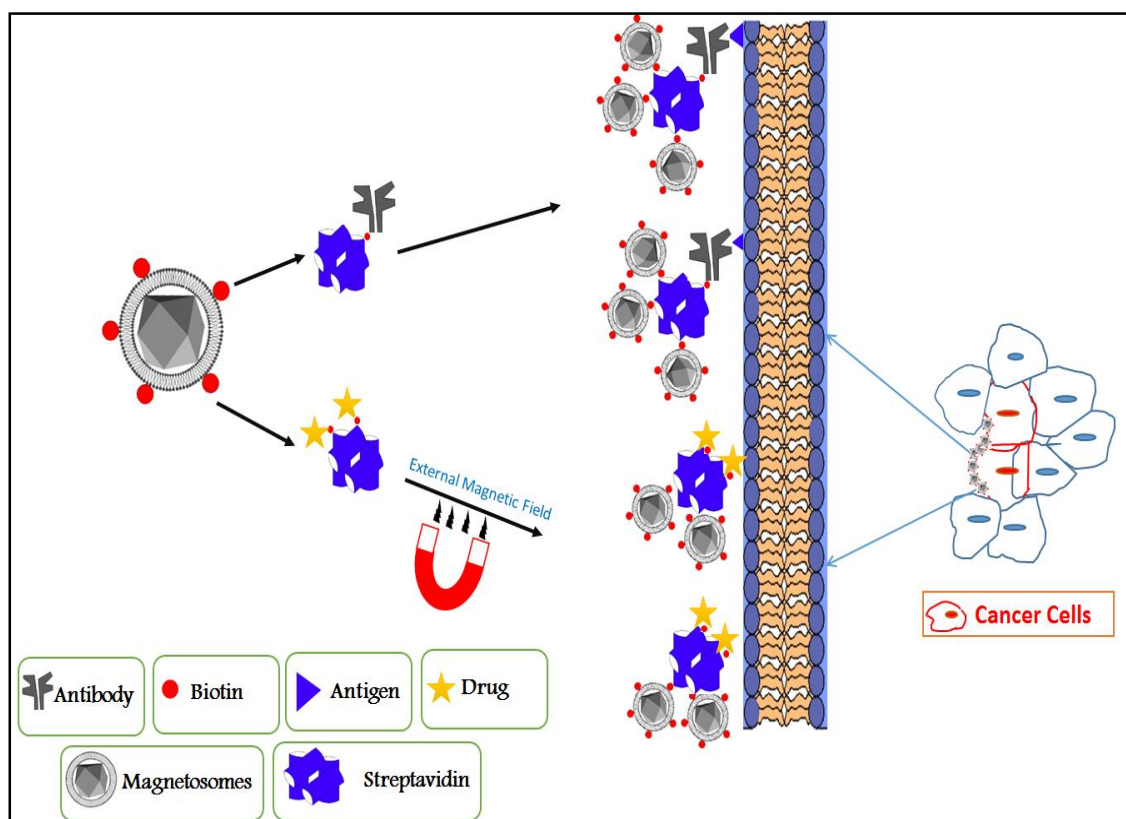
Figure 5-1: Scheme representing the possible interaction of streptavidin with biotinylated magnetosomes particles, and their immobilisation on cancer cells by conjugation of a tumour specific antibodies. An additional methodology can be used where drug molecules are immobilized on the streptavidin-coated magnetosomes and an external magnetic field is used to drive the particles to the cancer cell.

5.2 In vitro cell uptake

5.2.1 Flow cytometry

MDA-MB-231 cells seeded in 6-well plates with 300,000 cells/well and incubated with MNPs prepared from the concentrations (between 0.022 mg/ml, 0.043 mg/ml, 0.087 mg/ml, 0.18 mg/ml, 0.35 mg/ml, 0.5mg/ml, 1 mg/ml, and 1.5 mg/ml) 24 hours after incubation the culture media was removed and the cells washed with PBS as stated in the procedure described in

section 2.16. Following that the cells with MNPs were collected for centrifugation. To quantify and evaluate the cell uptake of MNPs flow cytometry was used. In Figure 5-2 at low concentrations (< 0.18 mg/ml,) the uptake was the same for all types of MNPs at each concentration, with the cell uptake increasing linearly with the dosage for all other MNPs types. At concentrations of 0.18 mg/ml and differences in uptake of the various MNP begin to be seen. What was particularly interesting was that above 0.18 mg/ml there is no significant increase in uptake of magnetosomes. It appears that there is a maximum uptake threshold of approximately 40%, while the SNPs and OA-SNPs continue to increase up to a maximum uptake of 65% at dosages of 0.35 mg/ml and above after subtracting the control (untreated cells without MNPs) from all the samples.
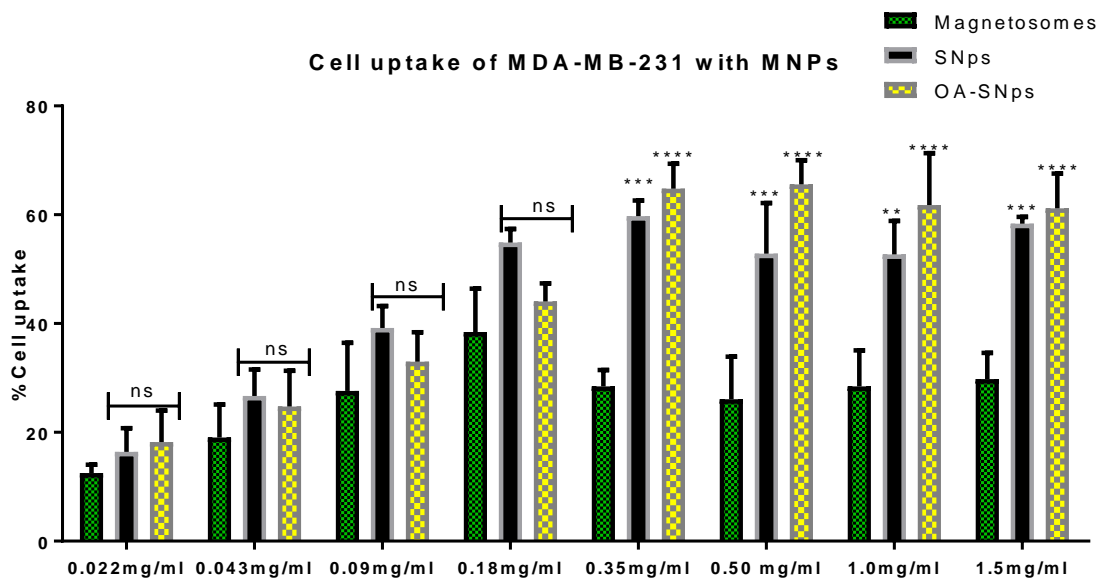
Figure 5-2: Cellular uptake of magnetosomes, SNPs, OA-SNPs by MDA-MB-231 cells after 24hours at a range of concentration test (from 0.022 to 1.5mg/ml). The control (untreated cells without MNPs) sample was subtracted from all the samples. **, *** and **** mean p=0.0027, p=0.0008 and p< 0.0001 (significant) respectively.

There does not appear to be any apparent differences between coated and uncoated SNPs. Where the SNPs seems to reach the maximum uptake and become plateau at 0.18 mg/ml, and the OA-SNPs also seems to reach the maximum uptake and begins to plateau at 0.35 mg/ml. This could be because both of them have almost the same size (SNPs with 37 nm and OA-SNPs with 40 nm), and the same zeta potential that made these particles equal in dispersion (-49.00± 0.87 mV for the SNPs, while 50.00 ±mV for the OA-SNPs). The cellular uptake for the magnetosomes was highest at 0.18 mg/ml so that is why I have chosen this concentration as

144

the ideal for magnetosomes cell uptake, while the SNPs was 0.18 mg/ml and above, and OA-SNPs was 0.35 mg/ml and above. I have picked these concentrations for all of my experiment in this flat area, that shown consistency in uptake, this could be due to the mechanism of uptake by the cells reaching saturation at these concentrations. The magnetosomes shows the worst efficiency and internalization compared to other SNPs and OA-SNPs, this could be attributed to the magnetosomes membranes, that is made up from; neutral lipids and free fatty acids, glycolipids and sulfo-lipids, and phospholipids furthermore, the amino groups in the magnetosomes membrane that consisting of lipid and proteins [101][209].This membrane could have a different effect on the internalization of the magnetosomes by the diffusion mechanism or endocytosis mechanism through the cell membrane compared to other MNPs
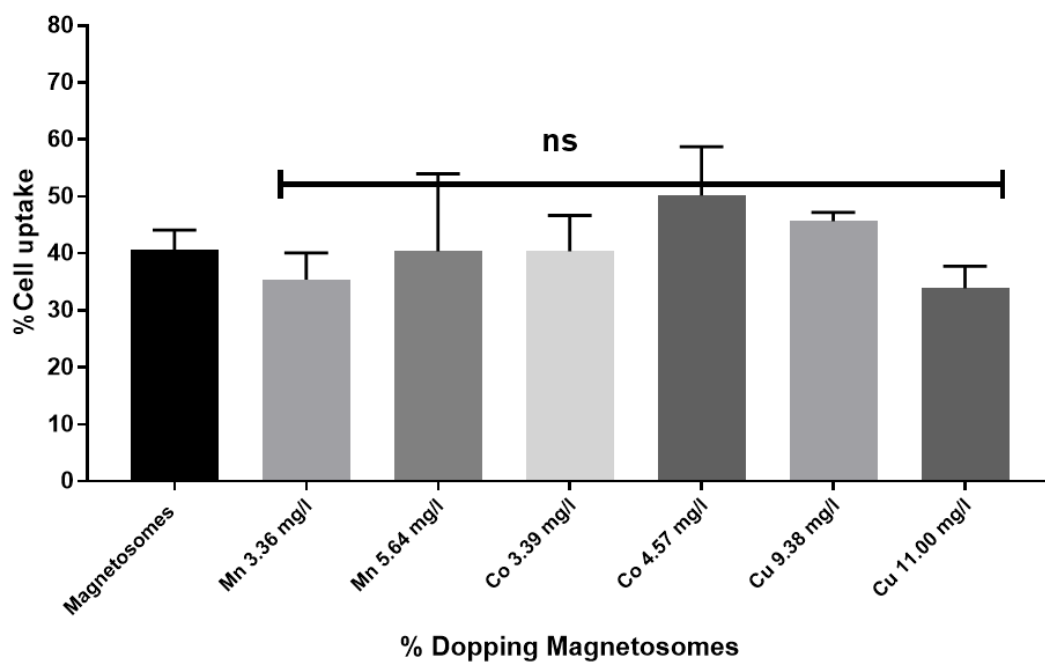
Figure 5-3: The Cellular uptake of native and doping magnetosomes after 24hours incubation with MDA-MB-231 cells at concentration test (from 0.18mg/ml). The control has been subtracted for all the samples.

In chapter 3 we successfully incorporated nonferrous metals such as cobalt, copper, and manganese into magnetosomes. Here we analysed if this causes any increased toxicity in tumour cells to compare with native magnetosomes. Analysing the internalisation of doped magnetosomes within cancer cell MDA-MB-231 after 24 hours at 0.18 mg/ml, concentration, where again performed by flow cytometry. Figure 5-3 showed there was no significant change

in cell uptake of doped magnetosomes compared to native magnetosomes. The cell uptake of doped magnetosomes was approximately 40% with slight increase shown for cobalt doping at 4.57% while copper doping magnetosomes at 11.00% shown lower uptake at 30%.

5.2.2 ICP-AES analysis of Iron content in MDA-MB-231 cell line
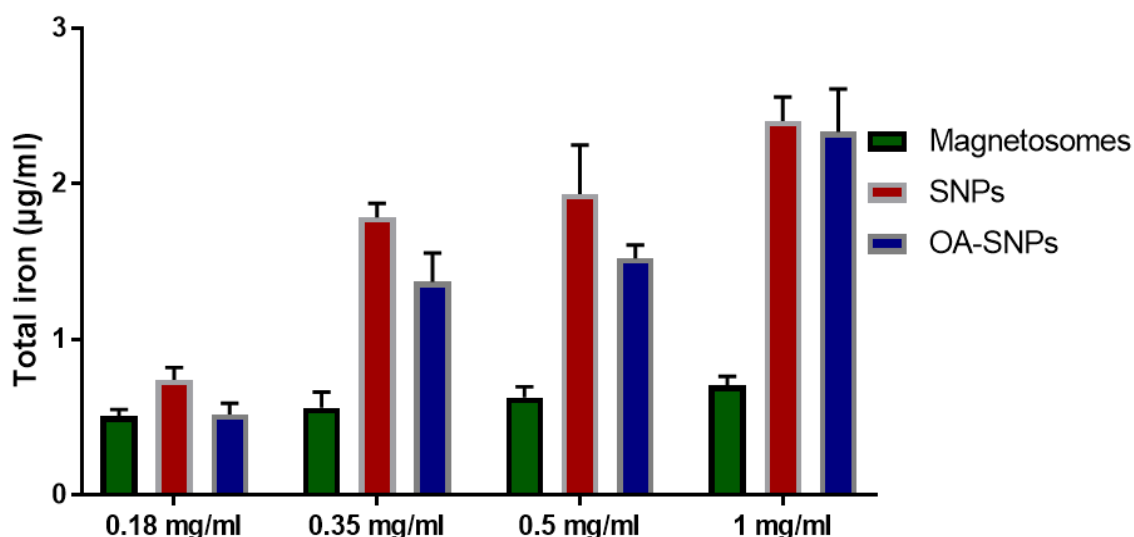
Figure 5-4: ICP-AES data for the content of Fe in MDA-MB-231 cell line, with seed density 200,000, which are treated by magnetosomes, OA-SNPs and SNPs.

The ICP-AES was used to measure the content of iron in the MDA-MB-231 cells, which were dosed with magnetosomes, SNPs and OA-SNPs for 24 hours. Figure 5-4, shows three-fold higher iron concentration for both SNPs and OA-SNPs at high-level concentration 1 mg/ml compare to magnetosomes, while at low concentration of MNP (0.18 mg/ml) the iron concentration was almost the same level. In all concentration the magnetosomes showed the same concentration of iron with a slight increase at 1 mg/ml concentration. The data suggests the increasing iron concentration is due to increasing MNP concentration. The maximum iron content (2.40-2.33 µg/ml) was achieved at a 1 mg/ml dose of SNP and OA-SNP. This variation in the content of iron in MDA-MB-231 may be due to the difference in size of these particles (magnetosomes 52 nm, SNPs 37 nm and OA-SNPs 40 nm) and also the coated layer surround them that could cause a different uptake pathway as will discuss later.

The ICP-AES was used to measure the content of iron in the MDA-231 cell, which was dosed with magnetosomes, SNPs and OA-SNPs for 24 hours. Figure 5-4, shows three-fold higher iron concentration for both SNPs and OA-SNPs at high-level concentration 1 mg/ml compare to magnetosomes, while at low concentration of MNP (0.18 mg/ml) the iron concentration was almost the same level. In all concentration the magnetosomes showed the same concentration of iron with a slight increase at 1 mg/ml concentration. The data suggests the increasing iron concentration is due to increasing MNP concentration. The maximum iron content (2.40-2.33 µg/ml) was achieved at a 1 mg/ml dose of SNP and OA-SNP. This variation in the content of iron in MDA-MB-231 may be due to the difference in size of these particles (magnetosomes 52 nm, SNPs 37 nm and OA-SNPs 40 nm) also the coated layer surround them that could be uptake with different pathway as it will discuss later.

5.3 Visualization of MNPs in MDA-MB-231 cell line

Optical data on cell uptake has been obtained, but it is still necessary to find out where the MNPs are located within the cells or on the cell membrane. There are many techniques that have been used such as fluorescence imaging in a previous chapter (section 4.3), Prussian blue and TEM in this chapter.

5.3.1 Prussian blue assay

There are some factors such as size, shape and surface charge of MNPs that can determine their cellular distribution and internalization of MNPs [210]. To investigate the fate of the different MNP samples in cells, the qualitative internalisation of MNPs with MDA-MB-231 cancer cells were visualised using Prussian blue. Prussian blue staining is a common stain to detect the iron content in biopsy specimens and indicates iron uptake of all the magnetic nanoparticles (magnetosomes, SNPs and OA-SNPs) by MDA-231 cells as shown in Figure 5-5 B, C and D, where MNPs were detected and visible within the cytoplasm with dark blue staining compared to the nanoparticle free Figure 5-5 A. However it is hard to draw a conclusion from Prussian blue staining, so TEM was carried out in next section.
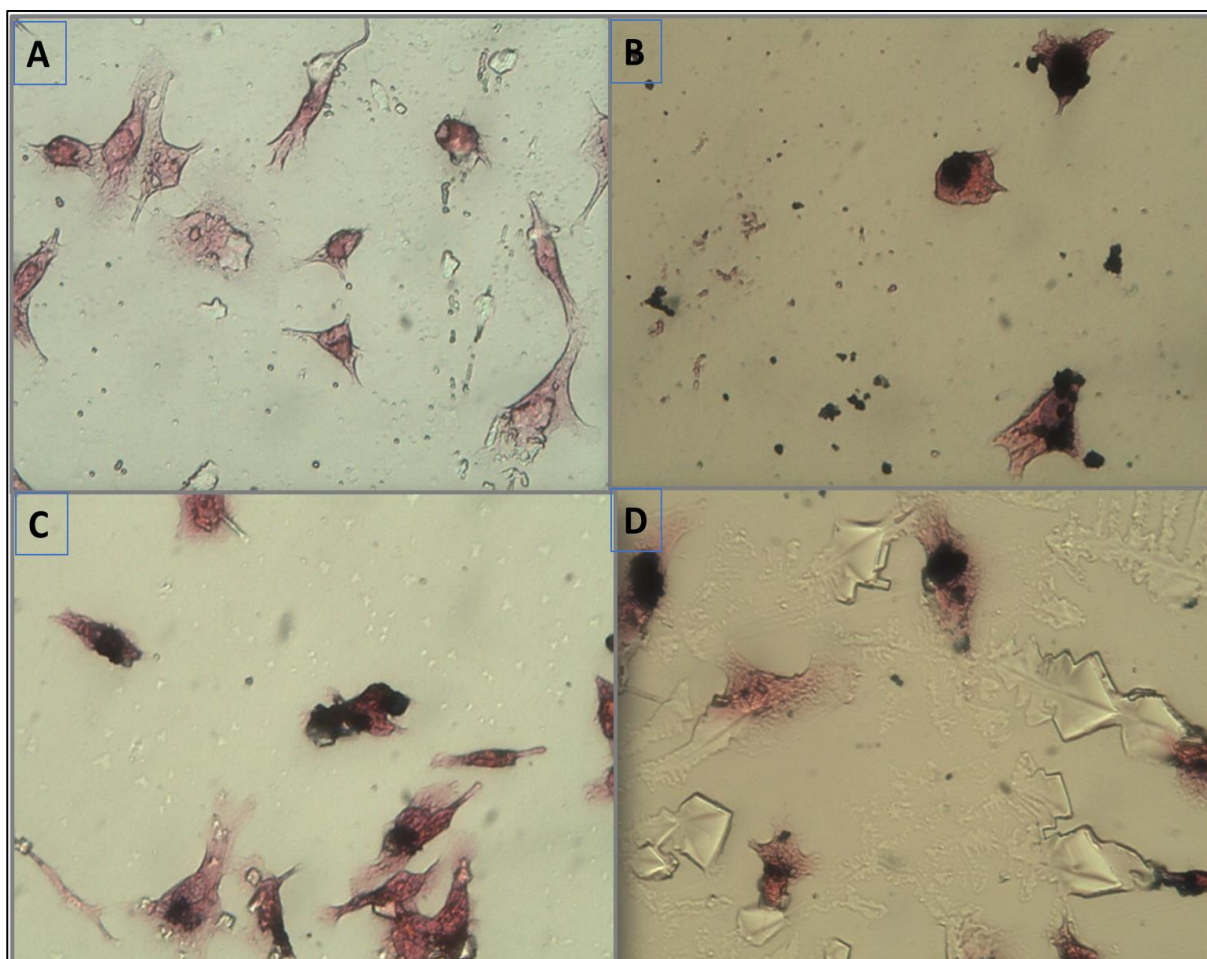
Figure 5-5: MNPs cell interaction image of Prussian blue staining of MDA-MB-231cell incubation for 72 hours with 0.2 mg/ml of MNPs where: A, Control B. Magnetosomes C, bare SNPs, D. OA-SNPs

5.3.2 Transmission electron microscopy

The internalisation process as shown in Figure 5-6. The magnetosome particles are clearly visible as black spots in TEM images. There are some magnetosomes that appear to be arranged in small chains, even after cellular internalisation or as a discrete non-aggregate that indicates some chains are degraded but not all as shown in Figure 5-6 a), b). The presence of small chains in these vesicles confirms the stability of the chain structure, in agreement with previous results [93]. Some of the magnetosomes are not observed in a chain; this could be due to the degradation of the chain of magnetosomes by the cells following their internalisation [179] or even before when the magnetosomes are extracted from the MTB. This could prevent aggregation and could lead to an increase in the rate of cellular internalisation, and should also enable them to generate uniform heating throughout a tumour for treatment applications later [92] [93] . There are at least three kinds of interaction

of magnetosomes, likely corresponding to three different internalisation steps. It described in literature where magnetosomes that extracted from *Magnetospirillum gryphiswaldense* strain MSR-1 by Mannucc and his groups [93], first adhere then cross to the phospholipid membrane and then enclosed in vesicles. Finally, the magnetosomes localised in vesicular formation lysosomes [93]. Where TEM of MSR-1 demonstrated strong uptake of these magnetosomes and revealed three phases in interaction; adherence, transport and accumulation in human colon carcinoma HT-29 cell [93].

In Figure 5-6 a, b the magnetosome short chains or small groups are localised in enclosed vesicles likely to be lysosomes in the cytoplasm. There were no notable differences between SNPs and OA-SNP in cell uptake following internalisation of these particles, they were largely confined to lysosome vesicles. TEM images showed these formations had a multi-vesicular aspect. The OA-SNPs have a coated layer like the magnetosomes lipid bilayer, but it still displays aggregation dispersion compared to magnetosomes. Macromolecules and molecular assemblies are internalised through different mechanisms. where the mechanism of uptake will vary depending on many factors, such as the incubation time, condition within the cell, cell treatment, type of cell, and surface chemical composition and size of MNPs [211][212].

Low magnification   High magnification

a Magnetosomes

b

Clumped of magnetosomes in lysosome

Small groups of short magnetosomes chains

Cytoplasm

Nucleus

c SNPs

d

Clumped of SNps in lysosome

Cytoplasm

Nucleus

e OA-SNPs

f

Clumped of OA-SNps in lysosome

Cytoplasm

Nucleus
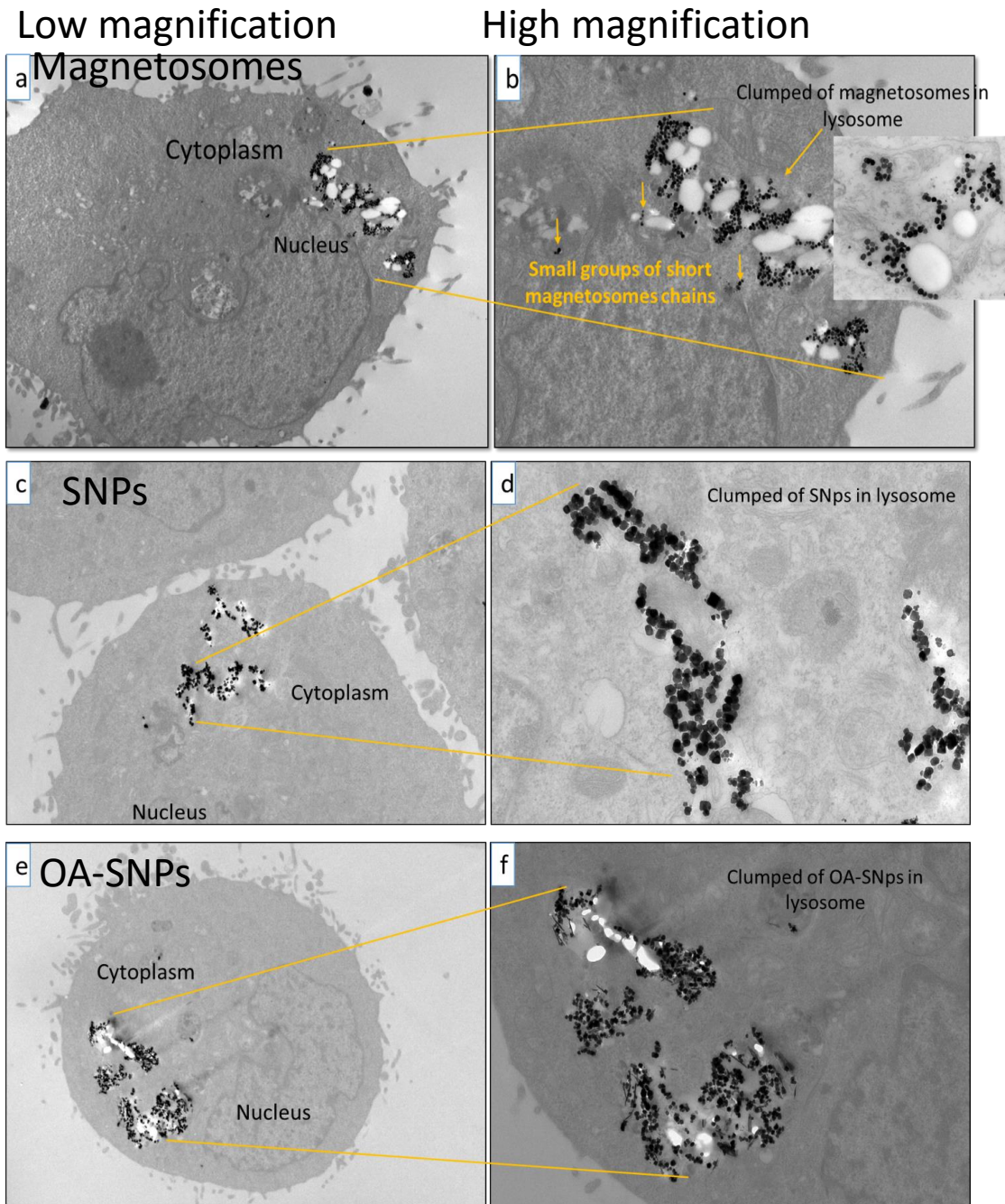
Figure 5-6: Uptake of MNPs types in MDA-MB-231 visualized by TEM, where the cells were incubated for 24 hours with MNPs. Ultrathin section of cells were prepared and imaged by TEM. a) TEM images of magnetosomes at 1µm. c) TEM images of SNPs at 1µm. e) TEM images of OA-SNPs at 1µm. b) ,d) and f) showing up take of MNPs at 0.5 µm were trapped inside the lysosome. Note: in d) image shows some short chain of magnetosomes closed to nuclei

So when particles are internalised by the cell, different uptake pathways and mechanisms are used for different particles. The pinocytotic pathways have four significant processes (with <0.2 µM macroparticles route) which are: 1) clathrin-mediated, 2) caveolae-mediated, 3)

micropinocytosis, and 4) clathrin caveolin-independent endocytosis see in Figure 5-7. The pathway is determined by different types of receptor-ligand interaction that are mainly dependent on a particle's size and chemical surface [211]. This suggests the magnetosomes with lipid bilayer membrane with different functions groups have different properties compared to SNPs and OA-SNP leading to various cellular internalisation methods but this needs further study with more details based on the type of cells.

The incorporation of MNP inside the cells can follow two endocytic pathways depending on the size of the particle aggregates. The clathrin pathway is used by small particle aggregates, while the macropinocytosis pathway is used by large aggregates [210][213] [211]. So this could be the increase in cell uptake for SNPs in the data presented in section 5.2.1, this is attributed to large aggregation and a macropinocytosis mechanism to internalise these particles compared to the homogeneous distribution of magnetosomes in the clathrin-coated pathway.

Wilhelm has found the anionic iron oxide nanoparticles without surface coating have a high level of internalisation, by interacting actively and non-specifically with the plasma membrane [214]. This is consistent with our finding, where SNPs have a higher level of cell uptake compared to others, and this may be because of the non-specific uptake by the plasma membrane.

The incubation period was 24 hours based on the literature where MNPs appear to reach a saturation point in cells after 24 hours [210] [78]. TEM revealed that the magnetosomes, SNPs and OA-SNPs were located in intracellular vesicles which were likely lysosomes, but did not appear in the nucleus. Other processes have been proposed for iron oxide nanoparticle internalisation[215][212]. Pisanic *et al*. showed dimercaptosuccinic acid coated superparamagnetic iron oxide nanoparticles (DMSA) coated iron oxide nanoparticles are found either in the cytoplasm, inside the endosome, or accumulated in perinuclear regions within the cell [216]. However, the magnetosomes appear to reach closer than the synthetic particles to the nuclei [179]. The magnetosomes were still organised in chains, which may help them to be less prone to uncontrolled aggregation. Indeed several chains of magnetosomes appear inside the cell, shown clearly in Figure 5-6 a, b. The TEM also showed no obvious pathological changes after MNP uptake. There was, however, an increased number of vacuoles in cells after magnetosome uptake, which agrees with reports in the

literature [186], compared to SNP/OA-SNPs. The TEM indicates there are no MNPs bound at the cell surfaces. All weakly bound particles were removed by washing the cells before observation by TEM. Also, the magnetosomes distribution were distributed in a small stable chain, which is less likely to aggregate than other MNPs [186].
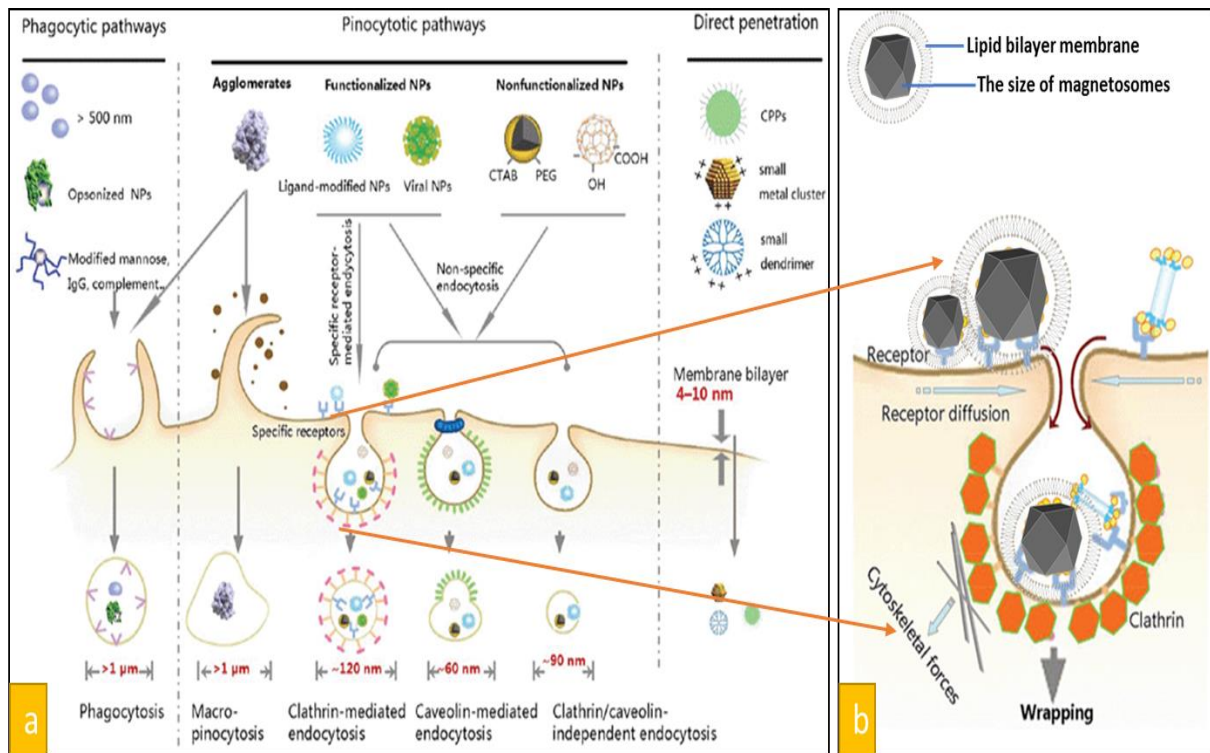
Figure 5-7: The cellular uptake of the particles is considered by the natural size, also the heterogenetic of particles surface requires multiple uptake pathways. Where the large particles can be taken by phagocytosis, the nonphagocytic mammalian cell internalizes the particles mainly through pinocytosis or direct penetration. While the particles with different modifications, may be taken up via specific 9receptor-mediated) endocytosis or nonspecific endocytosis reference [211].

5.4 Cytotoxicity

5.4.1 Cytotoxicity measurement using Propidium iodide (PI) staining

Propidium iodide (PI), used as DNA stain in flow cytometry. PI staining is based on the loss of the nuclear DNA content that has been damaged, where PI binds to double-stranded DNA and then evaluate the amount by flow cytometry. Where flow cytometry was used for the evaluation of cell death for the MNPs after 24 hours. Since it is crucial to choose the ideal concentration with low cell death for biomedical application such as hyperthermia and MRI later.

Death Cell of MDA-MB-231 with MNP
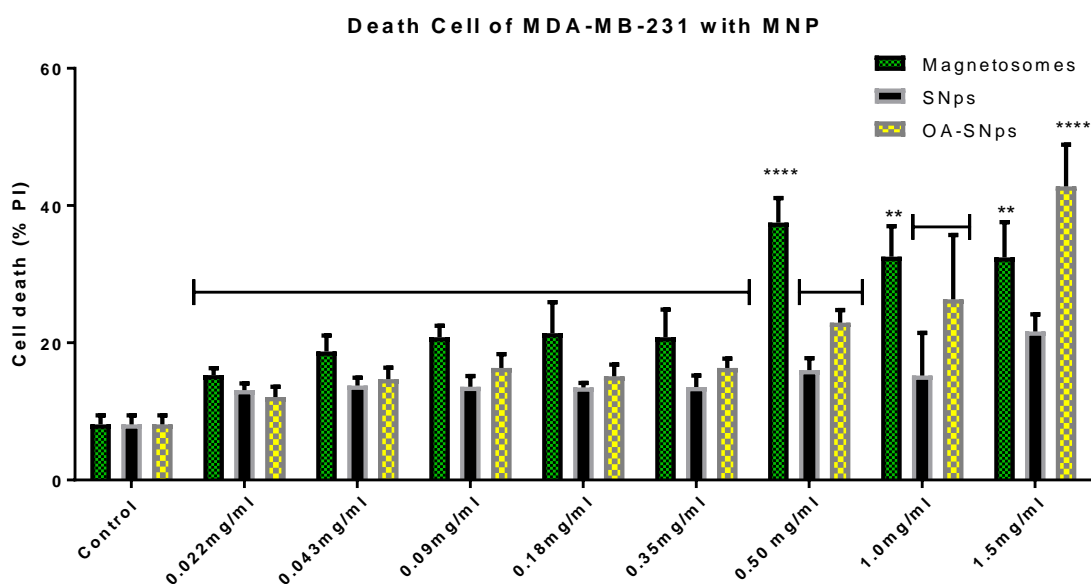
Figure 5-8: Cell death of magnetosomes SNPs, SNPs, OA-SNPs by MDA-MB-231 cells after 24hours at concentration test (from 0.022 to 1.5mg/ml) and ** and *** mean P< 0.0001.

The cell death results from the flow cytometry analysis for magnetosomes, SNPs and OA-SNPs at range concentration (from 0.022 to 1.5 mg/ml) shown in Figure 5-8. Magnetosomes show a significant increase in cell death at a concentration of 0.5 mg/ml, also at 1.0 mg/ml, and 1.5mg/ml compared to untreated cells (control). The OA-SNPs give rise to a highly significant increase in cell death at 1.5 mg/ml concentration with 45% of dead cells. At low concentration, up to 0.35 mg/ml, the cell death for all type of MNPs was the same with a slight increase in magnetosomes cell death up to 0.35, however at above 0.50 mg/ml the dead cell percentage significantly increases, giving more than 40% cell death. However, we begin to see the significant increase in the death cell of OA-SNPs only at 1.5 mg/ml. There is also an increase in cell death of SNPs, but this is not statistically significant.

The results of the quantitative analysis of MNP samples using flow cytometry showed that among the different concentrations tested (ranging from 0.022- 1.5 mg/ml), the ideal doses for internalization was 0.18 mg/ml for magnetosomes, 0.5 mg/ml for OA-SNPs and 1.5 mg/ml for SNPs, with high amount of cell uptake and low level of toxicity.

There are many studies that are interested in synthetic MNPs in biological applications, but there are no studies focused on the efficiency and biological application of doped magnetosomes with nonferrous metals. However, some previous studies are using the magnetosomes in cancer treatment, one of these studies by Alphandéry, where he found that the magnetosomes were not toxic at concentrations of 0.125 mg/ml when they were incubated with MDA-231 and Hela cell in agreement with this result [101] [179]. While no attempt to use nonferrous doped magnetosomes to address, or offer some alternative treatment or diagnostic, for cancer cells.
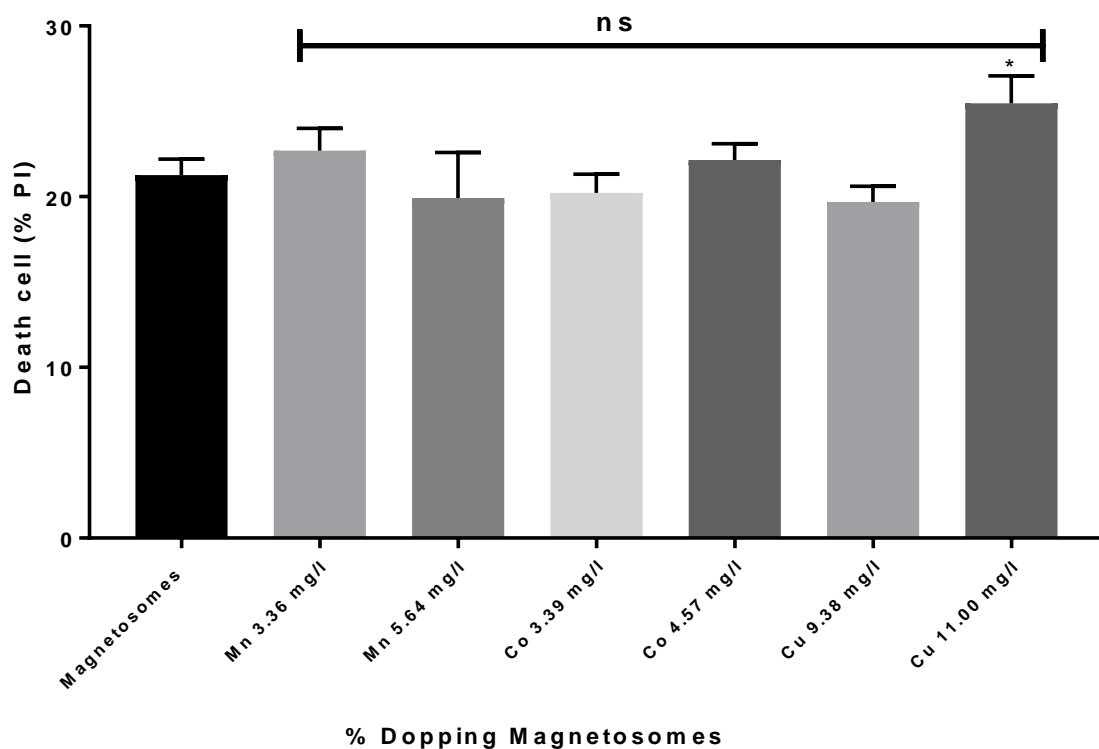
 Figure 5-9: The cell death of native and doping magnetosomes after 24hours incubation with MDA-MB-231 cells at concentration test (from 0.18mg/ml), significant (p<0.0001).

Furthermore, the effect on cell death was also investigated for doping magnetosomes. Figure 5-9 confirmed that there was no significant increase in cell death of doped magnetosomes compared to native magnetosomes. However, in the case of copper doping at 11% doping, there was a statistically small increase (9%) in cell death.

Findings in this research for the cytotoxic effects of the doped magnetosomes in Figure 5-9, suggest that Cu doped magnetosomes produce significant toxicity, with cell death increased by 20% to 27%. So far, the ferrous toxicity doping has not been investigated in other studies. One *in vivo* study has been reported showing high acute toxicity of copper nanoparticles (23.5 nm) when exposed orally to mice [217], and they concluded that the toxicity was due to an accumulation of Cu ions leading to metabolic alkalosis [218]. Another study showed that copper nanoparticles were capable of causing brain dysfunction in rats, especially in heat stressed animals [219]. A different study focused on cytotoxicity of different metal oxide particles (CuO, TiO_2, ZnO, $CuZnFe_2O_4$, Fe_3O_4, Fe_2O_3), incubated with the human lung epithelial cell line A549. The results showed that there was a high variation among different nanoparticles concerning their ability to cause toxic effects. The particles that included Cu nanoparticles were the most potent regarding cytotoxicity and DNA damage [219]. In agreement with this study, it highlights the *in vivo* toxicity of Cu nanoparticles. The reasons for toxicity of Cu could be the same reasons that cause cytotoxicity of Cu doped magnetosomes in this study which may have caused DNA damage. It was confirmed in the ICP results of Cu doped magnetosomes had the highest non-ferrous metal doping percentage (11.00%). Also we could explain that potentially there is a higher amount of copper ion on the magnetosomes membrane than is taken to the core, so when these particles have been taken by in cells, then this doping Cu has dispersed in the media and cause toxicity, or in another scenario that this copper could leach into the medium and this causes toxicity. While Mn-doped magnetosomes showed no significant cytotoxicity in this work, in agreement with a study on particles with the same element, were 12 nm MnMEIO (manganese magnetism-engineered iron oxide) nanoparticles, and MnMEIO-Herceptin conjugates with two different cell lines (Hela and HepG2), this study showed that both the nanoparticles and the conjugated nanoparticles were biologically nontoxic at the test concentration of $\approx$ 0.2 mg/ml [78] in agreement with my result with doped magnetosomes.

The most important finding in our study is the cytotoxicity of Cu doped magnetosomes, which agrees with other published accounts, that show copper containing nanoparticles are able to cause high cytotoxicity, DNA damage and oxidative lesions [219]. However, it is hard to draw a comparison of particles made of a different material which may behave differently *in vivo* and in *vitro*. The chemical composition of the MNP is one of the possible reasons for adverse

effects on cells. They may release toxic elements when interacting with cells. Finally, evidence suggests that MNPs have an influence on the cell functions after cell uptake, and thus requires more careful studying. Also, the different cell types may respond differently to the same MNPs, and this can cause a more complicated problem for researchers to compare and study.

5.4.2 The colourimetric assay MTT

The MTT assay, which quantifies cell viability and proliferation, was used to evaluate the cytotoxicity properties of magnetosomes, SNPs and OA-SNPs after 72 hours, the MTT can provide information for longer-term effects of MNPs on cells for applying MNPs for tumour therapy and another experiment *in vivo*.
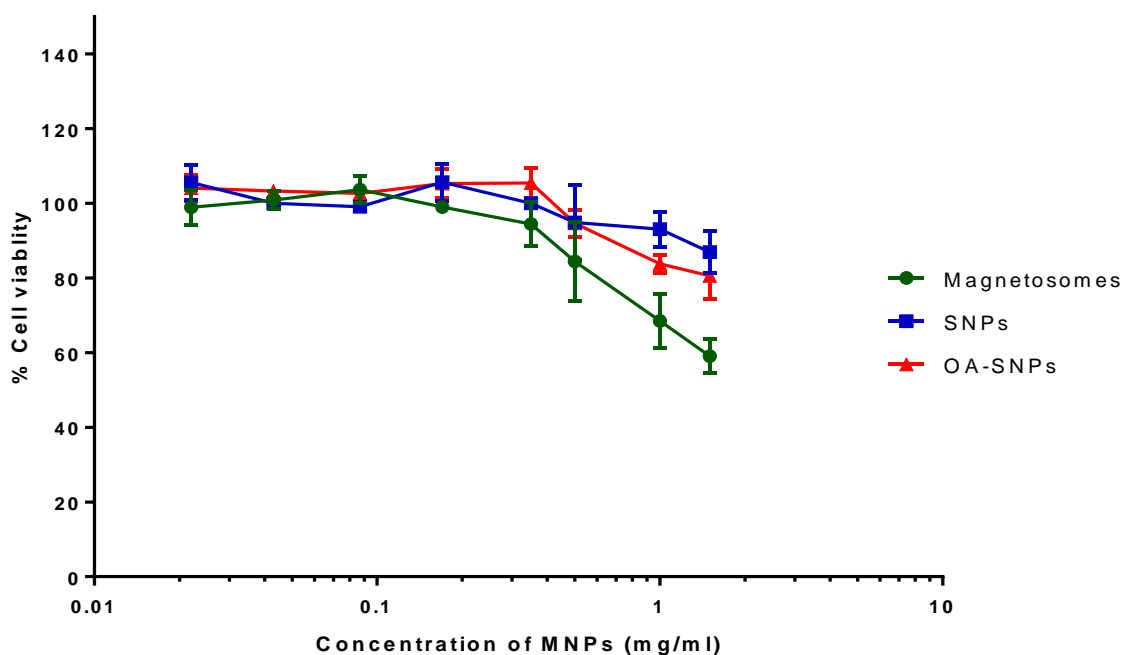
Figure 5-10 Cytotoxicity of magnetosomes, SNPs and OA-SNPs uptake by MDA-MB-231 cell line after 72 hours.

The cytotoxicity of magnetosomes, SNPs and OA-SNPs were evaluated by MTT impaired mitochondrial function assay after 72 hours' incubation. The MTT results shown in

Figure 5-10, reveal the cytotoxic effects of MNPs after 72 hours incubation time so after preparing the 6 well plates with 300,000 cells/well with a range concentration of MNPs (0.022, 0.043, 0.087, 0.17, 0.35, 0.5, 1, 1.5 mg/ml) as described in section 2.17. It is clear that

the cytotoxicity gradually increases with increasing dose. The toxicity starts to exhibit above 1.0 mg/ml for SNPs, while 0.5 mg/ml for OA-SNPs and 0.18 mg/ml for magnetosomes. Where at higher concentration (1.5 mg/ml) the cell viability was reduced by approximately 40%, 20% and 16% for the magnetosomes, OA-SNPs and SNPs respectively.

All together the data suggest that the magnetosomes incubated with MDA-231 cells induce cell death at concentrations above 0.18 mg/ml, while OA-SNPs and SNPs induce cell death above 0.5 and 1.0 mg/ml respectively, with cell viability 96% for magnetosomes, 94% for OA-SNPs, and 86% for SNPs. It seems that the cytotoxicity of magnetosomes, SNPs and OA-SNPs increase in relation to an increase in particle concentration. Several reports have studied bare and coated iron oxide nanoparticles with various sizes, different cell lines, and different exposure durations [220] [197] [210] [221] [78]. One study in particular used 30 nm dextran coated Fe_3O_4 for cytotoxicity measurement using MTT, showed that 1 mg/ml particles were not toxic after 72 hours, and 10 mg/ml mildly toxic [222]. The very low solubility of uncoated iron oxide nanoparticles can lead to precipitation and a high rate of agglomeration under physiological conditions, which could block the blood vessels in a clinical trial. Therefore it is not suitable to use in any clinical application unless their biocompatibility and biodistribution can be improved [223]. While the magnetosomes with intact membrane show more stability and better distribution within cells they also have a biocompatible membrane, but there is a higher level of toxicity that is produced from the magnetosomes that needs further study, therefore the Endotoxin assay carried out in next section.

The cytotoxicity of magnetosomes, SNPs and OA-SNPs were evaluated by MTT impaired mitochondrial function assay after 72 hours' incubation. The MTT results shown in the

Figure 5-10, reveal the cytotoxic effects of MNPs after 72 hours incubation time so after prepared the 6 well plates with 300,000 cells/well with range concentration of MNPs (0.022, 0.043, 0.087, 0.17, 0.35, 0.5, 1, 1.5 mg/ml) described in section 2.17. It is clear that the cytotoxicity gradually increases with increasing dose. The toxicity starts to exhibit above 1.0 mg/ml for SNPs, while 0.5 mg/ml for OA-SNPs and 0.18 mg/ml for magnetosomes. Where at higher concentration (1.5 mg/ml) the cell viability was reduced by approximately 40%, 20% and 16% for the magnetosomes, OA-SNPs and SNPs respectively.

All data together suggest that the magnetosomes incubated with MDA-231 cells induce cell death at magnetosome concentrations above 0.18 mg/ml, while OA-SNPs and SNPs induce cell death above 0.5 and 1.0 mg/ml respectively, with cell viability 96% for magnetosomes, 94% for OA-SNPs, and 86% for SNPs. It seems that the cytotoxicity of magnetosomes, SNPs and OA-SNPs increase in relation to increases in the concentration. Several reports have studied bare and coated iron oxide nanoparticles with various sizes, different cell lines, and different exposure durations [220] [197] [210] [221] [78]. One study in particular used 30 nm dextran coated Fe_3O_4 for cytotoxicity measurement using MTT, showed that 1 mg/ml particles were not toxic after 72 hours, and 10 mg/ml mildly toxic [222]. The very low solubility of uncoated iron oxide nanoparticles can lead to precipitation and a high rate of agglomeration under physiological conditions, which could block the blood vessels in a clinical trial. Therefore it is not suitable to use in any clinical application unless their biocompatibility and biodistribution can be improved [223]. While the magnetosomes with the membrane show more stability and well distribution in the cell also they have a biocompatible membrane, but there is toxicity that produced from the magnetosomes uptake that needs further study, therefore Endotoxin assay carried out in next section.

5.4.3 Endotoxin assay

MNPs for biomedical application must be controlled with specific characteristics and biodegradability of the magnetic core. The coating must avoid exposure and leaching of the magnetic core to the kidneys, and avoid the reticuloendothelial system (RES) and immune system [107]. The toxicity of MNPs, in general, depends on many key factors, such as; dose, chemical composition, size, biodegradability, solubility, and surface chemistry. The results of quantitative analysis of MNP samples using flow cytometry showed that among the different concentrations tested (ranging from 0.022- 1.5 mg/ml), the ideal doses for internalisation was 0.18 mg/ml for magnetosomes, 0.5 mg/ml for OA-SNPs and 1.5 mg/ml for SNPs. Testing for endotoxin contamination for these doses is mandatary in pharmaceutical production and is often required in life science and medical research. The cytotoxicity of magnetosomes, SNPs and OA-SNPs was also determined using LAL assay, at concentration 0.18 mg/ml, OA-SNPs at concentration 0.5 mg/ml and SNPs at concentration 1.5 mg/ml, where LAL assay used to detect the bacterial endotoxins by reacting with lipopolysaccharide (LPS) on the gram-negative bacteria membrane. Where SNPs showed the lowest concentration of endotoxin

with 0.055 EU/ml at 1.5 mg/ml, OA-SNPs were second with 0.16 EU/ml at 0.5 mg/ml concentration, and lastly the magnetosomes with 0.218 EU/ml at 0.18 mg/ml concentration (Figure 5-11).
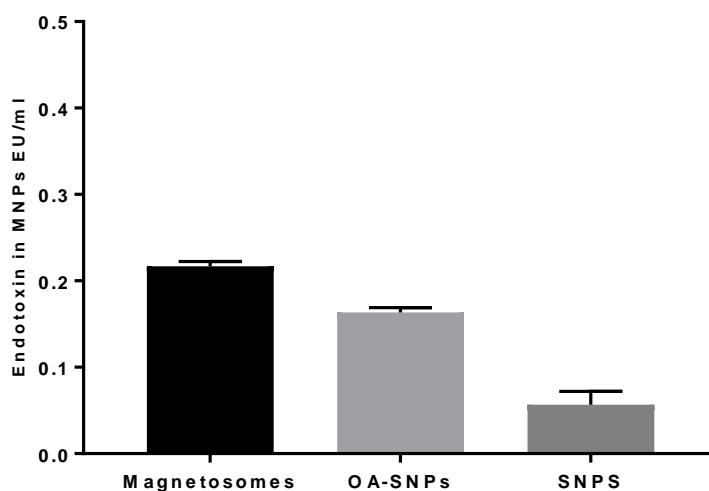
Figure 5-11: The endotoxin concentration for culture incubation concentration for the magnetosomes sample at concentration 0.18 mg/ml, OA-SNPs at concentration 0.5 mg/ml and SNPs at concentration 1.5 mg/ml.

The threshold of toxicity is 0.5 EU/mL which is defined as the threshold between pyrogenic and non-pyrogenic samples [108], while it is 0.4 ± 0.2 for according to the United States Pharmacopeia standards and the Food and Drug Administration mandated limits of acceptable endotoxin concentration spiked in water or various nanoparticles [224]. The toxicity of magnetosomes at 0.18 mg/ml was lower than the threshold of toxicity level but compared to other SNPs and OA-SNPs, it was still higher. The toxicity can give rise to a high level with high doses of up to 0.2 mg/ml. This is not likely to be due to iron ion toxicity in magnetosomes since Fe_3O_4 is relatively insoluble. Since the extraction of magnetosomes by sonication can be purified by washing eight to ten times with PBS buffer, during this cellular process debris is removed while the lipid bilayer membrane remains, as confirmed by TEM images and IR measurement in section 3.3.2. The magnetosomes have kept the biological material surrounding them after extraction from AMB-1, as the peaks at 1251 cm^{-1} and 1050 cm^{-1} can be attributed to absorption of phospholipids or lipopolysaccharide (LPS) [179] [225].

The results from the cytotoxicity assay agree with findings presented in the literature, where the high concentration of SNPs elicits cytotoxicity, while the magnetosomes show strong

cytotoxicity even at low concentrations. The MTT assay indicates no significant loss in cell viability except for magnetosomes at concentrations above 0.35 mg/ml. cell death measurements from flow cytometry were also used for validation, and it is confirmed via the MTT result, where the high concentration of magnetosomes produces significant cytotoxicity. The magnetosomes have another factor, which is the LPS the toxicity of magnetosomes might result from this is biological impurity. The nucleic acids, proteins and polysaccharides (LPS) that are potentially surrounding the magnetosomes could cause immunotoxicity, suggesting the presence of a pyrogenic effect on in *vivo* test.

Magnetosomes are suggested to be highly biocompatible because they are formed by bacterial cells rather than through artificial synthesis methods. However, this seems not to be the case as they are isolated from bacterial cells, and their membrane contains endotoxin [186]. The endotoxin associated with magnetosomes are most likely the cause of the toxicity, particularly proteins, nucleic acids and polysaccharides, that induce an immune response *in vivo* [186]. While the chemical toxicity of magnetosomes from iron ions is negligible since the iron is present within the magnetite nanocrystal. However, there were studies by Sun group [186] who administered a 1 mg suspension of magnetosomes into rabbits ears, then monitored the temperature of the body after this injection, finding that the temperature of the body did not increase. This result suggests there is no pyrogenic effect [186]. The researchers suggested that the magnetosomes may not be pyrogenic in some specific conditions, and concluded that it was unclear whether purified magnetosomes contained antigens or pyrogens [101].

A prior study by Sun *et al.* have used mouse fibroblast H22, HL60 and EMT-6 cells, which have been incubated with suspensions of magnetosomes at various concentrations, which were extracted from MSR-1, where the researchers have noted the 9 µg/ml of MSR-1 magnetosomes has no cytotoxic effect on H22, HL60 or EMT-6cell. Also, it has shown no obvious pathological changes in the histological tissue of major organs [186]. The results reveal that no cytotoxic effects were observed at concentrations below 1.3 mg/ml,[178] while in another study when the magnetosomes were extracted from AMB-1 and incubated with MDA-231 cells, the results showed there is no induced cell death at concentrations below 0.125 mg/ml, [177] [101] which agree with this results. A prior study by Han and his co-workers have shown the cell viability of magnetosomes (45 nm), which were extracted from

MSR-1, after incubating for 72 h with L929 cell line, the cell viability was reduced to just 90% at 1 mg/ml [168]. There are several possible explanations for this result. Firstly, the type of cell line (L929) was different from the MDA-231 used here so every cell line has a different defence system and different sensitivity. Secondly, the magnetosomes were extracted from MRS-1 are different from those that have been extracted from AMB-1 where It is seems that the cytotoxicity of magnetosomes depends strongly on the type of cell tested and incubation time [94], with fibroblasts and breast cancer cells, such as MDA-MB-231 and EMT6 cells there was no magnetosome toxicity at concentrations below 1 mg/ml. However, for H22 hepatoma cells (Leukemia cells), the toxicity of magnetosomes was only 9 µg/ml concentration, which is a much lower concentration [94]. Concentrations higher than 1 mg/ml of magnetosomes was found with lower cytotoxicity when incubated for 24 hours [94].

Several studies [226][223] report that exposure of cells to SPIONs is associated with significant toxic effects due to the generation of ROS, leading to cell death [226][223]. Conversely, dimercaptosuccinic acid coated superparamagnetic iron oxide nanoparticles (DMSA-coated magnetic nanoparticles) have shown little effect on cell viability with uptake concentration 0.05-0.4 mg/ml. This agrees with the results described here, which suggest that the coated synthetic nanoparticles (OA-SNPs) are less toxic at 0.5 mg/ml. It appears that MNPs with different sizes and different cell lines may give different levels of toxicity, compared to our finding where SNPs were not toxic at 1.5 mg/ml. Another study examined the effect of different surface coatings on cell behaviour and morphology and found that dextran-magnetite (Fe_3O_4) nanoparticles result in cell death and proliferation reducing, as the uncoated iron oxide particles did. The authors believed that the reason behind the cytotoxicity with dextran coating could be attributed to breakdown of the dextran shell exposing the cellular components to aggregates of these particles [227], which could be similar to OA-SNP that can be broken down to cause toxicity at concentrations higher than 0.5 mg/ml compares to uncoated SNP that was nontoxic at 1.5 mg/ml. However, a study by Mahmoudi *et al*. [228] about cytotoxicity of uncoated particles, showed that uncoated particles induce the greater toxicity on a mouse fibroblast cell line than biocompatible polyvinyl alcohol (PVA)-coated particles. The particle coating is clearly important for biomedical applications. The coating provides a barrier between the MNPs and the body to prevent leaching out of any toxic material components, however, this coating must be robust,

biocompatible, and nontoxic. The coating layer on MNPs also enables the attachment of any functional biomolecules. A study by Singh has shown that magnetite can cause high levels of oxidative DNA lesions in an A549 human lung epithelial cell line, and this cytotoxicity can be decreased by coating the magnetite particles resulting in fewer oxidative sites that are less reactive and thereby produce less DNA damage [223].

The potential cytotoxicity of several different types of MNP has been examined with a range of surface coating, and they have found low or no cytotoxicity associated with these MNP at specific concentrations. However, it is difficult to draw conclusions about MNP toxicity due to variable methods, materials and cell lines used. The size values vary between the different methods of SNP synthesis. It has been reported in many studies that the characteristics of the MNP such as charge, size, and surface modification play a significant role in biomedical applications and effects on cancer cells. Furthermore, there has been relatively little research on magnetosomes in such situations, especially from the AMB-1 species. Toxicity studies need to move to *in vivo* evaluation and doped magnetosomes and investigate their effect on cancer and multiple exposures.

Interestingly, a significant difference in cellular uptake depends on the magnetic nanoparticles and cell types, however, a high concentration of MNP for a long duration may cause cytotoxicity [210]. The difference in cell uptake and toxicity between magnetosomes, SNPs and OA-SNPs, may be attributed to an increase in aggregate size, where SNPs and OA-SNPs have the same size (37 nm and 40 nm respectively) with more probability of accumulation as shown in TEM images and confirm by ICP measurement. The magnetosomes with size 51.7 nm are internalised as stable chains compared to SNPs that exist as fewer aggregates and are internalised in small amounts, as confirmed by ICP. While another factor is LPS (endotoxin) where the toxicity of magnetosomes may result from magnetosomes membrane.

5.5 Modification of Uptake Conditions

5.5.1 Altering *in vitro* Cellular uptake with magnetic targeting

To see if the cell uptake of MNPs could be increased in the presence of an EMF, the magnetic sheet (bar of neodymium magnetic vertical put under 6 wells plate Figure 2-8) was used to drive the MNPs into cells Figure 5-12. Figure presents the cellular uptake of the different

amount (0.18 mg/ml of magnetosomes, 0.5 of OA-SNPs and 1.5 mg/ml of SNPs) as the ideal concentration for cell uptake with low cell death. In this experiment we have used the magnetic sheet that has been placed under a 6 well plate which was seeded with 300,000 cells/well for 24 hours and compared cell uptake and toxicity in the presence and absence of the magnetic sheet. The magnetic sheet placed below the culture plate as described in section 2.19. From this data, we can see that the magnetic sheet produces no statistically significant difference in cell uptake between the MNPs. However, there is an increase in cell uptake in all MNPs about 10% when the magnetic sheet is present (Figure 5-12). Furthermore, the presence of cell death results shows a slight increase in cell death in all MNPs in present the magnetic sheet but still no significant difference in cell death.
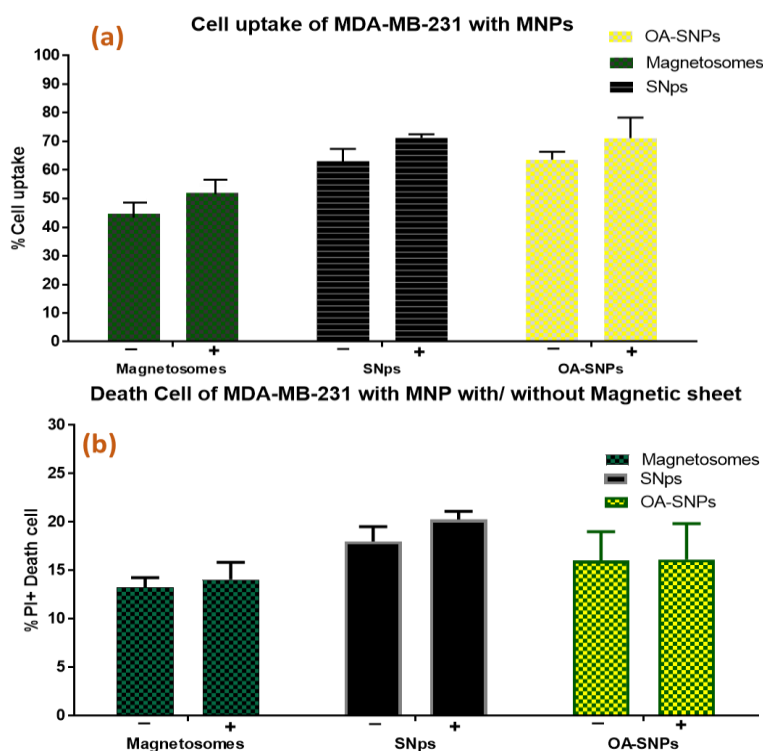
Figure 5-12: Cellular uptake and cell Death of magnetosomes by MDA-MB-231 cells after 24 hours incubation with 0.18 mg/ml of magnetosomes, 0.5 of OA-SNPs and 1.5 of SNPs with (+) and without (-) magnetic. a) the cell uptake of MDA-MB-231 with MNPs. b) The control has been subtracting.

The results of cellular uptake of MNPs with and without the magnetic sheet suggest that using the magnetic sheet, could help MNPs to penetrate more within the cancer cells. It was not

as much as we expect and this could be attributed to the one dimension of the plate compare if we have used three dimensions structure to represent the real body. It is obvious that the MNP will exhibit a magnetic interaction when placed near to the magnetic sheet if there is depth surface.

5.5.2 Cellular Uptake and Cell Death Of Magnetosomes By MDA-MB-231 Cells With And Without Magnetosome Membrane
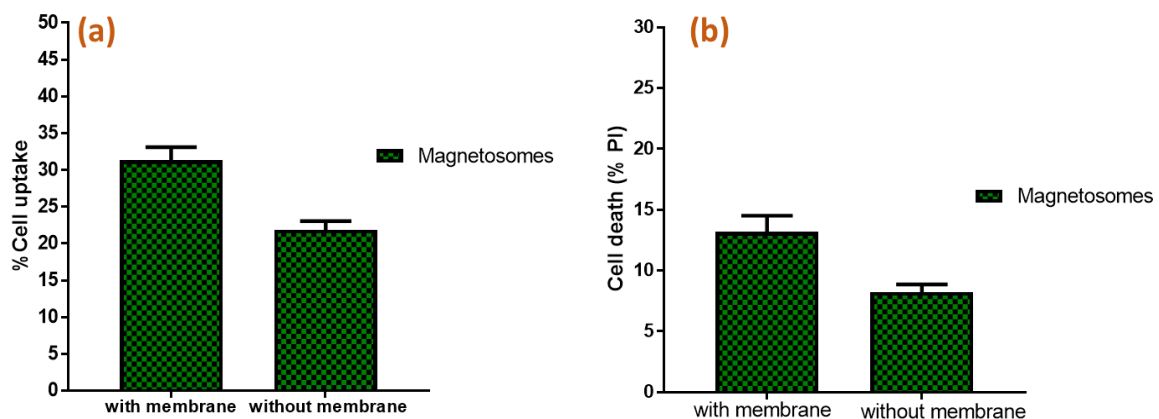
Figure 5-13: cellular uptake and cell death of the magnetosomes by MDA-231 cell line after 24 hours with and without the membrane at concentration test 0.18 mg/ml after subtracting the control from the data

Flow cytometry was also used to measure uptake and cell death for magnetosomes with and without the magnetosome membrane. When the magnetosome membrane has been removed with a lysis buffer then sonicated for 1 hour then washed several time with acetone, the percentage of the cell which have uptake particles decreases by 10% after subtracting the control cells. Likewise, the percentage of dead cells decreases by 5% shown in Figure 5-13 when the magnetosomes membrane has been removed.

The result of removing the magnetosomes membrane suggest that the magnetosomes poorly penetrate within the cells when they are naked in contrast to the magnetosomes with membrane, but what was interesting is that the cell death was low when compared to the magnetosomes with a membranepresent this confirms the endotoxin results which suggest the toxicity of the magnetosomes is possibly because of the membrane. We can explain this because the magnetosomes without membrane may be more aggregated and may have poor

164

efficient internalization and remain located outside of the cells. This is confirmed by another study [179] which has shown that individual magnetosomes (magnetosomes without membrane) remain outside of the cells compared to the chains of magnetosomes, suggesting the chain of magnetosomes with membrane penetrate more easily than without membrane within the cancer cells [179]. Figure 5-14 a,b where the schematic summary demonstration the different distributions of full magnetosomes and magnetosomes without membrane in an MDA-231 cancer cell is proposed. Where the chain of magnetosomes withmembrane has better internalization and more homogenous distribution than magnetosomes without membrane, and this could provide a reasonable explanation for higher uptake for magnetosomes with membrane, as also confirmed in Figure 5-13 and with Alphandéry, study [179]. Figure 5-14 c (which shown in orange circle), the chains of the magnetosomes with membrane inside the cancer cell without aggregation. This also agrees with E. Alphandéry study that has shown the magnetosomes with membrane penetrate more than individual magnetosomes that have detached from the chain by removing their membrane [177] [179].

We can conclude that the magnetosomes membrane is important for stable cell uptake and for the functionalization with bioactive substance, but to keep this membrane it require to remove the endotoxin on their membrane and this requires further study. Also using the magnetic sheet shows increased cell uptake that could be promising for future applications to use magnetic sheet outside the tumours to increase the percentage of cell uptake for treatment. The magnetosomes at 0.18 mg/ml was the preferable concentration for cell uptake with low toxicity, while 0.5 mg/ml for OA-SNPs and 1.5 mg/ml for SNPs.
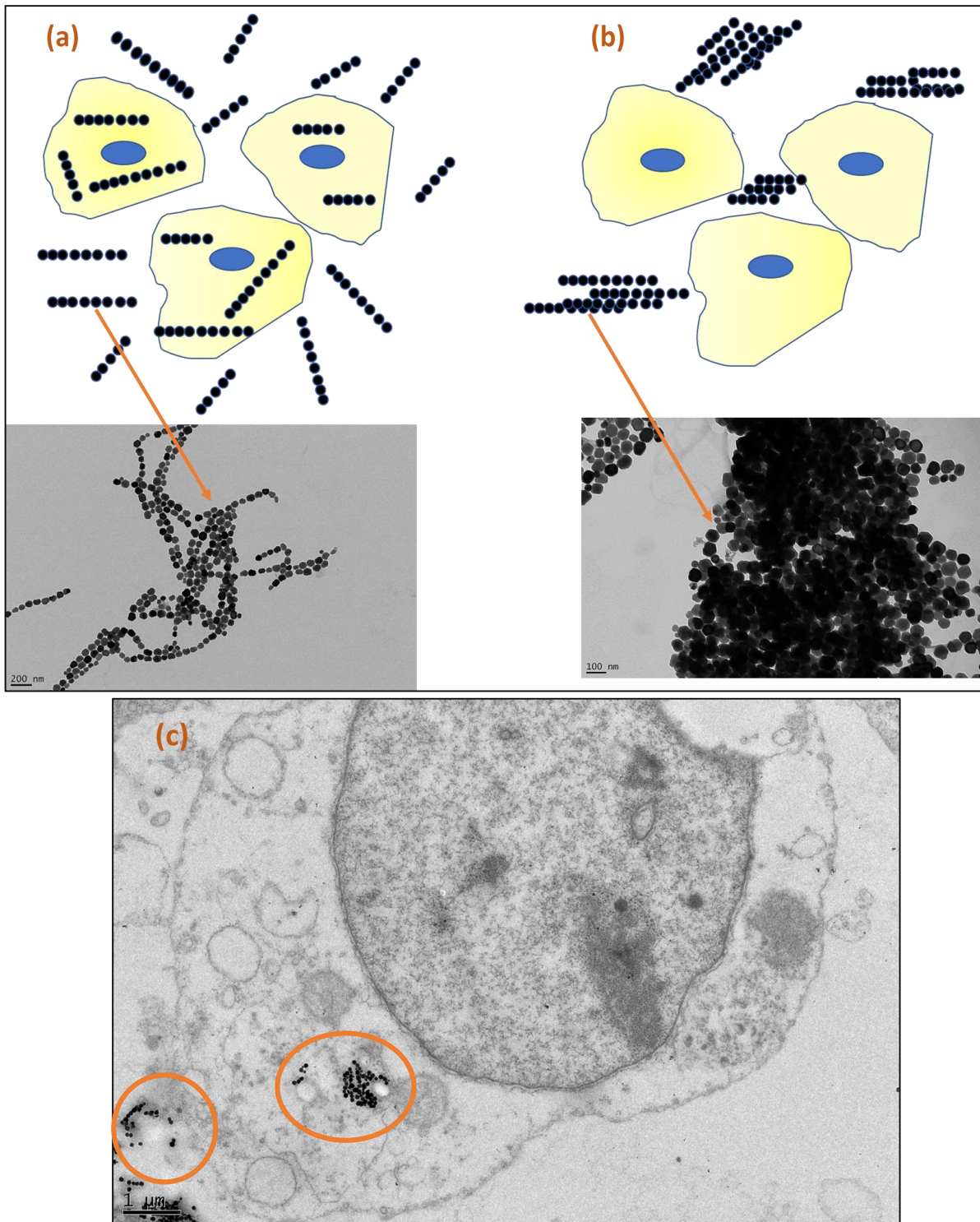
Figure 5-14: Effect of aggregation on the magnetosome spatial distribution and penetration within MDA-231 cancer cells. The magnetosomes are either with the membrane (a) or without membrane (b). (c) TEM for the stable chains in MDA-231 cancer cells with orange the circle.

Chapter 6:

Magnetosomes *in vitro* applications

6.1   Introduction of Magnetosomes in vitro application

Cancer is one of the most common causes of death, and most treatments for this disease are either administration therapy or injection; however, there is an increased risk of toxicity and some associated clinical complications. One factor that contributes to toxicity is nonspecific [203]. Also, another factor is the large dose required to achieve high local concentration, which could cause biodistribution of a drug through the body [203]. The use of MNPs in biomedical processes and biotechnology have dramatically increased. The MNP has the unique feature that it can be guided by EMF to target tissues and has been used in diagnosis as MRI, hyperthermia, and drug delivery [5]. Furthermore, the MNP enables localisation around or near to the area of interest, with low toxicity to other tissue[229]. In some situations, the MRI signal can be weak and gives an image with low sensitivity, particularly in the early stages of cancer. The magnetic properties of MNP reflect the efficiency of the contrast agent, by measuring the relaxivity [230].

MHT of a cancer cell can cause several death cells such as apoptosis and necrosis to emerge, depending on the exposure temperature [231] [203]. Apoptosis can cause a range of damage, including one of the variations in nuclear morphology such as chromatin condensation and fragmentation, cell shrinkage, and blebbing of the plasma membrane in cytoplasmic or nuclear responses materials with no inflammatory damage [232]. After the MHT at a therapeutic level (almost 42°C), the cellular responses demonstrated disrupted cytoskeleton and genomic fragment in the cells, leading to the death cell, and this could be the lunch indication apoptotic cell death after treating the cell with MNPs under an applied AC magnetic field. In contrast to apoptosis, necrosis, which causes inflammatory damage to surrounding cells, occurred as a result of a thermal injury that caused increased cell volume, and the swelling organelles led to the loss of intracellular contents. The apoptotic cell death exhibited directly at 42°C during MHT, while the necrotic cell death was at 52°C during MHT, where MHT was dependent upon the property of MNPs and type of cancerous tissue [232]. Hence, optimal therapeutic temperature is required to avoid overheating and for the effective induction of apoptosis.

In chapter 3, the magnetosomes were doped with non-ferrous metals (Mn, Co and Cu), in order to alter and potentially enhance the magnetic properties. Then in chapter 5, the cell uptake and toxicity of the magnetosomes were tested in preparation for *in vitro* and *in vivo* application. In this chapter, how the magnetosomes doping effects magnetic hyperthermia heating and contrast ability for cancer treatment and MRI diagnostics respectively is investigated.

In this study, the MRI signal was measured for the native and doping magnetosomes in an attempt to ascertain the relationship between changing the composition of MNP and the MRI contrast, as well as the effect on heating and enhance imaging by changing the magnetic properties such as hysteresis, coercivity and relaxivity. Doping magnetosomes with Co, Cu and Mn could have some advantages with MHT: such as general consistent heat because the magnetosome has a similar uniform shape and size. Also, changing the composition by incorporating M^{2+} into magnetosomes can affect the magnetic properties compared to undoped magnetosomes; this change implies that M^{2+} is incorporated into the magnetosomes' crystal structure by substituting Fe^{2+} ions.

The chapter 3 results confirmed that cobalt doped magnetosomes have the highest coercivity (292 Oe) compared to non-doped magnetosomes (125 Oe). Conversely, the concentration of doped magnetosomes for the applications in this chapter was chosen based on the highest percentage of doping with low toxicity: 50 µM of cobalt at 4.57% doping, 30 µM of copper at 9.38% doping, and 60 µM of manganese at 5.64% doping.

When the Fe^{2+} is replaced by M^{2+}= Mn, Co and Cu, the magnetic moment can change. The magnetic moment of these ions can be estimated as 5 µB, 3 µB and 1 µB respectively, as shown in the spin electron configuration in Table 6-1. Mn^{2+}-doped magnetosomes are expected to exhibit a higher saturation magnetisation than Co^{2+} or Cu^{2+} because it has a higher electron configuration. Therefore, it is expected that the M_s of Mn-doped magnetosomes will increase when EMF has been applied, and subsequently, the magnetic spin aligns parallel to EMF, which results in the high magnetic moment and high saturation magnetisation.

Table 6-1: The electron configuration and magnetic moment of Mn^{2+}, Co^{2+} and Cu^{2+}.

Metals	Electron configuration	Magnetic moment
Mn^{2+} d^5	↑ ↑ ↑ ↑ ↑	5µB
Co^{2+} d^7	↑↓ ↑↓ ↑ ↑ ↑	3µB
Cu^{2+} d^9	↑↓ ↑↓ ↑↓ ↑↓ ↑	1µB

6.2 In vitro Hyperthermia treatment

To date, there have been limited studies on the feasibility of inducing hyperthermia with magnetosomes as a cancer therapy [179][177][101], and there are no studies on doped magnetosomes (with Co^{2+}, Cu^{2+} and Mn^{2+}) with cancer cell for MRI and hyperthermia. In this chapter, the focus has been on the treatment consisting of delivering native and doping magnetosomes where the absorbent energy by magnetosomes under EMF would convert into heating *in vivo* [1]. The heat capacity of a tumour depends on its type, size, shape, stage and hardness, so these factors may cause challenges for delivering optimal thermal energy [232]. Consequently, local heating (40-45°C) on cancer cells during the hyperthermia treatment causes cellular death via apoptosis [232]. Conversely, local heating under higher temperatures (52°C or above) can weaken both normal and cancer cells or directly kill them via necrosis, and during the heating process this necrosis can cause chronic inflammation [232]. Therefore, it is crucial to ensure consistent heating, with an appropriate dose of nanoparticles to be under apoptosis process, with low toxicity.
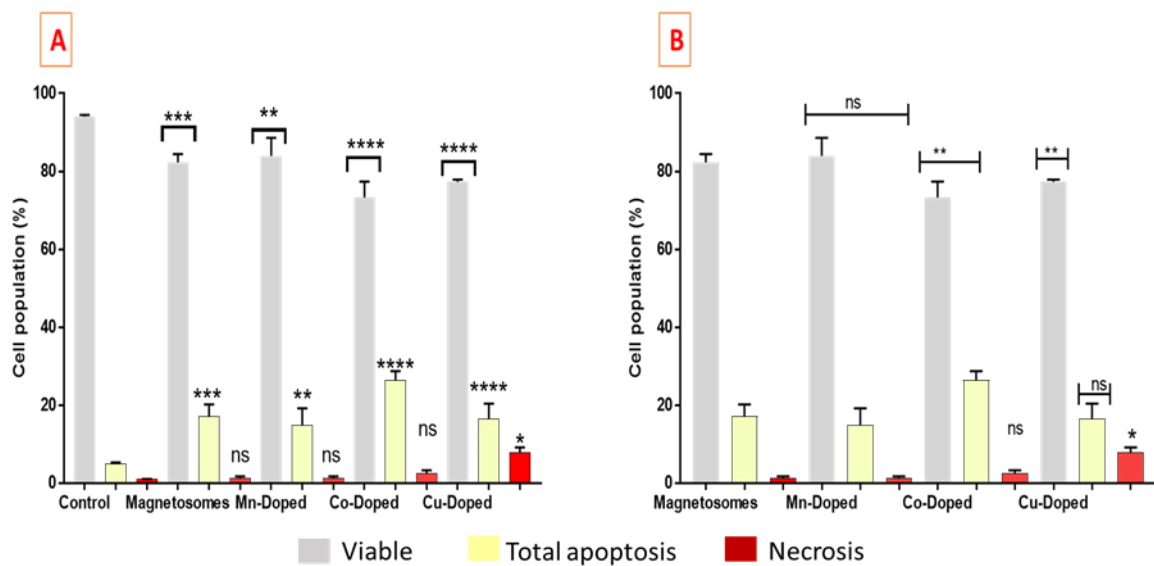
Figure 6-1 Quantitative analysis of percentage of cell viability, necrosis, total apoptosis (early and late). Mean (p< 0.004) *** mean (p< 0.0004 and ****mean (p< 0.0001) and with 0.18 mg/ml magnetosomes and incubation time of 24 hours. 60 µM of cobalt at 4.57% doping, 30 of µM copper at 9.38% doping, and 50 µM of manganese at 5.64% doping. Graph A compares the control (untreated cells) with native and doped magnetosomes cells. Graph B compares native magnetosomes (treated cell) with doped magnetosomes cells.

To investigate the hyperthermia effect on breast cancer cell MDA-231 *in vitro*, the native and doping magnetosomes Co, Cu and Mn (0.18mg/ml) were seeded in a 35mm petri dish containing the MDA-231 cell for a period of 24 hours. Following this, the MF was applied for 20 minutes to enhance these particles so as to generate heating with magnetic field frequency of 174 KHz and magnetic field amplitude of 9.7 mT. Next, 24 hours after the heating treatment, the cell viability, total apoptosis and necrosis were measured. Figure 6-1 demonstrated flow cytometric analysis on apoptosis and necrosis MDA-231 cells and the cell viability. Annexin V-FITC was used to examine cellular death due to apoptosis and necrosis, and PI (Propidium iodide) solution was applied to detect the late apoptosis or necrosis cells by permeating the membrane of the damaged and dead cells. Figure 6-1 A, illustrated a comparison of the quantitative analysis on the viable, total apoptosis and necrosis cell population at different cancer treatment conditions. The control represented MDA-MD-231 cell untreated without magnetosomes and showed no change in the cell viability (95%) after MHT. In the case of native and Mn-doped magnetosomes, the cell viability was found to be slightly lower with 82.3% and 84% cell viability respectively in comparison with the control. Additionally, the Co and Cu magnetosomes showed a significant decrease in cell viability

(73.3% and 77.3%) respectively. The results were shown to decrease cell viability via total apoptosis of Co, Cu doped magnetosomes at a concentration. An interesting point is that the necrosis effect of native, Mn-doped magnetosomes and Co-doped magnetosomes were non-significant compared to an untreated control cell (1.8%, 1.5% and 2.4% respectively). Only Cu shows a significant effect (7.5%), which may be attributed to its toxicity rather than MHT, where necrosis is also described as a consequence of physical-chemical stress [20]. Necrosis can lead to local inflammation due to the emergence of intracellular factors from the dead cell. All magnetosomes demonstrated a substantial impact on cell viability (73.3% Co, 77.3% Cu, 84% Mn, and 82.3% native) compared to the untreated control cell. Furthermore, a significant change in total apoptosis between native and doping magnetosomes Mn, Co, and Cu compared to the control (14.3%, 26.4%, 16.1% and 16.6%) was identified.

Figure 6-1 (B) showed flow cytometry analysis on apoptosis and necrosis MDA-231 cells and the cell viability of magnetosomes, Co, Cu and Mn-doped compared with the control that represents MDA-MD-231 treated with native magnetosomes. There was a significant change in the cell viability of the control MDA-231 treated with native magnetosomes compare to the Co and Cu doped magnetosomes, which exhibited a significant decrease in cell viability (73.3% and 77.3%) respectively. In contrast, the Mn-doped magnetosomes shown a non-significant change in cell viability (84.3%). Total apoptosis and necrosis of MDA-231 treated with Mn doped magnetosomes exhibited an insignificant change in total apoptosis and necrosis. However, as expected, only the Co-doped cell showed a significant increase in total apoptosis (26.42%). Again the necrosis effect can be seen as significant with just the Cu-doped magnetosomes. The average cell viability of the magnetosomes and doping magnetosomes in the same experiment without undergoing hyperthermia treatment showed the same level of viability, between 88% and 90%, and the total apoptosis average was between 10% and 12%, which is lower than treated cells.

Good dispersion of magnetosome in media and inside the cell is critical to provide uniform distribution of heating, which is necessary to prevent any local hot spots when targeting a tumour. The efficacy of treatment of the magnetosomes was mentioned in literature for two reasons. Firstly, the chain of the magnetosomes was reported to appear to have homogenous distribution within a tumour without aggregation. Secondly, the existing lipid membrane surrounding the magnetic core prevented aggregation, resulting in its low level [180] [93],

[94]. This has been confirmed by TEM, which demonstrated that the majority of the magnetosomes inside the cell presented as the chain in the cytoplasm (section 5.3.2). Furthermore, the colloidal stability result (-43.37± 1.52 mV) confirmed the stable dispersion in media of the magnetosomes.

It was reported by Tang *et al.* that magnetosomes of 10 mg/ml in MCF-7 cells could inhibit 80% of the cell proliferation when exposed to AMF (300KHz) until the temperature reached 47°C [229]. In different a study, Alphandèry *et al.* used MDA-231 breast cancer cells and Hela cells incubated with 0.125 mg/ml of magnetosomes chains (AMB-1) which were then exposed to AMF of 20mT for 20 minutes. The tumour temperature reached 43°C, and up to 20% of the cells were destroyed. The authors explained that this was due to the chain arrangement of the magnetosomes, which gives a homogenous temperature distribution within the tumour tissue [177]. This agrees with the findings in this chapter where magnetosomes showed 14.3% in dead cells after heating. However, Co-doped magnetosomes in this study showed a rate of 26.4% of cell death from apoptosis compared to native magnetosomes at the same dosage. This seems to indicate cobalt doping produces more heating that can kill the cancer cells at low magnetic field strength 9mT compared to 20mT in the Alphandèry study, which was higher than this study. However, in both the Tang and Alphandèry studies, MTT assay was employed to measure the percentage of cell death. In this chapter flow cytometric analysis using Annexin V was used which allows the percentage of all cells that died due to apoptosis and necrosis to be determined.

Co-doped magnetosomes displays high thermal energy transfer capability compared to other doped magnetosomes, so they should be considered as efficient magnetic hyperthermia agents. Where $Co_xFe_{3-x}O_4$ doped magnetosomes under the EMF convert the applied magnetics into thermal energy, it can kill the cancer cell by elevating their temperature compared to native magnetosomes. This confirms that the high of the cobalt anisotropy and the high coercivity, that has losses, converted into heat in the hyperthermia treatment, which agrees with the existing literature [185]. In comparison to conventional chemotherapy and radiotherapy, the MHT specialised with localised thermal energy to the area of interest is associated with reducing several side effects on normal cells [232].

Both results that compared the untreated cells and the cells treated with magnetosomes and doped magnetosomes indicated that the cellular death after MHT was primarily due to apoptosis. Because the tumour cells have a compact vascular and disorganised structure, they have difficulty in dissipating heat [203]. Therefore, the hyperthermia may cause the cancer cell to undergo apoptosis in direct response to applied heat. In contrast, the necrosis was determined to be rarely responsible for the cellular death. Results of local heating that had been produced by these doped magnetosomes showed that the MHT setting with 0.18 mg/ml magnetosomes generate heat that induces apoptotic death cell.

6.3   The magnetization of doped magnetosomes for *in vitro* applications

One of the most desired properties of MNP is the magnetic properties, and this can impact size, composition and shell core. The goal of this research was to optimise the magnetisation by changing the composition of magnetosomes, through the use of Co, Cu, and Mn as doping metals for the magnetosomes (Fe_3O_4).
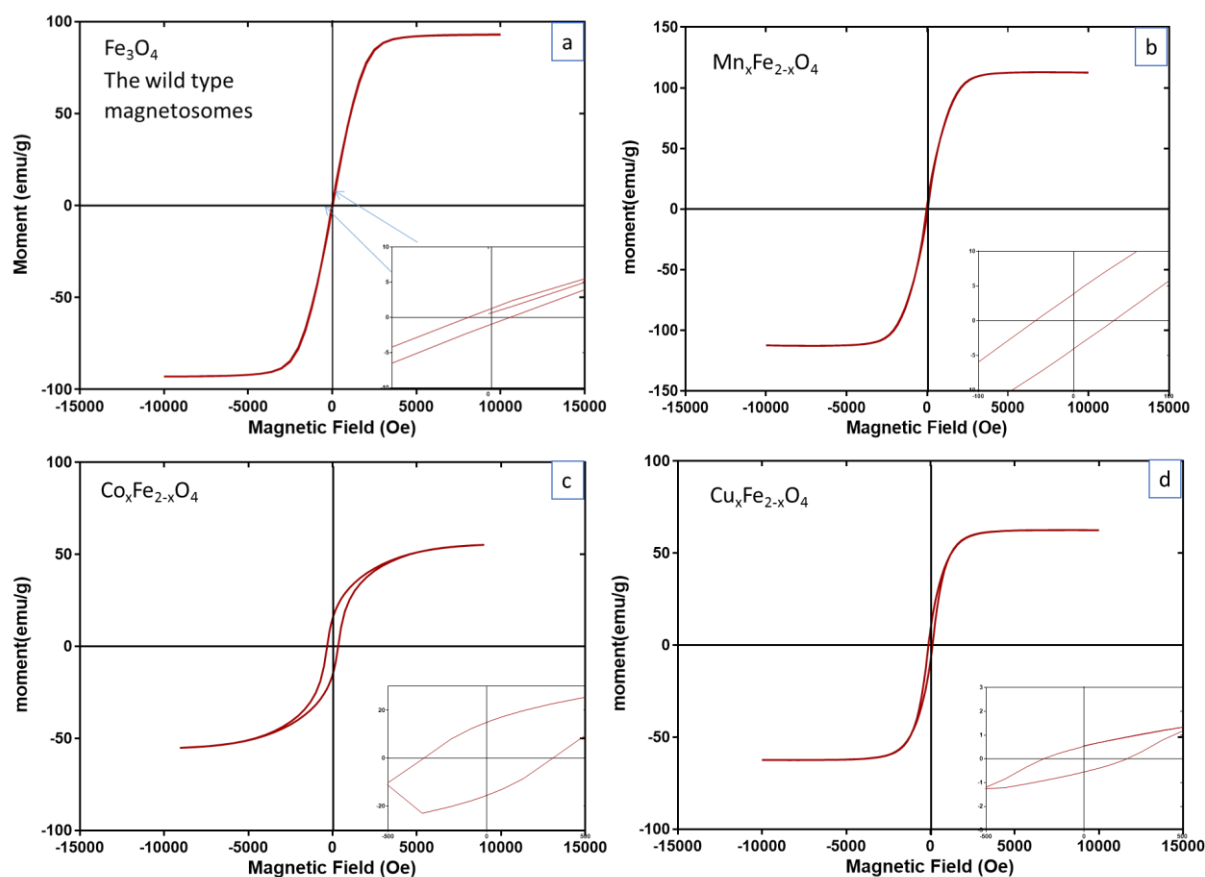
Figure 6-2: Superconducting Quantum Interference Device (SQUID) analysis of magnetosomes. The hysteresis loops recorded at T=300K. a) -Fe_3O_4 wild-type magnetosomes, b)-$Mn_xFe_{2-x}O_4$ doped at 50 µM , c) -$Co_xFe_{3-x}O_4$ doped at 60 µM , and d) - $Cu_xFe_{2-x}O_4$ doped at 30 µM.

The preferable nanoparticles would provide higher sensitivity and efficiency, which means signifies that MNPs have higher saturation magnetisation for MRI, and higher coercivity for hyperthermia [18]. The heating of the magnetosomes results in hysteresis losses during the reversal of magnetization, and relaxation losses accompanying the demagnetization, hence hysteresis of the magnetization curve is irreversible and the energy of MF is dissipated into the medium with flux reversal cycle in the form of heat [233], which is a result of absorbing energy from AMF and converting it into heat.

The magnetization curve for biosynthesis doped magnetosomes are present in Figure 6-2 where the magnetosomes was doped (50 µM of Mn, 60 µM of Cobalt and 30 µM of copper), which indicates that the doped magnetosomes rapidly approach a saturation magnetization of 112.6, 56.4 and 63.0 emu/g for Mn, Co and Cu respectively, which is higher than other fabrication synthesis nanoparticles [78] [187] [13]. The Mn-doped magnetosomes have demonstrated the highest saturation compared to the bulk value of 90 emu/g of Fe [234].

This value is much higher than that of corresponding bulk, and this may because, as explained earlier in this section, Mn has the highest magnetic moment.

The coercivity of the doped magnetosomes in M-H curves (Figure 6-2) shows an open hysteresis loop at room temperature with coercive filed 133, 420 and 236 Oe for Mn, Co and Cu respectively. The saturation magnetisation (M_s), coercivity (H_c) and size of doped magnetosomes are presented in Table 6-2.

Table 6-2: Summary of the size and the magnetic properties of doped and non-doped magnetosomes.

Magnetization for the doped magnetosomes	The mean of particles size on TEM d(nm)	M_s (emug^{-1})	H_c (Oe)	% doping
Fe_3O_4	51.70 ± 11.95	92.99	125	
$Mn_xFe_{2-x}O_4$	81.86 ± 11.23	112.6	133	5.64
$Co_xFe_{2-x}O_4$	55.33 ± 17.75	56.4	420	4.57
$Cu_xFe_{2-x}O_4$	78.71 ± 27.30	63.0	236	9.38

The Co-doped shows the highest coercivity compared to native and other doped magnetosomes, with a minor decrease in saturation magnetisation, which is in accordance with the existing literature [183]. Also confirmed by the study is that precise doping, through which the valence, site occupancy and content of cobalt in the spinel structure of magnetite can be regulated, is crucial for producing promising MNPs with precisely controlled magnetic properties [166]. Furthermore, it has been reported that magnetosomes extracted from Geobacter sulfurreducens doped with a various range of Cobalt, show an overall increase in coercivity with increased cobalt doping concentration and with a minor decrease in saturation magnetisation at room temperature [183].

The native and all of the doped magnetosomes have the same cubic nanoparticles shape and well packed crystalline form, and excellent colloidal stability, and are well dispersed in media. All of this could provide a uniform distribution of heating, but the composition of the magnetosomes are different, since the viscosity of the surrounding environment and magnetic properties are affected by the amount of heat dispersal from relaxation loss. Thus, cobalt doped magnetosomes have demonstrated high heat which proves that when the cobalt replaces ferrous in magnetosomes, it can increase the effectiveness of hyperthermia. This agrees with our finding *in vivo* magnetic hyperthermia treatment with a cancer cell (section 6.2.). Some studies have shown that the coercivity of the specific magnetisation of cobalt doped iron oxide nanoparticles is high due to the anisotropy, and crystalline by cobalt substitutions compare to Fe_3O_4 [13][183]. The magnetic anisotropy of cobalt doped magnetosomes has been studied by other researchers, and the Co-doped was found to have the highest anisotropy in doped magnetosomes [24][166]. This result indicates strongly that doped magnetosomes have different unique magnetic properties according to increasing the concentration of cobalt ions in the growing medium. This is evidence that the presence of cobalt in magnetosomes can increase the anisotropy magnetocrystalline, magnetic hysteresis, which will consequently raise the heating efficiency, which is also in accordance with the existing literature [24] [166]. Cobalt ferrite is a hard magnetic material with an inverse spinel structure, with large coercivity and high magnetic anisotropy [13]. In a comparison study with the SNPs of cobalt ferrite, the magnetic moment relaxes much slower than magnetite, so cobalt ferrite crystalline anisotropy is greater than that of magnetite [13][235]. This agrees with our finding, where the cobalt doped magnetosomes could be used for many medical applications, particularly hyperthermia therapy.

Consistent with previous studies, the cobalt can be exclusively incorporated into the spinel structure of magnetosomes magnetite at the Oh sites as cobalt, which significantly increases the coercivity [166] [24]. Incorporation of Co^{2+} can tune magnetic properties and the chemical of magnetosomes into Oh sites of magnetite through the replacement of Fe^{2+} ions. The controlled doping of magnetosomes in Oh sites through the replacement of ferrous ion magnetite resulted in a pronounced increase in magnetocrystalline anisotropy and magnetic coercivity, which has been confirmed by other authors [166] [24]. Additionally, it has been

177

determined that magnetosomes containing cobalt could be produced by three strains of *Magnetospirillum,* and the coercivity was 36-45% higher than not doping MTB [24].

6.4   *In vitro* magnetic resonance imaging
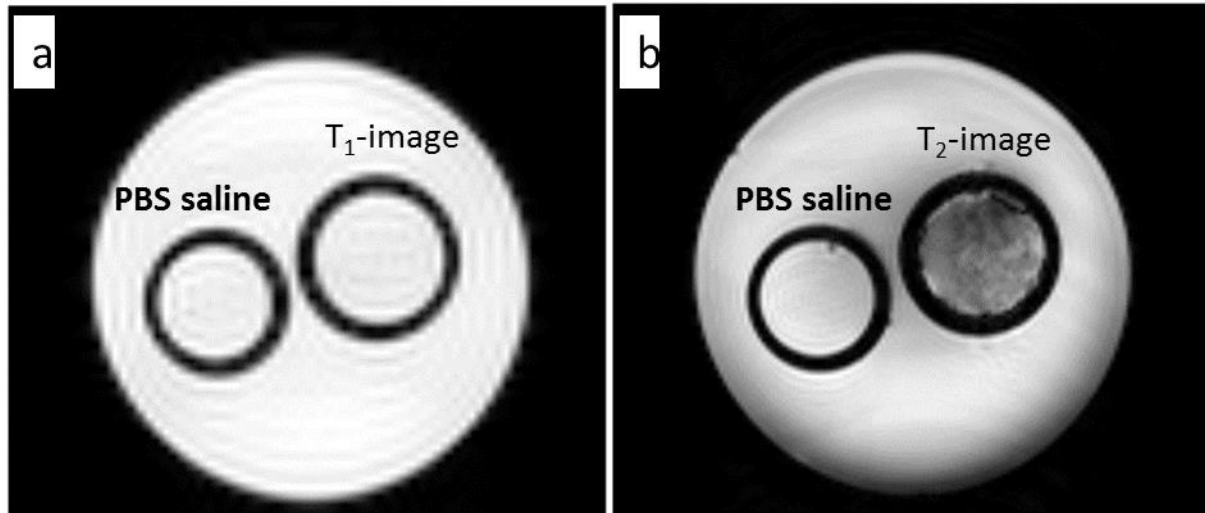
Figure 6-3: T-weighted MRI, of the PBS saline sample and the magnetosomes sample
a) the T_1-weight image where the first ring represents the Eppendorf tube that was filled with PBS and the second was filled with magnetosomes suspended in PBS and b) T_2-weight image, where the first ring represents the Eppendorf tube that was filled with PBS and the second was filled with magnetosomes suspended in PBS.

Various contrasting agents has been proposed and employed to differentiate the healthy and pathologic tissue. Since magnetosomes and magnetic nanoparticles can generally be used as T_2-weight MRI imaging contrast agents due to their magnetic properties [236][237][192], they could be enhanced to develop an MRI contrast agent for a stronger signal with smaller amounts of MNP. The effectiveness of native and doping magnetosomes was tested in this study to be used as a targeting contrast agent. The contrast enhancement ability of the doped magnetosome samples was measured *in vitro* in an MRI experiment. 1ml Eppendorf tubes were prepared to contain a suspension of native magnetosomes, Co-doped magnetosomes, Cu-doped magnetosomes and Mn-doped magnetosomes, all at a range of concentrations in PBS saline. A saline control sample was also tested to reflect the physiological conditions and to prevent sedimentation. An initial concentration of ~ 0.05mg/ml was placed inside a 50 ml tube of saline, and this was placed at the iso-center of a 7 Tesla magnet. In Figure 6-3 (a) the control saline sample and the magnetosome sample showed no contrast in T_1-weighted

image, while in Figure 6-3 (b), the T_2-weighted image shows the difference in contrast compared to saline. The results confirm that the magnetosomes can be used as a T_2 contrast agent for MRI, with the magnetosomes capable of acting as a negative contrast agent.
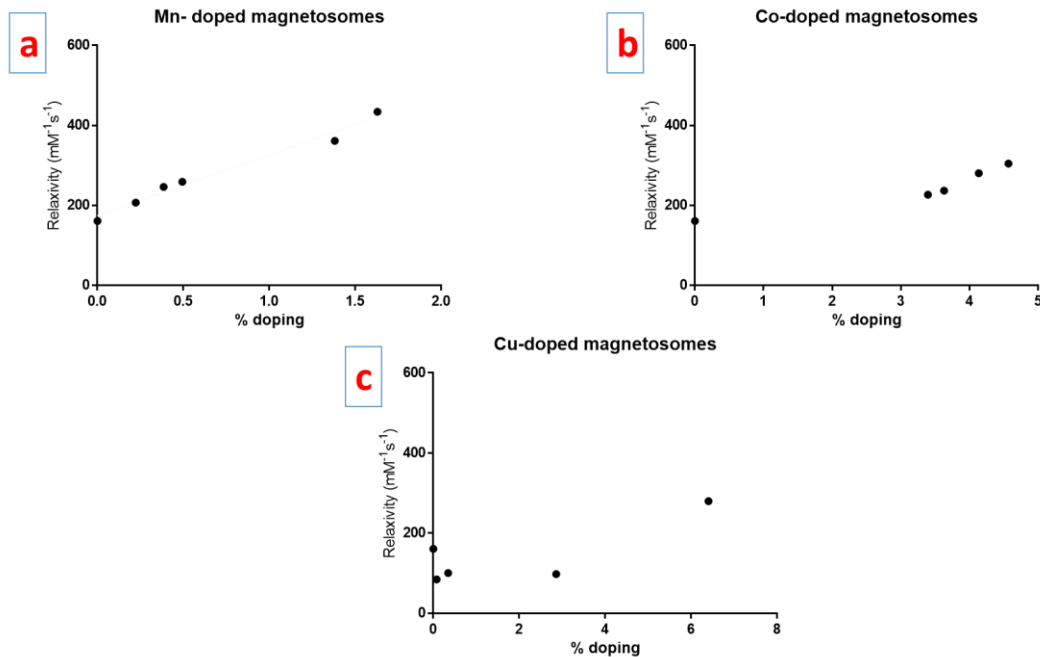
Figure 6-4: the relaxivity (T_2) of magnetosomes doped by a) manganese, b) cobalt and c) copper at different % doping.

Changes in the magnetisation of the proton in water molecules were measured by MRI, where the H^+ of water molecules in a magnetic field was pulsed by a radio frequency [204] and the relaxation back to ground state was visualised. Since tissue reacts differently, that gave a picture of the anatomical structure [204]. Moreover, the images can be optimised by adding a contrast agent that increases this contrast, by enhancing the behaviours of the proton. The relaxation time of the proton can vary, and is commonly measured as T_2 relaxation (transverse), which is dark [238], meaning that the T_2-weight imaging is ideal for picking up tissue, where matter is a darker contrast in T_2, providing different intensities of images. Conversely, fat, H_2O, and fluid are bright in the scan.

The T_2 relaxivity data for the native and doped magnetosomes is presented in Figure 6-4, where the T_2 relaxivity for Mn-doped data for various dopant concentrations of Mn, Co and Cu are also shown. From these curves in Figure 6-4 a, b and c, it is clear that there is continual

growth of relaxivity as the percentage of doping Mn, Co and Cu magnetosomes is increased. Interestingly, in Figure 6-4 a the highest rate of relaxivity of Mn-doped magnetosomes is at lowest level of doped (1.6%) compared to Co (4.5%) and Cu (6.4%) doped magnetosomes.

Mn doping enhances the T_2 relaxation with the presence of Mn-doped compared to native magnetosomes, where the native magnetosomes show 261 $mM^{-1}S^{-1}$, while Mn-doped shows a high increase in T_2 relaxation at 1.6% doping (434 $mM^{-1}S^{-1}$). Furthermore, there is evidently a correlation between the presence of Mn-doped and T_2relaxivity, as the greater the concentration, the more relaxivity. This seems comparable to the native magnetosomes, in that increasing the small amount of Mn within the magnetosomes has positive effects on the contrast in the MRI, and this has also been confirmed by the magnetisation measurement, where Mn has the highest saturation magnetisation of 112 $emug^{-1}$ compared to native magnetosomes and other doped magnetosomes.

Although copper doped magnetosomes have a low saturation magnetisation of 63 $emug^{1}$, they continue to demonstrate high relaxivity. This could be attributed to the size of the Cu-doped magnetosomes, which show a reduced size at high levels of doping. These small particles have a larger surface, which could provide more contact to the surrounding proteins. There may consequently be an increase in the relaxivity.

Figure 6-4 b, for Co-doped, also shows an increase in T_2 relaxation, (304 $mM^{-1}S^{-1}$) at 4.5% of doping compared to native magnetosomes. However, the Cu shows a slight increase in T_2 relaxation (280 $mM^{-1}S^{-1}$) at 6.4% doped, so the Mn-doped magnetosomes have enhanced the contrast to a greater degree than other metal doped. Comparing the percentage of doped with the relaxivity shows that even Mn has a small amount of doping (1.6%) compare to Co and Cu, but it has the highest relaxivity. Therefore, if we could increase the amount of Mn-doped that has been taken by MTB, this could help to improve the relaxivity.

$MnFe_2O_4$ nanoparticles have been reported as an MRI contrast agent [192] because of their strong T_2 phase contrast. Brazel *et al.* measured T_2 relaxation for SNPs ($MnFe_2O_4$ and $CoFe_2O_4$ were 392.5 and 255.9 $mM^{-1}S^{-1}$respectively at 9.4 T) [192]. This results in this study are in accordance with the literature, where the $MnFe_2O_4$ structure does not have inverse electrons, but does have excellent properties such as high saturation magnetisation [13], as when EMF has been applied, the magnetic spin of the non-inverse electrons will be parallel to EMF, which

results in the high magnetic moment and high saturation magnetisation, thereby likely increasing the Ms of Mn-doped magnetosomes.

It has been reported that the composition of the MNP is key for tuning the MRI contrast effects because it is responsible for tuning the magnetisation of nanoparticles by introducing other transition metals [75]. Lee *et al.* [78] reported that the ferrite nanoparticle with Ni, Co, Mn (MFe_2O_4, M=Ni, Co, Fe and Mn) can affect the magnetisation and relaxivity values, where Mn with Ms 110 emug-1 has the highest value of relaxivity at 358 $mM^{-1}S^{-1}$, providing a highly sensitive MRI [78]. It is difficult to compare particles made of different materials with doped magnetosomes, which may behave differently *in vivo* or *in vitro*. However, biological nanoparticles with very low levels of doping do produce high levels of relaxivity. Therefore, if this could be increased through genetic modification, it may be possible to generate a highly sensitive contrast reagent.

The only study that used the MTB as contrast agent has done by Felfoul and his group, where they have used bacteria cell of MC-1 as contrast agent in MRI, it has magnetosomes size between 30-80 as negative contrast T_2 agent create signal as dark area in MRI image and the T_2 measurement was 203 $mM^{-1}S^{-1}$ compare with 161 $mM^{-1}S^{-1}$ in this result [239].

So these results confirm that T_2-weighted images show increased negative contrast gradually with increasing concentration special it was the highest with manganese doped, in agreement with the literature [192], also due to that Mn has large number of unpaired electrons, that could facilitate the relaxation of protons by providing a stronger local magnetic field in the media [230]. The relaxivity is proportional to saturation magnetisation and the concentration MNPs [192], where $Mn_xFe_{3-x}O_4$, (which had highest Ms of tested doped magnetosomes), showed the highest relaxivity of 434 $mM^{-1}S^{-1}$ in comparison with favourable clinical approved MRI contrast agent Ferridex® (121.6 $mM^{-1}S^{-1}$), [192]. This confirms doping magnetosomes with Mn can modify their intrinsic parameters madding them a good candidate for T_2 contrast agents for MRI. In the case of T_2 weighted MRI contrast agent, Iron oxide nanoparticles, their magnetic moment can be changed by doping with other metal ions into iron oxide, as it is illustrated by Cheon et.al., that ferrites incorporation with different cation $(Fe^{3+})_{Td}$ $(M^{2+}Fe^{3+})_{Oh}$ on M= Mn, Fe, Co, Ni. At the octahedral site (Oh) demonstrate different relaxivity base on their different magnetic moment [240]. Because it has the highest magnetic moment among these ferrites doping [240].

Although Fe_3O_4 has commonly been used in medical applications, doped ferrite with Mn and Co has elevated the status of magnetic nanoparticles in biomedical applications. Together these results suggest that the Mn-doped magnetosomes have the higher saturation magnetisation, which is beneficial for its application as a contrast agent in MRI, to produce the darkening of contrast-enhanced tissue with relatively high relaxivity and at low concentration. The relaxivity has been shown to increase with an increasing percentage of Mn-doped, even at a small quantities. Also, Co-doped magnetosomes could be considered as magnetic hyperthermia treatment, because it has high magnetic coercivity and anisotropy. Confirming this when the Co-doped the magnetosomes shows the high percentage of death cell in the magnetic hyperthermia treatment of cancer cells.

Chapter 7:

Magnetosomes in *Vivo* application

7.1 Introduction

One of the leading causes of mortality in females is breast cancer [241][100]. Surgical resection is the most effective method to treat breast cancer; however, success relies on early detection and is invasive. Together with the emerging resistance of tumour metastases to anticancer drugs such as drugs target topoisomerase II [242], it is crucial to develop new therapies against breast cancer without surgery [243]. Many treatments have been developed to treat breast cancer including hormone therapy, chemotherapy, and irradiation [100]. More recently, hyperthermia has demonstrated the potential for direct killings of cancer cells by using MNPs to focus heat on the interested area without damaging the surrounding healthy tissue [241]. The temperature of the MNPs can be controlled by their intrinsic magnetic properties as well as the strength and frequency of the magnetic field applied to them [29], with magnetosomes exhibiting better heating under an AMF [177] [229] [244]. MHT may, therefore, benefit types of cancer resistant to traditional anticancer drugs [243] in a non-invasive manner with potentially fewer side effects.

Investigation of hyperthermia treatment using Mn, Co and Cu doped magnetosomes *in vitro* on MDA-231 breast cancer cell line in chapter 6 demonstrated that Co-doped magnetosomes induced greater cell death compared to native, Mn and Cu-doped magnetosomes and has the potential for further development as magnetic hyperthermia treatment. In this chapter, I investigate the feasibility of magnetic hyperthermia using native magnetosomes and potential for increased efficacy by using Co-doped magnetosomes for breast cancer treatment *in vivo*.

All animal procedures were performed by a postdoctoral research associate (Dr Faith Howard) while I attended, within the Medical School of The University of Sheffield and carried out under license according to regulations laid down by Her Majesty's Government, United Kingdom (Animals Scientific Procedures Act, 1986). Briefly, the brain seeking, luciferase-expressing 4T1 (4T1-Luc-BR) cell line ($1x10^5$ cell/ml) were injected into mammary fat pads via intra-nipple injection (20µl) for the development of primary breast tumours. Treatment was initiated once tumour volume reached 550 mm^3. Mice were anaesthetised by isofluorane and magnetosomes, and Co-doped magnetosomes were injected intratumorally (0.1ml). Directly after the injection the mice were positioned within the magnetic hyperthermia instrument

(Magnetherm, NanoTherics) aligned with the coil using a polystyrene bed linked to anaesthesia as it has been described in methodology chapter (section 22.2) The mice were subjected to AMF for 20 minutes (at a frequency of 174 KHz and magnetic field amplitude of 9.7 mT), directly after treatment was injected which they were euthanised, tumour samples harvested for histological examination.

Tumour samples were formalin fixed in 10% formalin solution for 24 hours prior to paraffin wax embedding and sectioning. The other half was minced and snapped frozen in 90% FBS/10% DMSO, for slices of thickness 4 μm. The changes in cell morphology were observed by light microscopy using two different stainings H&E staining and Prussian blue. The section was stained with H&E and Prussian blue to detect the presence of the magnetosomes. Mice tolerated approximately 20 minutes of anaesthesia in combination with MHT with no signs of respiratory distress or other adverse events. Anaesthetic recovery was not investigated as this had to be a terminal experiment due to the maturity of the tumours.

7.2   *In vivo* Magnetic hyperthermia treatment (MHT) in carcinoma

Upon injection of the magnetosomes, it was observed that the intended volume of 0.1 ml as per [94] [177] [153] was too large to be administrable with the suspension leaking out of a tumour, especially in surrounding lesions present on the tumour surface (Figure 7-1).
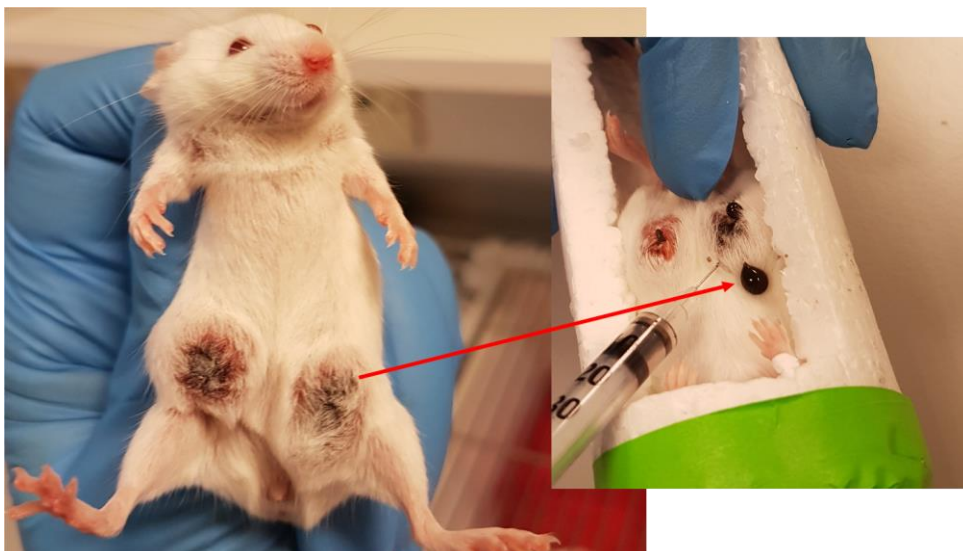
Figure 7-1: showing the treatment of the mice with a breast tumour underwent mammary fat pad, where the magnetosomes are administered intra-tumour, with some leaking out of a tumour

Table 7-1: Dosage of magnetosomes by intratumoral injection

	Left	Right
Mouse	20 µl PBS	20 µl PBS
Mouse 1	0.6 mg native magnetosomes	0.5 mg native magnetosomes
Mouse 2	0.2 mg cobalt doping magnetosomes	0.2 mg cobalt doping magnetosomes
Mouse 3	0.4 mg cobalt doping magnetosomes	0.3 mg native magnetosomes

Table 7-1 the amount of administered magnetosome suspension to each mice on the left and right tumour breast. The different volume of a 10 mg/ml suspension was administrated as complete 100 µl (1mg) dose was not achievable. Figure 7-1 shows the volume was unadministerable with the suspension leaking out of a tumour, especially surrounding lesions present on the tumour surface.

Figure 7-2: Tumour samples a) a control tumour without the biodistribution of magnetosomes and the red circles shows the surface of a tumour with white hair b) a tumour with the biodistribution of magnetosomes the red arrows shows the deep magnetosomes distribution inside a tumour, c) the biodistribution of Co-doped magnetosomes in a mice tumour red arrows shows the deep magnetosomes distribution inside a tumour

Figure 7-2 shows the mice tumours that were treated and non-treated with the magnetosomes. Figure 7-2 a show the visible surface tumour lesion in a red circle with the necrotic effect that could be due to the large growth of the tumours, but there is no other visible for the necrotic effect in the deep tumours (see later figures). While in Figure 7-2 b and

c the biodistribution of magnetosomes is visible (the red arrows) showing the deep magnetosomes distribution inside a tumour.

7.2.1 Histological Analysis Of Tumour Cell In The Breast

The presence of magnetosomes within tumour sections was visualised by both H&E and Prussian blue staining, (Figure 7-3 a and b respectively). Within the sections, there were areas of viable cells (V= represent viable area) compared to necrotic areas (N= necrotic) that seemed to localise near the magnetosomes.
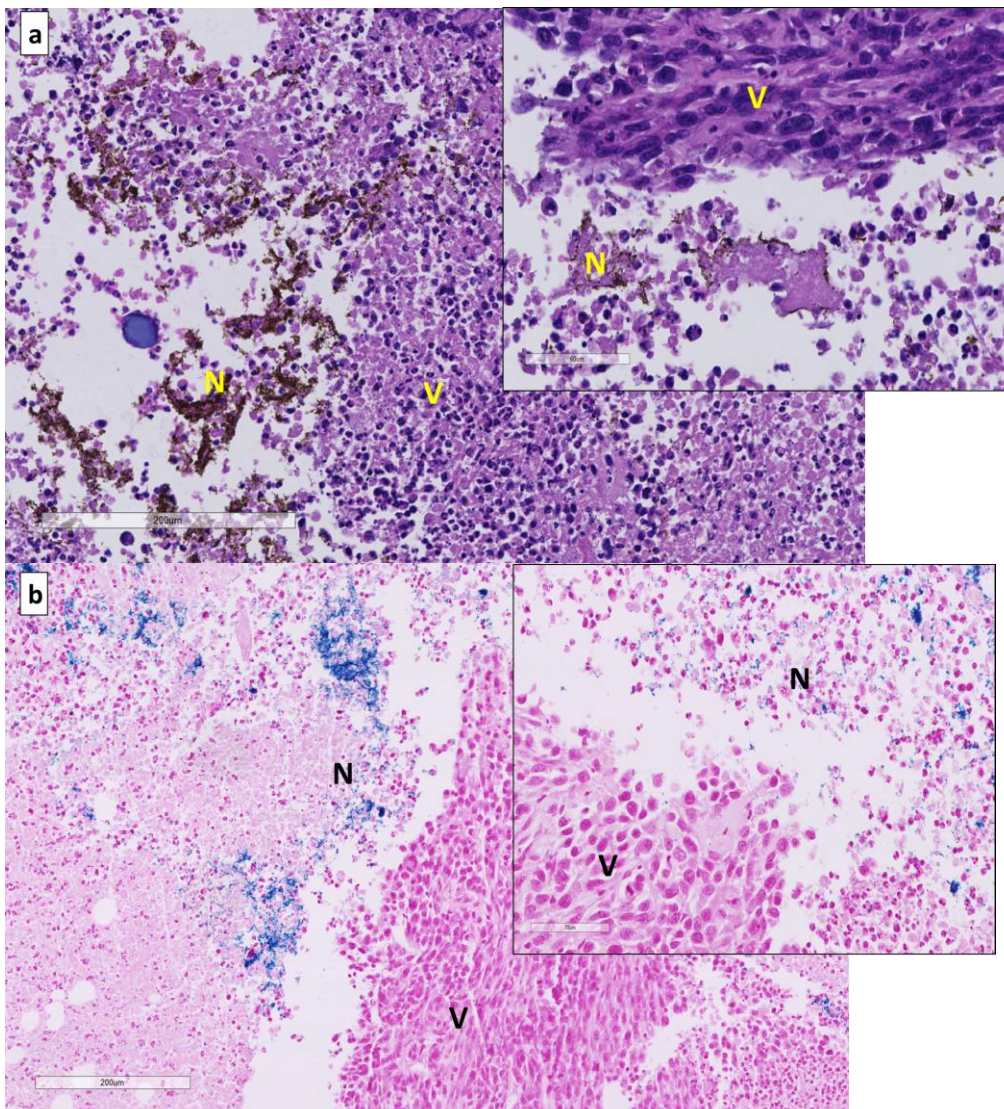
Figure 7-3: Histological analysis tumor: a) H &E staining shows necrosis area in tumor cells observed in tumor after MHT, where iron stain with dark dots indicate iron deposit where cells shows necrosis area =N, and viable area =V with scale bar 200, 70 µm and b) Prussian blue staining were performed in tumour section to study the magnetosomes distribution, where the iron staining with blue show location of magnetosomes within tumours with scale bar 200, 60 µm, where the pink colour is cytoplasm and red colour is nucleoli .

Necrotic cells display no nuclei presence (staining with purple colour) and cytoplasm as well (staining with pink colour) and there is no cells remain in the area that surrounds with the magnetosomes because of the nuclear division and ischemic necrotic effect. Also, there is coagulation necrosis tumour cell in some areas compared with the area that does not have the magnetosomes particle, where the tumour cell shows the nucleoli and the cytoplasm heavily stained (where V represents the viable area in Figure 7-3 a). Prussian blue staining shows the location of the magnetosome particles (stained blue) and the tumour cell surrounding them have no nucleoli (stained red) and no cytoplasm (staining with pink), compare with the viable area (V= represent viable area) where the nucleoli and the cytoplasm are heavily stained Figure 7-3 b.

Because the magnetosomes are injected directly into tumours, it is believed that retention of magnetosomes has a remarkable effect on the tumour. Where the concentration of the magnetosomes in a tumour could be high to enhance the death cell.

If the MHT using the magnetosomes is carried out at temperatures around 42°C the tumour treatment will undergo apoptosis, where apoptosis is death cell programme, and the content of the cell undergo MHT (including tumour antigens) are not released into outside the cells [100]. While if the MHT results in higher temperature, the necrosis cell death will occur, and the cell content will be released into the environment [100].
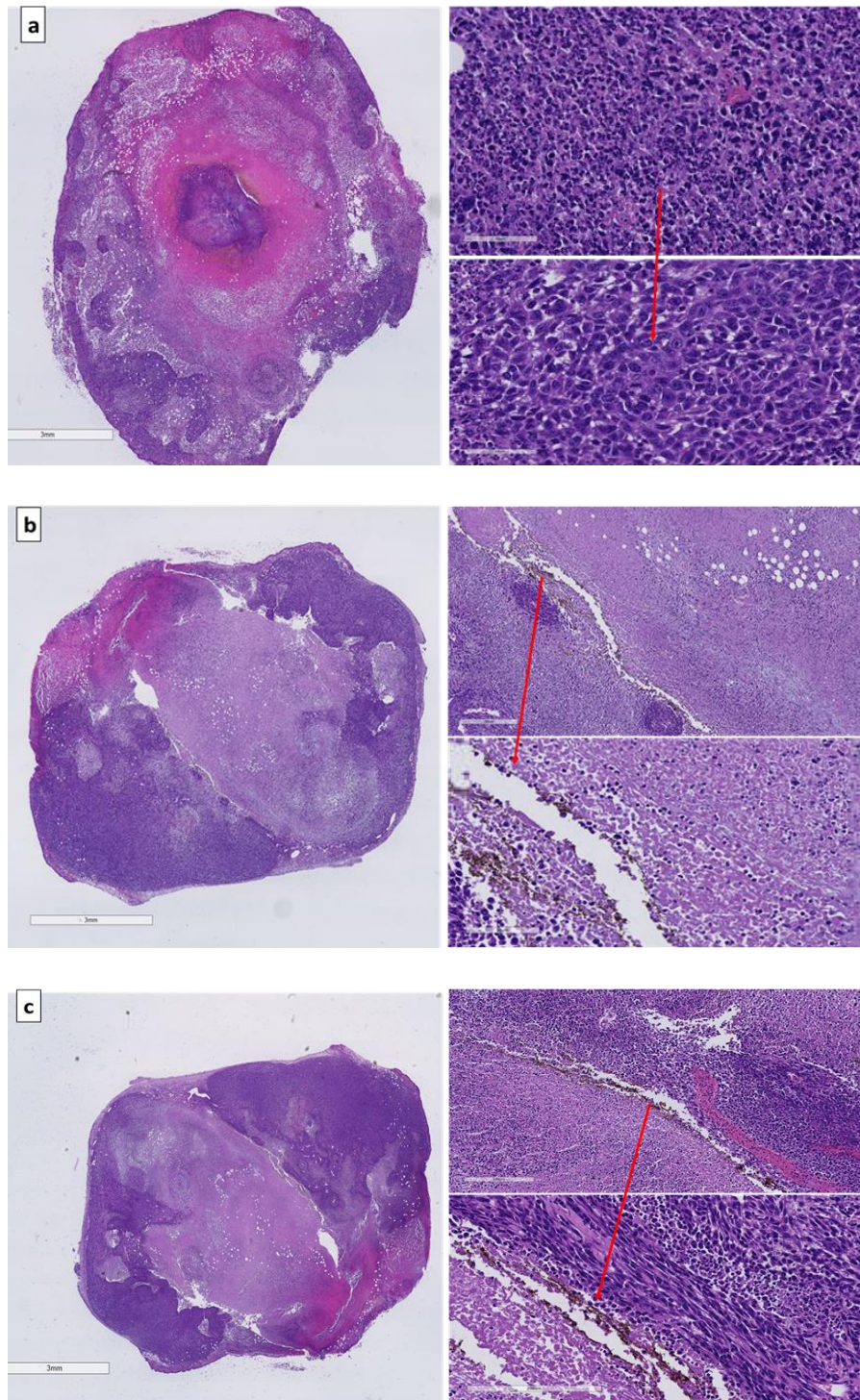
Figure 7-4: Histological analysis of tumor necrotic after H&E staining observe changes in cell morphology by using light microscopy, a) control tumor (without magnetosomes) where the necrosis was not induce in tumour, b) treatment tumor with native magnetosomes, the tumour cell around the magnetosome shows broad necrosis of after MHT, c) treatment tumor with Co-doped magnetosomes, the tumour cell around the Co-doped magnetosome shows broad necrosis of after MHT, the treatment tumor was exposure to AMF for 20 minute, with scale bar 3mm.

Figure 7-4 b and c show that the tissue surrounding magnetosomes shows death effect to the area not surround with magnetosomes and Figure 7-4 a, control (a tumour subjected to the Magnotherm but with no magnetosomes) shows there is no necrosis without magnetosomes injection. This study cannot be treated to a quantitative analysis of the sections due to the leakage, resulting in different amounts of sample added to each a tumour resulting in no replicated experiments. This study must be treated as a more qualitative, descriptive study. Even so, I can confirm that the magnetosomes are absorbent agent where they absorb energy and dissipate it in the form of heat, enough to result in necrosis within the tumour cells.

The native and Co-doped magnetosomes were injected directly into tumours, then after MHT were seen to destroy cancer cells by dispersed heat produced by the magnetosomes. Furthermore, this treatment could prevent healthy tissues from heating because only magnetosomes absorb the magnetic field energy and convert it to heat.
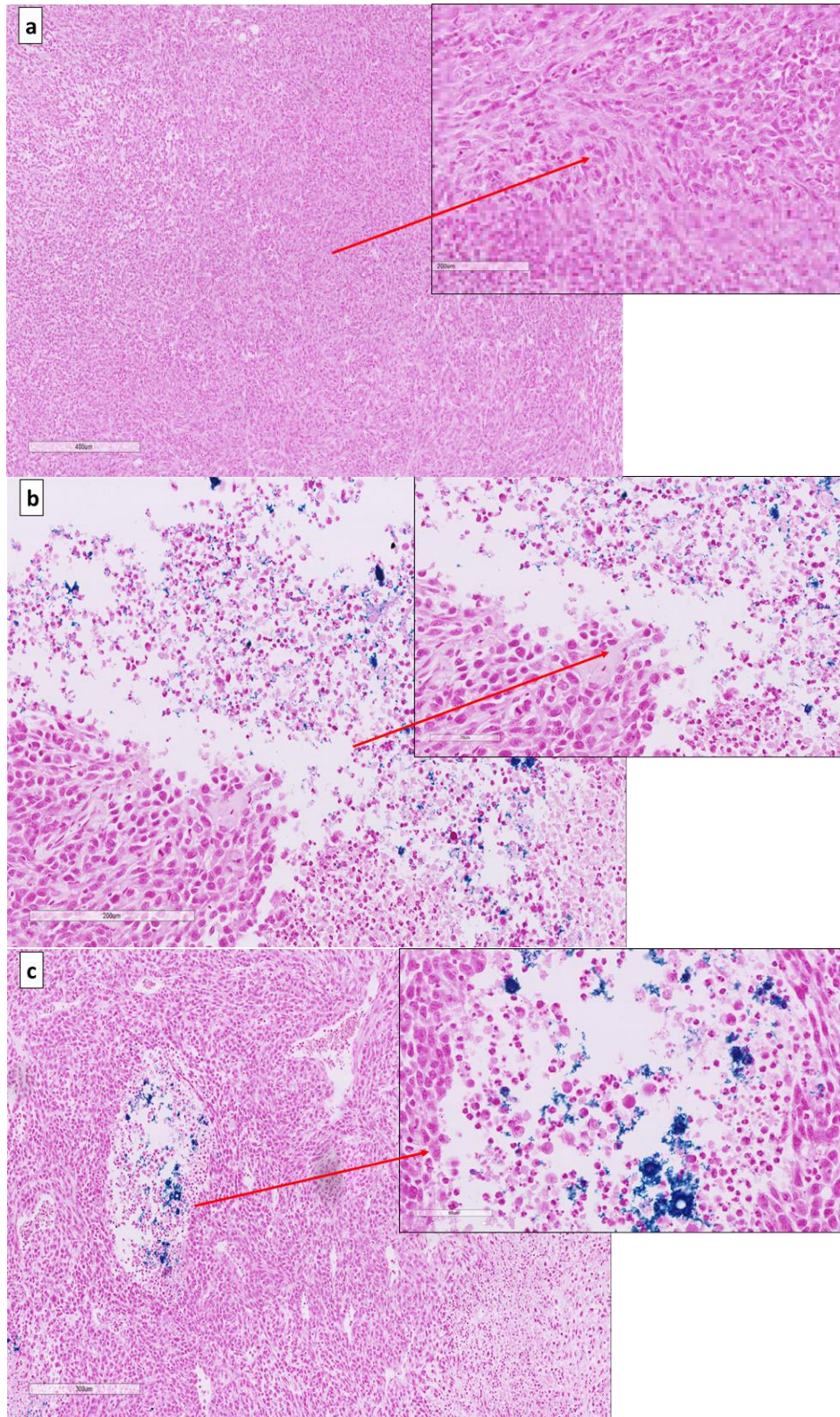
Figure 7-5: Histological analysis of tumor after prussian blue staining observe changes in cell morphology by using light microscopy, a) control tumor (without magnetosomes) where was not biodistribution of any magnetosomes to induce heat in tumour, b) treatment tumor with native magnetosomes, the tumour cell contain the magnetosome stained with blue, c) treatment tumor with Co-doped magnetosomes blue stained. The tumour cell around the Co-doped and magnetosome shows broad necrosis of after MHT, and the nuclear stained with red while the cytopalsm with pink colour, scale bar between 200-300 μm.

Prussian blue staining Figure 7-5 b and c Indicating the presence of the magnetosomes tends to co-localise to areas of cell death characterised by rounded cell morphology, where nucleoli (staining with purple colour) presence in some area without cytoplasm or the cytoplasm(staining with pink colour) without nucleoli. Where the heat is generated in 10 -100 μm leading to the high temperature raised locally during treatment, for partial or total tumour destruction. The intra-tumour injection has been chosen to localised treatment in these initial studies, but it is clear that treatment is localised only to where the magnetosomes are located. This mechanism could be more efficient than the extra-cellular hyperthermia. Since the tumour cells are more sensitive to heat than a healthy one. Because the aim of this *in vivo* MHT to target the magnetosomes in the position of the tumour cell environment. This suggests that MHT is demonstrating an effect although further investigation is needed, such as the addition of magnetosome treatment minus MHT to ensure magnetosomes alone are not responsible for cell toxicity, as well as optimising tumour size and addition volume to ensure replicates can be obtained.
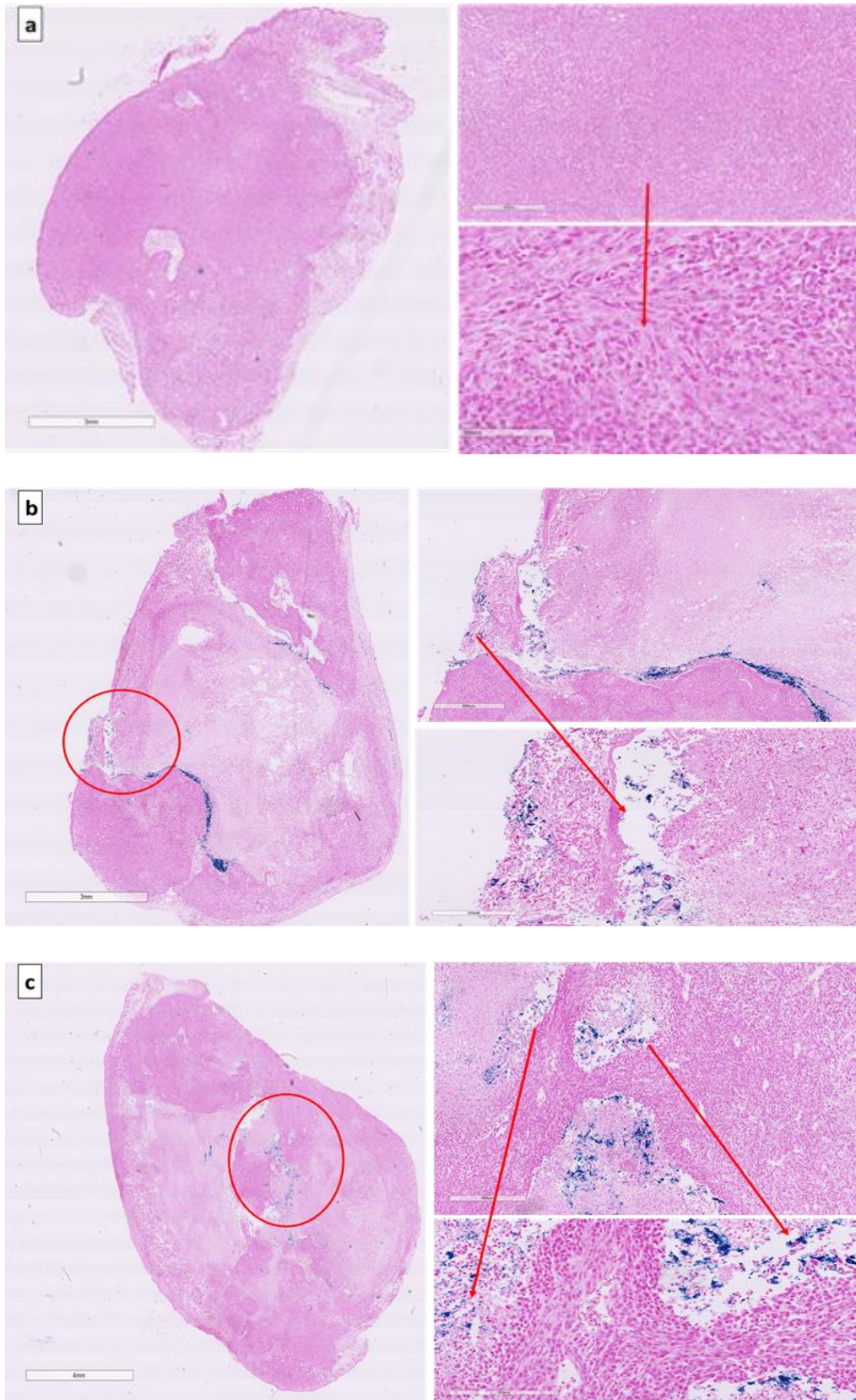
 Figure 7-6: Histological analysis of tumor after prussian blue staining represent from different concentration contain a) control, b) tumor treat with Co-doped magnetosomes 2 mg/ml, b) tumor treat with native magnetosomes 6 mg/ml after exposure to AMF for 20 minutes with scale bar 3 mm.

Figure 7-6 a shows a control tumour (which has been injected with PBS only); however, there are still areas of necrosis. This is probably due to the growth of the large size of a tumour prior to treatment. While Figure 7-6 b and c show changes to cell morphology due to the magnetosomes injection. Co-doped magnetosomes (Figure 7-6 c) shows more necrotic areas than native magnetosomes (Figure 7-6 b), even at a lower concentration (2 mg/ml compared with native magnetosomes concentration of 6 mg/ml). Where both of them have the same intra-cellular injection and the same condition of treatment but administered were different. Due to the small number of mice, no quantified change can be given, but we could attribute the visual effects seen to mostly due to the magnetocrystalline anisotropy and higher hysteresis losses of cobalt as it has been confirming these properties for the cobalt by other studies [103] [24] [155] where the presence of cobalt increased the magnetic coercivity (see chapter 6: coercivity of 420 Oe for Co-doped magnetosomes compared to 125 Oe for the native magnetosomes (at 300K)) and this has an effect on the MHT.

There is a distinct pattern to the location of the magnetosomes in Figure 7-6 b, they are not diffuse within the tissue but seem to line the transition between healthy cells and necrotic areas which could be veins compare to Figure 7-6 c where the magnetosomes are diffuse within the centre of tissue. This necrosis could be the lesion that was present on the surface of a control tumour (see Figure 7-2 a) and therefore may not be attributed to the treatment. However, in Figure 7-6 c, the orange circle shows that the leaking of the magnetosomes outside a tumour after the injection, demonstrating size and condition of a tumour is important for the treatment of this model.
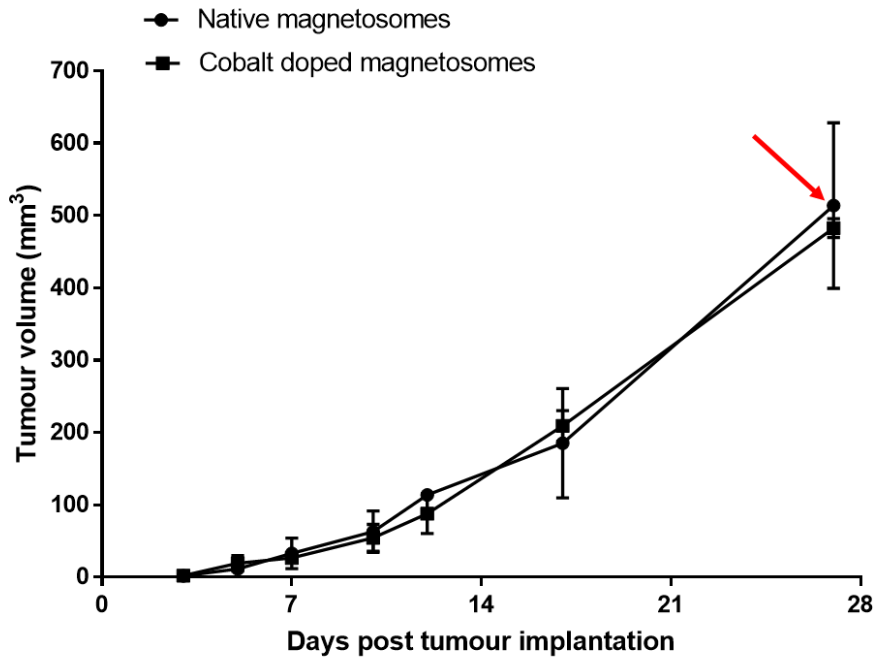
Figure 7-7: Time course of tumour growth in native and Co-doped magnetosomes, where the administrated for treatment was on day 28, as shown with a red arrow.

Unfortunately, not the entire injected amount of the magnetosomes was taken into a tumour as shown in Table 7-1, where some of the magnetosomes concentration was leaking from a tumour (Figure 7-1). The results indicate that tumours have different concentration of magnetosomes.

This must be considered a preliminary experiment, 100 µl of PBS was too large a volume to inject into this size tumour and much of the solution leaked out (Figure 7-1). Thus the concentration of the magnetosomes used during the therapy should be increased and the volume of the injection decreased, to administer the same quantity of magnetosomes. In a study by Mannucci [93], magnetosomes were extracted from *Magnetospirillum gryphiswaldense* strain MSR-1 for injection subcutaneous into mice with HT-29 (human colon carcinoma). The treatment started when the size of a tumour reaches between 400-500 mm^3, but in Mannucci's experiment they did not face the same problem as in my study, and in fact, injected 200 µl of total volume. This may have been possible because they used 3 to 4 separate punctures without relevant leakage of fluid from a tumour. While in Alphandéry's study [177], the treatment started when native magnetosomes were injected into a tumour of 100 mm^3 volume size, where the mice received 100 µl of magnetosomes suspension containing 1 mg of magnetosomes. Importantly, Alphandéry study used MDA-231 human

breast cancer. So there are many factors that control when to start treatment, one of them is the tumour size and the type of cancer and its ability to retain the injected volume.

Figure 7-7 shows the tumour volume in native and Co-doped magnetosomes groups prior to treatment increasing at the same volume at the time of treatment. The tumours grow to reach 550 mm^3 in size during a period of 28 days, at which point the treatment was started. While in another study by Alphandéry [177], the treatment starts with native magnetosomes at volume size 100 mm^3 that was after 21 days from the breast cancer cell was injection, taken in consideration that in Alphandéry study MDA-231 human breast cancer was injected while in this study 4T1-BR cell line was used. In another study [93] MSR-1 was an injected subcutaneously into mice with HT-29 (human colon carcinoma), when the size of the tumour reach between 400-500 mm^3, inject 200 μl of the total volume of treatment. So in these studies, the size of a tumour various and the time of the treatment was different, based on the type and the position of the tumours.

If the tumour size is less than 550 mm^3, it will be healthier and more likely to hold and take the dose of injection treatment, while if it is larger than 550 mm^3, it may be unhealthy and there may be a leakage of treatment injection. So there are many factors that control the treatment starts, one of them the tumour size and the type of the cancer cell. But in each case, the size of a tumour should be smaller than 500 mm^3 to start treatment to avoid leaking and have efficiency treatment in this model. So for a future experiment, we should start the treatment after 16 days growth in our model (shown in Figure 7-7). This means the treatment could start on a tumour 200 mm^3 in size instead of 550 mm^3. Such a tumour will be healthier and thus should avoid the leaking and have efficiency treatment in this model. 4T1 cells are more ulcerative than other murine cell lines such as E0771 and TS-1. MDA231 are human cell lines but can only be used in immunocompromised mice. Generally, we would perform these studies in an immunocompetent model first and then a humanised model. Because we do not know if the lack of an immune response impacts the efficacy of the treatment or tumour growth.

In some clinical studies [245] [246], heat treatment plays a crucial role, but the limitations of currently available techniques have led to magnetic hyperthermia being developed as a clinical treatment to select target tumour area and distribute heat within the tumour tissue. MNPs induce heating to solve these limitations, especially for a poorly accessible deep

tumour. Where the magnetosomes are injected into the tumour tissue then directly they are stimulated by AMF to generate heat. Unfortunately, we were not able to measure the heating temperature during the MHT, to determine the average of heat that induces tumour cell and whether this localised heating increases overall body temperature.

In Alphandéry study when 2×10^6 MDA-231 human breast cancer cells were injected subcutaneously on both flanks and the tumour size reached 100 mm^3 when the treatment was carried out and the result of subjecting the mice to AMF with field strength 43 mT (183 KHz) for 20 minutes repeated 3 times at 3 days interval. The temperature spread within a tumour reaching 43°C and show that the presence of magnetosomes produced an anti-tumoral activity by inducing anti-tumour immune responses against a tumour. They showed the size of a treated tumour reduced in some mice and disappeared in other [247][101]. In a study for the treatment of xenograft, breast tumours were tested using four different types of suspensions of: SPION; whole MTB; magnetosomes organised in chains; and individual magnetosomes [101]. 10 mg/ml of iron oxide suspension was administered by injection into the centre of the xenograft MDA-231breast cancer tumour. Then the mice were exposed to the AMF strength of 40 mT and frequency of 198 KHz thrice for 20 minutes [101]. The treatments which used chains of magnetosome suspensions were efficient in several mice, where the tumours disappeared. In contrast, the heat treatment with full MTB and individual magnetosomes and SPION suspension were unable to stop tumour growth. The efficiency of magnetosomes bacteria in these results cannot be only due to their large size, but also due to their arrangement in chains that made them less prone to aggregation. Rats survived an administered amount of magnetosomes up to (480 mg/Kg), so their acute toxicity was low [101]. In another study magnetosomes that were extracted from *Magnetospirillum gryphiswaldense* strain MSR-1, were used to treat the mice model that were injected into HT-29 cell (human colon carcinoma). *In vivo* study after the MSR-1 magnetosomes were injected and exposure to AMF with strength 29 mT at 187 HKz for 20 minutes for alternative days when the size of the tumour reach between 400-500 mm^3 [93]. The histological results showed the necrotic areas were close to MSR-1 injection sites, while other areas not surrounding these particles were unaffected [93]. This agrees with our results, while in Figure 7-3 a, b, shows there is the necrotic cell in a tumour in areas where the magnetosome particles are present, while other tumour cells show heavy staining which indicates healthy

nucleoli and cytoplasm in areas that do not contain magnetosomes. In all these studies above, they have been used different cell lines, but the treatment time was similar to my study (20 minutes). However, the strength of AMF filed was varied between 43, 40 and 29 mT compare to 9 mT in this study, which is less strong. Despite the lower field strength, it has shown some effect on tumours treatment, which means that the Co-doped magnetosomes have a more significant heating effect compared to native magnetosomes even at lower field strength (9mT). The strength of AMF and a number of the repetitions of the treatment should be considered. Also, measures the temperature during the MHT using heating optical fibre probe and measure the volume of a tumour after the treatment.

MHT represents an innovative method to heat deep-steady tumours, and it may have some advantages over conventional method, since the temperature direct injection of the magnetosomes into the tumour helps to localise magnetosomes in a tumour, but not affecting the peripheral normal tissue, so the temperature of this normal cell does not significantly increase, because the hyperthermia treatment is specifically limited to tumour area. Also, the temperature during MHT can be controlled by changing the strength of AMF that allows inducing the apoptosis or necrosis into tumour cells without damaging the surrounding normal tissue. Minimising the damage with consistent heating of MNPs, increasing the temperature for therapeutic is one of the crucial challenges in MHT. The Co-doped magnetosomes show the highest increase in coercivity in chapter 3, and here in this chapter have shown this translates into breast cell death, presumably through enhanced heating capacity, due to the high anisotropy of cobalt's influence of the heating. However, the exact amount of heat that magnetosomes produce *in vivo* could not be measuring or even predicted using their hysteresis losses, because there are many factors that affect it, such as a solid tumour, size, depth, type of a tumour.

From these results, we conclude that magnetosomes are able to cause more necrotic area under the application of AMF, compare to the absence of magnetosomes in a tumour while Co-doped magnetosomes had a greater effect with a smaller dose. Despite the advantages of using magnetosomes and Co-doped magnetosomes and their satisfactory effect on the tumour, the quantities analysis and issues with reproducibility mean quantitative results could not be extracted from this study due to an insufficient number of animals to do statistical analysis and the size of a tumour was too large. So it is necessary for a future

experiment study to achieve several goals. 1. Reducing the magnetosomes suspension volume to be less than 100 µl and start the treatment at tumour size smaller than 550 mm^3, so optimise tumour size with a volume of injection to ensure all the solution is retained by a tumour. 2. Non-terminal experiment, repeat on smaller tumours to monitor is tumours shrink over time, 3. Use optical fibre probe to verify the tumour temperature if it increases locally or within the whole body of mice. Furthermore using an infrared camera to global the picture of variation of the temperature of the tumours. 4. Measuring the size of a tumour after treatment. 5. Investigate the need to show the apoptosis effect and confirm the effectiveness and safety of this method in breast cancer treatment. We need to estimate the quantity of magnetosomes concentration within the tumours and study the biodistribution of the magnetosomes with the tumours after some days after the injection and how magnetosomes eliminate from the body.

8

Chapter 8:

Conclusion

And Future Work

8.1 Conclusion

This work has described the optimisation of bacterial magnetic nanoparticles and magnetosomes for biomedical applications as having the advantageous properties of narrow size, uniform shape, and single domain. An important aspect of the magnetosome is the magnetite core. The magnetic properties of the magnetosome can be altered by doping this core material with different metals. Additionally, it is covered by a lipid bilayer that could easily be functionalized with bioactive substances. The introduction of Mn, Co, and Cu divalent metal ions within the AMB-1 growth medium at various concentrations ranging between 10 μm and 100 μm yield improved coercivity and saturation magnetisation of the extracted magnetosomes, which can consequently increase both the heating properties for medical application and the relaxivity for MRI diagnosis. The doped magnetosomes were tested to identify their magnetic material properties using SQUID magnetometry, and the precise level of doping was determined using analyses of bulk magnetosomes with ICP, as well as elemental analysis of individual magnetosomes using EEL. In this research, the levels of both Mn^{2+} and Co^{2+} doping in AMB-1 were increased to a height of 6.23% for $Mn_xFe_{3-x}O_4$ and 4.57% for $Co_xFe_{3-x}O_4$, which are higher levels than were applied in the existing literature [24] [155] [156].

This work has confirmed that it is possible to use non-ferrous doped magnetosomes, especially Co-doped magnetosomes, as promising biomedical treatments in MHT *in vivo* and *in vitro*. Mn-doped magnetosomes appear to be particularly useful as a diagnostic material for MRI *in vitro*. According to the results, it seems that the biosynthesized magnetite has enhanced the levels of magnetic properties by doping with Mn^{2+} and Co^{2+}. The coercivity of Co-doped magnetosomes increased to 420 Oe compared to 125.1 Oe for native magnetosomes. The saturation magnetisation of Mn-doped magnetosomes increased to 112 $emug^{-1}$ from 92.99 emu g^{-1} for native magnetosomes. Mn-doped magnetosomes produced the highest M_s of any other doped magnetosomes. MRI measurements *in vitro* proved that the Mn-doped magnetosomes produced the highest relaxivity (434 $mM^{-1}S^{-1}$) compared to the native magnetosomes, and magnetosomes doped with other metals.

The magnetosomes were compared to synthetic magnetite nanoparticles with and without an oleic acid coating. These synthetic particles had a much smaller coercivity and saturation

magnetisation compared to magnetosomes of coercivity 10 and 33 Oe, and 73 and 67 emug^{-1} for SNPs and OA-SNP respectively. This suggests that the magnetic properties can be affected by factors other than the composition of the MNP. The data presented in this study and from the previous literature shows that the MTB is capable of forming magnetite crystals with precise size and shape under ambient conditions, and has a high level of crystallinity [46] [47] [248] [52]. This means that the magnetosomes have good heating properties, as a consequence of their high level of crystallinity and ferromagnetic behaviour at physiological temperature.

The ability of enhanced magnetic properties of the Mn, Co and Cu doped magnetosomes to release heat and kill cells during MHT treatment were tested in cell cultures. The results of the cellular uptake and the toxicity of the native and doped magnetosomes confirmed that dosages of 0.18 mg/ml were nontoxic for breast cancer cell lines, except in the Cu doped magnetosomes, which were proven to produce toxicity at this concentration. Using MDA-231 cells, the Co-doped magnetosomes revealed a higher percentage of dead cells (26.4%) via apoptosis, compared to the native magnetosomes (16.6%). This was an expected result, based on their high coercivity (420 Oe) confirmed by SQUID, which should allow more heat to be generated.

The magnetosomes particles were examined within cells using TEM imaging. This revealed that the magnetosomes were arranged in small chains, even after cellular internalisation, which appears to prevent them aggregating. This could increase the rate of cellular internalisation, and help to generate uniform heating throughout a tumour. If the magnetosome membrane is removed, then the cellular uptake at a concentration of 0.18 mg/ml decreases by 10%, compared to membrane intact magnetosomes. Interestingly, upon removal of the magnetosomes membrane, there was a 5% decrease in the level of toxicity. TEM showed that these magnetosomes aggregated more, and may prevent uptake and subsequent toxicity. Endotoxin measurements revealed that magnetosomes have a low level of endotoxin (0.218 EU/ml with high doses up to 0.2 mg/ml), based on the threshold of toxicity defined by the FDA. However, it is higher than the SNPs (0.16 EU/ml) at 1.5 mg/ml and OA-SNPs (0.055 EU/ml) at 0.5 mg/ml.

This thesis details the first account of quantitative simultaneous doping of multiple diverse non-ferrous metal ions into magnetosomes. Manganese, cobalt and copper ions were

introduced into the growth medium in various combinations to produce double and triple doped magnetosomes ($Co_{n-x}Mn_{n-y}Fe_{3-x-y}O_4$, $Co_{n-x}Cu_{n-y}Fe_{3-x-y}O_4$, $Cu_{n-x}Mn_{n-y}Fe_{3-x-y}O_4$, and $Co_{n-x}Cu_{n-y}Mn_{n-z}Fe_{3-x-y-z}O_4$). The combined levels of dopant metals in the magnetosomes ranged between 13% and 18% of the total metal content of the magnetosomes. This could be indicative of the maximum percentage of doping of nonferrous metal that can be drawn from the environment and inserted into magnetosomes. Furthermore, the coercivity for combinations with cobalt present was 399 Oe. When cobalt was absent from the combination the coercivity was 73.13 Oe. This signifies that the uptake of Co^{2+} ions and their incorporation into magnetosomes was responsible for the increase in the coercivity. This discovery could be developed to synthesize novel high quality double or triple doped magnetosomes with tunable magnetic properties for various nanotechnological applications.

Magnetosomes with intact membranes were successfully functionalized with biotin using chemical biotinylation. These magnetosomes could be conjugated to fluorescently labelled streptavidin and its uptake into MDA-231 cells was confirmed by fluorescence microscopy, showing this functionalization was not blocking it. The biotinylation of magnetosomes could be one means of easily coupling them to bioactive substances. This may be an attractive platform to engineer novel enzymes, drug, and other bioactive substances onto the magnetosomes for future treatments and diagnostic assays [120].

Another significant finding of this study was the ability of magnetosomes and Co-doped magnetosomes to affect breast cancer tumours in mouse models. A high temperature induced from these magnetosomes potentially improved the therapeutic effect on breast cancer compared to the control, even with a low magnetosomes dose. Histological examination revealed that black nano-sized accumulations (magnetosomes) appeared at stroma in tumours. The necrotic zone was found surrounding these accumulations. This suggests that the magnetosomes were successfully releasing heat to the surrounding tissue during MHT. Qualitative analysis showed that Co-doped magnetosomes demonstrate greater levels of necrosis compared to native magnetosomes. It is expected that Co-doped magnetosomes may release more heat during MHT due to their increased coercivity. This makes Co-doped magnetosomes a promising target for inducing efficient heating in the treatment of breast cancer.

8.2 Future work

The results and conclusions reached in this work appear to show that doped magnetosomes have potential as a future treatment and diagnostic tool for cancer. However, there is still much work to be done to optimise the magnetosomes and enhance the potential treatment. More studies are required to develop these magnetosomes for effective application as a multimodal therapeutic agent in areas such as drug delivery or magnetite hyperthermia.

One area of future study would be to further investigate the functionalization of the magnetosome membrane.This work described the successful biotinylation of magnetosomes, and this approach could be developed further by conjugating biotinylated bioactive molecules to the magnetosome surface via streptavidin. The bioactive molecules, such as antibodies, may specifically recognise cancer cells as a targeting step. This could favour intracellular uptake and avoid recognition of the magnetosome by macrophages. This would entail identifying suitable antibodies for certain cancer cell types, and analysing the magnetosome uptake, both with and without an antibody. Another similar approach would be to attach drug molecules to the magnetosomes to create a combined MHT and chemotherapy. Combining antibodies and drugs on the magnetosomes would allow for targeted MHT and chemotherapy with lower drug doses to minimise side effects, compared to normal chemotherapy treatments.

Raising the cobalt concentration even further could increase the magnetic anisotropy of the magnetosomes, and increase the energy lost as heat during MHT. This could be achieved by producing more cobalt tolerant forms of magnetotactic bacteria. One method for this would be to make random mutations in the genome and select bacterial colonies which can survive on increasing amounts of cobalt due to favourable mutations. Also, conducting a more genetic study to ascertain more information about how the magnetosomes could be forced to internalize more than 18% of just Co or Mn would be beneficial.

The *in vivo* experiments reported in this study show that magnetosomes and MHT have the potential to be effective in the treatment of cancer. However, further experiments are necessary in order to produce quantitative data and optimum treatment conditions. A range of different parameters need to be tested. For example, the dose of magnetosomes required for effective MHT depends on the size of a tumour, with larger tumours requiring a higher

dose of magnetosomes. The temperature required for cell death is also important, meaning that the length of treatment and the field conditions must be optimised and adjusted based on the tumour size. Surface and body temperatures should be measured during treatment to ensure that the temperature of the overlying skin is lower than that of the underlying tumour. Multiple MHT treatments should be delivered on the same tumour with a 24-hour interval between each, as a single treatment may not be sufficient to completely destroy a tumour. The mice should also be kept alive after treatment so that the size of the tumour can be measured over time to see if the size decreases. This would also enable the safety of the technique to be tested. Performing these experiments on more mice would allow statistical analysis to be conducted, and immunohistochemical analysis of tumours using apoptosis markers on tissue sections would facilitate the observation of the apoptotic and necrotic effects from MHT.

References

[1]   Brougham Dermot F. and GunKo Yurii, "Magnetosomes: Bacterial Biosynthesis of Magnetic Nanoparticles and Potential Biomedical Application," in *Magnetic Nanomaterials*, C. S. S. R. Kumar, Ed. Germany: WILY-VCH Weinheim, 2009, pp. 399–428.

[2]   M. Arruebo, R. Fernández-Pacheco, M. R. Ibarra, and J. Santamaría, "Magnetic nanoparticles for drug delivery," *Nano Today*, vol. 2, no. 3, pp. 22–32, Jun. 2007.

[3]   H. Shokrollahi, "Structure, synthetic methods, magnetic properties and biomedical applications of ferrofluids.," *Mater. Sci. Eng. C. Mater. Biol. Appl.*, vol. 33, no. 5, pp. 2476–87, Jul. 2013.

[4]   A. L. I. Yadollahpour and S. Rashidi, "Magnetic Nanoparticles : A Review of Chemical and Physical Characteristics Important in Medical Applications," *Orient J Chem*, vol. 31, pp. 25–30, 2015.

[5]   J. H. Lee, J. W. Kim, and J. Cheon, "Magnetic nanoparticles for multi-imaging and drug delivery," *Molecules and Cells*, vol. 35, no. 4. pp. 274–284, 2013.

[6]   L. Perrone, "Peter the Fuller," *EECh*, vol. II, no. September, p. 678~f., 1992.

[7]   F. Liu, Y. Hou, and S. Gao, "Exchange-couple nanocomposites: chemical synthesis, characterization and applications," *Chem. Soc. Rev.*, vol. 43, pp. 8098–8113, 2014.

[8]   S. Martel, "Magnetic nanoparticles in medical nanorobotics," *J. Nanoparticle Res.*, vol. 17, no. 2, pp. 1–15, 2015.

[9]   R. Hergt, S. Dutz, R. Müller, and M. Zeisberger, "Magnetic particle hyperthermia: nanoparticle magnetism and materials development for cancer therapy," *J. Phys. Condens. Matter*, vol. 18, no. 38, pp. S2919–S2934, 2006.

[10]   Q. A. Pankhurst, J. Connolly, S. K. Jones, and J. Dobson, "Applications of magnetic nanoparticles in biomedicine," *J. Phys. D Appl. Phys*, vol. 36, no. 03, pp. 167–181, 2003.

[11]   Hervault Aziliz and T. N. T. Kim, "magnetic nanoparticle- based therapeutic agents for thermo-chemotherapy treatment of cancer," *Nanoscale*, vol. 6, pp. 11553–11573,

2014.

[12] H. L. Gabor, *Fundamentals of nanotechnology Nanotechnology; Nanostructured materials industry*. Boca Raton, Fla. : CRC Press Taylor & Francis Group, 2009.

[13] Z. Karimi, L. Karimi, and H. Shokrollahi, "Nano-magnetic particles used in biomedicine : Core and coating materials," *Mater. Sci. Eng. C*, vol. 33, no. 5, pp. 2465–2475, 2013.

[14] A. L. Daniel-da-silva and T. Trindade, "Biofunctional Composites of Polysaccharides Containing Inorganic Nanoparticles," 2011.

[15] A.-H. Lu, E. L. Salabas, and F. Schüth, "Magnetic nanoparticles: synthesis, protection, functionalization, and application.," *Angew. Chem. Int. Ed. Engl.*, vol. 46, no. 8, pp. 1222–44, Jan. 2007.

[16] R. M. Cornell and U. Schwertmann, *The iron oxides : structure, properties, reactions, occurrence and uses*, vol. 39, no. 8. 1997.

[17] L. Chang *et al.*, "Magnetic structure of greigite (Fe3S4) probed by neutron powder diffraction and polarized neutron diffraction," *J. Geophys. Res. Solid Earth*, vol. 114, no. 7, pp. 1–10, 2009.

[18] A. Kolhatkar, A. Jamison, D. Litvinov, R. Willson, and T. Lee, *Tuning the Magnetic Properties of Nanoparticles*, vol. 14, no. 8. 2013.

[19] J. Bain, "Biomimetic synthesis of magnetosomes for biomedical application," The University of Sheffield, 2016.

[20] L. Yan, S. Zhang, P. Chen, H. Liu, H. Yin, and H. Li, "Magnetotactic bacteria, magnetosomes and their application.," *Microbiol. Res.*, vol. 167, no. 9, pp. 507–19, Oct. 2012.

[21] S. Laurent *et al.*, "Magnetic Iron Oxide Nanoparticles : Synthesis , Stabilization , Vectorization , Physicochemical Characterizations , and Biological Applications," *Am. Chem. Soc.*, vol. 108, pp. 2064–2110, 2008.

[22] H. Fischer, G. Mastrogiacomo, J. F. Löffler, R. J. Warthmann, P. G. Weidler, and A. U. Gehring, "Ferromagnetic resonance and magnetic characteristics of intact magnetosome chains in Magnetospirillum gryphiswaldense," *Earth Planet. Sci. Lett.*,

vol. 270, no. 3–4, pp. 200–208, Jun. 2008.

[23]   C. Desvaux *et al.*, "Multimillimetre-large superlattices of air-stable iron-cobalt nanoparticles.," *Nat. Mater.*, vol. 4, no. 10, pp. 750–753, 2005.

[24]   S. Staniland, W. Williams, N. Telling, G. Van Der Laan, A. Harrison, and B. Ward, "Controlled cobalt doping of magnetosomes in vivo.," *Nat. Nanotechnol.*, vol. 3, no. 3, pp. 158–162, 2008.

[25]   A. K. Gupta and M. Gupta, "Cytotoxicity suppression and cellular uptake enhancement of surface modified magnetic nanoparticles," *Biomaterials*, vol. 26, no. 13, pp. 1565–1573, 2005.

[26]   D. Kim, N. Lee, M. Park, B. H. Kim, K. An, and T. Hyeon, "Synthesis of Uniform Ferrimagnetic Magnetite Nanocubes - Journal of the American Chemical Society (ACS Publications)," *J. Am. Chem. Soc.*, vol. 131, no. 2, pp. 454–5, 2009.

[27]   X. Li, H. Xu, Z. S. Chen, and G. Chen, "Biosynthesis of nanoparticles by microorganisms and their applications," *J. Nanomater.*, vol. 2011, 2011.

[28]   Y. W. Marvin G Marvin, Cynthia L. Warner, Addleman Shane, "Magnetic nanomaterial for Environment Applications," in *Magnetic Nanomaterials*, WILEY-VCH., K. S. S. R. Challa, Ed. Weinheim: WILEY-VCH, 2009, pp. 311–344.

[29]   A. K. Gupta and M. Gupta, "Synthesis and surface engineering of iron oxide nanoparticles for biomedical applications.," *Biomaterials*, vol. 26, no. 18, pp. 3995–4021, Jun. 2005.

[30]   G. S. Demirer, A. C. Okur, and S. Kizilel, "Synthesis and design of biologically inspired biocompatible iron oxide nanoparticles for biomedical applications," *J. Mater. Chem. B*, vol. 3, no. 40, pp. 7831–7849, 2015.

[31]   Y. Amemiya, A. Arakaki, S. S. Staniland, T. Tanaka, and T. Matsunaga, "Controlled formation of magnetite crystal by partial oxidation of ferrous hydroxide in the presence of recombinant magnetotactic bacterial protein Mms6," *Biomaterials*, vol. 28, no. 35, pp. 5381–5389, 2007.

[32]   a. E. Regazzoni, G. a. Urrutia, M. a. Blesa, and a. J. G. Maroto, "Some observations on

the composition and morphology of synthetic magnetites obtained by different routes," *J. Inorg. Nucl. Chem.*, vol. 43, no. 7, pp. 1489–1493, 1981.

[33]   A. Arakaki, F. Masuda, Y. Amemiya, T. Tanaka, and T. Matsunaga, "Control of the morphology and size of magnetite particles with peptides mimicking the Mms6 protein from magnetotactic bacteria," *J. Colloid Interface Sci.*, vol. 343, no. 1, pp. 65–70, 2010.

[34]   T. Sugimoto and E. Matijević, "Formation of uniform spherical magnetite particles by crystallization from ferrous hydroxide gels," *J. Colloid Interface Sci.*, vol. 74, no. 1, pp. 227–243, 1980.

[35]   D. Yoo, J. H. Lee, T. H. Shin, and J. Cheon, "Theranostic magnetic nanoparticles," *Acc. Chem. Res.*, vol. 44, no. 10, pp. 863–874, 2011.

[36]   A. Andrade, R. Ferreira, J. Fabris, and R. Domingues, "Coating Nanomagnetic Particles for Biomedical Applications," *Biomed. Eng. - Front. Challenges*, 2011.

[37]   E. Umut, "Surface Modification of Nanoparticles Used in Biomedical Applications," *Mod. Surf. Eng. Treat.*, vol. 05, no. 22, pp. 185–208, 2013.

[38]   A. Arakaki, H. Nakazawa, M. Nemoto, T. Mori, and T. Matsunaga, "Formation of magnetite by bacteria and its application.," *J. R. Soc. Interface*, vol. 5, pp. 977–999, 2008.

[39]   X. Liu, M. D. Kaminski, Y. Guan, H. Chen, H. Liu, and A. J. Rosengart, "Preparation and characterization of hydrophobic superparamagnetic magnetite gel," *J. Magn. Magn. Mater.*, vol. 306, no. 2, pp. 248–253, 2006.

[40]   A. Komeili, "Molecular mechanisms of magnetosome formation.," *Annu. Rev. Biochem.*, vol. 76, pp. 351–366, 2007.

[41]   C. Jogler, D. Schuler, and D. Schüler, "Genomics, Genetics, and Cell Biology of Magnetosome Formation," *Annu. Rev. Microbiol.*, vol. 63, pp. 501–521, 2009.

[42]   R. Blakemore, "Magnetotactic Bacteria Abstract," *Science (80-.).*, no. October, pp. 1–4, 1975.

[43]   T. S. Silveira, J. L. Martins, K. T. Silva, F. Abreu, and U. Lins, "Microscopy studies on uncultivated magnetotactic bacteria," *Mod. Res. Educ. Top. Microsc.*, pp. 111–121,

2007.

[44] T. Matsunaga and Y. Okamura, "Genes and proteins involved in bacterial magnetic particle formation," *Trends Microbiol.*, vol. 11, no. 11, pp. 536–541, Nov. 2003.

[45] C. B. Flies and D. Schu, "Combined Approach for Characterization of Uncultivated Magnetotactic Bacteria from Various Aquatic Environments," *Appl. Environ. Microbiol.*, vol. 71, no. 5, pp. 2723–2731, 2005.

[46] D. a. Bazylinski, "Controlled biomineralization of magnetic minerals by magnetotactic bacteria," *Chem. Geol.*, vol. 132, no. 1–4, pp. 191–198, 1996.

[47] S. Dasdag, "Magnetotactic Bacteria and their Application in Medicine," *J. Phys. Chem. Biophys.*, vol. 2, no. 2, 2014.

[48] A. Arakaki, K. Shimizu, M. Oda, T. Sakamoto, T. Nishimura, and T. Kato, "Biomineralization-inspired synthesis of functional organic/inorganic hybrid materials: organic molecular control of self-organization of hybrids.," *Org. Biomol. Chem.*, vol. 13, no. 4, pp. 974–89, Jan. 2015.

[49] T. Matsunaga, Y. Okamura, Y. Fukuda, A. T. Wahyudi, Y. Murase, and H. Takeyama, "Complete genome sequence of the facultative anaerobic magnetotactic bacterium Magnetospirillum sp. strain AMB-1," *DNA Res.*, vol. 12, no. 3, pp. 157–166, 2005.

[50] M. Richter *et al.*, "Comparative genome analysis of four magnetotactic bacteria reveals a complex set of group-specific genes implicated in magnetosome biomineralization and function," *J. Bacteriol.*, vol. 189, no. 13, pp. 4899–4910, 2007.

[51] D. Schüler, "Genetics and cell biology of magnetosome formation in magnetotactic bacteria," *FEMS Microbiol. Rev.*, vol. 32, no. 4, pp. 654–672, 2008.

[52] R. Uebe and D. Schüler, "Magnetosome biogenesis in magnetotactic bacteria," *Nat. Rev. Microbiol.*, vol. 14, no. 10, pp. 621–637, 2016.

[53] A. Komeili, H. Vali, T. J. Beveridge, and D. K. Newman, "Magnetosome vesicles are present before magnetite formation, and MamA is required for their activation.," *Proc. Natl. Acad. Sci. U. S. A.*, vol. 101, no. 11, pp. 3839–3844, 2004.

[54] S. Schübbe *et al.*, "Characterization of a Spontaneous Nonmagnetic Mutant of

Magnetospirillum gryphiswaldense Reveals a Large Deletion Comprising a Putative Magnetosome Island," *Society*, vol. 185, no. 19, pp. 5779–5790, 2003.

[55]   Y. Fukuda, Y. Okamura, H. Takeyama, and T. Matsunaga, "Dynamic analysis of a genomic island in Magnetospirillum sp. strain AMB-1 reveals how magnetosome synthesis developed," *FEBS Lett.*, vol. 580, no. 3, pp. 801–812, 2006.

[56]   S. Barber-Zucker, N. Keren-Khadmy, and R. Zarivach, "From invagination to navigation: The story of magnetosome-associated proteins in magnetotactic bacteria," *Protein Sci.*, vol. 25, pp. 338–351, 2016.

[57]   D. Faiver and D. Schüler, "Magnetotactic Bacteria and magnetosomes," *Am. Chem. Soc.*, vol. 108, no. September, pp. 4875–4898, 2008.

[58]   A. Arakaki, K. Shimizu, M. Oda, T. Sakamoto, T. Nishimura, and T. Kato, "Biomineralization-inspired synthesis of functional organic/inorganic hybrid materials: organic molecular control of self-organization of hybrids," *Org. Biomol. Chem.*, vol. 13, no. 4, pp. 974–989, 2015.

[59]   A. Lohße *et al.*, "Genetic dissection of the mamAB and mms6 operons reveals a gene set essential for magnetosome biogenesis in magnetospirillum gryphiswaldense," *J. Bacteriol.*, vol. 196, no. 14, pp. 2658–2669, 2014.

[60]   M. Tanaka, Y. Okamura, A. Arakaki, T. Tanaka, H. Takeyama, and T. Matsunaga, "Origin of magnetosome membrane: Proteomic analysis of magnetosome membrane and comparison with cytoplasmic membrane," *Proteomics*, vol. 6, no. 19, pp. 5234–5247, 2006.

[61]   R. R. and D. S. Karen Grünberg, Eva-Christina Müller, Albrecht Otto, Regina Reszka, Dietmar Linder, Michael Kube, "Biochemical and Proteomic Analysis of the Magnetosome Membrane in Magnetospirillum gryphiswaldense," *Appl. Environ. Microbiol.*, vol. 70, no. 2, pp. 1040–1050, 2004.

[62]   Y. A. Gorby, T. J. Beveridge, and R. P. Blakemore1, "Characterization of the Bacterial Magnetosome Membrane," *J. Bacteriol.*, vol. 170, no. 2, pp. 834–841, 1988.

[63]   Y. Okuda, K. Denda, and Y. Fukumori, "Cloning and sequencing of a gene encoding a

new member of the tetratricopeptide protein family from magnetosomes of Magnetospirillum magnetotacticum," *Gene*, vol. 171, no. 1, pp. 99–102, 1996.

[64] K. Grünberg, C. Wawer, and B. M. Tebo, "A Large Gene Cluster Encoding Several Magnetosome Proteins Is Conserved in Different Species of Magnetotactic Bacteria A Large Gene Cluster Encoding Several Magnetosome Proteins Is Conserved in Different Species of Magnetotactic Bacteria," *Appl. Environ. Microbiol.*, vol. 67, no. 10, pp. 4573–4582, 2001.

[65] A. Taoka, R. Asada, H. Sasaki, K. Anzawa, L. F. Wu, and Y. Fukumori, "Spatial localizations of Mam22 and Mam12 in the magnetosomes of Magnetospirillum magnetotacticum," *J. Bacteriol.*, vol. 188, no. 11, pp. 3805–3812, 2006.

[66] D. Schüler and E. Baeuerlein, "Iron-limited growth and kinetics of iron uptake in Magnetospirilum gryphiswaldense," *Arch. Microbiol.*, vol. 166, pp. 301–307, 1996.

[67] S. D. Grunberg Karen, Reszka Regina, "Biochemical and Genetic Analysis of the Magnetosome Membrane in Magnetospirillum gryphiswaldense," *Appl. Environ. Microbiol.*, vol. 70, no. 2, pp. 1040–1050, 2004.

[68] O. Raschdorf, Y. Forstner, I. Kolinko, R. Uebe, J. M. Plitzko, and D. Schüler, "Genetic and Ultrastructural Analysis Reveals the Key Players and Initial Steps of Bacterial Magnetosome Membrane Biogenesis," *PLoS Genet.*, vol. 12, no. 6, pp. 1–23, 2016.

[69] O. Raschdorf, F. D. Müller, M. Pósfai, J. M. Plitzko, and D. Schüler, "The magnetosome proteins MamX, MamZ and MamH are involved in redox control of magnetite biomineralization in Magnetospirillum gryphiswaldense," *Mol. Microbiol.*, vol. 89, no. 5, pp. 872–886, 2013.

[70] A. Arakaki, J. Webb, and T. Matsunaga, "A novel protein tightly bound to bacterial magnetic particles in Magnetospirillum magneticum strain AMB-1," *J. Biol. Chem.*, vol. 278, no. 10, pp. 8745–8750, 2003.

[71] A. Scheffel, A. Gärdes, K. Grünberg, G. Wanner, and D. Schüler, "The major magnetosome proteins MamGFDC are not essential for magnetite biomineralization in Magnetospirillum gryphiswaldense but regulate the size of magnetosome crystals," *J. Bacteriol.*, vol. 190, no. 1, pp. 377–386, 2008.

[72] S. R. Jones *et al.*, "Genetic and biochemical investigations of the role of MamP in redox control of iron biomineralization in *Magnetospirillum magneticum*.," *Proc. Natl. Acad. Sci. U. S. A.*, vol. 112, no. 13, pp. 3904–3909, 2015.

[73] M. Richter *et al.*, "Comparative genome analysis of four magnetotactic bacteria reveals a complex set of group-specific genes implicated in magnetosome biomineralization and function," *J. Bacteriol.*, vol. 189, no. 13, pp. 4899–4910, 2007.

[74] N. D. and J. G. J. Komeili Arash, "Magnetosomes are cell membrane invagination organized by the actin-like protein MamK," *J. Meteorol. Soc. Japan*, vol. 311, no. February, pp. 1141–1146, 2006.

[75] T. Shin, Y. Choi, S. Kim, and J. Cheon, "Recent advances in magnetic nanoparticle-based multi-modal imaging," *Chem. Soc. Rev.*, 2015.

[76] A. S. Mathuriya, "Magnetotactic bacteria for cancer therapy," *Biotechnol. Lett.*, vol. 37, no. 3, pp. 491–498, 2015.

[77] Lightbox Radiology Education, *Introducrtion to Magnetic Resonance Image (MRI) Physical*. 2013.

[78] J.-H. Lee *et al.*, "Artificially engineered magnetic nanoparticles for ultra-sensitive molecular imaging.," *Nat. Med.*, vol. 13, no. 1, pp. 95–99, 2007.

[79] Brougham Dermot F. and Gun' Ko Yurii, "Magnetic Nanomaterials as MRI Contrast Agent," in *Magnetic Nanomaterials*, Volume 4., C. S. S. R. Kumar, Ed. Germany: WILY-VCH Weinheim, 2009, pp. 119–185.

[80] Y. Jun, J. Choi, and J. Cheon, "Heterostructured magnetic nanoparticles : their versatility and high performance capabilities," *R. Soc. Chem.*, pp. 1203–1214, 2007.

[81] Y. Cao, L. Xu, Y. Kuang, D. Xiong, and R. Pei, "Gadolinium-based nanoscale MRI contrast agents for tumor imaging," *J. Mater. Chem. B*, vol. 5, no. 19, pp. 3431–3461, 2017.

[82] T. D. Schladt, K. Schneider, H. Schild, and W. Tremel, "Synthesis and bio-functionalization of magnetic nanoparticles for medical diagnosis and treatment," *Dalt. Trans.*, vol. 40, no. 24, p. 6315, 2011.

[83] C. Sun, J. Lee, and M. Zhang, "Magnetic nanoparticles in MR imaging and drug delivery,"

Adv. Drug Deliv. Rev., vol. 60, no. 11, pp. 1252–1265, Aug. 2008.

[84]   P. Sprawls, "Magnetic Resonance Imaging: Principles, Methods, and Technique," in *medical physical*, Volume 177., 2001, pp. 173–177.

[85]   L. Yang *et al.*, "Receptor-Targeted Nanoparticles for In vivo Imaging of Breast Cancer," *Clin. Cancer Res.*, vol. 15, no. 14, pp. 4722–4732, 2009.

[86]   M. Benoit, D. Mayer, Y. Barak, and I. Chen, "Visualizing implanted tumors in mice with magnetic resonance imaging using magnetotactic bacteria," *Clin. Cancer …*, vol. 15, no. 16, pp. 5170–5177, 2009.

[87]   F. C. Therapy, B. Flandrin, and L. Anbiophy-fre, "Chains of Magnetosomes Extracted from AMB-1 Magnetotactic Bacteria for Application in Alternative Magnetic Field Cancer Therapy.," *Am. Chem. socitey*, vol. 5, no. 8, pp. 6279–6296, 2011.

[88]   National Cancer Institute (NCI), "hyperthermia to treat cancer," *American cancer society*, 2013. [Online]. Available: http://www.cancer.org/treatment/treatmentsandsideeffects/treatmenttypes/hypert hermia. [Accessed: 24-Apr-2015].

[89]   R. T. Gordon, J. R. Hines, and D. Gordon, "Intracellular hyperthermia a biophysical approach to cancer treatment via intracellular temperature and biophysical alterations," *Med. Hypotheses*, vol. 5, no. 1, pp. 83–102, 1979.

[90]   R. sundrarajan and S. J. D. Arutselvan Natarajan, "Magnetic Nanomaterials," in *Magntect Nanomaterials as MRI contrast Agent*, C. Kumar, Ed. WILY-VCH Weinheim, 2009, pp. 209–257.

[91]   V. Mulens, P. Morales, and D. F. Barber, "Development of Magnetic Nanoparticles for Cancer Gene Therapy : A Comprehensive Review," *ISRN Nanomater.*, vol. 2013, p. 14, 2013.

[92]   E. Alphandéry and R. Frankel, "Applications of magnetosomes synthesized by magnetotactic bacteria in medicine," *Bioeng. Biotechnol.*, vol. 2, no. 2014, 2014.

[93]   S. Mannucci *et al.*, "Magnetic nanoparticles from Magnetospirillum gryphiswaldense increase the efficacy of thermotherapy in a model of colon carcinoma.," *PLoS One*, vol.

9, no. 10, p. e108959, Jan. 2014.

[94]   E. Alphandéry, "Applications of magnetosomes synthesized by magnetotactic bacteria in medicine.," *Front. Bioeng. Biotechnol.*, vol. 2, no. March, p. 5, 2014.

[95]   H. S. Huang and J. F. Hainfeld, "Intravenous magnetic nanoparticle cancer hyperthermia," *Int. J. Nanomedicine*, vol. 8, pp. 2521–2532, 2013.

[96]   V. Zǎvišová *et al.*, "Magnetic fluid poly(ethylene glycol) with moderate anticancer activity," *J. Magn. Magn. Mater.*, vol. 323, no. 10, pp. 1408–1412, 2011.

[97]   S. Balivada *et al.*, "A/C magnetic hyperthermia of melanoma mediated by iron(0)/iron oxide core/shell magnetic nanoparticles: A mouse study," *BMC Cancer*, vol. 10, 2010.

[98]   D. H. Kim, K. N. Kim, K. M. Kim, and Y. K. Lee, "Targeting to carcinoma cells with chitosan- and starch-coated magnetic nanoparticles for magnetic hyperthermia," *J. Biomed. Mater. Res. - Part A*, vol. 88, no. 1, pp. 1–11, 2009.

[99]   A. Ito *et al.*, "Magnetite nanoparticle-loaded anti-HER2 immunoliposomes for combination of antibody therapy with hyperthermia," *Cancer Lett.*, vol. 212, no. 2, pp. 167–175, 2004.

[100]   T. Kikumori, T. Kobayashi, M. Sawaki, and T. Imai, "Anti-cancer effect of hyperthermia on breast cancer by magnetite nanoparticle-loaded anti-HER2 immunoliposomes," *Breast Cancer Res. Treat.*, vol. 113, no. 3, pp. 435–441, 2009.

[101]   E. Alphandéry, I. Chebbi, F. Guyot, and M. Durand-Dubief, "Use of bacterial magnetosomes in the magnetic hyperthermia treatment of tumours: a review.," *Int. J. Hyperthermia*, vol. 29, no. 8, pp. 801–9, 2013.

[102]   K. Hayashi *et al.*, "High-frequency, magnetic-field-responsive drug release from magnetic nanoparticle/organic hybrid based on hyperthermic effect," *ACS Appl. Mater. Interfaces*, vol. 2, no. 7, pp. 1903–1911, 2010.

[103]   C. Carvallo, N. Menguy, and I. Chebbi, "Chains of Cobalt Doped Magnetosomes Extracted from AMB-1 Magnetotactic Bacteria for Application in Alternative Magnetic Field Cancer Therapy," *J. Phys. Chem.*, vol. 115, no. 24, pp. 11920–11924, 2011.

[104]   K. Park, "Facing the truth about nanotechnology in drug delivery," *ACS Nano*, vol. 7, no.

215

9, pp. 7442–7447, 2013.

[105] F. X. Gu *et al.*, "Targeted nanoparticles for cancer therapy," *Nano Today*, vol. 2, no. 3, pp. 14–21, Jun. 2007.

[106] A. S. Lãbbe, C. Bergemann, W. Huhnt, T. Fricke, and H. Riess, "Predinical Experiences Drug Targeting : Tolerance and Efficacy," *Cancer Res.*, vol. 56, pp. 4694–4701, 1996.

[107] D. Jon, "Magnetic Nanoparticles for Drug Delivery," *drug Dev. Res.*, vol. 67, pp. 55–60, 2006.

[108] P. O. Magalhães, A. M. Lopes, P. G. Mazzola, C. Rangel-yagui, and T. C. V Penna, "Methods of Endotoxin Removal from Biological Preparations : a Review Methods of Endotoxin Removal from Biological Preparations : a Review Methods of Endotoxin Removal from Biological Preparations : a Review," *J pharm Pharm. Sci*, vol. 10, no. 3, pp. 388–404, 2011.

[109] and C. F. N. C R Raetz, R J Ulevitch, S D Wright, C H Sibley, A Ding, "Gram-negative endotoxin: an extraordinary lipid with profound effects on eukaryotic signal transduction," *the FASEB*, vol. 5, no. 12, pp. 2652–2660, 1991.

[110] C. Hirayama and M. Sakata, "Chromatographic removal of endotoxin from protein solutions by polymer particles," *J. Chromatogr. B Anal. Technol. Biomed. Life Sci.*, vol. 781, no. 1–2, pp. 419–432, 2002.

[111] B. Barat and A. M. Wu, "Metabolic biotinylation of recombinant antibody by biotin ligase retained in the endoplasmic reticulum," *Biomol. Eng.*, vol. 24, no. 3, pp. 283–291, 2007.

[112] Y. Li and R. Sousa, "Expression and purification of E. coli BirA biotin ligase for in vitro biotinylation," *Protein Expr. Purif.*, vol. 82, no. 1, pp. 162–167, 2012.

[113] J. Piehler, A. Brecht, and G. Gauglitz, "Affinity detection of low molecular weight analytes," *Anal. Chem.*, vol. 68, no. 1, pp. 139–143, 1996.

[114] T. Scientific, "Biotination," *ThermoFisher scientific*, 2016. [Online]. Available: https://www.thermofisher.com/uk/en/home/life-science/protein-biology/protein-biology-learning-center/protein-biology-resource-library/pierce-protein-

methods/biotinylation.html.

[115] T. Scientific, "biotinylation Protein Biology Resource," *Scientific, ThermoFisher*, 2016. [Online]. Available: https://www.thermofisher.com/uk/en/home/life-science/protein-biology/protein-biology-learning-center/protein-biology-resource-library/pierce-protein-methods/biotinylation.html.

[116] M. G. Cull and P. J. Schatz, "Biotinylation of proteins in vivo and in vitro using small peptide tags," *Appl. Chimeric Genes Hybrid Proteins Part A Gene Expr. Protein Purif.*, vol. Volume 326, no. 1996, pp. 430–440, 2000.

[117] E. Choi-Rhee, H. Schulman, and J. E. Cronan, "Promiscuous protein biotinylation by Escherichia coli biotin protein ligase.," *Protein Sci.*, vol. 13, no. 11, pp. 3043–50, 2004.

[118] A. B. Emerman, Z.-R. Zhang, O. Chakrabarti, and R. S. Hegde, "Compartment-restricted biotinylation reveals novel features of prion protein metabolism in vivo.," *Mol. Biol. Cell*, vol. 21, no. 24, pp. 4325–4337, 2010.

[119] A. Gautier and M. J. Hinner, "Site-Specific Protein Labeling: Methods and Protocols," *Eur. PMC Funders Gr. Author Manuscr.*, no. 4, pp. 171–184, 2015.

[120] C. M. Dundas, D. Demonte, and S. Park, "Streptavidin-biotin technology: Improvements and innovations in chemical and biological applications," *Appl. Microbiol. Biotechnol.*, vol. 97, no. 21, pp. 9343–9353, 2013.

[121] T. Scientific, "Biotinylation _ Thermo Fisher Scientific," *Biotinylation Protein Biology Resource Library Pierce Protein Methods*, 2018. [Online]. Available: https://www.thermofisher.com/uk/en/home/life-science/protein-biology/protein-biology-learning-center/protein-biology-resource-library/pierce-protein-methods/biotinylation.html. [Accessed: 22-Sep-2017].

[122] J. Alftrén, K. E. Ottow, and T. J. Hobley, "In vivo biotinylation of recombinant beta-glucosidase enables simultaneous purification and immobilization on streptavidin coated magnetic particles," *J. Mol. Catal. B Enzym.*, vol. 94, pp. 29–35, 2013.

[123] Y. Maeda, T. Yoshino, and T. Matsunaga, "In vivo biotinylation of bacterial magnetic particles by a truncated form of escherichia coli biotin ligase and biotin acceptor

peptide," *Appl. Environ. Microbiol.*, vol. 76, no. 17, pp. 5785–5790, 2010.

[124] J. Y. Lee *et al.*, "Concurrent chemotherapy and pulsed high-intensity focused ultrasound therapy for the treatment of unresectable pancreatic cancer: initial experiences.," *Korean J. Radiol.*, vol. 12, no. 2, pp. 176–186, 2011.

[125] E. Alphandéry, "Perspectives of breast cancer thermotherapies," *J. Cancer*, vol. 5, no. 6, pp. 472–479, 2014.

[126] Cancer Treatment Centers of America, "Triple-Negative Breast Cancer – Treatment Options | CTCA." 2017.

[127] ECACC, "Cell line profile," *Eur. Collect. Cell Cult.*, vol. 2780, no. 93112519, p. 87092802, 2017.

[128] E. Alphandéry, "Perspectives of breast cancer thermotherapies," *Journal of Cancer*. pp. 472–479, 2014.

[129] Y. Amemiya, T. Tanaka, B. Yoza, and T. Matsunaga, "Novel detection system for biomolecules using nano-sized bacterial magnetic particles and magnetic force microscopy.," *J. Biotechnol.*, vol. 120, no. 3, pp. 308–14, Nov. 2005.

[130] N. Vitamin, B. D. Bacto, and N. Distilled, "380. magnetospirillum medium," 2014. .

[131] F. Herranz *et al.*, "Superparamagnetic Nanoparticles for Atherosclerosis Imaging," *Nanomaterials*, vol. 4, no. 2, pp. 408–438, 2014.

[132] P. B. Shete, R. M. Patil, B. M. Tiwale, and S. H. Pawar, "Water dispersible oleic acid-coated Fe_3O_4 nanoparticles for biomedical applications," *J. Magn. Magn. Mater.*, vol. 377, pp. 406–410, 2015.

[133] H. Reimer, Ludwig, Kohl, *Transmission Electron Microscopy*, vol. 36. Springer New York, 2008.

[134] R. Brydson, "Electron energy loss spectroscopy," *Microsc. imaging Sci. Pract. approaches to Appl. Res. Educ.*, 2001.

[135] Robert J. Hunter, *Zeta Potential in Colloid Science: Principles and Applications*, Third. Academic press limited, 1988.

[136] M. Instruments, "Zeta potential: An Introduction in 30 minutes," *Zetasizer Nano Serles Technical Note. MRK654-01*, 2006. [Online]. Available: http://scholar.google.com/scholar?hl=en&btnG=Search&q=intitle:Zeta+Potential+An +Introduction+in+30+Minutes#0. [Accessed: 11-May-2016].

[137] S. Dutz and R. Hergt, "Magnetic particle hyperthermia--a promising tumour therapy?," *Nanotechnology*, vol. 25, no. 45, p. 452001, 2014.

[138] R. M. Cornell and U. Sshwertmann, *The iron oxides: structures, properties, reactions, occurrences and uses*, First. New York: VCH, New York, 1996.

[139] D. Gao, S. Shi, K. Tao, B. Xia, and D. Xue, "Tunable ferromagnetic ordering in MoS 2 nanosheets with fluorine adsorption," *Nanoscale*, vol. 7, no. 9, pp. 4211–4216, 2015.

[140] D. W. R. Joseph Sambrook, *Molecular cloning : a laboratory manual*, Third. Cold Spring Harbor, NY: Cold Spring Harbor, N.Y. : Cold Spring Harbor Laboratory, c2001., 2001.

[141] S. Das and H. R. Dash, *Microbial Biotechnology- A Laboratory Manual for Bacterial Systems*, vol. 2. 2015.

[142] R. Green and E. J. Rogers, "Chemical Transformation of E. coli Rachel," *NIH Public*, vol. 529, pp. 329–33, 2013.

[143] S. lakshmi Reddy, T. Endo, and G. silv. reddy claudia Simones, "Basic UV / Visible Spectrophotometry," 2012.

[144] wikipedia, "Peomoter (genetics)," *wikipedia*, 2018. [Online]. Available: https://simple.wikipedia.org/wiki/Promoter_(genetics).

[145] D. F. Westra, G. W. Welling, D. G. A. M. Koedijk, A. J. Scheffer, T. H. The, and S. Welling-Wester, "Immobilised metal-ion affinity chromatography purification of histidine-tagged recombinant proteins: A wash step with a low concentration of EDTA," *J. Chromatogr. B Biomed. Sci. Appl.*, vol. 760, no. 1, pp. 129–136, 2001.

[146] Life Science Group, "A Guide to Polyacrylamide Gel Electrophoresis and Detection I : Theory and Product Selection Part II : Methods Part III : Troubleshooting Part IV :," *Bio-Rad laboratories*, 2012. [Online]. Available: http://www.bio-rad.com/webroot/web/pdf/lsr/literature/Bulletin_6040.pdf.

[147] U. K. Laemmli, "Cleavage of structural proteins during the assembly of bacteriophage T4," *Nature*, vol. 227, pp. 680–685, 1970.

[148] B. Fadeel and S. Orrenius, "Apoptosis: A basic biological phenomenon with wide-ranging implications in human disease," *Journal of Internal Medicine*, vol. 258, no. 6. pp. 479–517, 2005.

[149] S. L. Fink, B. T. Cookson, S. L. Fink, and B. T. Cookson, "Apoptosis , Pyroptosis , and Necrosis : Mechanistic Description of Dead and Dying Eukaryotic Cells," *Infect. Immun.*, vol. 73, no. 4, pp. 1907–1916, 2005.

[150] D. Wlodkowic, J. Skommer, and Z. Darzynkiewicz, "Flow cytometry-based apoptosis detection.," *Methods Mol. Biol.*, vol. 559, no. 0, pp. 19–32, 2009.

[151] L. Casciola-Rosen, A. Rosen, M. Petri, and M. Schlissel, "Surface blebs on apoptotic cells are sites of enhanced procoagulant activity: implications for coagulation events and antigenic spread in systemic lupus erythematosus.," *Proc. Natl. Acad. Sci. U. S. A.*, vol. 93, no. 4, pp. 1624–1629, 1996.

[152] I. Vermes, C. Haanen, H. Steffens-Nakken, and C. Reutellingsperger, "A novel assay for apoptosis Flow cytometric detection of phosphatidylserine expression on early apoptotic cells using fluorescein labelled Annexin V," *J. Immunol. Methods*, vol. 184, no. 1, pp. 39–51, 1995.

[153] E. Alphandéry, "TREATMENT OF CANCER OR TUMORS INDUCED BY THE RELEASE OF HEAT GENERATED BY VARIOUS CHAINS OF MAGNETOSOMES EXTRACTED FROM MAGNETOTACTIC BACTERIA AND SUBMITTED TO AN ALTERNATIVE MAGNETIC FIELD," *Methods*, vol. 61, no. 19, 2012.

[154] Y.-W. Jun *et al.*, "Nanoscale size effect of magnetic nanocrystals and their utilization for cancer diagnosis via magnetic resonance imaging.," *J. Am. Chem. Soc.*, vol. 127, no. 16, pp. 5732–5733, 2005.

[155] M. Tanaka, R. Brown, N. Hondow, A. Arakaki, T. Matsunaga, and S. Staniland, "Highest levels of Cu, Mn and Co doped into nanomagnetic magnetosomes through optimized biomineralisation," *J. Mater. Chem.*, vol. 22, no. 24, p. 11919, 2012.

[156] T. Perez-Gonzalez, T. Prosorov, A. Yebra-Rodriguez, D. a Bazylinski, and C. Jiminez-Lopez, "Mn incorporation in magnetosomes: New possibilities for the nanotechnological applications of biomagnetite," *Macla*, vol. 13, pp. 171–172, 2010.

[157] D. A. Bazylinski, A. J. Garratt-Reed, A. Abedi, and R. B. Frankel, "Copper association with iron sulfide magnetosomes in a magnetotactic bacterium," *Arch. Microbiol.*, vol. 160, no. 1, pp. 35–42, 1993.

[158] G. Mirabello, J. J. M. Lenders, and N. A. J. M. Sommerdijk, "Bioinspired synthesis of magnetite nanoparticles," *Chem. Soc. Rev.*, vol. 45, no. 18, pp. 5085–5106, 2016.

[159] O. Veiseh, J. W. Gunn, and M. Zhang, "Design and fabrication of magnetic nanoparticles for targeted drug delivery and imaging.," *Adv. Drug Deliv. Rev.*, vol. 62, no. 3, pp. 284–304, Mar. 2010.

[160] K. Petcharoen and A. Sirivat, "Synthesis and characterization of magnetite nanoparticles via the chemical co-precipitation method," *Mater. Sci. Eng. B Solid-State Mater. Adv. Technol.*, vol. 177, no. 5, pp. 421–427, 2012.

[161] S. A. Kahani and Z. Yagini, "A comparison between chemical synthesis magnetite nanoparticles and biosynthesis magnetite," *Bioinorg. Chem. Appl.*, vol. 2014, 2014.

[162] Y. Cedeño-Mattei, O. Perales-Perez, M. S. Tomar, F. Roman, P. M. Voyles, and W. G. Stratton, "Tuning of magnetic properties in cobalt ferrite nanocrystals," *J. Appl. Phys.*, vol. 103, no. 7, 2008.

[163] C. Lang and D. Sch??ler, "Biogenic nanoparticles: Production, characterization, and application of bacterial magnetosomes," *J. Phys. Condens. Matter*, vol. 18, no. 38, 2006.

[164] J.-W. Moon *et al.*, "Large-scale production of magnetic nanoparticles using bacterial fermentation," *J. Ind. Microbiol. Biotechnol.*, vol. 37, no. 10, pp. 1023–1031, 2010.

[165] J. W. Moon *et al.*, "Magnetic response of microbially synthesized transition metal- and lanthanide-substituted nano-sized magnetites," *J. Magn. Magn. Mater.*, vol. 313, no. 2, pp. 283–292, 2007.

[166] J. Li *et al.*, "Controlled cobalt doping in the spinel structure of magnetosome magnetite: new evidences from element- and site-specific X-ray magnetic circular dichroism

analyses," *J. R. Soc. Interface*, vol. 13, no. 121, p. 20160355, 2016.

[167] D. E. Kile, D. D. Eberl, A. R. Hoch, and M. M. Reddy, "An assessment of calcite crystal growth mechanisms based on crystal size distributions," *Geochim. Cosmochim. Acta*, vol. 64, no. 17, pp. 2937–2950, 2000.

[168] L. Han, S. Li, Y. Yang, F. Zhao, J. Huang, and J. Chang, "Comparison of magnetite nanocrystal formed by biomineralization and chemosynthesis," *J. Magn. Magn. Mater.*, vol. 313, no. 1, pp. 236–242, 2007.

[169] J. R. Correa, D. Canetti, R. Castillo, J. C. Llópiz, and J. Dufour, "Influence of the precipitation pH of magnetite in the oxidation process to maghemite," *Mater. Res. Bull.*, vol. 41, no. 4, pp. 703–713, 2006.

[170] J. M. Galloway, A. Arakaki, F. Masuda, T. Tanaka, T. Matsunaga, and S. S. Staniland, "Magnetic bacterial protein Mms6 controls morphology, crystallinity and magnetism of cobalt-doped magnetite nanoparticles in vitro," *J. Mater. Chem.*, vol. 21, no. 39, p. 15244, 2011.

[171] M. C. Mascolo, Y. Pei, and T. A. Ring, "Room Temperature Co-Precipitation Synthesis of Magnetite Nanoparticles in a Large ph Window with Different Bases," *Materials (Basel).*, vol. 6, no. 12, pp. 5549–5567, 2013.

[172] F. Herranz, M. P. Morales, A. G. Roca, M. Desco, and J. Ruiz-Cabello, "A New Method for the Rapid Synthesis of Water Stable Superparamagnetic Nanoparticles," *Chem. - A Eur. J.*, vol. 14, no. 30, pp. 9126–9130, 2008.

[173] E. Vismara *et al.*, "Non-covalent synthesis of metal oxide nanoparticle-heparin hybrid systems: a new approach to bioactive nanoparticles.," *Int. J. Mol. Sci.*, vol. 14, pp. 13463–13481, 2013.

[174] S. Shukla, V. Arora, A. Jadaun, J. Kumar, N. Singh, and V. K. Jain, "Magnetic removal of entamoeba cysts from water using chitosan oligosaccharide-coated iron oxide nanoparticles," *Int. J. Nanomedicine*, vol. 10, pp. 4901–4917, 2015.

[175] P. B. Shete *et al.*, "Magnetic chitosan nanocomposite for hyperthermia therapy application: Preparation, characterization and in vitro experiments," *Appl. Surf. Sci.*,

vol. 288, pp. 149–157, 2014.

[176] V. a Karande *et al.*, "THE ISOLATION AND CHARACTERIZATION OF MAGNETOTACTIC BACTERIA FROM IRON ORE SOIL FOR SYNTHESIS OF MAGNETIC NANOPARTICLES AS POTENTIAL USE IN MAGNETIC HYPERTHERMIA Magnetic Measurements of Soil Enrichment and Cultivation of MTB Induction heating study of Sa," *Int. J. plant, Anim. Environ. Sci.*, vol. 4, no. 2, pp. 321–327, 2014.

[177] E. Alphandéry, S. Faure, O. Seksek, F. Guyot, and I. Chebbi, "Chains of magnetosomes extracted from AMB-1 magnetotactic bacteria for application in alternative magnetic field cancer therapy," *ACS Nano*, vol. 5, no. 8, pp. 6279–6296, 2011.

[178] L. Xiang, J. Wei, S. Jianbo, W. Guili, G. Feng, and L. Ying, "Purified and sterilized magnetosomes from Magnetospirillum gryphiswaldense MSR-1 were not toxic to mouse fibroblasts in vitro.," *Lett. Appl. Microbiol.*, vol. 45, no. 1, pp. 75–81, Jul. 2007.

[179] E. Alphandéry, F. Guyot, and I. Chebbi, "Preparation of chains of magnetosomes, isolated from Magnetospirillum magneticum strain AMB-1 magnetotactic bacteria, yielding efficient treatment of tumors using magnetic hyperthermia.," *Int. J. Pharm.*, vol. 434, no. 1–2, pp. 444–52, Sep. 2012.

[180] Lei Han, S.-Y. Li, Yong Yang, F.-M. Zhao, Jie Huang, and Jin Chang, "Research on the structure and performance of bacterial magnetic nanoparticles.," *J. Biomater. Appl.*, vol. 22, no. 5, pp. 433–448, 2008.

[181] S. Laurent *et al.*, "Magnetic Iron Oxide Nanoparticles: Synthesis, Stabilization, Vectorization, Physicochemical Characterizations, and Biological Applications (vol 108, pg 2064, 2008)," *Chem. Rev.*, vol. 108, no. 6, pp. 2064–2110, 2008.

[182] S. Prijic and G. Sersa, "Magnetic nanoparticles as targeted delivery systems in oncology," *Radiol. Oncol.*, vol. 45, no. 1, pp. 1–16, 2011.

[183] J. M. Byrne *et al.*, "Controlled cobalt doping in biogenic magnetite nanoparticles.," *J. R. Soc. Interface*, vol. 10, no. Iii, p. 20130134, 2013.

[184] R. Jevprasesphant, "The influence of surface modification on the cytotoxicity of PAMAM dendrimers," *Int. J. Pharm.*, vol. 252, pp. 263–266, 2003.

223

[185] J. Sun, Y. Li, X.-J. Liang, and P. C. Wang, "Bacterial Magnetosome: A Novel Biogenetic Magnetic Targeted Drug Carrier with Potential Multifunctions," *J. Nanomater.*, vol. 2011, pp. 1–13, 2011.

[186] J. Sun *et al.*, "Biocompatibility of bacterial magnetosomes: Acute toxicity, immunotoxicity and cytotoxicity," *Nanotoxicology*, vol. 4, no. 3, pp. 271–283, 2010.

[187] H. Deng, X. Li, Q. Peng, X. Wang, J. Chen, and Y. Li, "Monodisperse magnetic single-crystal ferrite microspheres," *Angew. Chemie - Int. Ed.*, vol. 44, no. 18, pp. 2782–2785, 2005.

[188] C. N. Keim, U. Lins, and M. Farina, "Manganese in biogenic magnetite crystals from magnetotactic bacteria," *FEMS Microbiol. Lett.*, vol. 292, no. 2, pp. 250–253, 2009.

[189] J. H. Li *et al.*, "A comparative study of magnetic properties between whole cells and isolated magnetosomes of Magnetospirillum magneticum AMB-1," *Chinese Sci. Bull.*, vol. 55, no. 1, pp. 38–44, 2010.

[190] J. Li, Y. Pan, G. Chen, Q. Liu, L. Tian, and W. Lin, "Magnetite magnetosome and fragmental chain formation of Magnetospirillum magneticum AMB-1: Transmission electron microscopy and magnetic observations," *Geophys. J. Int.*, vol. 177, no. 1, pp. 33–42, 2009.

[191] D. Faivre, L. H. Böttger, B. F. Matzanke, and D. Schüler, "Intracellular magnetite biomineralization in bacteria proceeds by a distinct pathway involving membrane-bound ferritin and an iron(II) species," *Angew. Chemie - Int. Ed.*, vol. 46, no. 44, pp. 8495–8499, 2007.

[192] D. H. Kim, H. Zeng, T. C. Ng, and C. S. Brazel, "T1 and T2 relaxivities of succimer-coated $MFe2^{3+}O_4$ (M=Mn2+, Fe2+ and Co2+) inverse spinel ferrites for potential use as phase-contrast agents in medical MRI," *J. Magn. Magn. Mater.*, vol. 321, no. 23, pp. 3899–3904, 2009.

[193] T. Hyeon, "Chemical synthesis of magnetic nanoparticles," *Chem. Commun.*, no. 8, pp. 927–934, 2003.

[194] B. D. Cullity and C. D. Graham, *Introduction to Magnetic Materials*. 2009.

[195] J. C. Aphesteguy, S. E. Jacobo, N. N. Schegoleva, and G. V Kurlyandskaya, "Characterization of nanosized spinel ferrite powders synthesized by coprecipitation and autocombustion method," *J. Alloys Compd.*, vol. 495, no. 2, pp. 509–512, 2010.

[196] S. A. Gómez-Lopera, R. C. Plaza, and A. V. Delgado, "Synthesis and characterization of spherical magnetite/biodegradable polymer composite particles," *J. Colloid Interface Sci.*, vol. 240, no. 1, pp. 40–47, 2001.

[197] Y. Oh, N. Lee, H. W. Kang, and J. Oh, "In vitro study on apoptotic cell death by effective magnetic hyperthermia with chitosan-coated MnFe2O4," *Nanotechnology*, vol. 27, no. 11, pp. 1–22, 2016.

[198] K. Donadel, M. D. V Felisberto, and M. C. M. Laranjeira, "Preparation and characterization of hydroxyapatite-coated iron oxide particles by spray-drying technique," *An. Acad. Bras. Cienc.*, vol. 81, no. 2, pp. 179–186, 2009.

[199] A. Józefczak, B. Leszczyński, A. Skumiel, and T. Hornowski, "A comparison between acoustic properties and heat effects in biogenic (magnetosomes) and abiotic magnetite nanoparticle suspensions," *J. Magn. Magn. Mater.*, vol. 407, pp. 92–100, 2016.

[200] A. Akbarzadeh, M. Samiei, and S. Davaran, "Magnetic nanoparticles: preparation, physical properties, and applications in biomedicine," *Nanoscale Res. Lett.*, vol. 7, pp. 1–13, 2012.

[201] M. Sytnyk *et al.*, "Tuning the magnetic properties of metal oxide nanocrystal heterostructures by cation exchange," *Nano Lett.*, vol. 13, no. 2, pp. 586–593, 2013.

[202] M. Sincai, D. Ganga, M. Ganga, D. Argherie, and D. Bica, "Antitumor effect of magnetite nanoparticles in cat mammary adenocarcinoma," *J. Magn. Magn. Mater.*, vol. 293, no. 1, pp. 438–441, 2005.

[203] G. Hegyi, G. P. Szigeti, and A. Szász, "Hyperthermia versus oncothermia: Cellular effects in complementary cancer therapy," *Evidence-based Complement. Altern. Med.*, vol. 2013, 2013.

[204] C. C. Berry and A. S. G. Curtis, "Functionalisation of magnetic nanoparticles for applications in biomedicine," *Inst. Phys. Publ.*, vol. 198, no. 36, pp. 198–206, 2003.

225

[205] Thermo scientific, "NHS-Biotin Labeling_Instruction.pdf."

[206] D. F. Barker and A. M. Campbell, "The birA gene of Escherichia coli encodes a biotin holoenzyme synthetase," *J. Mol. Biol.*, vol. 146, no. 4, pp. 451–467, 1981.

[207] J. Xie, K. Chen, and X. Chen, "Production , Modi fi cation and Bio-Applications of Magnetic Nanoparticles Gestated by Magnetotactic Bacteria," *Nano Res*, vol. 2, pp. 261–278, 2009.

[208] A. Barat Bhaswati and Wu., "Metabolic biotinylation of recombinant antibody by biotin ligase retained in the endoplasmic reticulum," vol. 24, no. 3, pp. 283–291, 2007.

[209] J. B. Sun *et al.*, "Preparation and anti-tumor efficiency evaluation of doxorubicin-loaded bacterial magnetosomes: Magnetic nanoparticles as drug carriers isolated from Magnetospirillum gryphiswaldense," *Biotechnol. Bioeng.*, vol. 101, no. 6, pp. 1313–1320, 2008.

[210] M. Calero *et al.*, "Characterization of interaction of magnetic nanoparticles with breast cancer cells," *J. Nanobiotechnology*, vol. 13, no. 1, pp. 1–15, 2015.

[211] Z. Mao, X. Zhou, C. Gao, Z. Mao, X. Zhou, and C. Gao, "Influence of structure and properties of colloidal biomaterials on cellular uptake and cell functions," *Biomater. Sci.*, vol. 1, no. 9, p. 896, 2013.

[212] A. Verma and F. Stellacci, "Effect of surface properties on nanoparticle-cell interactions," *Small*, vol. 6, no. 1, pp. 12–21, 2010.

[213] J. Nam *et al.*, "Surface engineering of inorganic nanoparticles for imaging and therapy," *Adv. Drug Deliv. Rev.*, vol. 65, no. 5, pp. 622–648, 2013.

[214] C. Wilhelm, C. Billotey, J. Roger, J. N. Pons, J. C. Bacri, and F. Gazeau, "Intracellular uptake of anionic superparamagnetic nanoparticles as a function of their surface coating," *Biomaterials*, vol. 24, no. 6, pp. 1001–1011, 2003.

[215] M. C. J. S. A. V. A. G. R. S. V. C. J. S. R. M. M. D. P. Morales, "The endocytic penetration mechanism of iron oxide magnetic nanoparticles with positively charged cover: A morphological approach," *Int. J. Mol. Med.*, vol. 26, pp. 533–539, 2010.

[216] T. R. Pisanic, J. D. Blackwell, V. I. Shubayev, R. R. Fiñones, and S. Jin, "Nanotoxicity of

iron oxide nanoparticle internalization in growing neurons," *Biomaterials*, vol. 28, no. 16, pp. 2572–2581, 2007.

[217] Z. Chen *et al.*, "Acute toxicological effects of copper nanoparticles in vivo," *Toxicol. Lett.*, vol. 163, no. 2, pp. 109–120, 2006.

[218] H. Meng *et al.*, "Ultrahigh reactivity provokes nanotoxicity: Explanation of oral toxicity of nano-copper particles," *Toxicol. Lett.*, vol. 175, no. 1–3, pp. 102–110, 2007.

[219] H. L. Karlsson, P. Cronholm, J. Gustafsson, and L. Moeller, "Copper oxide nanoparticles are highly toxic: A comparison between metal oxide nanoparticles and carbon nanotubes," *Chem. Res. Toxicol.*, vol. 21, no. 9, pp. 1726–1732, 2008.

[220] C. S. S. R. Kumar and F. Mohammad, "Magnetic nanomaterials for hyperthermia-based therapy and controlled drug delivery.," *Adv. Drug Deliv. Rev.*, vol. 63, no. 9, pp. 789–808, Aug. 2011.

[221] S. Laurent and M. Mahmoudi, "Superparamagnetic iron oxide nanoparticles: Promises for diagnosis and treatment of cancer," *Int. J. Mol. Epidemiol. Genet.*, vol. 2, no. 4, pp. 367–390, 2011.

[222] K. Müller *et al.*, "Effect of ultrasmall superparamagnetic iron oxide nanoparticles (Ferumoxtran-10) on human monocyte-macrophages in vitro," *Biomaterials*, vol. 28, no. 9, pp. 1629–1642, 2007.

[223] N. Singh, G. J. S. Jenkins, R. Asadi, and S. H. Doak, "Potential toxicity of superparamagnetic iron oxide nanoparticles (SPION)," *Nano Rev.*, vol. 1, no. 1, p. 5358, 2010.

[224] J. D. C. and A. K. Patri and Franz Gabor, *"Characterization of Nanoparticles Intended for Drug Delivery."* Springer New York Dordrecht Heidelberg London 2011: Humana Press, 2011.

[225] M. B. Abramson and W. T. Norton, "Study of ionic structures in phospholipis by infrared spectra," *J. Biol. Chem.*, vol. 240, no. 6, pp. 2389–2395, 1965.

[226] A. Hanini, A. Schmitt, K. Kacem, F. Chau, S. Ammar, and J. Gavard, "Evaluation of iron oxide nanoparticle biocompatibility.," *Int. J. Nanomedicine*, vol. 6, pp. 787–794, 2011.

[227] C. C. Berry, S. Wells, S. Charles, and A. S. G. Curtis, "Dextran and albumin derivatised iron oxide nanoparticles: Influence on fibroblasts in vitro," *Biomaterials*, vol. 24, no. 25, pp. 4551–4557, 2003.

[228] M. Mahmoudi *et al.*, "A new approach for the in vitro identification of the cytotoxicity of superparamagnetic iron oxide nanoparticles," *Colloids Surfaces B Biointerfaces*, vol. 75, no. 1, pp. 300–309, 2010.

[229] R. T. Liu *et al.*, "Heating effect and biocompatibility of bacterial magnetosomes as potential materials used in magnetic fluid hyperthermia," *Prog. Nat. Sci. Mater. Int.*, vol. 22, no. 1, pp. 31–39, 2012.

[230] J. Huang, X. Zhong, L. Wang, L. Yang, and H. Mao, "Improving the magnetic resonance imaging contrast and detection methods with engineered magnetic nanoparticles," *Theranostics*, vol. 2, no. 1, pp. 86–102, 2012.

[231] N. P. Matylevitch *et al.*, "Apoptosis and accidental cell death in cultured human keratinocytes after thermal injury," *Am. J. Pathol.*, vol. 153, no. 2, pp. 567–577, 1998.

[232] Y. Oh, N. Lee, H. W. Kang, and J. Oh, "In vitro study on apoptotic cell death by effective magnetic hyperthermia with chitosan-coated MnFe2O4," *Nanotechnology*, vol. 27, no. 11, 2016.

[233] M. Timko *et al.*, "Magnetic properties and heating effect in bacterial magnetic nanoparticles," *J. Magn. Magn. Mater.*, vol. 321, no. 10, pp. 1521–1524, 2009.

[234] J. D. Obayemi *et al.*, "Biosynthesis and the conjugation of magnetite nanoparticles with luteinizing hormone releasing hormone (LHRH).," *Mater. Sci. Eng. C. Mater. Biol. Appl.*, vol. 46C, pp. 482–496, Jan. 2015.

[235] G. Baldi *et al.*, "Synthesis and coating of cobalt ferrite nanoparticles: A first step toward the obtainment of new magnetic nanocarriers," *Langmuir*, vol. 23, no. 7, pp. 4026–4028, 2007.

[236] Z. Xiang *et al.*, "Tumor detection using magnetosome nanoparticles functionalized with a newly screened EGFR/HER2 targeting peptide," *Biomaterials*, vol. 115, pp. 53–64, 2017.

[237] M. V. Yigit, A. Moore, and Z. Medarova, "Magnetic nanoparticles for cancer diagnosis and therapy," *Pharm. Res.*, vol. 29, no. 5, pp. 1180–1188, 2012.

[238] H. Bin Na, I. C. Song, and T. Hyeon, "Inorganic nanoparticles for MRI contrast agents," *Adv. Mater.*, vol. 21, no. 21, pp. 2133–2148, 2009.

[239] O. Felfoul, N. Mokrani, M. Mohammadi, and S. Martel, "Effect of the chain of magnetosomes embedded in magnetotactic bacteria and their motility on magnetic resonance imaging," *2010 Annu. Int. Conf. IEEE Eng. Med. Biol. Soc. EMBC'10*, vol. 1, pp. 4367–4370, 2010.

[240] J. T. Jang, H. Nah, J. H. Lee, S. H. Moon, M. G. Kim, and J. Cheon, "Critical enhancements of MRI contrast and hyperthermic effects by dopant-controlled magnetic nanoparticles," *Angew. Chemie - Int. Ed.*, vol. 48, no. 7, pp. 1234–1238, 2009.

[241] T. Araya *et al.*, "Antitumor effects of inductive hyperthermia using magnetic ferucarbotran nanoparticles on human lung cancer xenografts in nude mice," *Onco. Targets. Ther.*, vol. 6, pp. 237–242, 2013.

[242] G. Housman *et al.*, "Drug resistance in cancer: An overview," *Cancers (Basel).*, vol. 6, no. 3, pp. 1769–1792, 2014.

[243] R. Hu *et al.*, "Higher temperature improves the efficacy of magnetic fluid hyperthermia for Lewis lung cancer in a mouse model," *Thorac. Cancer*, vol. 3, no. 1, pp. 34–39, 2012.

[244] E. Alphandéry, S. Faure, L. Raison, E. Duguet, P. A. Howse, and D. A. Bazylinski, "Heat production by bacterial magnetosomes exposed to an oscillating magnetic field," *J. Phys. Chem. C*, vol. 115, no. 1, pp. 18–22, 2011.

[245] R. Cavaliere *et al.*, "Selective heat sensitivity of cancer cells," *Cancer*, vol. 20, no. 9, pp. 1351–1381, 1967.

[246] K. Hayashi *et al.*, "Magnetically responsive smart nanoparticles for cancer treatment with a combination of magnetic hyperthermia and remote-control drug release," *Theranostics*, vol. 4, no. 8, pp. 834–844, 2014.

[247] E. Alphandéry, M. Amor, F. Guyot, and I. Chebbi, "The effect of iron-chelating agents on Magnetospirillum magneticum strain AMB-1: stimulated growth and magnetosome

production and improved magnetosome heating properties.," *Appl. Microbiol. Biotechnol.*, vol. 96, no. 3, pp. 663–70, Nov. 2012.

[248] A. Arakaki, H. Nakazawa, M. Nemoto, T. Mori, and T. Matsunaga, "Formation of magnetite by bacteria and its application," *J. R. Soc. Interface*, vol. 5, no. 26, pp. 977–999, 2008.